

**Investigation of Polishing Algorithms and Removal Processes
for a Deterministic Subaperture Polisher**

by

Christophe Bouvier

Submitted in Partial Fulfillment
of the
Requirement for the Degree
Doctor of Philosophy

Supervised by
Professor Sheryl M. Gracewski
Professor Stephen J. Burns

Department of Mechanical Engineering
The College
School of Engineering and Applied Sciences

University of Rochester
Rochester, New York

2007

Curriculum Vitae

The author was born in Briey, France on March 11, 1980. He attended the Ecole Nationale Supérieure d'Electricité et de Mécanique (ENSEM) in Nancy, France and graduated in 2003 with a French Engineer's degree. He began graduate studies at the University of Rochester in the fall of 2002 as an exchange student from ENSEM. He received a Master of Science degree in 2003. He pursued his research on deterministic polishing of aspheres and ogives with compliant subaperture CNC tools under the direction of Professor Sheryl M. Gracewski and Professor Stephen J. Burns.

Acknowledgements

I want to express my sincere gratitude to my thesis advisors, Professor Sheryl M. Gracewski and Professor Stephen J. Burns. I am thankful for their always relevant criticisms and encouragements. I have learned a great deal from both of them, not only about my research work, but also about life.

I also want to thank Professor John C. Lambropoulos and Paul D. Funkenbusch for their insightful discussions and comments about this research. My gratitude also goes to Professor Stephen D. Jacobs for his encouragements and help on different matters.

I have been very fortunate to collaborate with OptiPro Systems on this exciting research project. Everybody there has always been very helpful. The constant support and patience of Mike Bechtold and Dave Mohring are highly appreciated. I also want to particularly thank Scott Bambrick, Joe Meisenzahl and Scott DeFisher for helping with the machine.

Financial support from Army and Navy SBIRs through OptiPro Systems is greatly appreciated. I thank Dan Harris, Jim Kirsch and Roy Lindberg with the Army and Navy for their interest in my work and support.

I would also like to thank Ed Fess at the Laboratory for Laser Energetics as he was always very helpful. Alex Maltsev has been a great friend during these years, always offering kind words and coffee. The friendship of my successive officemates: Dr. Anka Trajkovska Petkoska, Dr. Jessica DeGroote, Dr. Shai Shafrir, Jerry Cox and Chunlin Miao is also greatly appreciated.

My parents have been supportive as they have always been despite the distance. They and the rest of my family have always highly valued education and they have given everything possible so that I could succeed. For all that I am very thankful.

Last but not least, my wife, Li, who has been wonderfully supportive and patient during all these years, deserves the greatest thanks. This thesis is dedicated to her.

Abstract

This thesis provided a basis for deterministic optical polishing of aspheres and ogives with compliant tools. A new deterministic subaperture computer numerically controlled (CNC) polisher called UltraForm Finishing (UFF) is developed by OptiPro Systems (Ontario, NY). The UltraForm Finishing process was designed to remove midspatial frequency surface errors generated by grinding tools, preserve or correct the form of parts and polish the concave surface of tangent ogives made of tough optical materials. The three main goals of this thesis are 1) to develop polishing algorithms that specify collision free tool paths to correct part form, 2) to investigate a local removal model and 3) to investigate sources of any induced surface errors.

The form of the part after polishing can be predicted by expressing the removal profile as a convolution integral of the tool removal function and crossfeed velocity. For form correction, the inverse problem is solved to obtain a tool crossfeed velocity profile that can achieve a desired removal profile. Explicit expressions for form correction problem were defined for plano and spherical parts. An approximate formulation was introduced for aspheres and ogives. The form correction problem was solved as a constrained optimization problem using regularization to achieve feasible solutions and overcome ill-conditioning.

Algorithms establishing a collision free tool path have been developed. For that purpose, a two-dimensional model was introduced to detect tool-part collisions. Search strategies were defined to adjust the tool position and prevent such collisions.

Some properties of the UFF removal function have been characterized. It was shown that a generalized form of Preston's equation combined with Hertz contact mechanics theory predicts fairly accurately the removal function for hard tools and convex surfaces over a range of process parameters.

Errors that can produce discrepancies between actual and predicted removal profiles were modeled. Their effects were examined with numerical simulations and shown to depend strongly on the removal function. A diagnostic method was developed to determine the origin of spiral marks induced by UFF. These spirals are formed of discrete marks left on the part by the tool at a constant frequency. The method establishes all the possible frequencies that can create a given pattern and identifies the relevant one. The method was successfully used to identify the frequency that generated spiral marks in a series of experiments and lead to the discovery of a tool defect.

Table of Contents

<u>Chapter 1</u> Introduction	1
1.1 Aspherical and conformal optics	2
1.2 Grinding, polishing and deterministic solutions	4
1.3 UltraForm Finishing	11
1.4 Thesis overview	15
1.5 References	19
Figures	27
<u>Chapter 2</u> Form correction problem	33
2.1 Forward problem	33
2.1.1 Equations for the depth of removal on flats and spheres	34
2.1.2 Model validation	36
2.2 Inverse problem	37
2.2.1 Formulation of the problem	37
2.2.2 Review of approaches reported in the literature	38
2.2.3 Solution to the form correction problem	42
2.2.3.1 Matrix formulation of the form correction problem	42
2.2.3.2 Computing \underline{RM}	44
2.2.3.3 Solving for \underline{sc}	46
2.3 References	53
Figures	57
<u>Chapter 3</u> Tool path geometry determination	66
3.1 Definition and preferred configuration	66
3.2 Preventing tool-part collisions	69
3.2.1 2D symmetric model	69
3.2.1.1 Geometry	69
3.2.1.2 Operations to determine tool-part collisions	75

3.2.2 <i>B</i> angle search strategies	82
3.3 Tool pivot point coordinates	87
3.4 Experimental validation	88
3.5 References	89
Figures	90
<u>Chapter 4</u> Removal function	112
4.1 Definition	112
4.2 Local material removal model	113
4.2.1 Preston's equation	113
4.2.2 Generalized form of Preston's equation	114
4.2.3 Model for UFF	115
4.3 Hertz contact mechanics theory	124
4.3.1 Surfaces of the bodies in contact	124
4.3.2 Pressure distribution	128
4.3.3 Size of the contact and load-displacement relation	129
4.3.4 Some simplifications and procedure to predict interfacial pressures and contact patch dimensions in the case of UFF	131
4.3.5 Experimental results	132
4.3.5.1 Preliminary results	132
4.3.5.2 Applicability of Hertz contact mechanics theory to UFF	134
4.3.5.2.1 Removal spots making experiment	134
4.3.5.2.2 Load displacement relationship	136
4.3.5.2.3 Pressure distribution	138
4.3.5.2.4 Removal function size and amplitude	140
4.4 Alternative to the prediction of the removal function	141
4.5 Other properties of UFF removal	143
4.5.1 Effect of α	143
4.5.2 Effect of the workpiece material	145

4.6 References	146
Figures	150
<u>Chapter 5</u> Surface errors	164
5.1 Surface roughness and subsurface damage (SSD)	164
5.2 Figure error	166
5.2.1 Sources of form errors	166
5.2.2 Approach for the evaluation of the effect of the errors	168
5.2.3 Numerical simulations	172
5.3 Midspatials frequency errors and diagnostic of induced spiral marks	176
5.3.1 Experimental procedure and characterization of the induced marks	177
5.3.2 Model for the generation of the marks and simulation tool	178
5.3.3 Evaluation of candidate frequencies and simulations	182
5.3.4 Establishing the values of f_{marks} generating a given pattern	186
5.3.5 Results for the experimentally observed spirals	193
5.3.6 Summary of the diagnostic method for induced residual marks	195
5.4 References	196
Figures	199
<u>Chapter 6</u> Summary and suggestions for future work	221
6.1 Summary	221
6.2 Suggestions for future work	225
6.2.1 Form correction	226
6.2.2 Tool path geometry	231
6.2.3 Removal function	231
6.3 References	234
<u>Appendices</u>	236
Appendix 1 Initial operations	236

1.1 Description	236
1.2 Profile discretizer	239
1.3 Part principal radii of curvature	244
Appendix 2 MATLAB code for tool path geometry	253

List of Tables

<u>Table</u>	<u>Title</u>	<u>Page</u>
Table 3.1	Error codes and their causes.	83
Table 4.1	Three removal models for CMP.	115
Table 4.2	Removal spots parameters and corresponding values of C_{GP} .	120
Table 4.3	Simplifications for the contact of the part and tool.	132
Table 4.4	Carrier wheels durometer and tool geometry.	135
Table 4.5	Process parameters used to make the removal spots.	135
Table 4.6	Properties of the removal spots.	136
Table 4.7	Coefficient used to fit the load displacement curves and resulting tool mechanical properties.	138
Table 4.8	Results of fitting Eq. (4.34) to the different removal spots.	140
Table 4.9	Table 4.9 Theoretical size and depth of the removal spots.	140
Table 4.10	Coefficients defining the asphere polished with UFF.	143
Table 4.11	Values of β and standard deviation for different values of α .	145
Table 4.12	Mechanical properties and FOM of SF6, FS, BK7 and LaF2.	146
Table 5.1	Surface errors definition and possible sources. (Adapted from [2])	164
Table 5.2	Potential sources of form errors, their cause and effect.	168
Table 5.3	Sources of form errors, model and simulation for flats.	171
Table 5.4	Variable names and descriptions of the calculated candidate frequencies	185
Table 5.5	Values of the calculated and measured frequencies and corresponding number of marks (*for half of a 20 mins run).	186
Table 5.6	Values of the frequencies creating the 3 spiral pattern of Figure 5.19 and corresponding number of marks (*for half of a 20 mins run).	193
Table 5.7	Values of the frequencies creating the 12 spiral pattern of Figure 5.13.b) and corresponding number of marks (*for half of a 20 mins run).	195

List of Figures

<u>Figure</u>	<u>Title</u>	<u>Page</u>
Figure 1.1	Geometry of a tangent ogive.	27
Figure 1.2	Views of UFF a) on CNC platform; b) close up.	28
Figure 1.3	Figure 1.3 Compliance of the tool and removal of cutter marks.	29
Figure 1.4	Hemisphere polishing and geometry definition.	30
Figure 1.5	Schematic of the tool path.	31
Figure 1.6	Tool position definition.	31
Figure 1.7	Flow chart of the UFF process.	32
Figure 2.1	Geometry of the problem for flats.	57
Figure 2.2	Geometry for spheres polishing.	57
Figure 2.3	Linear relation between removal spot volume and spot dwell time.	58
Figure 2.4	Removal spot used for comparison between predicted and actual depth of removal.	58
Figure 2.5	Comparison between the predicted depth of removal and the actual part profile.	59
Figure 2.6	Polishing with a subaperture lap.	59
Figure 2.7	Mapping of the removal function on the workpiece.	60
Figure 2.8	Tool crossfeed velocity obtained with Eq. (2.24) for uniform removal of 5 μm on flat using the removal spot of Figure 2.9.	60
Figure 2.9	Removal spot used to compute the solutions of Figure 2.8.	61
Figure 2.10	Tool crossfeed velocity solution and predicted removal profile with the MATLAB function fmincon.m.	61
Figure 2.11	Tool crossfeed velocity proportional to $1/y_0$ and predicted removal profile.	62
Figure 2.12	Tool crossfeed velocity approximation for uniform removal and predicted removal profile.	63
Figure 2.13	Tool crossfeed velocity solution and predicted removal profile with the form algorithms developed for UFF.	64

Figure 2.14	Wavefront map of a part polished uniformly using the form algorithms developed for UFF.	65
Figure 3.1	Definition of the parameters for the tool path geometry.	90
Figure 3.2	Feasible tool path with $\alpha = 0$ on a convex part.	90
Figure 3.3	Unacceptable tool-part collision for a tool path with $\alpha = 0$ on a concave part.	91
Figure 3.4	Front view of UFF Army configuration.	92
Figure 3.5	Bottom view of UFF Army configuration.	92
Figure 3.6	Left view of UFF Army configuration.	93
Figure 3.7	Right view of UFF Army configuration.	93
Figure 3.8	Front view of UFF Navy configuration.	94
Figure 3.9	Bottom view of UFF Navy configuration.	94
Figure 3.10	Left view of UFF Navy configuration.	95
Figure 3.11	Right view of UFF Navy configuration.	95
Figure 3.12	Illustration of tool interior region definition.	96
Figure 3.13	Geometry of the tool 2D model a) Tool interior region and points and dimensions used for its definition; b) Tool safety region and points defining the 2D model.	97
Figure 3.14	Geometry to define $y_{P'_2}$.	98
Figure 3.15	Geometry to define Δb .	98
Figure 3.16	2D model used to define the tool path geometry.	99
Figure 3.17	Points and regions defining the tool full 2D model.	100
Figure 3.18	Regions and equations used to define the tool interior region.	101
Figure 3.19	Overall flow chart for safe B angles search.	102
Figure 3.20	Flow chart of the <i>Concave</i> algorithms.	103
Figure 3.21	Strategy for adjusting B on concave parts a) solution B_{j-1} at y_{0j-1} ; b) tool and part normals aligned at y_{0j} ; c) using solution B_{j-1} at y_{0j} ; d) solution B_j at y_{0j} after increasing B .	104
Figure 3.22	Flow chart of the <i>Convex</i> algorithms.	105
Figure 3.23	Flow chart of the <i>Generic</i> algorithms.	106

Figure 3.24	Flow chart of the <i>Generic1</i> algorithms.	107
Figure 3.25	Flow chart of the <i>Generic2</i> algorithms.	108
Figure 3.26	Hemispherical PCA dome.	109
Figure 3.27	Plots of the tool path for the concave surface of a hemisphere of diameter 67.5 mm.	110
Figure 3.28	Plot of the B angles used to polish the concave surface of a hemisphere of diameter 67.5 mm.	111
Figure 3.29	Plot of the difference between the B angles used to polish the concave surface of a hemisphere of diameter 67.5 mm and the angle of the local part normal.	111
Figure 4.1	Structure of the Tekscan system. (Figure adapted from [18])	150
Figure 4.2	Geometry of the Tekscan system. (Figure adapted from [19])	150
Figure 4.3	Removal spot volume versus applied load and linear fit.	151
Figure 4.4	Removal spot volume versus band velocity and linear fit.	151
Figure 4.5	Removal spot volume versus band velocity and power fit.	152
Figure 4.6	Illustration of v_{rel} as a function of (x, y, y_0) on a flat.	152
Figure 4.7	Definition of the surface used to model a contacting body in Hertz theory.	153
Figure 4.8	Geometry of the part and tool motion.	153
Figure 4.9	Geometry used for the definition of R_{Px} .	154
Figure 4.10	Carrier wheel geometry.	154
Figure 4.11	Principal radii of curvature of the tool.	155
Figure 4.12	Tool profile in the plane x_T-z_T showing the anticlastic curvature of the polishing band.	155
Figure 4.13	Contact of the part and the tool in the x_T-z_T and y_T-z_T planes.	156
Figure 4.14	Geometry of the contact patch.	156
Figure 4.15	Hertz pressure distribution.	157
Figure 4.16	Functions of interest for Hertz theory. (Figure adapted from [26])	157
Figure 4.17	High speed camera frames revealing the inconsistency of the contact patch on the first version of UFF.	158

Figure 4.18	High speed camera frames showing the consistency of the contact patch.	158
Figure 4.19	High speed camera frames for the tool at $\Omega_T = 0, 50$ and 500 rpm.	159
Figure 4.20	Tekscan measurement of the interfacial pressures encountered with the V2 tool.	159
Figure 4.21	STIL measurement of a removal spot made with the V2 tool.	159
Figure 4.22	Removal spots made with the process parameters reported in Table 4.5.	160
Figure 4.23	Load displacement curve in the conditions of the removal spot number 6. Data in red, theoretical curve in blue.	161
Figure 4.24	Desired form of an asphere polished with UFF.	161
Figure 4.25	Form errors of the asphere polished with UFF a) initial; b) final.	162
Figure 4.26	Removal rate versus mechanical figure of merit.	163
Figure 5.1	Principle of the numerical simulations.	199
Figure 5.2	Detailed procedure for the numerical simulations.	200
Figure 5.3	Static removal functions used for numerical simulations.	201
Figure 5.4	Error free removal function and induced alterations a) error free removal function; b) shift in x by $\Delta x = 1$ mm; c) shift in y by $\Delta y = 1$ mm; d) size scaling, new size is 0.9 times the original size; e) amplitude scaling, new amplitude is 1.1 times the original amplitude.	202
Figure 5.5	Effect of shifts in x of the elliptical Hertzian removal function a) error-free elliptical Hertzian removal function; b) desired, reference and actual profiles for $\Delta x = 1$ mm; c) desired, reference and actual profiles for $\Delta x = -1$ mm.	203
Figure 5.6	Effect of shifts in y of the elliptical Hertzian removal function a) error-free elliptical Hertzian removal function; b) desired, reference and actual profiles for $\Delta y = 1$ mm; c) desired, reference and actual profiles for $\Delta y = -1$ mm.	204
Figure 5.7	Effect of shifts in x of the real removal function a) error-free removal function; b) desired, reference and actual profiles for $\Delta x = 1$ mm; c) desired, reference and actual profiles for $\Delta x = -1$ mm.	205

Figure 5.8	Effect of shifts in y of the real removal function a) error-free removal function; b) desired, reference and actual profiles for $\Delta y = 1$ mm; c) desired, reference and actual profiles for $\Delta y = -1$ mm.	206
Figure 5.9	Effect of a change in amplitude of the removal function.	207
Figure 5.10	Effect of a change in size of the removal function while the volumetric removal rate is kept constant a) desired, reference and actual profiles with size and amplitude multiplied by 0.9 and 1.25, respectively; b) desired, reference and actual profiles with size and amplitude multiplied by 1.1 and 0.83, respectively.	208
Figure 5.11	Effect of a systematic clock error.	209
Figure 5.12	Effect of two simultaneous errors, $\Delta x = 1$ mm and $\Delta y = 0.75$ mm.	209
Figure 5.13	Raw and filtered measurement of part polished at 300 rpm a) interferometric measurement; b) after high pass average filtering.	210
Figure 5.14	Composite images showing the induced marks at a) 100 part rpm; b) 500 part rpm.	211
Figure 5.15	Piecewise linear functions for $r_{\text{tool}}(t)$ and $\theta_{\text{part}}(t)$.	211
Figure 5.16	Geometry of a ball bearing. (Figure taken from [19])	212
Figure 5.17	Power spectral density (PSD) plots for actual vibrations measurements in the x and y directions.	213
Figure 5.18	Simulations with the 9 candidate frequencies of table 5.5.	214
Figure 5.19	3 spirals patterns achieved with the tool path file used to polish the part shown in Figure 5.13, $f_{\text{part}} = 5$ Hz and a) $f_{\text{marks}} = 15.05$ Hz; b) $f_{\text{marks}} = 0.5 * 15.05 = 7.525$ Hz.	215
Figure 5.20	Schematic of a part with a pattern consisting of 4 segments.	215
Figure 5.21	3 spirals patterns achieved with the 6 lower frequencies of Table 5.6.	216
Figure 5.22	Observed and simulated patterns with $f_{\text{marks}} = 59.9$ Hz and part at 300 rpm.	217
Figure 5.23	Plots of the candidate frequencies: calculated, measured and predicting the observed pattern.	217
Figure 5.24	Observed and simulated patterns with $f_{\text{marks}} = 59.9/7$ Hz and part at 100 rpm.	218

Figure 5.25	Observed and simulated patterns with $f_{\text{marks}} = 59.9/7$ Hz and part at 500 rpm.	218
Figure 5.26	Observed and simulated patterns with $f_{\text{marks}} = 59.9/7$ Hz, part at 300 rpm and scratches of constant length equal to 0.8 mm.	219
Figure 5.27	Observed and simulated patterns with $f_{\text{marks}} = 59.9/7$ Hz, part at 100 rpm and scratches of constant length equal to 0.8 mm.	219
Figure 5.28	Observed and simulated patterns with $f_{\text{marks}} = 59.9/7$ Hz, part at 500 rpm and scratches of constant length equal to 0.8 mm.	220
Figure 6.1	Edge strategy.	230
Figure A.1	Illustration of approximation to establish points spaced by the desired arc length.	242
Figure A.2	Illustration of the use of intermediate points to improve the arc length spacing between the selected points.	242
Figure A.3	Numerical approximation of R_{Px} .	249
Figure A.4	Coordinate systems (x, y, z) and (x_T, y_T, z_T) .	250

Chapter 1 Introduction

Aristophanes' play *The Clouds* mentions a burning-glass used to produce fire from the sun, which is believed to be a convex lens focusing the sun's rays. If this is true, then this play, dated 424 BC, is the earliest written records of a lens. It is unknown how Aristophanes' lens was produced. Since then, the principles of optics have been established and lenses have found multiple uses, for example in spectacles, telescopes and microscopes. Fabrication of precision optics has evolved as the demand and applications grew. However, for centuries most lenses were spherical. Only during the last few decades, the need for better imaging or aerodynamic performance has stimulated the development of efficient solutions for the production of aspherical and conformed optics. These geometries and their applications are described in Section 1.1. Even though these shapes differ from the traditional spheres, they are also produced according to the traditional steps of optical fabrication which are grinding and polishing. These processes are defined in Section 1.2. In addition to the need for new shapes, higher accuracy and reduction in production time are required. For that purpose deterministic processes have been developed. Existing deterministic solutions for grinding and polishing of precision optics are also reviewed in Section 1.2. UltraForm Finishing, a new deterministic polishing apparatus, is presented in Section 1.3. Section 1.4 summarizes the overview of this thesis.

1.1 Aspherical and conformal optics

Optics with spherical surfaces have long been the primary choice for optical designs. However, it is known that a plano-convex lens with a spherical surface does not focus all incoming rays at a perfect point. This focus error is called spherical aberration as it is due to the spherical shape of the lens. Designers have to use several optical elements to compensate for spherical aberrations. On the other hand, a plano-convex lens with an aspheric surface can theoretically focus all incoming light rays to a single point. The profile, z_{Part} , of these axisymmetric surfaces is defined as a function of the radial distance, r , from its center by the aspheric equation

$$z_{Part}(r) = \frac{Cr^2}{1 + (1 - (K + 1)C^2r^2)^{1/2}} + A_3r^3 + A_4r^4 + A_5r^5 + \dots, \quad (1.1)$$

where the first term describes a conic surface, defined by its conic constant, K , and curvature, C , which is equal to the inverse of the radius of curvature. A_3, A_4, A_5, \dots are the aspheric deformation constants. Aspheres allow high performance with a minimum number of lens elements [1, 2]. The reduced number of components translates into easier mounting, lighter assembly and potentially lower cost and higher reliability than with multiple spherical optical elements. However, spherical optics have wide acceptance because their manufacturing is well controlled. Manufacturing of high quality aspheric optics was expensive and difficult until the development of recent commercial processes. These processes, which are reviewed later in this Chapter, initiated a more common use of aspheres by optical designers. However,

because of current limitations, none of these processes has yet become a standard in the industry.

Conformal optics also require non spherical shapes but for benefits other than optical. These optics interface to the environment and are shaped for optimal aerodynamics, rather than forced to fit commonly used optical shapes [3]. Conformal shapes are of particular interest for military applications, for example, for the front ends of projectiles. Because of manufacturing considerations, a section of a sphere is conventionally used for that purpose. However this form produces considerable aerodynamic drag [3]. Replacing a spherical front end with a tangent ogive shape will make the projectile more aerodynamically efficient and therefore improve speed and range. A tangent ogive is axisymmetric and its profile is formed of two arcs of a circle tangent to the projectile body at its base. This shape is illustrated in Figure 1.1. The profile of an axisymmetric tangent ogive shape is given by

$$z_{part}(r) = \sqrt{R_C^2 - (|r| + R_C - d_B / 2)^2} - \sqrt{d_B(R_C - d_B / 4)}, \quad (1.2)$$

where R_C is the radius of the circle and d_B is the base diameter of the ogive. Eq. (1.2) is the equation of a half circle of radius R_C translated so that the tip of the ogive is located at the origin ($r = z_{part} = 0$). Similar to aspheres, polynomial terms can be added to refine the shape. The aerodynamics and environmental constraints also require that these conformal parts must be made of tough materials. The combination of hard materials and extreme shapes makes the manufacturing of these conformal optics challenging.

1.2 Grinding, polishing and deterministic solutions

Optical surfacing is the process by which a surface suitable for optical applications is produced. Grinding and polishing are the two processes on which optical surfacing is based. During grinding, the workpiece is shaped using a rapid material removal technique which leaves the surface in a microscopically rough state. The purpose of polishing is to correct the form and reduce the roughness of the surface to meet the desired specifications. Subsurface damages (SSD) and midspatial frequency errors left from grinding must also be removed. Midspatial frequency errors are errors such as tool marks with spatial frequencies intermediate to the spatial frequencies of surface roughness and form errors. Grinding and polishing are typically accomplished in such a way that successively finer abrasives are applied to successively remove the SSD created by a given stage and gradually improve the surface.

Optical fabrication is challenging, because optical glasses and ceramics are typically brittle materials and the form and roughness specifications required by precision optics are very demanding. The consequence is that for a long time, grinding and polishing have been labor intensive, requiring specialized tooling and processes used by skilled opticians to fabricate precision surfaces. To make low, mid and large volume production of various aspherical and conformal shapes cost effective, it was necessary to invent new fabrication methods. The goal of these methods is to make optical surfacing fully deterministic. This means removing

randomness from the fabrication process. For that purpose, optical fabrication is examined on a scientific level with advanced technology rather than on the intuitive level of the experienced optician. This is achieved by establishing the effect of different process parameters. These parameters must then be set appropriately and controlled during the process to achieve the desired goal. The emergence of computer numerically controlled (CNC) machining centers made it possible to introduced determinism into the production of precision optics.

Deterministic grinding is a reality. The Center for Optics Manufacturing at the University of Rochester has made significant contributions to the development of deterministic microgrinding for the fabrication of precision optics [4-10]. Deterministic microgrinding uses rigid, computer numerically controlled (CNC) machining centers and high speed tool spindles. A bound diamond abrasive tool is positioned by a CNC machine to generate plano, spherical, or aspherical surfaces. The motion and position of the microgrinding tool on the optical workpiece is imposed by taking advantage of precise speed and positional control on the CNC machine. Because the tooling and machine are nearly rigid, all the material in the tool's path is removed. Therefore, the tool path determines the workpiece surface shape and the amount of removed material is ideally precisely known.

Two types of grinding tools are commonly used. Ring tools are cup shaped with a rim that consists of either a metal, resin or vitrified annular matrix in which diamonds are embedded [9]. The ring tool is inclined so that its edge cuts and shapes

plano and spherical parts of various radii of curvature. Contour grinding can be used to generate aspheric surfaces as well as flats and spheres. For contour grinding, the tool is a disk having on its periphery a metal, resin or vitrified matrix with embedded diamond abrasives [9]. However, grinding of shapes such as deep concave domes can be impossible with this tooling. Special tooling, such as ball tools, is needed for that purpose.

Typically as one workpiece is ground, several tools are used with diamonds in the range 100 microns down to 2-4 microns. Each tool is used to remove the damaged layer or SSD resulting from the previous tool and to progressively reduce the surface roughness. Deterministic microgrinding is able to produce parts with a very good form accuracy (0.3 μm peak-to-valley (PV)), low surface roughness (30-100 \AA) and SSD (under 1 μm) [6]. Deterministic microgrinding can generate surfaces with minimum defects requiring short polishing times.

Single point diamond turning can also achieve deterministic grinding of optics. This process uses a gem quality single crystal diamond tool on a precision lathe [11]. As for deterministic microgrinding, rigid accurate CNC machines are required. Diamond turning was initially developed for metals and in particular lens molds production. It is a promising process for grinding of optical materials as it is capable of submicrometer form accuracy and surface roughness in the nanometer range [12, 13]. However, diamond turning can induce considerable SSD [14] and tool wear is a serious issue [11, 12, 15]. Tool wear is excessive in diamond turning of optical glasses because of the brittle nature of the material and relatively small

surface area of the tool which is in permanent contact with the part. Tool life can be improved by applying ultrasonic vibration to the diamond cutting tool [12, 15, 16]. These vibrations reduce tool-part contact time and permit better cooling and lubrication. Tool wear can also be reduced with heat assisted cutting [12], as the part material becomes less brittle when heated.

Even though deterministic polishing processes have been under development since the 1970s, commercial deterministic aspheric polishers have only been available since the 1990s. This long development time is explained by the very challenging nature of the polishing operation.

The earliest approaches considered for deterministic polishing were inspired by conventional polishing, which uses contact tools made of elastic materials such as pitch that precisely conform to the workpiece surface. Computer Controlled Polisher (CCP) [17-20] and Computer Assisted Optical Surfacing (CAOS) [21-24] were developed in the 1970s at the PerkinElmer [25] and now defunct Itek Corporations, respectively. They use a small pitch polishing tool, which is moved by a CNC platform to remove high points on a large optic. Canon [26] Super Smooth Polisher (CSSP) [27, 28] developed in the 1990s uses the same principle. These apparatus are not appropriate for polishing of extreme shapes such as conformal optics and remain proprietary to the respective companies.

Another technology inspired by traditional polishing uses a stressed lap. It was developed for large optics at University of Arizona [29-31]. The lap changes shape

actively to follow the local curvature of the optics. A similar apparatus is also used at the Nanjing Institute of Astronomical Optics in China [32, 33]. These technologies are not commercially available and are not appropriate for polishing deep concave surfaces.

Processes using an ion beam that bombards a part in vacuum to achieve material removal have been considered. The surface is shaped by sputtering. Wilson et al. at the University of New Mexico [34, 35] reported on their ion beam figuring method in the late 1980s. A similar process was developed at Eastman Kodak with the name Ion Figuring System (IFS) [36, 39], as well as at the German Institut für Oberflächenmodifizierung (IOM - Institute for Surface Modification) named Ion Beam Etching (IBE) [40-42]. Fawcett and Bifano at Boston University have also been involved in the development of the Precision Ion-Machining System (PIMS) [43, 44] at NASA's Marshall Space Flight Center. None of these machines have become commercially available. Ion beam figuring is advantageous over contact polishing because there is no edge effect and the removal is well characterized and near Gaussian, which is practical for figure correction. However, this process figures and does not smooth [45], therefore it cannot improve the surface roughness of the part. Furthermore ion beam figuring is well suited for large optics but not for the concave surface of conformal optics and has the disadvantage of requiring vacuum chambers.

Chemical etching is another material removal mechanism that has been considered. It was first used for Plasma Assisted Chemical Etching (PACE) [46-49] at PerkinElmer [25] in the late 1980s. Nikon [50] and Osaka University collaborated

to develop Plasma Chemical Vaporization Machining (CVM) [51-53]. Reactive Atom Plasma (RAP) [54-56] is a similar technology in use at RAPT industries [57]. These three apparatus have been developed for precision optics. Chemical etching is rapid and produces damage free surfaces resulting in high laser damage threshold values [56]. However, the nozzle at the tip of which the plasma is generated has to remain perpendicular to the etched surface [52]. It also requires the selection of a gas reacting properly with the workpiece material [52] and tends to increase surface roughness because of varying etching rates at damage sites, grain boundaries, etc. [55]. Because of these two characteristics, these processes are inappropriate for deep concave surfaces and materials prone to grain highlighting such as aluminum oxynitride, ALON [58], which is of interest for ogives. These processes are best suited for specific applications. CVM and RAP are not commercially available. PACE became commercially available for precision shaping of ultra-flat silicon wafers and silicon-on-insulator wafers [49]. RAP is principally used for silicon carbide optics.

HyDra [59-62] developed at the Universidad Nacional Autónoma de México (National Autonomous University of Mexico) is a hydrodynamic tool that uses a flow of slurry to achieve removal. The flow exits a disk tangentially to the surface of the workpiece, creating an annular tool footprint. This technology is not commercially available and, because of the tool size, it is not appropriate for deep concave surfaces.

Only two technologies have been commercially available for polishing precision aspheres. They are QED Technologies [63] Magneto-rheological Finishing (MRF) [64-66] and the Zeeko [67] Precessions process [68-71]. Both are

tribochemical processes. MRF was developed in part at the Center for Optics Manufacturing in the mid 1990s and commercialized by QED Technologies starting in 1997 [45]. In MRF, a magnetorheological fluid consisting of nonmagnetic polishing abrasives and carbonyl iron particles in water is circulated on a wheel. The fluid stiffens when subjected to a magnetic field, creating a polishing tool. The consistency of the tool footprint makes MRF a very good solution for fine form correction. The Precessions process is more recent and the result of a collaboration between University College of London, Zeeko and Satisloh [72]. It uses bound abrasive commercial polishing pads or polyurethane pads with abrasive slurries. The pads are mounted on a spherical pressurized membrane. That membrane is rotated against the part at discrete precession angles to produce a near-Gaussian tool footprint. A combination of consistent tool footprints and efficient softwares make MRF and “Precessions” highly suitable for most conventional aspheres. However, neither process can remove midspatial frequency errors such as cutter marks left by the rigid tools used during grinding. They are also not appropriate for polishing deep concave workpieces.

Two processes based on fluid jet have potential for polishing conformal optics. By using jets, removal can be achieved on the concave surface of an ogive. Delft Technical University in Holland and Fisba Optik [73] collaborated to develop Fluid Jet Polishing (FJP) [74-76]. FJP uses abrasive loaded slurry which is sprayed through a nozzle onto the workpiece surface. QED Technologies has developed MR Jet [77-79] specifically for the polishing of conformal ogives. A magnetic field is

used to stabilize the magnetorheological fluid which exits the apparatus' nozzle. The added stability makes removal highly deterministic. However, both MR Jet and FJP are not yet commercially available. In addition, the footprint is small resulting in low removal rates and midspatial frequency errors can not be corrected.

Therefore, there is currently no solution available for satisfactory polishing of steep concave surfaces of ogives made of tough materials. Because there is a demand for such shapes, a rapid process, able to correct form errors and remove cutter marks is needed. Successful polishing of such shapes should also guarantee similar performance on most aspheres. This would make such a process very desirable for the optical fabrication industry and therefore, make that process commercially viable. By combining that process with deterministic grinding, a fully deterministic process for the fabrication of spherical, aspherical and conformal surfaces would be achieved.

1.3 UltraForm Finishing

UltraForm Finishing (UFF) is a deterministic CNC polisher developed by OptiPro Systems [80] with the University of Rochester. It is designed to meet the current needs for aspherical and conformal optics polishing. For that purpose, it must reduce the surface roughness and remove midspatial frequency surface errors generated by stiffer grinding tools. It must also preserve or correct the form of parts and be able to polish the inside surface of tangent ogives.

Figure 1.2 shows the CNC platform and a close up of the UFF tool. The tool is composed of a carrier wheel made of polyurethane, a rubberlike material, that circulates a belt of polishing material and deforms when the tool is pressed against the workpiece. Removal is created by the relative motion between the part and the abrasive material that is pressed against the part. The tool footprint is much smaller than the polished optics, therefore UFF, like all the polishers reviewed in Section 1.2, is a subaperture polishing process.

UFF has an elongated shape due to the geometry of the shaft supporting the carrier wheel. Its design makes UFF capable of polishing the inside surface of deep domes. The concave surface of tangent ogives presents a tip that is inaccessible to UFF, because of the size of the carrier wheel. However, it is not necessary to polish the central region of ogives, since their tip will be removed before or after polishing. The rest of the part surface, that must be polished, can be reached by UFF.

The tool compliance can be tuned by selecting the durometer, measured on the A scale, of the carrier wheel. The requirement for surface roughness reduction and cutter marks removal is met by adjusting the compliance and tool footprint. A soft wheel would produce a smoothing effect, while a hard wheel would result in higher removal rates. Hard wheels are of particular interest for tangent ogives which are made of tough, hard materials like aluminum oxynitride, ALON, or fine grained polycrystalline alumina, PCA. The durometer of the wheel will also affect the extent of the contact patch. To remove cutter marks, a footprint larger than the marks' spacing and preferential wear at the top of the marks are needed. Compliant tools

imply a large contact patch, however if the tool is too compliant, it might conform to the cutter marks and result in uniform removal below the patch, thus preserving the cutter marks. Therefore, the tool compliance needs to be tuned to conform to the surface and achieve higher removal near the top of the marks. These different cases are illustrated in Figure 1.3. UFF offers the flexibility needed to achieve the appropriate configuration. Furthermore, the removal rate and extent of the tool footprint can be varied by adjusting the tool compression. The potential of UFF to reduce surface roughness and remove mid-spatial frequency surface errors has been demonstrated [58] and is not the subject of this thesis.

A large variety of abrasives can be used with UFF. These abrasives consist of either a band of bound abrasive (e.g. cerium or aluminum oxide TrizactTM from 3M [81]) or abrasive slurry for which a polyurethane band is used. A band is transformed into the needed belt by splicing its ends together.

The parameters adjustable on UFF create many process options. This is advantageous for establishing a polishing solution that will produce a desired surface finish for a given material. As for deterministic microgrinding, different abrasives, wheel durometers and tool compressions could be used successively to progressively reduce surface roughness and achieve finer correction.

For onboard measurement of the tool footprint and part form, a retractable non-contact profilometer, STIL [82] optical pen, is mounted on the tool. Its operation is based on the chromatic-coded confocal imaging principle [83]. The pen model OP

300VM, which permits a depth of field of 300 μm and an accuracy of 90 nm [84], is used.

The initial goal with UFF is to polish and correct rotationally symmetric form errors of axisymmetric workpieces. The coordinate system (x, y, z) , shown in Figure 1.4, where UFF polishes a hemisphere, is attached to the CNC platform. z is the axis of rotation of the workpiece and is oriented positively upward. x is parallel to the axis of rotation of the carrier wheel and oriented positively toward the front of the platform. The origin of (x, y, z) is the center of the workpiece surface. The entire surface of the workpiece is polished as the tool traverses the part along y with crossfeed velocity, v_c . The workpiece and the carrier wheel rotate at the rotational speeds Ω_w and Ω_T , respectively, as illustrated in Figure 1.5. The simultaneous motions of the tool and the part produce a spiral tool path. The position of the tool as it traverses the part is defined by the location of the center of the contact patch as y_0 , as illustrated in Figure 1.6. Precise tool-workpiece contact is achieved by using the accurate positioning and motions capabilities of the CNC platform. The tool can be rotated around its B axis that is parallel to x to achieve a desired contact angle with the workpiece. Tool x , y and z translations are also available.

UFF compliant polishing as considered in this thesis is accomplished with a soft tool and a large contact patch. As for the polishers reviewed in Section 1.2, the material is removed by controlling the dwell time that the polisher resides over a particular spot on the part. The tool dwell time is controlled by varying v_c . To achieve form correction, an appropriate tool crossfeed velocity needs to be established. For

that purpose, the tool footprint must be taken into account. The tool footprint can be evaluated by dwelling on a stationary part to generate a removal spot. The topography of the resulting spot divided by the dwell time used to create that spot is a map of the removal rate or static removal function c_{ST} .

1.4 Thesis overview

The objective of this thesis is to provide a basis for deterministic polishing with UFF with an emphasis on ogive polishing. The main purpose of this work is the development of algorithms creating a tool path for axisymmetric workpieces. The tool path not only defines the spatial positions occupied by the tool during polishing but also the tool crossfeed velocity profile. The present work is also applicable to other deterministic polishers.

The steps of the process needed to define the tool path are illustrated in the flow chart of Figure 1.7 and described in the following paragraphs.

Step 1. To start the process, the desired part form, S_{des} , is specified to the onboard computer. Either an aspheric, Eq. (1.1), or tangent ogive, Eq. (1.2), equation can be used. Tolerances on the form error as well as the minimum removal thickness must also be specified. This thickness ensures that the subsurface damage left by the previous manufacturing operations is removed.

Step 2. The actual form, S_{act} , is measured with a metrology instrument and imported to the onboard computer. This instrument could be the onboard STIL sensor, directly connected to that computer or another offline instrument, such as a stylus profilometer or interferometer.

Step 3. For the first iteration, the answer to the question “Is the form satisfactory? AND Is the minimum thickness removed?” is negative, because no removal has yet occurred.

Step 4. The removal map is created by subtracting the actual part profile from the desired one. The difference indicates the depth of material that must be removed as a function of the radial distance from the part center.

Step 5. The geometry of the part from Step 1 is used to generate the tool path geometry. It defines the tool positions so that the carrier wheel is safely brought in contact with the part without producing tool-part collisions.

Step 6. A removal spot is made on a spare part made of the same material and of geometry similar to the processed part. This spot is measured either onboard with the STIL sensor or offline with another instrument and data are imported to the machine.

Step 7. This removal spot is be used to generate the tool removal function.

Step 8. The removal function and map from Step 7 and Step 4, respectively, are used as the main inputs for the algorithm that will generate a tool crossfeed velocity solution.

Step 9. The tool crossfeed velocities from Step 8 are combined with the tool path geometry from Step 5 to form the machine commands.

Step 10. The part is polished according to the commands from Step 9.

The process is then iterated, starting over at Step 2, where the form of the part is measured after each polishing run. The actual form is then compared with the desired form at Step 3. If the results are satisfactory, the process is completed, Step 11. If that is not the case, the process is iterated again, as steps 4 to 10 are repeated.

Algorithms are needed to create a satisfactory tool path and so that UFF can be operated according to the flow chart of Figure 1.7.

To produce the desired form correction, it is necessary to formulate and solve at step 8 the form correction problem, which consists in establishing the tool crossfeed velocities satisfying constraints on the tool velocity and acceleration and such that the desired removal profile is achieved. For that purpose, chapter 2 includes a model predicting the depth of removal profile for a given removal function and tool crossfeed velocity. A method for solving the form correction problem formulated as a constrained optimization problem is also presented.

A model needed to detect tool-part collisions and search strategies to prevent such collisions are described in Chapter 3. Two dimensional models for the tool and the part and search strategies for a variety of part shapes are defined. They are used for the tool path geometry algorithms used at step 5.

Removal is achieved by the local removal function generated along the tool path. Therefore, determinism can be greatly improved if the effect of the process parameters on this removal function can be predicted. For that purpose, Chapter 4 investigates the effect of process parameters on the removal function as well as the predictability of this function as these parameters vary. The validity of Preston's equation and the applicability of Hertz contact mechanics theory are evaluated. This approach is intended to complete step 7 of the flow chart. An alternative method to achieve accurate form correction without accurate prediction of the removal function is also presented.

Furthermore, an understanding of surface errors, in particular causes of form errors and their effect as well as the origin of UFF induced midspatial frequency surface errors, is required to achieve the predicted form and minimize induced tool marks to a satisfactory level. Chapter 5 focuses on the effect of the possible sources of deviation between predicted and actual removal profiles. A method for the analysis of UFF induced tool marks, which take the form of spirals, is also introduced.

Finally, Chapter 6 summarizes the methods developed and conclusions obtained throughout the thesis. It also presents suggestions for future study.

This work involves the development of algorithms which must be fast and easily integrated into a graphical user interface. To meet these requirements, the MATLAB [85] language was chosen to write these algorithms. MATLAB stands for MATrix LABoratory and is very efficient for matrix and vector operations required by this work. Furthermore, vectorization [86] is a technique that uses matrices and vectors to perform multiple simultaneous operations in MATLAB. Extensive use of vectorization produces fast algorithms that partially overcome the hardware limitations of the onboard computer. In addition, algorithms written with MATLAB can be compiled and run as stand alone programs, which can be integrated into a graphical user interface.

1.5 References

- [1] T. Miller, "Aspherics Come of Age," *Photonics Spectra* 38 (2), 76-81 (2004).
- [2] J. Hall and J. Vizgaitis, "Asphere Diet," *Photonics Spectra* 34 (12), 102-106 (2000).
- [3] R. S. Shannon, J. P. Mills, H. M. Pollicove, P. A. Trotta and L. N. Durvasula, "Optics that fit," *Photonics Spectra* 35 (4), 86-88 (2001).
- [4] H. Pollicove and D. Moore, "Automation for optics manufacturing," *Advanced Optical Manufacturing and Testing, Proc. SPIE* 1333, 2-6 (1990).
- [5] H. Pollicove and D. Moore, "COM: Working to move the optics industry into the 21st century", *Photonics Spectra* 26, 127-134 (1992).
- [6] H. Pollicove, D. Golini and J. Ruckman, "Computer aided optics manufacturing," *Optics & Photonics News* 5, 15-19 (1994).
- [7] D. Golini and W. Czajkowski, "Mircogrinding makes ultrasmooth optics fast," *Laser Focus World* 31, 83 (1995).

- [8] G. Paula, "Automating Lens Manufacturing," *Mechanical Engineering* 119, 88 (1997).
- [9] Y. Li, "Surface errors in deterministic microgrinding of optical materials," Ph.D. thesis, 2000, University of Rochester.
- [10] S. Tong, "Chatter in contour deterministic microgrinding," Ph.D. thesis, 2004, University of Rochester.
- [11] C. G. Blough, "Single point diamond turning of glass," Ph.D. thesis, 1992, University of Rochester.
- [12] F. Z. Zhang, X. D. Liu and L. C. Lee, "Micro-machining of optical glasses – A review of diamond cutting glasses," *Sādhanā* 28, 945-955 (2003).
- [13] C. F. Cheung and W. B. Lee, "Characterisation of nanosurface generation in single-point diamond turning," *International Journal of Machine Tools & Manufacture* 41, 851-875 (2001).
- [14] J. Yan and T. Kuriyagawa, "Recent nano-precision ductile machining technology for advanced optical applications," *OSA Technical Digest, Optical Fabrication and Testing*, Rochester, October 8-12, OFTuD4 (2006).
- [15] M. Zhou, B. K. A. Ngoi, M. N. Yusoff and X. J. Wang, "Tool wear and surface finish in diamond cutting of optical glass," *Journal of Materials Processing Technology* 174, 29-33 (2006).
- [16] M. Zhou, X. D. Liu and S. N. Huang, "Ultraprecision cutting of glass BK7," *Key Engineering Materials* 315/316, 536-540 (2006).
- [17] R. A. Jones, "Optimization of computer controlled polishing," *Applied Optics* 16, 218-224 (1977).
- [18] R. A. Jones, "Grinding and polishing with small tools under computer control," *Optical Engineering* 18, 390-393, (1979).
- [19] R. C. Babish and R. R. Rigby, "Optical fabrication of a 60-inch mirror," *Space Optics, Proc. SPIE* 183, 105-108 (1979).
- [20] R. A. Jones, "Computer-Controlled polishing of telescope mirror segments," *Optical Engineering* 22, 236-240 (1983).

- [21] R. Aspden, R. McDonough, and F. R. Nitchie, Jr., "Computer assisted optical surfacing," *Applied Optics* 16, 218-222 (1972).
- [22] A. H. Greenleaf, "Computer-controlled optical surfacing," *Active Optical Devices and Applications, Proc. SPIE 228*, 41-54 (1980).
- [23] R. A. Jones, "Computer-controlled optical surfacing with orbital tool motion," *Optical Engineering* 25, 785-790 (1986).
- [24] R. A. Jones and W. J. Rupp, "Rapid optical fabrication with CCOS," *Advanced Optical Manufacturing and Testing, Proc. SPIE 1333*, 34-43 (1990).
- [25] PerkinElmer Inc., 940 Winter Street, Waltham, MA 02451, Phone: 800-762-4000, www.perkinelmer.com.
- [26] Canon Inc., 30-2, Shimomaruko 3-chome, Ohta-ku, Tokyo 146-8501, Japan, Phone: +91 3-3758-2111, www.canon.com.
- [27] M. Ando, M. Negishi, M. Takimoto, A. Deguchi and N. Nakamura, "Super-smooth polishing on aspherical surfaces," *Nanotechnology* 6, 111-120 (1995).
- [28] M. Ando, M. Negishi, M. Takimoto, A. Deguchi, N. Nakamura, M. Higomura and H. Yamamoto, "Super-smooth surface polishing on aspherical optics," *International Symposium on Optical Fabrication, Testing, and Surface Evaluation, Proc. SPIE 1720*, 22-33 (1992).
- [29] J. R. P. Angel, "Steps toward 8m honeycomb mirrors V A method for polishing aspheres as fast as F/1," *Very Large Telescopes, Their Instrumentation and Programs, Proc. IAU Colloquium 79*, 11-21 (1984).
- [30] H. M. Martin, D. S. Anderson, J. R. P. Angel, R. H. Nagel, S. C. West and R. S. Young, "Progress in the stressed-lap polishing of 1.8 m f/1 mirror," *Advanced Technology Optical Telescopes IV, Proc. SPIE 1236*, 682-690 (1990).
- [31] H. M. Martin, J. H. Burge, S. M. Miller, B. K. Smith, R. Zehnder and C. Zhao, "Manufacture of a 1.7m prototype of the GMT primary mirror segments," *Optomechanical Technologies for Astronomy, Proc. SPIE 6273* (2006).
- [32] L. Wang, Y. T. Zhu and Q. F. Zhang, "Mechanical design of the stressed-lap polishing tool," *Optical Devices and Instruments, Proc SPIE 6024* (2006).
- [33] Y. Zheng, Y. Li, L. Wang and D. Wang, "Method of stressed lap shape control for large mirror fabrication," *Optomechanical Technologies for Astronomy, Proc. SPIE 6273* (2006).

- [34] S. R. Wilson, J. R. McNeil, "Neutral ion beam figuring of large optical surfaces," Current Developments in Optical Engineering II, Proc. SPIE 818, 320-324 (1987).
- [35] S. R. Wilson, D. W. Reicher, C. F. Kranenberg and J. R. McNeil, "Ion beam milling of fused silica for window fabrication," Laser-Induced Damage in Optical Materials, Proc. SPIE 1441, 82-86 (1990).
- [36] L. N. Allen, R. E. Keim, "An ion figuring system for large optic fabrication," Current Developments in Optical Engineering and Commercial Optics 1168, 33-50 (1989).
- [37] L. N. Allen and H. W. Romig, "Demonstration of an ion figuring process," Advanced Optical Manufacturing and Testing, Proc. SPIE 1333, 22-33 (1990).
- [38] L. N. Allen, R. E. Keim and T. S. Lewis, "Surface error of a Keck 10m telescope primary segment by ion figuring," Advanced Optical Manufacturing and Testing II, Proc. SPIE 1531, 195-204 (1991).
- [39] L. N. Allen, J. J. Hannon and R. W. Wambach, "Final surface error correction of an off-axis aspheric petal by ion figuring," Active and Adaptive Optical Components, Proc. SPIE 1543, 190-200 (1991).
- [40] A. Schindler, T. Hänsel, F. Frost, A. Nickel, R. Fechner and B. Rauschenbach, "Recent achievements on ion beam techniques for optic fabrication," OSA Technical Digest, Optical Fabrication and Testing, Rochester, October 10-13, OMD3 (2004).
- [41] T. Hänsel, A. Nickel, A. Schindler and H.-J. Thomas, "Ion beam figuring surface finishing of x-ray and synchrotron beam line optics using stitching interferometry for the surface topology measurement," OSA Technical Digest, Optical Fabrication and Testing, Rochester, October 10-13, OMD5 (2004).
- [42] T. Hänsel, A. Nickel, H.-J. Thomas, A. Schindler, R. Schwabe, "Local thickness correction of nanometer thin films by means of ion beam etching," OSA Technical Digest, Optical Fabrication and Testing, Tucson, Arizona, June 3-5, OWB2 (2005).
- [43] Fawcett, S. C., Bifano, T. G., and Drueding, T., "Neutral Ion Figuring of Chemically vapor Deposited Silicon Carbide," Optical Engineering, [33]3, pp. 967-974, 1994
- [44] Fawcett, S. C., Drueding, T., and Bifano, T. G., "Development of an Ion Figuring System for Centimeter Scale Optical Components," SPIE Volume 2263, San Diego, CA, July 1994

- [45] S. D. Jacobs, "International innovations in optical finishing," Current Developments in Lens Design and Optical Engineering V, Proc. SPIE 5523, 264-272 (2004).
- [46] L. D. Bollinger and C. B. Zarowin, "Rapid, nonmechanical, damage-free figuring of optical surfaces using plasma-assisted chemical etching (PACE): Part I Experimental Results," Advances in Fabrication and Metrology for Optics and Large Optics, Proc. SPIE 966, 82-90 (1988).
- [47] C. B. Zarowin and L. D. Bollinger, "Rapid, nonmechanical, damage-free figuring of optical surfaces using plasma-assisted chemical etching (PACE): Part II Theory and Process Control," Advances in Fabrication and Metrology for Optics and Large Optics, Proc. SPIE 966, 91-97 (1988).
- [48] D. Bollinger, G. Gallatin, J. Samuels, G. Steinberg and C. Zarowin, "Rapid, non-contact, optical figuring of aspheric surfaces with plasma assisted chemical etching (PACE)," Advanced Optical Manufacturing, Proc. SPIE 1333, 44-57 (1990).
- [49] <http://www.mdatechnology.net/techsearch.asp?articleid=105>, retrieved on August 27, 2007.
- [50] Nikon Corp., Fuji Bldg., 2-3, Marunouchi 3-chome, Chiyoda-ku, Tokyo 100-8331, Japan, Phone: +81 3-3214-5311, www.nikon.com.
- [51] H. Takino, N. Shibata, H. Itoh, T. Kobayashi, H. Tanaka, M. Ebi, K. Yamamura, Y. Sano and Y. Mori, "Computer numerically controlled plasma chemical vaporization machining with a pipe electrode for optical fabrication," Applied Optics 37, 5198-5210 (1998).
- [52] H. Takino, N. Shibata, H. Itoh, T. Kobayashi, K. Yamamura, Y. Sano and Y. Mori, "Fabrication of optics by use of plasma chemical vaporization machining with a pipe electrode," Applied Optics 41, 3971-3977 (2002).
- [53] H. Takino, N. Shibata, H. Itoh, T. Kobayashi, K. Nemoto, T. Fujii, N. Goto, K. Yamamura, Y. Sano and Y. Mori, "Fabrication of small complex-shaped optics by plasma chemical vaporization machining with a microelectrode," Applied Optics 45, 5897-5902 (2006)
- [54] Y. Verma, A. K. Chang, J. W. Berrett; K. Futterer; G. J. Gardopce; J. Kelley; T. Kyler; J. Lee; N. Lyford; D. Proscia and P. R. Sommer, "Rapid damage-free shaping of silicon carbide using reactive atom plasma (RAP) processing," Optomechanical Technologies for Astronomy, Proc. SPIE 6273 - (2006).

- [55] P. Subrahmanyam, G. Gardopee, P. S. Fiske and A. Chang, "Reactive Atom Plasma (RAP) processing of optical surfaces," Annual Proceedings of the American Society for Precision Engineering, 2006.
- [56] Y. Verma, P. S. Fiske, P. K. Subrahmanyam and G. J. Gardopee, "Damage-free processing of silicon carbide optics" Annual Proceedings of the American Society for Precision Engineering (2006).
- [57] RAPT Industries Inc., 46535 Fremont Boulevard, Fremont, CA 94538, Phone: 510-933-1000, www.raptindustries.com.
- [58] E. Fess, J. Schoen, M. Bechtold, D. Mohring, C. Bouvier, "UltraForm Finishing processes for optical materials," Optical Manufacturing and Testing VI, Proc. SPIE 5869, 0F1-0F6 (2005).
- [59] J. Gonzalez-Garcia, A. Cordero-Davila, E. Luna, M. Nunez, E. Ruiz, L. Salas, V. H. Cabrera-Davila, I. Cruz-Gonzalez and E. Sohn, "Static and dynamic removal rates of a new hydrodynamic polishing tool," Applied Optics 43, 3623-3631 (2004).
- [60] M. Núñez, J. Salinas, E. Luna, L. Salas, E. Ruiz, E. Sohn, A. Nava, I. Cruz and B. Martínez, "Surface roughness results using a hydrodynamic polishing tool (HyDra)," Proc. SPIE 5494, 459-467 (2004).
- [61] E. Sohn, E. Ruiz, E. Luna, L. Salas, M. Nunez, J. Valdes, B. Martinez and I. Cruz-Gonzalez, "HyDra: A novel hydrodynamic polishing tool for high quality optical surfaces," OptiFab 2005, Proc. SPIE TD03, 9-11 (2005).
- [62] US patent 7,169,012, E. G. Ruiz-Schneider, "Hydrodynamic radial flux polishing and grinding tool for optical and semiconductor surfaces" (2007).
- [63] QED Technologies, 1040 University Avenue, Rochester, NY 14607, Phone: 585-256-6540, www.qedmrf.com.
- [64] S. D. Jacobs, D. Golini, Y. Hsu, B. E. Puchebner, D. Strafford, W. I. Kordonski, I. V. Prokhorov, E Fess, D. Pietrowski, and V. W. Kordonski, "Magnetorheological Finishing: a deterministic process for optics manufacturing," Optical Fabrication and Testing, Proc. SPIE 2576, 372-382 (1995).
- [65] P. Dumas, D. Golini, P. Murphy and M. Tricard, "Improve Figure and Finish of Diamond Turned Surfaces with Magneto-Rheological Finishing (MRF)," Annual Proceedings of the American Society for Precision Engineering (2004).
- [66] M. Tricard, P. Dumas, G. Forbes and M. DeMarco, "Recent advances in sub-aperture approaches to finishing and metrology," 2nd International Symposium on

Advanced Optical Manufacturing and Testing Technologies: Advanced Optical Manufacturing Technologies, Proc. SPIE 6149 (2006).

[67] Zeeko Ltd, 4 Vulcan Way, Vulcan Court, Hermitage Industrial Estate, Coalville, Leicestershire, LE67 3FW, England, Phone: +44 530-815-832, www.zeeko.co.uk.

[68] D. D. Walker, D. Brooks, A. King, R. Freeman, R. Morton, G. McCavana, S-W Kim, "The 'Precessions' tooling for polishing and figuring flat, spherical and aspheric surfaces," Optics Express 11, 958-964 (2003).

[69] D. D. Walker, A. T. H. Beaucamp, R. G. Bingham, D. Brooks, R. Freeman, S. W. Kim, A. King, G. McCavana, R. Morton, D. Riley and J. Simms, "Precessions Aspheric Polishing: New Results from the Development Programme," Optical Manufacturing and Testing V, Proc. SPIE 5180, 15-28 (2003).

[70] D. D. Walker, A. T. H. Beaucamp, D. Brooks, V. Doubrovski, M. D. Cassie, C. Dunn, R. R. Freeman, A. King, M. Libert, G. McCavana, R. Morton, D. Riley and J. Simms, "Recent developments of *Precessions* polishing for larger components and free-form surfaces," Current Developments in Lens Design and Optical Engineering V, Proc. SPIE 5523, 281-289 (2004).

[71] D. D. Walker; A. T. H. Beaucamp; V. Doubrovski; C. Dunn; R. Freeman; G. McCavana; R. Morton; D. Riley; J. Simms; X. Wei, "New results extending the Precessions process to smoothing ground aspheres and producing freeform parts", Optical Manufacturing and Testing VI, Proc. SPIE 5869 (2005).

[72] Satisloh GmbH, Wilhelm-Loh Straße 2-4, 35578 Wetzlar, Germany, Phone: +49 6441-912-0, www.satisloh.com.

[73] Fisba Optik AG, Rorschacher Strasse 268, CH-9016 Saint Gallen, Switzerland, Phone: +41 71-282-3131, www.fisba.ch.

[74] O. W. Föhnle, H. van Brug, and H. J. Frankena, "Fluid jet polishing of optical surfaces," Applied Optics 37, 6771-6773 (1998).

[75] S. M. Booij, "Fluid jet polishing," Ph.D. thesis, 2003, Delft Technical University, The Netherlands.

[76] W. A. C. M. Messelink; R. Waeger; M. Meeder; H. Looser; T. Wons; K. C. Heiniger; O. W. Faehnle, "Development and optimization of FJP tools and their practical verification," Optical Manufacturing and Testing VI, Proc. SPIE 5869, 52-59 (2005).

- [77] W. Kordonski, A. Shorey and A. Sekeres, "New magnetically assisted finishing method: material removal with magnetorheological fluid jet," *Optical Manufacturing and Testing IV*, Proc. SPIE 5188, 107-114 (2003).
- [78] A. Shorey, W. Kordonski and M. Tricard "Deterministic precision finishing of domes and conformal optics," *Window and Dome Technologies and Materials IX*, Proc. SPIE 5786 310-318 (2005).
- [79] A. Shorey, W. Kordonski, J. Tracy and M. Tricard, "Developments in the finishing of domes and conformal optics," *Window and Dome Technologies and Materials X*, Proc. SPIE 6545 (2007).
- [80] OptiPro Systems, 6368 Dean Parkway, Ontario, NY 14519, Phone: 585-265-0160, www.optipro.com. Development of UltraForm Finishing by OptiPro Systems is funded by Army and Navy through the US Government SBIR Program; SBIR Data Rights Apply.
- [81] 3M Company, 3M Center, Building 42-6E-37 Saint Paul, MN 55144-1000, Phone : 888-364-3577, www.3m.com.
- [82] STIL SA, 595, Rue Pierre Berthier, Domaine de Saint Hilaire, 13855 Aix en Provence, France, Phone : +33 4-42-24-38-05, www.stilsa.com.
- [83] <http://www.stilsa.com/EN/prin.htm>, retrieved on August 27, 2007.
- [84] <http://www.stilsa.com/EN/pdf/micrometric%20pens.pdf>, retrieved on August 27, 2007.
- [85] MATLAB R2007a (Version 7.4.0.287), The Mathworks Inc., 3 Apple Hill Drive, Natick, MA 01760-2098, Phone: 508-647-7000, www.mathworks.com.
- [86] D. C. Hanselman, B. L. Littlefield, *Mastering MATLAB 7*, Prentice Hall, Upper Saddle River, New Jersey, 2005.

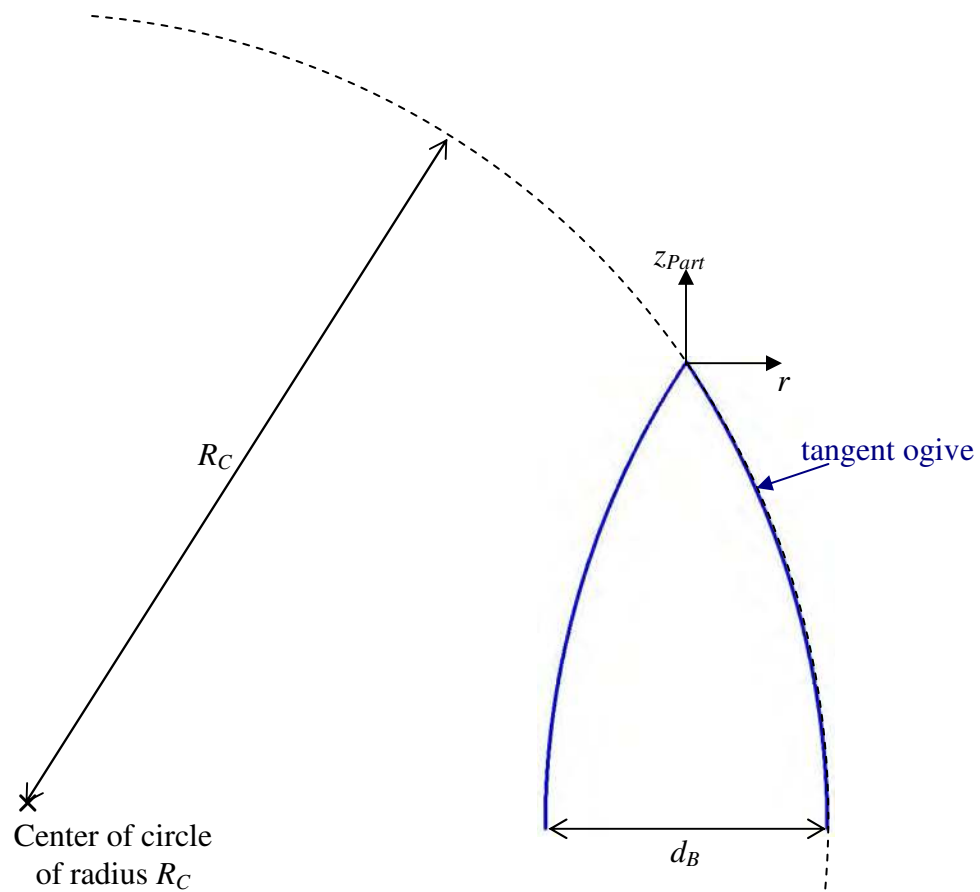


Figure 1.1 Geometry of a tangent ogive.

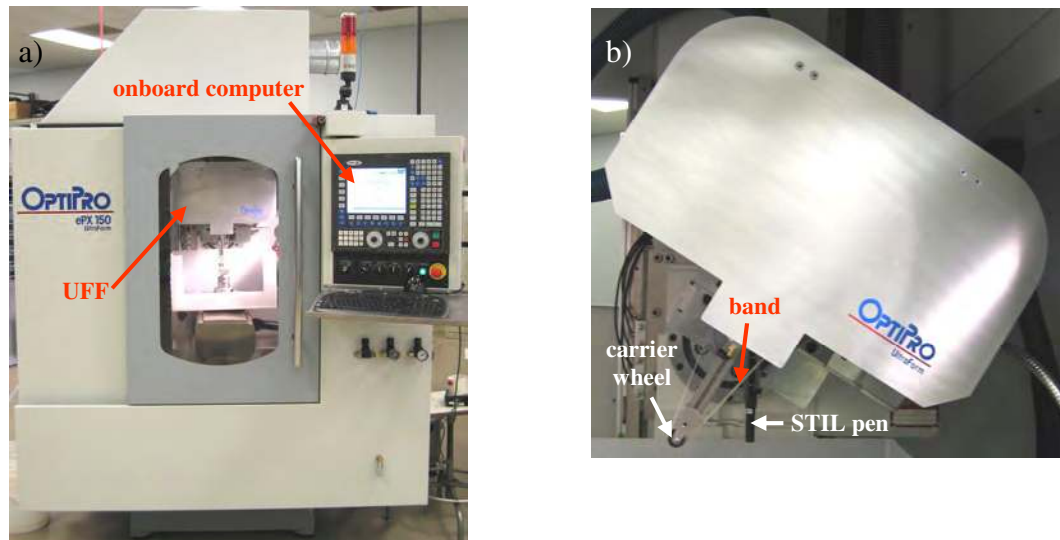


Figure 1.2 Views of UFF
a) on CNC platform;
b) close up.

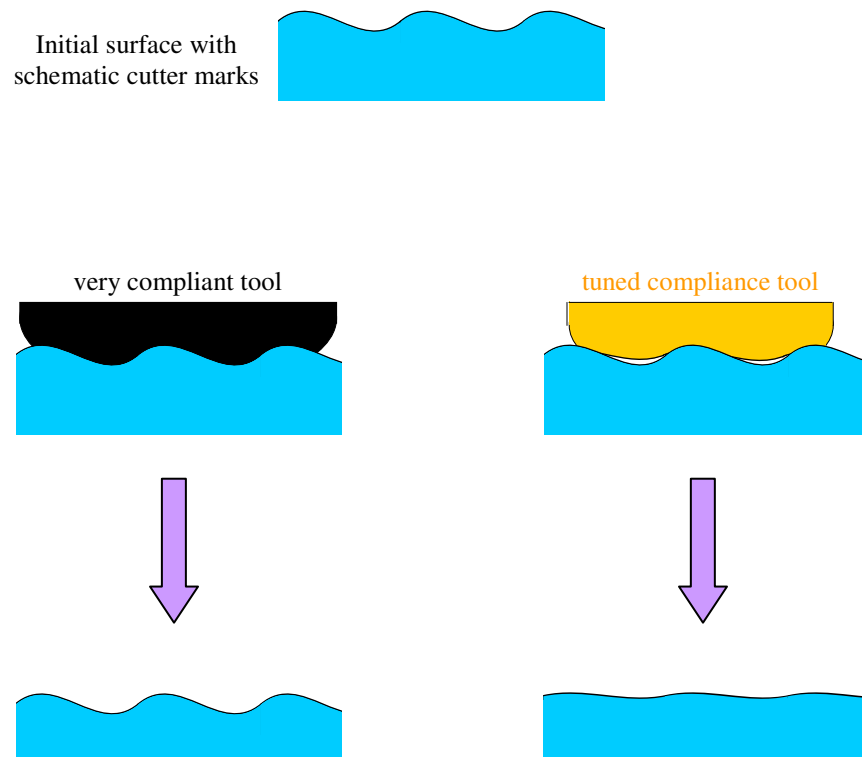


Figure 1.3 Compliance of the tool and removal of cutter marks.

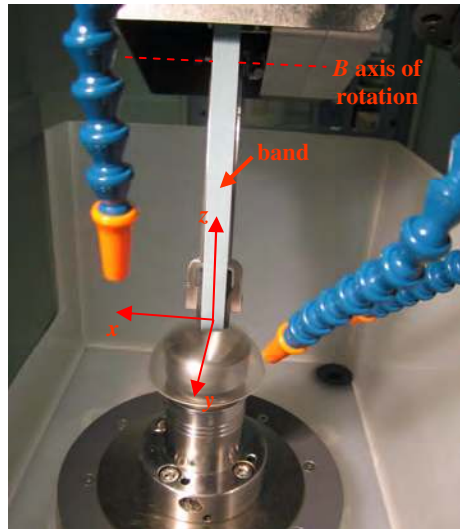


Figure 1.4 Hemisphere polishing and geometry definition.

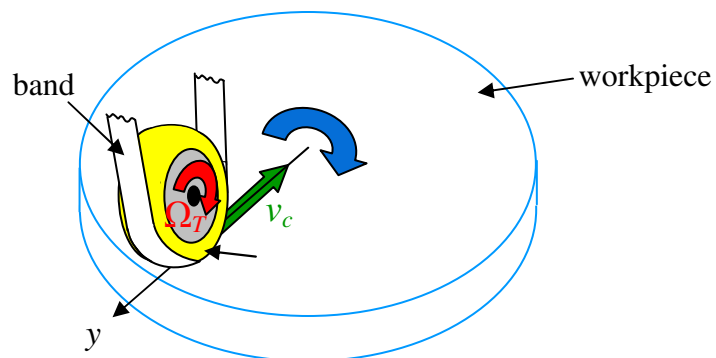


Figure 1.5 Schematic of the tool path.

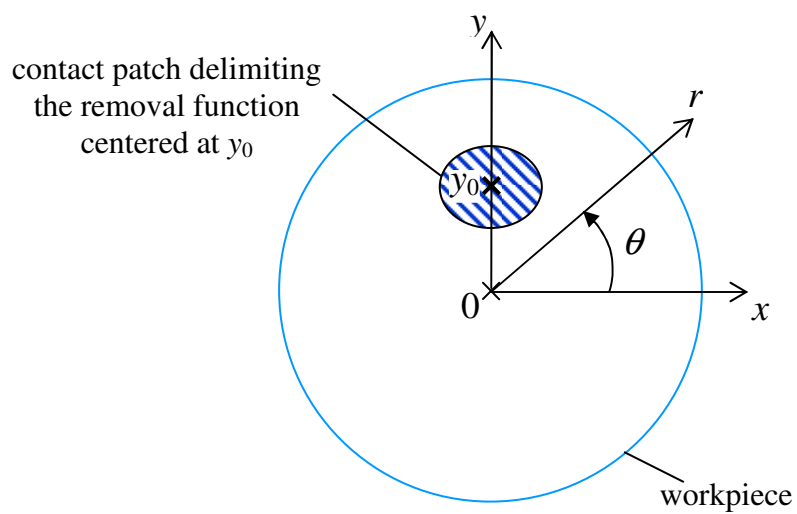


Figure 1.6 Tool position definition.

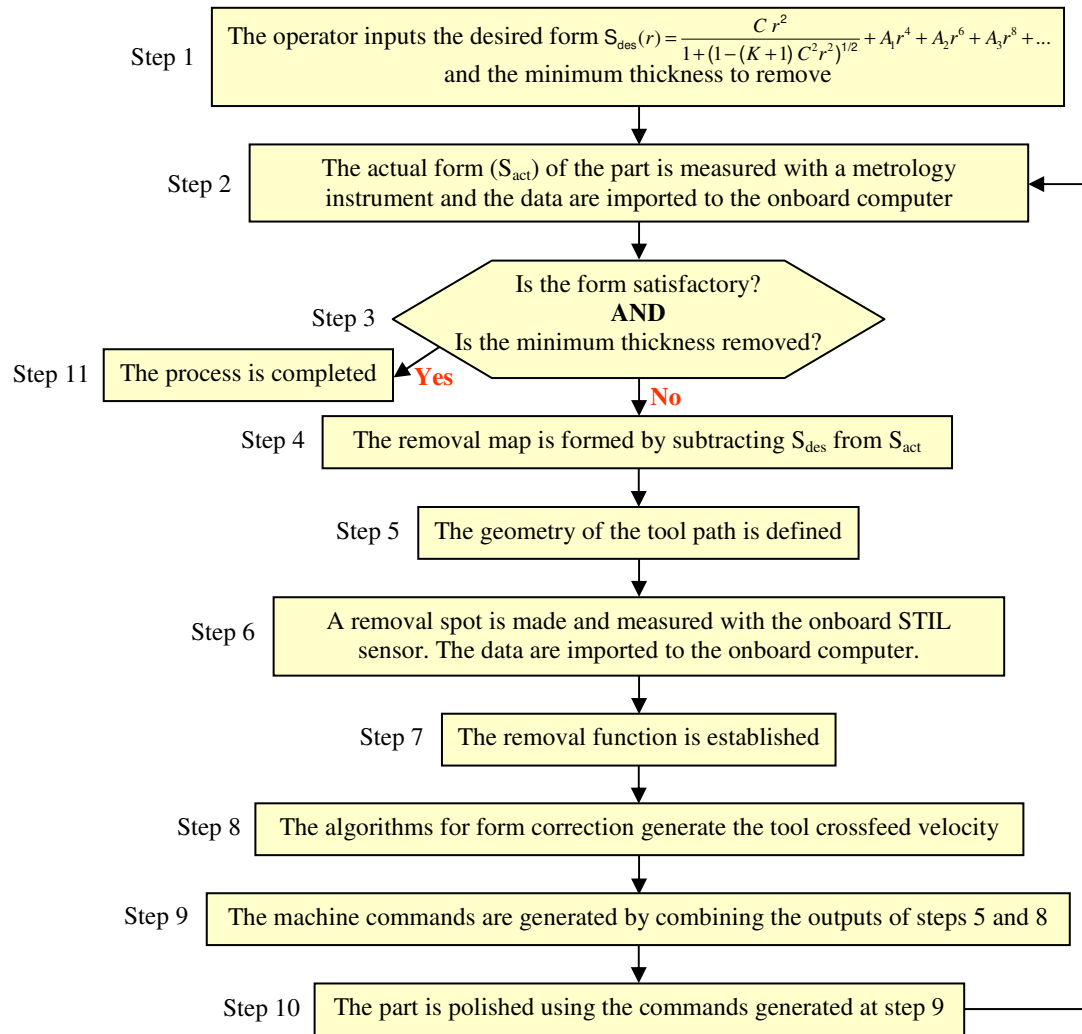


Figure 1.7 Flow chart of the UFF process.

Chapter 2 Form correction problem

Rigid grinding tools produce a small contact region between the tool and the workpiece and essentially remove all the material in the tool's path. However some polishing techniques use compliant subaperture tools with a large tool-part contact region. In this case, as for UFF, the depth of removal is prescribed by adjusting the tool dwell time. While polishing an axisymmetric workpiece, the tool is continuously moved radially across the part and appropriate dwell times for form correction are achieved by varying the tool crossfeed velocity v_c . The problem of establishing a tool crossfeed velocity schedule for form correction of plano, spheres and aspheres is the object of Section 2.2. This is an inverse problem. The forward problem, to predict the removal profile produced by a given removal function and tool crossfeed velocity schedule, is first examined in Section 2.1 for plano and spherical parts. The removal function is a map of the depth of material removed per unit of time within the tool-part contact patch. In this chapter, the removal function and its variations in size and amplitude, are assumed to be known along the tool path. The definition of that removal function is the object of Chapter 4.

2.1 Forward problem

The forward problem is defined as predicting the removal profile for a given tool crossfeed velocity schedule and removal function. A formulation of this problem is necessary before the inverse problem can be considered.

2.1.1 Equations for the depth of removal on flats and spheres

To perform form correction, a model predicting the form of the part after polishing is necessary. Since the part is axisymmetric and because only axisymmetric corrections are considered, only the radial part profile is needed. This simplifies the problem and reduces computational time. The final profile is equal to the initial profile minus the predicted depth of removal profile. The depth of removal profile is the result of summing the removal generated by the tool as it follows the tool path.

To predict the removal profile, the approach of Forbes [1] is used. The part is described with the coordinate system (x, y, z) defined in Chapter 1. The process is modeled for flats, as illustrated in Figure 2.1, by a removal function $c(x, y, y_0)$ centered at y_0 that traverses the part along the y axis at the crossfeed velocity $v_c(y_0)$. Using the polar coordinate system (r, θ) shown in Figure 2.1, an equivalent one-dimensional removal function $\sigma_F(r, y_0)$ is first defined, as follows

$$\sigma_F(r, y_0) = \frac{1}{2\pi} \int_0^{2\pi} c(x(r, \theta), y(r, \theta), y_0) d\theta, \quad (2.1)$$

where $x(r, \theta)$ and $y(r, \theta)$ are the coordinates in (x, y, z) of the point defined by (r, θ) in the polar coordinate system. $\sigma_F(r, y_0)$ is the average of $c(x, y, y_0)$ over θ and represents the removal rate at r on the part profile due to the two-dimensional removal function $c(x, y, y_0)$ centered at y_0 .

The removal profile can be interpreted as the sum of the one-dimensional removal functions multiplied by the corresponding tool dwell time as the tool traverses the part. However, since the tool is moved continuously at a crossfeed

velocity $v_c(y_0)$, the depth of removal $DR(r)$ is given by the integral over y_0 of $\sigma_F(r, y_0)$ multiplied by the inverse of v_c .

$$DR(r) = \int_{y_{0\min}}^{y_{0\max}} \frac{\sigma_F(r, y_0)}{v_c(y_0)} dy_0, \quad (2.2)$$

where $y_{0\min}$ and $y_{0\max}$ are the extreme positions occupied by the tool. $dy_0/v_c(y_0)$ represents the tool dwell time for the annular ring of width dy_0 centered at y_0 . Combining Eqs. (2.1) and (2.2), $DR(r)$ is expressed as a function of $c(x, y, y_0)$

$$DR(r) = \frac{1}{2\pi} \int_{y_{0\min}}^{y_{0\max}} \left(\int_0^{2\pi} c(x(r, \theta), y(r, \theta), y_0) d\theta \right) \frac{1}{v_c(y_0)} dy_0. \quad (2.3)$$

The expression for the depth of removal can be similarly derived for a sphere of radius R . For that purpose, the spherical coordinates (r, θ, ϕ) of Figure 2.2 are used. The position of the tool is defined by ϕ_0 or alternatively y_0 , such that $y_0 = R \sin(\phi_0)$. The tool traverses the part along its intersection with the y - z plane. The one-dimensional removal function $\sigma_S(\phi, \phi_0)$ for a spherical workpiece is given by

$$\sigma_S(\phi, \phi_0) = \frac{1}{2\pi} \int_0^{2\pi} c(x(\theta, \phi), y(\theta, \phi), \phi_0) d\theta \quad (2.4)$$

where $x(\theta, \phi)$, $y(\theta, \phi)$ are the coordinates in (x, y, z) of the point defined by (R, θ, ϕ) in the spherical coordinate system. The depth of a removal as a function of ϕ is given by

$$DR(\phi) = \int_{\phi_{0\min}}^{\phi_{0\max}} \frac{\sigma_S(\phi, \phi_0)}{v_c(\phi_0)} R d\phi_0 \quad (2.5)$$

and can also be expressed as a function of $c(x, y, y_0)$ as

$$DR(\phi) = \frac{1}{2\pi} \int_{\phi_{\min}}^{\phi_{\max}} \left(\int_0^{2\pi} c(x(\phi, \theta), y(\phi, \theta), \phi_0) d\theta \right) \frac{1}{v_c(\phi_0)} R d\phi_0. \quad (2.6)$$

Eq. (2.6) can be used for spheres and mild aspheres which can be treated as spheres.

2.1.2 Model validation

Eqs. (2.3) and (2.6) are convolution integrals and are derived under the assumption that there is a linear relation between depth of removal and dwell time. This last key hypothesis was verified by making removal spots with dwell times, t_d , of 2, 5, 10, 15 and 30 s on BK7 samples. The expected linear relation between the volume, V , of the spot and t_d is reported, in Figure 2.3, with R^2 larger than 0.99.

Predicted and actual depths of removal were compared for the simple case of a constant v_c . The goal of this experiment was not to reduce the form error but to verify the accuracy of the predictions. A flat Pyrex part of diameter 75 mm and previously pitch-polished with a peak-to-valley (PV) of less than 0.5 μm has been polished with the UFF tool traversing from $y_{0\min} = -30$ mm to $y_{0\max} = 30$ mm. Thus, the region close to the part edge was intact and provided an absolute reference for the depth of removal. The tool removal spot was evaluated from the removal spot shown in Figure 2.4. This spot was made with a previous version of UFF using larger, softer carrier wheels and $t_d = 30$ s. $DR(r)$ was evaluated for 35 values of r , according to Eq. (2.3). The actual part profile measured with a Talysurf stylus profilometer [2] is

superposed with the depth of removal predictions in Figure 2.5. Predictions and part profile are in very good agreement, R^2 is equal to 0.98.

2.2 Inverse problem

The goal of the inverse problem is to establish the tool crossfeed velocity v_c to achieve a desired part profile.

2.2.1 Formulation of the problem

The problem is to determine a crossfeed velocity schedule v_c to obtain a desired depth of removal, DR_{des} , with Eqs. (2.3) or (2.6). This problem is an inverse problem and actually has several names, depending on its form and interpretation. The problem can be seen as finding $v_c(y_0)$ resulting in a “good enough” approximation of $DR(r)$. Mathematicians [3, 4] can then state it as a best approximation problem. If $sc(y_0) = 1/v_c(y_0)$ is introduced, Eq. (2.3) could also be referred to as a Fredholm integral equation of the first kind [5-8], where $\sigma_F(r, y_0)$ is the Kernel and $sc(y_0)$ is the unknown function to be solved for. Because of the finite size of the removal function, Eq. (2.3) is a convolution integral. Therefore, this problem is also often stated as a deconvolution problem [9-14]. Deconvolution, as mentioned by Brown [12], is a technique commonly associated with image reconstruction.

The current problem of form correction is subjected to constraints. In fact, nonnegative crossfeed velocities are required because a negative velocity in Eqs. (2.3) or (2.6) would imply material deposition on the workpiece, which is not possible with this process. The tool crossfeed velocity cannot be larger than the value v_{cmax} imposed by the motors driving the different axes. In addition, for similar reasons, the absolute value of the tool crossfeed acceleration has to be less than a value a_{cmax} . These constraints impose bounds and a certain level of smoothness for the solution v_c . They can be expressed in terms of v_c or sc . For flats they are such that

$$0 < v_c(y_0) \leq v_{cmax} \text{ and } \left| \frac{dv_c}{dt} \right| < a_{cmax}, \quad (2.7)$$

or

$$sc(y_0) \text{ finite, } sc(y_0) \geq 1/v_{cmax} \text{ and } \left| \frac{d(1/sc)}{dt} \right| < a_{cmax}. \quad (2.8)$$

2.2.2 Review of approaches reported in the literature

This type of inverse problem has been considered for other subaperture deterministic polishing techniques. Two types of techniques are distinguished and described by Porsching et al. [15]. They are operator controlled that can be recursive and computer numerically controlled (CNC) finishing.

Early techniques were typically applied to single-spindle machines inspired by conventional polishing, and correspond to the so called operator controlled and recursive operator controlled finishing [12, 15-17]. These processes use a subaperture

lap as shown in Figure 2.6. For these approaches, the success of the process relies on the operator skills and experience. He has to choose different machine parameters, such as tool size, stroke characteristics and tool rpm, to create different removal functions, which are applied on specific regions of the part. For operator controlled finishing, the operator first defines all the removal functions. The dwell times to apply to each removal function are then estimated. In its recursive version, the part is measured after each iteration. This measurement is used by the operator to choose the parameters that will define the removal function for the next iteration. These techniques are not compatible with the way UFF is operated.

On the other hand, the UFF procedure is similar to ion beam figuring, the Precession process [18] and MRF [1].

The work by Wilson et al. [19] at the University of New Mexico constitutes one of the earliest treatments of figuring with an ion beam. The problem is expressed as a convolution problem in rectangular Cartesian coordinates, allowing for astigmatism correction. Fourier transforms are used to express the convolution integral as a multiplication in the frequency domain. The solution $sc(x, y)$ is then “simply” the inverse Fourier transform of the ratio of the Fourier transforms of the desired depth of removal and removal function. As reported by Wilson et al. [19] and Forbes [1], when the Fourier transform of the removal function is small, the result becomes noise sensitive. Furthermore, the frequencies at which it is zero are a

problem. These issues were addressed by Wilson et al. [19] with the use of a thresholded inverse filter. This approach does not handle constraints on the solution.

Two studies by Drueding et al. [13] and Shanbag et al. [20], also consider ion beam figuring in Cartesian coordinates. Their approaches are similar. In both cases, the known functions are expressed by series expansions so that the unknown function can be written in a similar form. This treatment converts the problem to a calculation of coefficients. Specifically, Drueding et al. [13] expand the terms in series of successive derivatives, whereas Shanbag et al. [20] used wavelet series.

The advantages of these methods are that they are more robust than the Fourier transform solution and negative solutions can be avoided by adjusting a constant term or offset. The disadvantages are that other constraints are not taken into account, limitations are observed when the order of the polynomials becomes large in reference [13], and wavelet expansions might not be suitable for removal functions that strongly deviate from the Gaussian model used for the ion beam.

Allen et al. [21] at Kodak and Hänsel et al. [14] at the German Institut für Oberflächenmodifizierung (IOM - Institute for Surface Modification) reported ion beam figuring apparatus named Ion Figuring System (IFS) and Ion Beam Etching (IBE), respectively. They both use iterative algorithms to establish the dwell times. These algorithms are not described, however, Hänsel et al. [14] qualifies the method used for IBE as a “modified iteration method in real space according to P. H. Van

Cittert”. This is a method based on the Van Cittert algorithm, widely used in spectroscopy, to which a relaxation factor has been introduced [22].

The IBE method also handles the constraints on the tool velocities and accelerations. In fact, the solution is checked after each iteration of the algorithm and corrected with a “smoothing procedure”, if necessary. The reported issue with this approach is the time required to achieve convergence. Moreover, the “smoothing procedure” is not described.

From this review of some ion beam figuring approaches, it seems that the solutions reported by Allen et al. [21] and Hänsel et al. [14] are of potential interest for UFF, but these techniques are not described in detail. Techniques developed by Wilson et al. [19], Drueding et al. [13] and Shanbag et al. [20] might be of interest for a future treatment of non-axisymmetric workpieces or non-rotationally symmetric errors.

A final approach formulates the form correction problem into matrix form. This technique is reported for ion beam figuring at Oak Ridge National Laboratory [23] and for many recent subaperture figuring processes, such as MRF [1], Zeeko Precessions process [18], HyDra [24]. This approach was selected for UFF and is described in further details in section 2.2.3.

2.2.3 Solution to the form correction problem

The form correction problem is formulated in matrix form for UFF and a wide range of geometries. A method establishing tool crossfeed velocities, which are feasible and minimize the deviation between desired and actual removal profiles, is described.

2.2.3.1 Matrix formulation of the form correction problem

To formulate the form correction problem for flats in matrix form, the integral over y_0 of Eq. (2.3) is approximated by summing the integrand over a finite number of equidistant points along the tool path. Therefore,

$$DR(r) = \int_{y_{0\min}}^{y_{0\max}} \frac{\sigma_F(r, y_0)}{v_c(y_0)} dy_0 \approx \sum_{j=1}^{N\Delta r_0} \frac{\sigma_F(r, y_{0j})}{v_c(y_{0j})} \Delta y_0, \quad (2.9)$$

where
$$\Delta y_0 = y_{0(j+1)} - y_{0j} \quad (2.10)$$

is constant. The depth of removal is evaluated at equidistant points r_i ,

$$DR(r_i) = \sum_{j=1}^{N\Delta r_0} \frac{\sigma_F(r_i, y_{0j})}{v_c(y_{0j})} \Delta y_0, \quad \text{for } i = 1, 2, \dots, N\Delta r, \quad (2.11)$$

where
$$\Delta r = r_{(i+1)} - r_i \quad (2.12)$$

is constant. $N\Delta r$ and $N\Delta r_0$ are the largest values taken by i and j , set to cover the ranges of radial positions where material is removed ($r \geq 0$) and where the tool is positioned ($y_{0\max} \geq y_0 \geq y_{0\min}$), respectively.

Eq. (2.11) can be written in matrix form as follows

$$\underline{DR} = \underline{RM} \underline{sc} \quad (2.13)$$

or

$$\begin{pmatrix} DR(0) \\ DR(\Delta r) \\ DR(2\Delta r) \\ \dots \\ DR(r_{\max}) \end{pmatrix} = \begin{pmatrix} RM_{11} & RM_{12} & \dots & RM_{1N\Delta y_0} \\ RM_{21} & \dots & \dots & \dots \\ \dots & \dots & \dots & \dots \\ \dots & \dots & \dots & \dots \\ RM_{N\Delta r 1} & \dots & \dots & RM_{N\Delta r N\Delta y_0} \end{pmatrix} \begin{pmatrix} 1/v_c(y_{0\min}) \\ 1/v_c(y_{0\min} + \Delta y_0) \\ 1/v_c(y_{0\min} + 2\Delta y_0) \\ \dots \\ 1/v_c(y_{0\max}) \end{pmatrix} \quad (2.14)$$

or

$$DR_i = RM_{ij} sc_j, \quad (2.15)$$

where RM is the “removal matrix” of dimension $N\Delta r \times N\Delta y_0$, and its $(i, j)^{\text{th}}$ element is given by

$$RM_{ij} = \sigma_F(r_i, y_{0j}) \Delta y_0. \quad (2.16)$$

sc is the vector of length $N\Delta y_0$, whose j^{th} components $sc_j = 1/v_c(y_{0j})$ is the inverse of the tool crossfeed velocity when the tool is at y_{0j} . DR is a vector of length $N\Delta r$, for which $DR_i = DR(r_i)$ is the depth of removal at r_i resulting from the tool traveling along its toolpath.

Similarly, for spheres and mild aspheres, Eq. (2.6) can be rewritten in the matrix form

$$\begin{pmatrix} DR(0) \\ DR(\Delta\phi) \\ DR(2\Delta\phi) \\ \dots \\ DR(\phi_{\max}) \end{pmatrix} = \begin{pmatrix} RM_{11} & RM_{12} & \dots & RM_{1N\Delta\phi_0} \\ RM_{21} & \dots & \dots & \dots \\ \dots & \dots & \dots & \dots \\ \dots & \dots & \dots & \dots \\ RM_{N\Delta\phi 1} & \dots & \dots & RM_{N\Delta\phi N\Delta\phi_0} \end{pmatrix} \begin{pmatrix} 1/v_c(\phi_{0\min}) \\ 1/v_c(\phi_{0\min} + \Delta\phi_0) \\ 1/v_c(\phi_{0\min} + 2\Delta\phi_0) \\ \dots \\ 1/v_c(\phi_{0\max}) \end{pmatrix}, \quad (2.17)$$

where

$$RM_{ij} = \sigma_S(\phi_i, \phi_{0j}) R \Delta\phi_0. \quad (2.18)$$

2.2.3.2 Computing RM

The first key to the inverse problem is the computation of the removal matrix. Starting with Eqs. (2.3) or (2.6) and discretizing as described in the previous section, a clear definition of RM is achieved for flats and spheres. It was possible to derive Eqs. (2.3) and (2.6), because flats and spheres can conveniently be described and mapped with polar and spherical coordinates, respectively. However, there is no coordinate system providing the same benefits for aspheres deviating significantly from their best-fit spheres. Therefore, there is no closed-form expression for the depth of removal on aspheres and no explicit definition for their removal matrices. Furthermore, the computations of the removal matrix for spheres using Eq. (2.18) require cumbersome coordinate manipulations. Therefore, a simpler, accurate and universal method is needed to compute the removal matrix on any shape.

This method is defined by inspecting Eqs. (2.16) and (2.18). The columns and lines of RM correspond to discrete points along the part profile such that the arc length, L_{arc} , between two consecutive points is constant. For spherical workpieces, the points ϕ_i and ϕ_{0j} can also be described by $r_i = R \sin(\phi_i)$ and $y_{0j} = R \sin(\phi_{0j})$, their respective y coordinates in (x, y, z) . With this alternative notation, for plano and spheres, the points y_{0j} associated with the columns of RM represent the positions occupied by the tool, while the points, r_i , associated with the lines represent the points at which the depth of removal is computed. RM_{ij} is obtained by evaluating at r_i the equivalent one-dimensional removal function generated for the tool at y_{0j} and

multiplying that value by the arc length between two consecutive tool positions. Therefore, independently of the part geometry, the assignment of the elements of RM is achieved by defining the points y_{0j} and r_i for a given part profile. These points are obtained by discretizing that part profile such that the arc length between two consecutive points along the part profile is constant. Algorithms performing that operation are described in Appendix 1.2.

To fill RM, the one-dimensional removal function must be evaluated. Because of the part rotation around the z axis, the value of a one-dimensional removal function at y_i is obtained by averaging that removal function over the circle of radius y_i , centered at $(0, 0, z_{Part}(y_i))$. To perform that operation it is necessary to know the points of the removal function lying on that circle. Therefore, the (x, y, z) locations on the workpiece of the points of the removal function need to be known. However, the removal function is defined in a plane. The coordinate system (x_{rf}, y_{rf}) is attached to that plane with its origin located at the center of the removal function. x_{rf} is parallel to the axis of rotation of the carrier wheel. To model removal, the points of this removal function need to be mapped onto the part, i.e. located in three dimensions. The chosen mapping method, illustrated in Figure 2.7, consists in positioning the plane on which the removal function is defined such that the normal to the part at y_0 is orthogonal to the plane (x_{rf}, y_{rf}) and intersects that plane at the center of the removal function. y_{rf} is in the plane (y, z) . The points of the removal function are then projected onto the workpiece.

The removal function is filled column by column. Each column, being a one-dimensional removal function obtained for a different discrete location of the tool on the part. This filling strategy permits varying removal functions, since at each column and therefore tool position a different removal function can be used.

The method for removal matrix computation described in this section was validated by observing that the terms of \underline{RM} computed for spheres differ only at the third significant digit from the terms computed with Eq. (2.6). Showing that the mapping method is equivalent to the one suggested by the equations for the spherical case. In addition, by using a constant removal function, polishing times computed from the solution obtained with this method and approximated based on a constant volumetric removal rate for various aspherical shapes differ by less than 1%. This result suggests that removal is properly mapped onto the part.

2.2.3.3 Solving for \underline{sc}

Once the removal matrix is computed, the matrix equation

$$\underline{DR}_{des} = \underline{RM}\underline{sc}, \quad (2.19)$$

where \underline{DR}_{des} is a vector having for elements the desired depth of removal at the points y_i , must be solved for \underline{sc} . This is the second key to the inverse problem.

Eq. (2.19) is a rather simple matrix equation. If \underline{RM} is a square matrix it might be possible to compute its inverse. \underline{sc} could then be set equal to

$$\underline{sc} = \underline{RM}^{-1} \underline{DR}_{des} \quad (2.20)$$

If \underline{RM} is not a square matrix, its pseudo-inverse [25], defined by

$$\underline{RM}^+ = (\underline{RM}^T \underline{RM})^{-1} \underline{RM}^T, \quad (2.21)$$

could be computed to have

$$\underline{sc} = \underline{RM}^+ \underline{DR}_{des}. \quad (2.22)$$

However, because of the convolution nature of the problem, \underline{RM} is typically ill-conditioned and Eqs. (2.20) and (2.22) produce a meaningless solution. Such a solution is illustrated in Figure 2.8. It was achieved with a desired uniform removal of 5 μm and \underline{RM} computed for a flat with the removal function derived from the removal spot shown in Figure 2.9. The tool crossfeed velocity solution is not satisfactory because the constraints of Eq. (2.7) are violated.

To overcome the ill-conditioning of \underline{RM} , the form correction problem is treated as a constrained optimization problem. Its solution is the vector \underline{sc} minimizing the norm of the error vector $\underline{\varepsilon}$ defined by

$$\underline{\varepsilon} = \underline{DR}_{des} - \underline{RM} \underline{sc}, \quad (2.23)$$

while satisfying the constraints of Eq. (2.8). In order to enforce these constraints they need to be written in discrete form. The constraint of Eq. (2.8) on the tool velocity can be formulated as

$$\frac{1}{v_{c \max}} < sc_j < \frac{1}{v_{c \min}}, \quad (2.24)$$

where v_{cmin} is the minimum permissible tool crossfeed velocity, introduced to prevent the tool from being too slow. The tool acceleration is evaluated at the midpoints of the arcs of length L_{arc} separating two consecutive tool positions on the part with the following approximation

$$\frac{dv_c}{dt} \approx \frac{\Delta v_c}{L_{arc}} v_c \approx \frac{1/sc_{j+1} - 1/sc_j}{L_{arc}} \frac{1/sc_{j+1} + 1/sc_j}{2}. \quad (2.25)$$

Therefore, the constraint of Eq. (2.8) on the tool acceleration becomes

$$\left| sc_j^2 - sc_{j+1}^2 \right| \leq 2a_{cmax} L_{arc} sc_{j+1}^2 sc_j^2 \quad (2.26)$$

The ℓ^2 -norm, defined by the following equation

$$\|\boldsymbol{\varepsilon}\|_2 = \sqrt{\sum_{i=1}^{N\Delta r} |\varepsilon_i|^2}, \quad (2.27)$$

is the most commonly used for this type of problem. Current processes such as HyDra [24] and Zeeko Precessions process [18] mention the use of that norm without any detail about the nature of the algorithm that they use. On the other hand, Carnal et al. [23] at Oak Ridge National Laboratory solved this problem with the documented LSQR (Least Squares) algorithm [26]. But it does not appear to allow for the necessary constraints defined by Eqs. (2.24) and (2.26). The nonnegative least squares algorithm [27] used by Lee et al. [28] has the advantage that it can prevent negative solutions but that is the only constraint that is enforced. The norm defined by Eq. (2.27) is used to solve the present form correction problem.

Such a constrained optimization problem can be solved with the `fmincon.m` [29] MATLAB [30] function available in the MATLAB optimization toolbox. Using

that function, a solution minimizing the norm of $\underline{\varepsilon}$ and satisfying the constraints is obtained. Such a feasible solution is shown in Figure 2.10. However, that solution lacks the smoothness that is necessary on the CNC machine.

Therefore, in addition to the constraints on the tool velocity and acceleration, the smoothness of the solution must be considered. A smoother solution can be obtained with Tikhonov regularization [31, 32, 33, 34, 35]. With this method, the smoothness of the solution is taken into account in the objective function, which is rewritten as

$$\|\underline{\varepsilon}\|_2^2 + \lambda^2 \|\underline{\underline{L}} \underline{sc}\|_2^2 = \|\underline{DR}_{des} - \underline{\underline{RM}} \underline{sc}\|_2^2 + \lambda^2 \|\underline{\underline{L}} \underline{sc}\|_2^2 \quad (2.28)$$

where λ and $\underline{\underline{L}}$ are a regularization parameter and regularization matrix respectively. λ controls the weight of the smoothing and $\underline{\underline{L}}$ its nature. $\underline{\underline{L}}$, for example, can be the identity matrix or an approximation of a first or second derivative operator. A formulation similar to Eq. (2.28) is also reported by Forbes [1], who also suggests the following form for $\underline{\underline{L}}$.

$$\underline{\underline{L}} = \begin{pmatrix} -\tilde{v}_c(y_{0\min}) & \tilde{v}_c(y_{0\min} + \Delta y_0) & 0 & \dots & \dots & 0 \\ 0 & -\tilde{v}_c(y_{0\min} + \Delta y_0) & \tilde{v}_c(y_{0\min} + 2\Delta y_0) & 0 & \dots & 0 \\ \dots & \dots & \dots & \dots & \dots & \dots \\ 0 & \dots & 0 & -\tilde{v}_c(y_{0\max} - 2\Delta y_0) & \tilde{v}_c(y_{0\max} - \Delta y_0) & 0 \\ 0 & \dots & \dots & 0 & -\tilde{v}_c(y_{0\max} - \Delta y_0) & \tilde{v}_c(y_{0\max}) \end{pmatrix}, \quad (2.29)$$

where \tilde{v}_c is an approximation of the solution. The definition of such an approximation is considered in the next paragraph. With $\underline{\underline{L}}$ defined according to Eq. (2.29), solutions

resembling \tilde{v}_c with smooth variations of their first derivatives are targeted. $\underline{\underline{L}}$ is also defined according to Eq. (2.29) for the present problem.

$\underline{\underline{L}}$ requires the knowledge of an approximate solution \tilde{v}_c . A solution roughly achieving a uniform removal profile of amplitude similar to the amplitude of the desired correction is satisfactory. It is known that for tools having an infinitesimal contact patch, a crossfeed velocity varying as $1/y_0$ results in a constant depth of removal [36]. The removal profile shown in Figure 2.11 was obtained with $\underline{\underline{RM}}$ used to compute the solution of Figure 2.10 and a crossfeed velocity proportional to $1/y_0$. The predicted depth of removal appears constant away from the part center. However, less material is removed at the center over a region approximately as large as the removal function and is responsible for a PV error of approximately 1.5 μm . Therefore, to obtain a constant depth of removal, the tool dwell time must be increased by decreasing its crossfeed velocity over the central region of the part. Such a behavior can be achieved by defining \tilde{v}_c as follows

$$\tilde{v}_c(y_0) = \frac{1}{c_1 \left(1 + \left(\frac{c_2}{c_1} y_0 \right)^n \right)^{1/n}}, \quad (2.30)$$

where c_1 , c_2 and n are coefficients that must be adjusted for given removal function and depth. \tilde{v}_c is approximately equal to $1/(c_2 y_0)$ away from the part center, therefore c_2 is adjusted so that $1/(c_2 y_0)$ produces the desired removal depth away from the part center. The distance from the part center from which the tool should be slowed down is a function of the size of the removal function. In Eq. (2.30), that distance is

adjusted with n , a large value of n reducing the extent of the region over which the tool is slowed down. For a given value of n , c_1 is chosen so that the ℓ^2 -norm of the difference between desired and predicted removal profiles is minimized. Algorithms developed for UFF uses a dichotomous search to find the values of c_1 for n taking the values 2, 3, ..., 15 and select the pair of (c_1, n) producing the most accurate removal profile.

\tilde{v}_c was evaluated in the case of the removal function and desired depth of removal considered in Figures 2.10 and 2.11. \tilde{v}_c and the corresponding removal profile are shown in Figure 2.12. The predicted removal profile reveals that the form error is now distributed evenly around the desired depth of removal. The PV error is less than 1 μm and significantly better than with a tool crossfeed velocity simply proportional to $1/y_0$. Therefore, Eq. (2.30) defines a satisfactory approximate solution to the form problem.

The methods used to select λ and solve the constrained optimization problem with the objective function defined by Eq. (2.28) are not described by Forbes [1]. The vector \underline{s}_c minimizing Eq. (2.28) is known to be [35]

$$\underline{s}_c = (\underline{RM}^T \underline{RM} + \lambda^2 \underline{L}^T \underline{L})^{-1} \underline{RM}^T \underline{DR}_{des} \quad (2.31)$$

However, to avoid the matrix inversion of Eq. (2.31), the solution is conveniently obtained from a computation of the Generalized Singular Value Decomposition (GSVD) [25, 32, 33, 34] of the pair of matrices $(\underline{RM}, \underline{L})$.

This method establishes a solution minimizing Eq. (2.28), but it does not guarantee that the constraints on the tool velocity and acceleration are satisfied. This requirement is achieved via the selection of the parameter λ . If λ was very low, Eq. (2.28) would be equivalent to minimizing the norm of Eq. (2.23). Facing ill-conditioning, a solution similar to the one shown in Figure 2.10 would be found. v_c would not be smooth, but the predicted residual form error would be minimum. On the other hand, if λ was very large, the solution would converge to $1/\tilde{v}_c$. This solution would be smooth but would produce a large residual form error. Smoothness of the solution is gained at the cost of an increase in the residual form error. The constraints on \underline{s}_c will be satisfied with a relatively smooth solution. Therefore, the desired solution is the solution for which λ is large enough to satisfy the constraints on the solution but low enough to produce a low residual form error. A dichotomous search is used to establish the lowest value of λ for which the solution is feasible. For that value, \underline{s}_c is such that Eqs. (2.24) and (2.26) are satisfied.

In summary, the removal matrix is first computed. The approximate solution \tilde{v}_c , defined by Eq. (2.30), is found by establishing c_1 , c_2 and n minimizing form error. That solution is used to compute the regularization matrix $\underline{\underline{L}}$ according to Eq. (2.29). That matrix is then used to establish with a dichotomous search the lowest value of λ for which Eqs. (2.24) and (2.26) are satisfied. At each step of that search, v_c is established by using the GSVD of the pair of matrices ($\underline{\underline{RM}}$, $\underline{\underline{L}}$).

The solution achieved with these algorithms and the same inputs as for Figure 2.10, 2.11 and 2.12 is shown in Figure 2.13. v_c is smooth and produces a nearly uniform removal profile since the PV error is on the order of $0.05 \mu\text{m}$. v_c follows the trend of the approximate solution with some oscillations to precisely achieve the desired removal profile.

The form correction algorithms based on the methods presented in this chapter have been used to polish uniformly a BK7 plano part of diameter 35 mm with cerium oxide bound abrasive. The desired uniform depth of removal of $5 \mu\text{m}$ was achieved in one pass of 20 minutes. The part edges were left untouched so they could be used as a height datum. The resulting surface, away from the edges, exhibits a peak-to-valley error of $0.26 \mu\text{m}$, which is slightly lower than the error of the initial surface. Figure 2.14 is a Zygo Mark IV [37] measurement of this part over an aperture of diameter 27 mm.

2.3 References

- [1] Greg Forbes - COM summer school notes, 1999.
- [2] Talysurf stylus profilometer, Taylor Hobson Ltd, P.O. Box 36, 2 New Star Road, Leicester, LE4 9JQ, England, Phone: +44 116-276-3771, www.taylor-hobson.com.
- [3] C. A. Hall, T. A. Porsching, "Approximation methods in the computer numerically controlled fabrication of optical surfaces, Part 1: Finite dimensional material removal profile spaces," IMA Journal of Numerical Analysis 12, 67-84 (1992).
- [4] T. A. Porsching, C. A. Hall, T. L. Bennett, "Minimax approximation of optical profiles," SIAM Journal of Applied Mathematics 58, 1951-1968 (1998).

- [5] G. B. Arfken, H. J. Weber, *Mathematical methods for physicists*. San Diego, CA: Academic Press, 1995.
- [6] R. G. Hohlfeld, J. I. F. King, T. W. Drueding and G. v. H. Sandris, "Solution of convolution integral equations by method of differential inversion," *SIAM Journal of Applied Mathematics* 53, 154-167 (1993).
- [7] A. S. Vasudeva Murthy, "A note on the differential inversion method of Hohlfeld et al.," *SIAM Journal of Applied Mathematics* 55, 719-722 (1995).
- [8] C. A. Hall, T. A. Porsching, "Approximation methods in the computer numerically controlled fabrication of optical surfaces, Part 2: Mollifications," *IMA Journal of Numerical Analysis* 12, 259-269 (1992).
- [9] P. A. Jansson, *Deconvolution with applications in spectroscopy*. Orlando, FL: Academic Press, 1984.
- [10] R. Aspden, R. McDonough, and F. R. Nitchie, Jr., "Computer assisted optical surfacing," *Applied Optics* 16, 218-222 (1972).
- [11] R. A. Jones, "Optimization of computer controlled polishing," *Applied Optics* 16, 218-224 (1977).
- [12] N. J. Brown, "Computationally directed axisymmetric aspheric figuring," *Optical Engineering* 17, 602-620 (1978).
- [13] T. W. Drueding, T. G. Bifano and S. C. Fawcett, "Contouring algorithm for ion figuring," *Precision Engineering* 17, 10-21 (1995).
- [14] T. Hänsel, A. Nickel, H.-J. Thomas, A. Schindler, R. Schwabe, "Local thickness correction of nanometer thin films by means of ion beam etching," *OSA Technical Digest, Optical Fabrication and Testing*, Tucson, Arizona, June 3-5 2005 (OWB2).
- [15] T. A. Porsching, C. A. Hall, "Computationally directed axisymmetric figuring (after N. J. Brown)," *Applied Optics* 35, 4463-4470 (1996).
- [16] R. E. Wagner and R. R. Shannon, "Fabrication of aspherics using a mathematical model for material removal," *Applied Optics* 13, 1683-1689 (1974).
- [17] D. J. Bajuk, "Computer controlled generation of rotationally symmetric aspheric surfaces," *Optical Engineering* 15, 401-406 (1976).

- [18] US patent 6,796,877, R. Bingham and D. C. Riley, "Abrading machine" (2004).
- [19] S. R. Wilson, J. R. McNeil, "Neutral ion beam figuring of large optical surfaces," *Current Developments in Optical Engineering II*, Proc. SPIE 818, 320-324 (1987).
- [20] P. M. Shanbag, M. R. Feinberg, G. Sandri, M. N. Horenstein, T. G. Bifano, "Ion-beam machining of millimeter scale optics," *Applied Optics* 39, 599-611 (2000).
- [21] L. N. Allen, R. E. Keim, "An ion figuring system for large optic fabrication," *Current Developments in Optical Engineering and Commercial Optics* 1168, 33-50 (1989).
- [22] C. Xu, I. Aissaoui, S. Jacquey, "Algebraic analysis of the Van Cittert iteration method of deconvolution with a general relaxation factor," *Journal of the Optical Society of America A* 11, 2804-2802 (1994).
- [23] C. L. Carnal, C. M. Egert, K. W. Hylton, "Advanced matrix-based algorithm for ion beam milling of optical components," *Current Developments in Optical Design and Optical Engineering II*, Proc. SPIE 1752, 54-62 (1992).
- [24] J. Gonzalez-Garcia, A. Cordero-Davila, E. Luna, M. Nunez, E. Ruiz, L. Salas, V. H. Cabrera-Davila, I. Cruz-Gonzalez, E. Sohn, "Static and dynamic removal rates of a new hydrodynamic polishing tool," *Applied Optics* 43, 3623-3631 (2004).
- [25] G. H. Golub, C. F. Van Loan, *Matrix Computations*, third edition, The Johns Hopkins University Press, London, 1996.
- [26] C. C. Paige, M. A. Saunders, "LSQR: An algorithm for sparse linear equations and sparse least squares," *ACM Trans. Math Software*, 8, 43-71, (1982).
- [27] C. L. Lawson, R. J. Hanson, *Solving least squares problems*. Englewood Cliffs, NJ: Prentice-Hall, 1974.
- [28] H. Lee, M. Yang, "Dwell time algorithm for computer-controlled polishing of small axis-symmetrical aspherical lens mold," *Optical Engineering* 40, 1936-1943 (2001).
- [29] www.mathworks.com/access/helpdesk/help/toolbox/optim/ug/fmincon.html, retrieved on October 17, 2007.
- [30] MATLAB R2007a (Version 7.4.0.287), The Mathworks Inc., 3 Apple Hill Drive, Natick, MA 01760-2098, Phone: 508-647-7000, www.mathworks.com.

- [31] A. N. Tikhonov, "Solution of incorrectly formulated problems and the regularization method," Soviet Mathematics Doklady 4, 1035-1038 (1963).
- [32] A. Neumaier, "Solving ill-conditioned and singular linear systems: a tutorial on regularization," SIAM Review, 40, 636-666 (1998).
- [33] P. C. Hansen, "Numerical tools for analysis and solution of Fredholm integral equations of the first kind," Inverse Problems 8, 849-872 (1992).
- [34] P. C. Hansen, "Regularization tools: A Matlab package for analysis and solution of discrete ill-posed problems," Numerical Algorithms 6, 1-35 (1994).
- [35] P. C. Hansen, *Rank-deficient and Discrete Ill-Posed Problems*, SIAM Monographs on Mathematical Modeling and Computation, Philadelphia, Pennsylvania, 1997.
- [36] P. Funkenbusch, T. Takahashi, S. Gracewski and J. Ruckman, "Use of a non-dimensional parameter to reduce errors in grinding of axisymmetric aspheric surfaces," Int. J. Japan Soc. Prec. Eng. 33, 337- 339, (1999).
- [37] Mark IV phase-shifting interferometer, Zygo Corp., Laurel Brook Road, Middlefield CT 06455-0448, Phone: 860-347-8506, www.zygo.com.

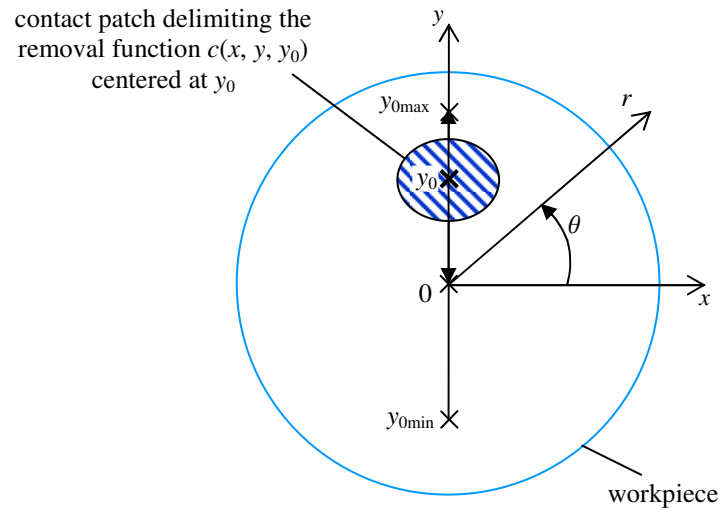


Figure 2.1 Geometry of the problem for flats.

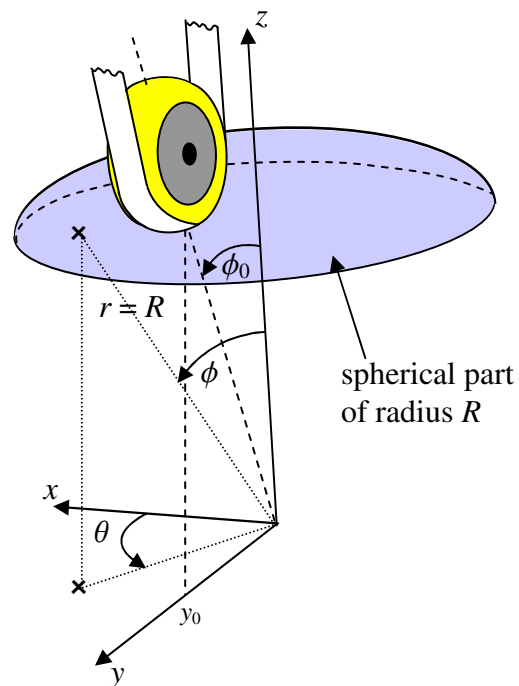


Figure 2.2 Geometry for spheres polishing.

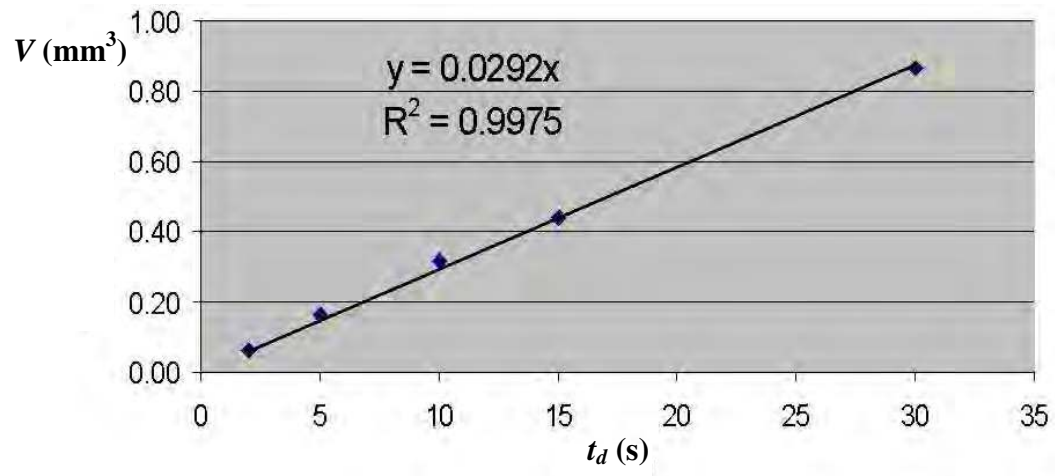


Figure 2.3 Linear relation between removal spot volume and spot dwell time.

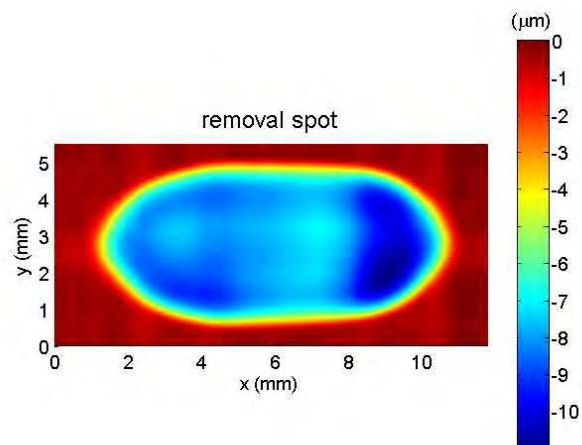


Figure 2.4 Removal spot used for comparison between predicted and actual depth of removal.

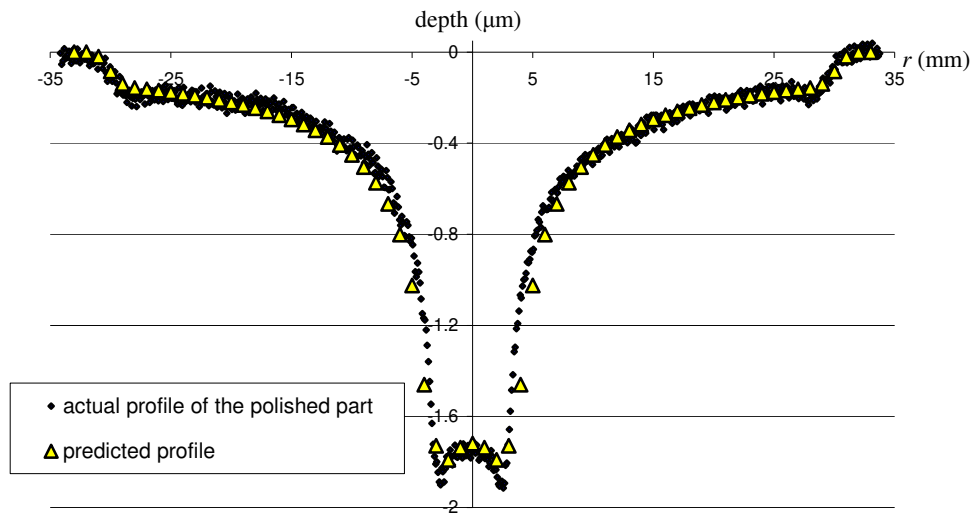


Figure 2.5 Comparison between the predicted depth of removal and the actual part profile.

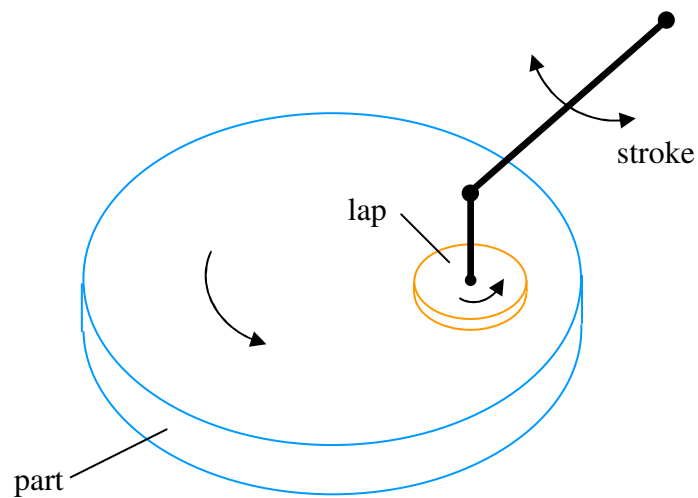


Figure 2.6 Polishing with a subaperture lap.

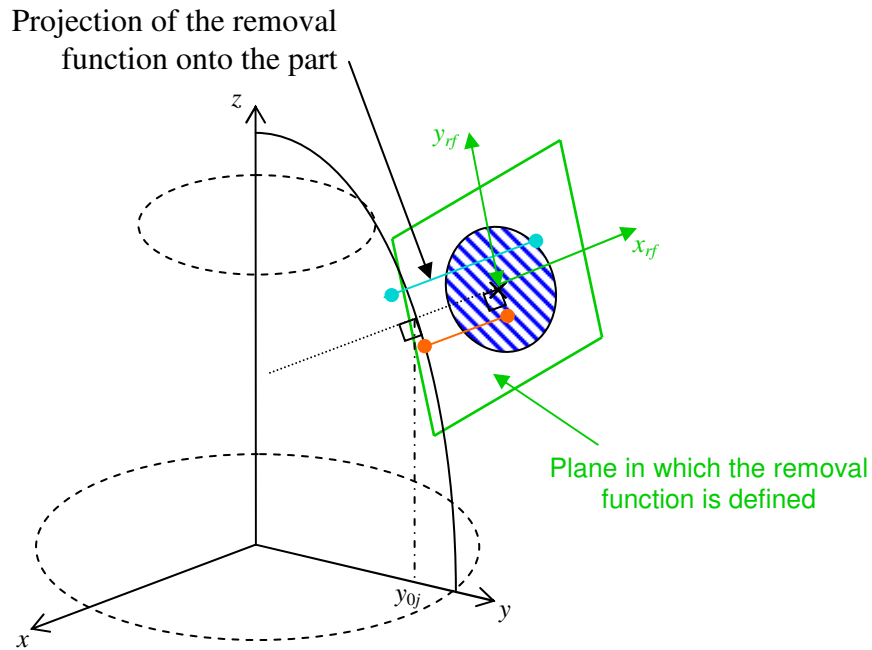


Figure 2.7 Mapping of the removal function on the workpiece.

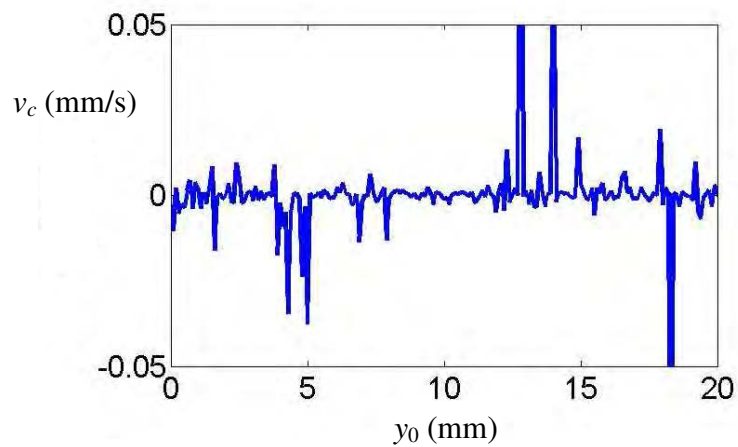


Figure 2.8 Tool crossfeed velocity obtained with Eq. (2.24) for uniform removal of $5 \mu\text{m}$ on flat using the removal spot of Figure 2.9.

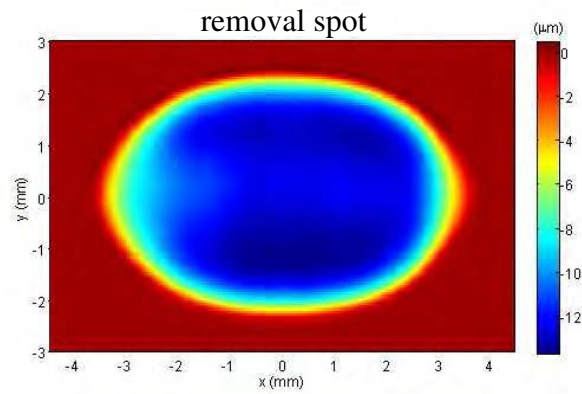


Figure 2.9 Removal spot used to compute the solutions of Figure 2.8.

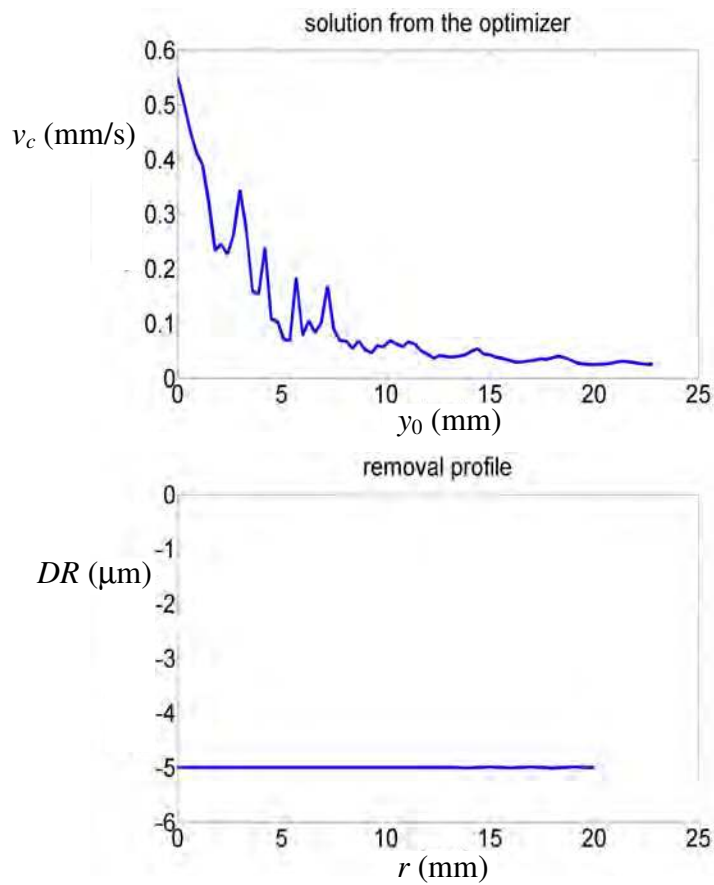


Figure 2.10 Tool crossfeed velocity solution and predicted removal profile with the MATLAB function `fmincon.m`.

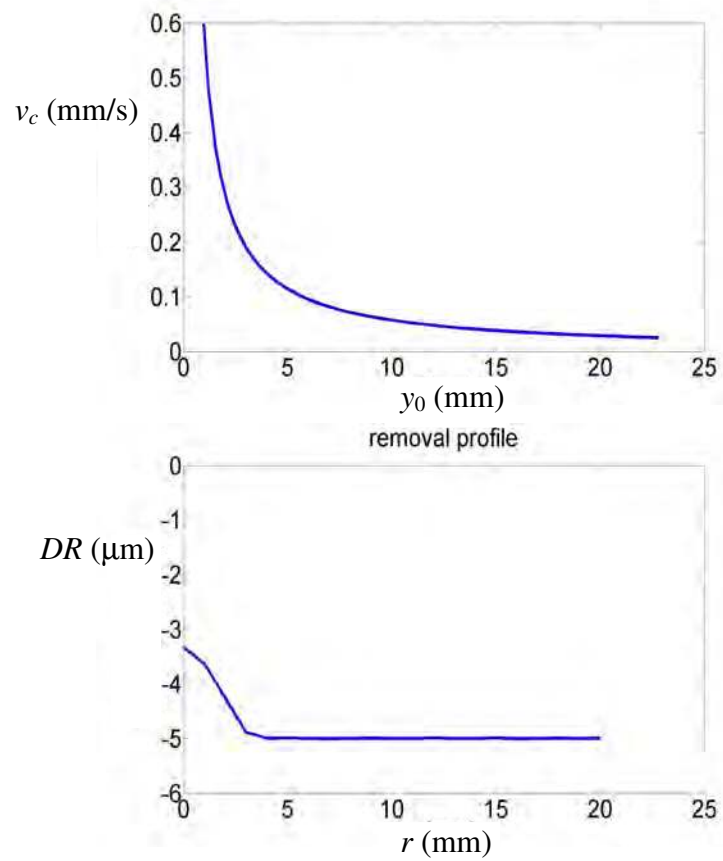


Figure 2.11 Tool crossfeed velocity proportional to $1/y_0$ and predicted removal profile.

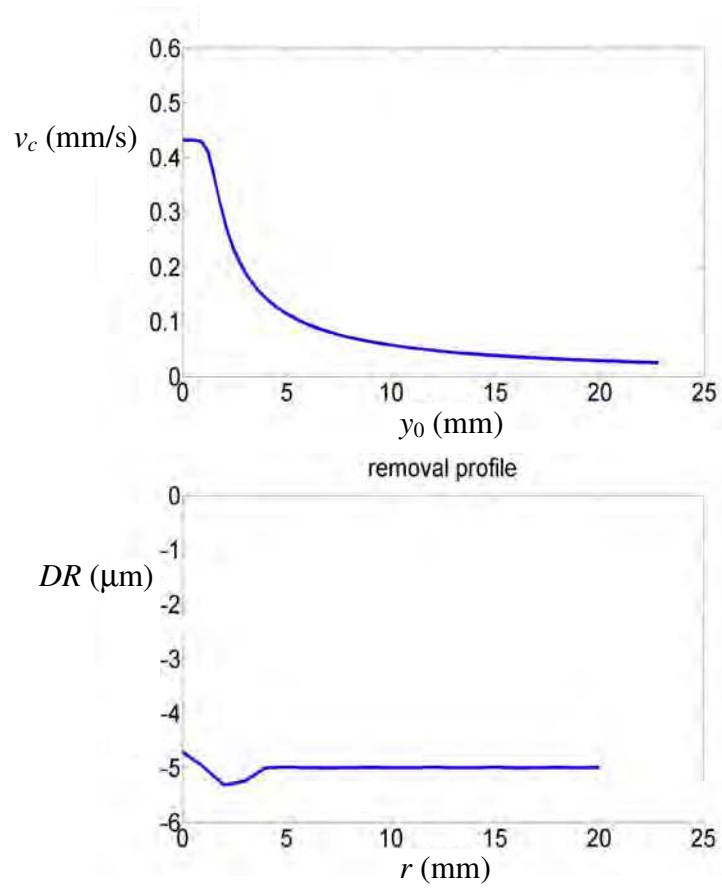


Figure 2.12 Tool crossfeed velocity approximation for uniform removal and predicted removal profile.

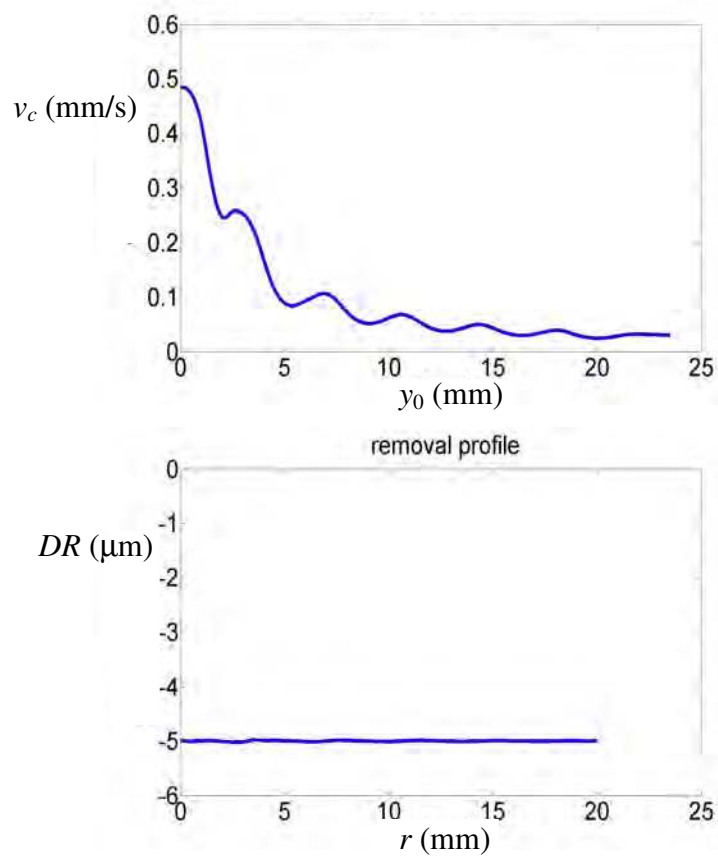


Figure 2.13 Tool crossfeed velocity solution and predicted removal profile with the form algorithms developed for UFF.

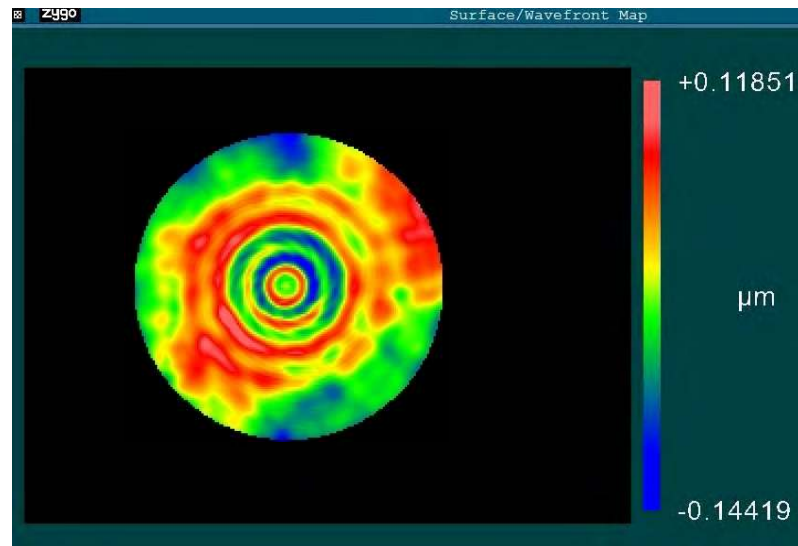


Figure 2.14 Wavefront map of a part polished uniformly using the form algorithms developed for UFF.

Chapter 3 Tool path geometry determination

The tool path geometry is defined at step 5 of the UFF process flow chart in Figure 1.7. This step defines how to position the tool to safely achieve the desired tool-part contact and compression as the tool is moved across the part.

3.1 Definition and preferred configuration

The tool path geometry is the series of spatial positions occupied by the tool during polishing. As the tool traverses the part, the tool positions and orientations must be defined according to the machine motion limits and the part and tool geometry. Since the parts considered here are axisymmetric, it is sufficient to polish with the tool traveling from the edge to the center of the rotating workpiece. However, tool lift off might induce artifacts that are unacceptable at the part center. Therefore, if the workpiece has a physical center that has to be polished, it is desirable to have the tool traverse the part from edge to edge. In the case of ogives, where the center of the part does not have to be polished or has been removed, the tool can be moved from the inner to the outer edge of the workpiece.

A coordinate system (x, y, z) attached to the CNC platform and the angle B , shown in Figure 3.1, are used to describe the tool positions in this work. The origin of the (x, y, z) coordinate system is located at the center of the surface to polish. The z axis coincides with the workspindle axis of rotation and is directed positive upward. This is the axis of symmetry of the part. The x axis is parallel to the axis of rotation of

the carrier wheel and oriented positively toward the front of the platform. The tool is moved across the part along a path in the y - z plane. The B axis of rotation is orthogonal to the plane (y, z) and B is the angle between z and the tool normal. B is equal to 0 when the tool normal is parallel to z and is positive for a counterclockwise rotation of the tool. The tool path consists of finite series of coordinates (y_j, z_j) and angle values B_j . The coordinates (y_j, z_j) are those of the B axis of rotation, i.e. the pivot point. The tool path position (y_j, z_j, B_j) is defined to produce a removal function centered at (y_{0j}, z_{0j}) on the part surface.

Linear interpolation is used by the machine onboard computer to continuously move the tool between the prescribed points. The tool positioning errors that might be induced by the interpolations are minimized by finely discretizing the tool path. For this work the arc length between two consecutive (y_{0j}, z_{0j}) points is 0.1 mm. This discretization is achieved according to the method and algorithms described in Appendix 1.2.

A removal function independent of (y_{0j}, z_{0j}) position along the tool path would be preferable for the computation of the removal matrix. In that case, only that single removal function is needed to compute all the elements of the removal matrix. In the current process, band velocity, v_{band} , and tool inward displacement, δ , are constant. The part radii of curvature, and the angle, α , between the tool and local part normals, shown in Figure 3.1, are the parameters that may vary across the part and affect the

removal function. The part radii of curvature control the extent of the removal function. These radii of curvature are invariant on flat and spherical parts but vary on aspheres. Also, as α varies, the wrapping of the polishing band might change on the portions of the tool brought in contact with the part, producing variation in the removal functions. Furthermore, α affects the in-line compliance of the tool and therefore the load-displacement characteristic of the tool. To avoid these variations in removal function with α , it is desirable to keep α constant and equal to 0 along the tool path so that the tool and part normals are aligned. An example tool path with $\alpha=0$ is shown in Figure 3.2 for a convex part. This preferred configuration will simplify the computation of the removal matrix on flats and spheres and it will provide some consistency between the removal functions that have to be used on aspheres.

The CNC platform allows maximum B tool rotation angles $-B_{\max}$ and B_{\max} of -90° and 90° , respectively. Therefore, the tool-part normals aligned, i.e. α equal to 0, configuration is typically feasible on convex surfaces with diameter within the machine capacity. This is illustrated in Figure 3.2. With this configuration, the points (y_{0j}, z_{0j}) are the intersections of the tool normal with the part surface along the tool path.

On the other hand, that preferred configuration is not possible for all concave surfaces. The restrictions are due to the possible tool-part collisions that might occur

in particular, with the concave surfaces of hemispheres, ogives or domes, as illustrated in Figure 3.3. Therefore, to polish a large range of concave surfaces, methods of adjusting the tool B_j angles are necessary to avoid tool-part collisions.

3.2 Preventing tool-part collisions

3.2.1 2D symmetric model

3.2.1.1 Geometry

The part and tool geometries have to be taken into account to define for each (y_{0j}, z_{0j}) a feasible B_j angle. This angle will be feasible if it prevents tool part collision and results in a tool position within the range of achievable motions on the machine.

Such angles could be established with algorithms using a 3D model taking accurately into account the tool and part geometries. These algorithms would rely on the detection of part-tool collisions and a search strategy to find feasible or “safe” B angles. But this 3D approach, in particular the detection of tool-part collision, would be very computationally demanding. The problem can be simplified with the use of a 2D model. This is possible because the workpiece is axisymmetric and the tool is only subjected to a planar (y - z) motion.

For this approach, the workpiece is modeled by the profile of the surface to be polished. The part profile is discretized according to the approach and algorithms defined in Appendix 1.2. The arc length between two consecutive points is typically on the order of 0.1 mm. For concave surfaces, the thickness of the part at its edge can

also be a source of collision. Therefore, segments are placed at both extremities of the profile to model the edge of the part.

The 2D model must take into account the 3D nature of the tool. The machine was developed by OptiPro Systems [1] with the CAD software SolidWorks [2]. This software is also a convenient tool for visualizing and evaluating the machine 3D geometry. SolidWorks views of the Army and Navy machine configurations are shown in Figures 3.4-3.7 and 3.8-3.11, respectively. They are the two existing UFF geometries. They both share the same UFF head, shown in Figures 3.7 and 3.11. The Army configuration includes a second tool spindle located at the back of the UFF tooling. This spindle is highlighted in Figure 3.6 and is available for ring or wheel grinding tools. The Navy configuration is dedicated to UFF only and the tool spindle of the Army version is replaced by a block of triangular cross section in the $(x-z)$ plane, as shown in Figure 3.10. These structural differences need not be taken into account as these regions are out of reach for parts of diameter less than 150 mm, the specified maximum capacity of the machine. Parts with such diameter can only interfere with the UFF head. Therefore, only that region of the tool needs to be modeled to evaluate tool-part collisions.

For this analysis, the coordinate system (x_T, y_T, z_T) is attached to the tool with origin at the tip of the tool. The z_T axis is oriented along the tool normal and positive into the tool. The x_T axis is parallel to the x axis. The 2D collision model was developed to be symmetric with respect to the z_T axis. As a consequence, the

established tool paths are symmetric with respect to the workpiece center. This is beneficial as it simplifies the removal matrix computation and removal function prediction. One additional advantage is that the whole tool path can then be established by only solving half the tool path problem.

The tool model is defined by considering cross sections of the tool orthogonal to the z_T axis. In a cross section at a given z_T , the distance from the tool normal to the furthest point of the tool in this plane, $L_{tool}(z_T)$, is identified as illustrated in Figure 3.12. The tool interior region is modeled in 2D by the region of the plane comprised between the curves $-L_{tool}(z_T)$ and $L_{tool}(z_T)$. Because of the relatively simple geometry of the UFF head, the complete tool geometry of the 2D model can be defined with the seven points P_1 through P_7 and the eight dimensions D_1 through D_8 shown in Figure 3.13.a). D_1 is equal to the carrier wheel radius R_W . The vertical dimensions D_7 and D_8 are defined to be invariant when the tool shaft or carrier wheel are modified. The points P_1, P_2, \dots, P_7 have the respective coordinates $(y_{P_1}, z_{P_1}), (y_{P_2}, z_{P_2}), \dots, (y_{P_7}, z_{P_7})$ in (y_T, z_T) , such that

$$(y_{P_1}, z_{P_1}) = (D_1, D_1), \quad (3.1)$$

$$(y_{P_2}, z_{P_2}) = (D_2, D_1 + D_6), \quad (3.2)$$

$$(y_{P_3}, z_{P_3}) = (D_3, D_1 + D_6), \quad (3.3)$$

$$(y_{P_4}, z_{P_4}) = (D_3, D_1 + D_6 + D_7), \quad (3.4)$$

$$(y_{P_5}, z_{P_5}) = (D_4, D_1 + D_6 + D_7), \quad (3.5)$$

$$(y_{P_6}, z_{P_6}) = (D_5, D_1 + D_6 + D_8), \quad (3.6)$$

$$(y_{P_7}, z_{P_7}) = (D_5, D_1 + D_6 + D_8 + offs), \quad (3.7)$$

where *offs* is a constant so that P_7 is such that $z_{P_7} \neq z_{P_6}$. $L_{tool}(z_T)$ can be described as a combination of a quarter circle modeling the carrier wheel, 5 segments and a half line, [P6P7]. $L_{tool}(z_T)$ resembles the front view of the tool even though the dimensions D_1 through D_8 do not match the dimensions of the front view but instead take into account the depth of the tool. A vertical half-line is used for z_T greater than z_{P_6} instead of a segment, because none of the points modeling the part should be in the region defined by $z_T \geq z_{P_6}$, that half-line and the one that is symmetric with respect to z_T . $L_{tool}(z_T)$ can be expressed as a piecewise function formed of the equations of a quarter circle and lines defined by P_1 through P_7 . This 2D model gives a conservative estimate for collision when a point modeling the part enters the region of the plane defined by $-L_{tool}(z_T)$ and $L_{tool}(z_T)$. But the present model does not guarantee any clearance between the part and the tool and therefore, there is no safety margin.

In order to provide some clearance between the tool and the part, a safety region surrounding the tool 2D model is added. This region is delimited by the curve $L_{safety}(z_T)$ illustrated in Figure 3.13.b). A uniform clearance, S_1 , is used for the top part of the tool. There is no clearance around the bottom half carrier wheel and a tapered safety region of width S_2 at z_1 is used in between. S_1 and S_2 are user defined inputs, but they should typically be of the order of 10 and 5 mm. The tapered shape prevents the tool model from becoming too large near its tip while allowing sufficient clearance elsewhere. This is important for the polishing of deep concave parts. As for

the tool interior region, the safety region is defined by 7 points, labeled P'_1, P'_2, \dots

P'_7 of coordinates

$$(y_{P'_1}, z_{P'_1}) = (y_{P_1} + S_2, z_{P_1}), \quad (3.8)$$

$$(y_{P'_2}, z_{P'_2}) = (y_{P_2}, z_{P_2} - S_1), \quad (3.9)$$

$$(y_{P'_3}, z_{P'_3}) = (y_{P_3} + S_1, z_{P_3} - S_1), \quad (3.10)$$

$$(y_{P'_4}, z_{P'_4}) = (y_{P_4} + S_1, z_{P_4} - S_1), \quad (3.11)$$

$$(y_{P'_5}, z_{P'_5}) = (y_{P_5}, z_{P_5} - S_1), \quad (3.12)$$

$$(y_{P'_6}, z_{P'_6}) = (y_{P_6} + S_1, z_{P_6}), \quad (3.13)$$

$$(y_{P'_7}, z_{P'_7}) = (y_{P_7} + S_1, z_{P_7}), \quad (3.14)$$

in (y_T, z_T) where $y_{P'_2}$, $y_{P'_5}$ and $z_{P'_6}$ are determined as follows. $y_{P'_2}$ is calculated, by considering, as shown in Figure 3.14, the intersection P_{int} of (P_1P_2) and the horizontal line defined by $z_T = z_{P'_2}$. The general equation of a line passing through two points of coordinates (y_a, z_a) and (y_b, z_b) is given by

$$y_T = \frac{y_b - y_a}{z_b - z_a} z_T + \frac{y_a z_b - y_b z_a}{z_b - z_a}. \quad (3.15)$$

Using Eq. (3.15) with the coordinates of the points $\{P_1, P_2\}$ and evaluating at $z_T = z_{P'_2}$,

$$y_{P_{int}} = D_2 + S_1 \frac{D_1 - D_2}{D_6}. \quad (3.16)$$

And the difference between the abscissas of P_{int} and P'_2 is

$$y_{P'_2} - y_{P_{int}} = \frac{S_1}{\cos(\psi)} \quad (3.17)$$

where

$$\psi = \arctan\left(\frac{D_2 - D_1}{D_6}\right) \quad (3.18)$$

is the angle between (P_1P_2) and the z_T axis. Therefore, by combining Eqs. (3.16) and (3.17),

$$y_{P'_2} = D_2 + S_1 \frac{D_1 - D_2}{D_6} + \frac{S_1}{\cos(\psi)}. \quad (3.19)$$

$y_{P'_5}$ is established by first noticing that $(P'_5P'_6)$ is simply a translation of (P_5P_6) , thus its equation is given by

$$(P'_5P'_6): y_T = \frac{y_{P_6} - y_{P_5}}{z_{P_6} - z_{P_5}} z_T + \frac{y_{P_5} z_{P_6} - y_{P_6} z_{P_5}}{z_{P_6} - z_{P_5}} + \Delta b, \quad (3.20)$$

where, since (P_5P_6) is at an angle

$$\psi' = \arctan\left(\frac{D_5 - D_4}{D_8 - D_7}\right) \quad (3.21)$$

from the z_T axis, as shown in Figure 3.15,

$$\Delta b = \frac{S_1}{\cos(\psi')}. \quad (3.22)$$

Therefore, by evaluating Eq. (3.20) at $z_T = z_{P'_5}$

$$y_{P'_5} = D_4 + S_1 \left(\frac{D_4 - D_5}{D_8 - D_7} + \frac{1}{\cos(\psi')} \right). \quad (3.23)$$

And by solving that same equation for z_T with $y_T = y_{P'_6}$

$$z_{P'_6} = D_1 + D_6 + D_8 + S_1 \left(1 - \frac{1}{\cos(\psi')} \right) \left(\frac{D_8 - D_7}{D_5 - D_4} \right) \quad (3.24)$$

Similarly to $L_{tool}(z_T)$, $L_{safety}(z_T)$ could be defined as a piecewise function of z_T .

3.2.1.2 Operations to determine tool-part collisions

The 2D model for tool-part collision is illustrated in Figure 3.16. The part is represented by discrete points, the tool by its symmetric interior and safety regions. Potential collisions while polishing the part with a removal function centered at (y_{0j}, z_{0j}) can be evaluated by rotating the tool model by the angle B_j and translating it so as to contact the desired part point. That translation is performed so that the point (y_{0j}, z_{0j}) is on the half circle modeling the carrier wheel and such that the local part normal at this point intercepts the carrier wheel axis of rotation, as illustrated in Figure 3.1. The coordinates of the points on the part initially defined in the (x, y, z) coordinate system could be evaluated in the (x_T, y_T, z_T) coordinate system attached to the tool. If any of these points is such that

$$-L_{safety}(z_T) \leq y_T \leq L_{safety}(z_T), \quad (3.25)$$

and therefore, becomes interior to the tool and safety regions, then the tool position would not qualify as feasible. Because of the large number of points representing the part, the operation of transforming their coordinates in the (x_T, y_T, z_T) coordinate system is rather time consuming. A faster solution for tool-part collision evaluation

consists in defining the interior region of the tool in terms of the coordinates y and z which are used to define the part, instead of (y_T, z_T) .

This approach requires the translation and rotation of the points forming the tool model. For that purpose, the full 2D symmetric model is considered. It is formed of the seven points P'_1, P'_2, \dots, P'_7 and $P''_1, P''_2, \dots, P''_7$, which are symmetric to the first seven points with respect to the axis z_T , as shown in Figure 3.17. In (y_T, z_T) ,

$$(y_{P'_i}, z_{P'_i}) = (-y_{P''_i}, z_{P''_i}). \quad (3.26)$$

Setting the tool reference position such that its tip ($y_T = z_T = 0$) is at the (y, z) origin and $B = 0$, the coordinate systems (x_T, y_T, z_T) and (x, y, z) are equal. Therefore, in that reference position, the coordinates of the points defining the tool safety regions in (y, z) are given by Eqs. (3.8) – (3.14). These fourteen points are rotated then translated so that the carrier wheel contacts the part at (y_{0j}, z_{0j}) . This rotation has for center the center of the carrier wheel and is of angle B_j . For that purpose, the polar coordinates (r, θ) with origin the center of the carrier wheel $(0, R_W)$ and such that θ is equal to 0 in the positive y direction is defined. The following operation transforms (y, z) into (r, θ) coordinates.

$$(r, \theta) = (\sqrt{y^2 + (z - R_W)^2}, \arctan((z - R_W) / y)) \quad (3.27)$$

A point of polar coordinates (r, θ) after rotation by an angle B_j is transformed into

$$(r, \theta) \rightarrow (r, \theta + B_j). \quad (3.28)$$

And the Cartesian coordinates of the rotated point are given by

$$(y, z) = (r \cos(\theta + B_j), r \sin(\theta + B_j) + R_W). \quad (3.29)$$

The translation is performed so as to place the center of the carrier wheel $(0, R_W)$ at a distance equal to R_W along the local part normal. This is achieved by transforming the point's coordinates as follows

$$(y, z) \rightarrow (y + y_{0j} - R_W \sin(B_{j\text{norm}}), z + z_{0j} - R_W(1 - \cos(B_{j\text{norm}}))), \quad (3.30)$$

where $B_{j\text{norm}}$ is the angle between z and the part local normal. Therefore, the operations to transform the points subjected to the rotation and translation described here are obtained by combining Eqs. (3.30) and (3.29)

$$(y, z) \rightarrow (r \cos(\theta + B_j) + y_{0j} - R_W \sin(B_{j\text{norm}}), r \sin(\theta + B_j) + z_{0j} - R_W \cos(B_{j\text{norm}})), \quad (3.31)$$

with r and θ defined according to Eq. (3.27).

The tool safety interior region has then to be defined dynamically as a function of tool translation and rotation.

For simplicity, the carrier wheel region is not modeled as the interior of the half circle shown in Figure 3.17, but as the interior of the full circle. This is satisfactory because that entire circle is within the tool safety region. Starting from the equation for the circle representing the carrier wheel of radius R_W and center the center of the carrier wheel (y_C, z_C) , which can be established with $(y, z) = (0, R_W)$ in Eq. (3.30),

$$(y - y_C)^2 + (z - z_C)^2 = R_W^2, \quad (3.32)$$

a point (y, z) is interior to the carrier wheel if its coordinates are such that

$$z < z_c + \sqrt{R_w^2 - (y - y_c)^2} \quad (3.33)$$

or

$$z > z_c - \sqrt{R_w^2 - (y - y_c)^2}. \quad (3.34)$$

When a point is detected in this region, a specific error code is outputted. This error code is used to indicate that a smaller carrier wheel might prevent the detected collision.

The rest of the tool safety and interior region is divided into 4 regions delimited by four segments or one segment and two half-lines

- (1) $[P_1'P_1'']$, $[P_1'P_2']$, $[P_2'P_2'']$ and $[P_2''P_1'']$
- (2) $[P_3'P_3'']$, $[P_3'P_4']$, $[P_4'P_4'']$ and $[P_4''P_3'']$
- (3) $[P_5'P_5'']$, $[P_5'P_6']$, $[P_6'P_6'']$ and $[P_6''P_5'']$
- (4) $[P_6'P_6'']$, $[P_6'P_7']$ and $[P_6''P_7'']$

which are shown in Figure 3.17. A point is within these regions depending on its relative position with respect to the lines supporting the segments or half-lines forming these regions. The equation of a line ℓ in the plane (y, z) is of the form

$$z = A_\ell y + B_\ell, \quad (3.35)$$

where A_ℓ and B_ℓ are constants. But a line cannot be described with this relation when it is vertical and A_L is infinite. This can occur for all the lines of interest, since the tool can achieve rotations between -90° and 90° . Therefore, to avoid large values of A_ℓ , when $|A_\ell| \geq 1$ the line is described with a relation of the form

$$y = C_\ell z + D_\ell, \quad (3.36)$$

where C_ℓ and D_ℓ are constants. Therefore, Eqs. (3.35) and (3.36) are used when $|A_\ell| < 1$ and $|A_\ell| \geq 1$, respectively. For a line ℓ passing through two points of coordinates (y_a, z_a) and (y_b, z_b) , A_ℓ , B_ℓ , C_ℓ and D_ℓ are given by

$$A_\ell = \frac{z_b - z_a}{y_b - y_a} \quad \text{and} \quad B_\ell = \frac{z_a y_b - z_b y_a}{y_b - y_a}, \quad (3.37)$$

$$C_\ell = \frac{y_b - y_a}{z_b - z_a} = 1/A_\ell \quad \text{and} \quad D_\ell = \frac{y_a z_b - y_b z_a}{z_b - z_a}. \quad (3.38)$$

To determine what relative position to the lines define the tool interior region for a given angle B_j , it is necessary to take into account the orientation of the line when $B = 0$. At that angle, the tool safety region is mainly defined by vertical, $[P_6''P_7'']$, $[P_4''P_3'']$, $[P_3'P_4']$ and $[P_6'P_7']$, and horizontal, $[P_1'P_1'']$, $[P_3'P_3'']$, $[P_5'P_5'']$ and $[P_6'P_6'']$, lines. $[P_3'P_4']$ and $[P_3'P_3'']$ are considered for illustration purposes. Figure 3.18 is also used for that purpose. By drawing the segment or half-line of interest in that figure, such that one of its extremity is placed at the origin, the equation to use to define the line of interest is indicated. As B varies, the position of the segment is visualized by rotating it by an angle B .

At $B = 0$, $[P_3'P_4']$ is vertical, P_3' is placed at the origin in Figure 3.18 and the line $(P_3'P_4')$ is defined using Eq. (3.36). The interior region is on the left of $(P_3'P_4')$, therefore a point interior to the region (2) will in particular be such that

$$y \leq C_{P_3'P_4'} z + D_{P_3'P_4'}. \quad (3.39)$$

This is true while $|A_{P'_3P'_4}| \geq 1$. As the tool is rotated with B taking values between -90° and 90° , $[P'_3P'_4]$ can be located in the regions (a) and (c) of Figure 3.18. In both (a) and (c), Eq. (3.35) is used for $(P'_3P'_4)$. But a point must be above and below $(P'_3P'_4)$ in (a) and (c), respectively to be interior to region (2). $[P'_3P'_4]$ can only be located in (a) and (b) with negative and positive values of B , respectively. Therefore, a point (y, z) can only be interior to (2) if it satisfies

$$\text{If } |A_{P'_3P'_4}| \geq 1 \quad \text{Eq. (3.39)}$$

$$\text{else if } B_j > 0 \quad z \leq A_{P'_3P'_4}y + B_{P'_3P'_4} \quad (3.40)$$

$$\text{if } B_j \leq 0 \quad z \geq A_{P'_3P'_4}y + B_{P'_3P'_4} \quad (3.41)$$

The case of $[P'_3P'_3]$, horizontal at $B = 0$ and can be similarly treated. By drawing such that P'_3 is the origin in Figure 3.18, $[P'_3P'_3]$ is located in region (a). In this case, while $|A|$ is less than 1, $(P'_3P'_3)$ is described with an equation of the form of Eq. (3.35). And to be interior to region (2), a point must be above $(P'_3P'_3)$. When B is varied between $+90^\circ$ and -90° , $[P'_3P'_3]$ is located in (a), (b) or (d). It can only be in (b) and (d) when B is negative and positive, respectively. When $[P'_3P'_3]$ is in (b) or (d), a point can only be interior to (2), if it is on the right or left, respectively, of $[P'_3P'_3]$. These observations indicate that a point can also only be interior to (2) if it also satisfies

$$\text{If } |C_{P'_3P'_3}| \geq 1 \quad z \geq A_{P'_3P'_3}y + B_{P'_3P'_3} \quad (3.42)$$

$$\text{else if } B_j > 0 \quad y \leq C_{P'_3P'_4}z + D_{P'_3P'_4} \quad (3.43)$$

$$\text{if } B_j \leq 0 \quad y \geq C_{P'_3P'_4}z + D_{P'_3P'_4} \quad (3.44)$$

A point is interior to the region (1), (2), (3) or (4), if it satisfies relations such as the ones derived for $[P'_3P'_4]$ and $[P'_3P'_3]$ for all the segments or half-lines forming that region. The criteria for the other vertical and horizontal segments or half-lines can be derived in the same manner as for $[P'_3P'_4]$ and $[P'_3P'_3]$. The approach presented here relies on the fact that with rotations ranging between $+90^\circ$ and -90° and the knowledge of the position of the line at $B = 0$, the position of the line as a function of its slope and B can be predetermined. $[P'_1P'_2]$ and $[P'_2P'_1]$, which are nearly vertical can be treated similarly. On the other hand, $[P'_5P'_6]$ and $[P'_6P'_5]$ need particular attention. Because, at $B = 0$, the absolute value of their slopes are close to 1 and with slight variations of D_4 , D_5 , D_7 and D_8 they could become greater or less than 1. Such variations affect the region (a), (b), (c) or (d), in which they are initially located and therefore, their location as B varies. For these two segments, the constraints on y and z must be defined for absolute values of the slope at $B = 0$ equal to, less than and greater than 1.

The MATLAB [3] function ToolRotation.m has been written to perform the needed point rotations and computations of A_ℓ , B_ℓ , C_ℓ and D_ℓ for given B_j , (y_{0j}, z_{0j}) . TestPtInterior.m verifies if the points modeling the part are interior to the tool safety

region based on the method presented in this section. The code for ToolRotation.m and TestPtInterior.m is in Appendix 2.

The 2D model presented in this section is used to evaluate possible collisions. In order to determine a safe tool path, a search strategy is needed. The search strategies used for UFF are the object of the following sections.

3.2.2 B angle search strategies

For a point (y_{0j}, z_{0j}) of the part, the interval of values of B that are feasible, form the feasible space for a solution to the present problem. This interval is unique for axisymmetric workpieces. The best solution is defined as the feasible solution that minimizes $|\alpha|$. But a low value for the difference between two consecutive solutions, B_j and B_{j+1} , is also desired to insure a smooth motion of the tool.

Specific strategies to find the best safe B angles are used for the different part geometries. Concave and convex parts are handled according to the flow chart of Figure 3.19. The difference in the treatment of these two geometries resides in the specific algorithms, *Convex* and *Concave* which are first used. Based on the outputs of these algorithms, *Generic* algorithms will be used, namely if an error of type 3 is identified. These three algorithms can fail for several reasons that can be diagnosed with the outputted error codes. These codes are summarized in Table 3.1. If the part has a physical center that has to be polished and the tool cannot reach with B equal to 0 without avoiding a collision, then the part is too deep or narrow and cannot be

polished with the current tool design. This is error code number 1, which is fatal. A collision might be due to the carrier wheel being too large. This is identified when points of the part model become interior to the region representing the wheel. The code corresponding to this error is 2. It indicates that the use of a smaller wheel might be appropriate. Error code 3 occurs when the algorithms are unable to find a safe B angle. Such an error can be due to the use of an inappropriate search method or the impossibility of preventing tool-part collisions with the given workpiece.

<i>Error code</i>	<i>Cause</i>
1	Cannot reach part center
2	Collision in the carrier wheel region
3	Failure to find a safe B angle
4	Unachievable tool linear motion

Table 3.1 Error codes and their causes.

For concave parts, the dedicated algorithms *Concave* are first used. These algorithms establish a safe B angle with a search strategy adapted to most deep concave parts. Figure 3.20 shows the detailed flow chart of these algorithms. Their principle consists in considering the n_{pts} points (y_{0j}, z_{0j}) such that y_{0j} is positive. At each of these points, the tool is first rotated and translated to contact the part at (y_{0j}, z_{0j}) with B_j equal to B_{jnorm} , the B angle such that tool and part normals are aligned. The answer to the question “Is a collision detected?” is systematically obtained by applying the 2D model presented in the previous section and looking for the points of the part model becoming interior to the tool and safety region. If no collision is detected, B_j is set equal to B_{jnorm} , the preferred solution. If a collision is

detected, the strategy illustrated in Figure 3.21 is used. At first B_j is set equal to B_{j-1} . If no collision occurs with that angle, B is increased by constant increments ΔB , until a collision is predicted. B_j is ultimately set equal to the value of the angle at which that collision is predicted minus ΔB . This search strategy is used because with deep concave surfaces, as the tool moves from the part center toward its edge, a safe angular position at a point y_{0j-1} will be safe at y_{0j} . This gives a feasible starting point for the search. Furthermore it is known that the starting value, B_{j-1} , must be increased to approach $B_{j\text{norm}}$ and therefore, minimize $|\alpha|$. Therefore, a starting point and the search direction are known in this case. These properties are advantageously used here to make the search fast and robust for most concave parts and in particular deep ones such as ogives. In addition, a smooth tool motion is achieved by using ΔB on the order of 0.1° . For the geometries of interest, the amplitude of the rotation to perform when B is varied is of the order of ΔB . Larger values of ΔB results in larger intervals over which B is constant, but the amplitude of the rotations, required to transition between these intervals is too large for the degree of smoothness desired for the tool motion.

Some aspects of the algorithms have not been included in the flow charts in order to keep them relatively simple. This is true for Figure 3.20 and the following flow charts. First of all, if B_j becomes greater than B_{max} or less than $-B_{\text{max}}$, it is set equal to the value of the upper or lower bound, respectively, under the condition that no collision is predicted. Error 2 does not appear in the flow chart, but anytime a part

point is found to be in the carrier wheel region, the algorithms are actually stopped and the error 2 is outputted. Similarly error code 1 is outputted if a collision is detected while dealing with the part center.

The *Convex* algorithms do not include any search method. Their flow chart is shown in Figure 3.22. They are formed of the first steps of the *Concave* algorithms. They only check that a convex part can be polished with the tool and part normals aligned along the tool path. As mentioned previously, even though it does not appear in the flow chart, if $B_{j\text{norm}}$ is greater or lower than the machine angular limits, these limits are used.

Both *Concave* and *Convex* algorithms could fail with error code 3 with parts being overall concave or convex but presenting changes in curvatures. In that case, which corresponds to more generic shapes, the feasible intervals for B are not known in advance. The *Generic* algorithms are used to find a solution for such workpieces. The overall algorithms flow chart is shown in Figure 3.23. These algorithms use the sub-algorithms *Generic1* and *Generic2* shown in Figure 3.24 and 3.25, respectively. They first operate in the same manner as *Concave*, by first setting B_j equal to $B_{j\text{norm}}$ and then, in case of collision, equal to B_{j-1} . Whether a collision occurs or not at that angle, the sub-algorithms *Generic2* or *Generic1*, respectively, are used to find a solution.

Generic1 first determine if B_j is greater or less than $B_{j\text{norm}}$. Based on that evaluation and since the current value of B_j is in a feasible interval, the algorithms look for the best solution by consistently adding or subtracting ΔB in a manner similar to what is done within *Concave*.

Generic2 are used when B_j is not in the feasible interval. In this case, the feasible interval is not known. The algorithms *Generic2* use B_j as a starting value stored as B_{ini} . They are able to search in both directions by adding and subtracting ΔB while in the range of B achievable on the machine. Since there is only one feasible interval, it is not necessary to search in both directions. But the correct search direction is not known a priori. However, the correct direction can likely be determined by using the trend of the solution achieved at the previous points. At the beginning of *Generic2*, $(B_{j-1} - B_{j-2})$, the difference between the two previous solutions, is evaluated. The search direction is then selected in agreement with the observed trend. Therefore, if the difference is positive, the algorithms search the solution by consecutively adding ΔB to B_j . If a feasible angle is found the algorithms stop and output the solution. If no solution is found, starting over at $B_j = B_{\text{ini}}$, the second search direction, consisting in subtracting ΔB to B_j , is used. If, at the beginning of *Generic2*, $(B_{j-1} - B_{j-2})$ is negative, the order in which the search directions are used is the inverse of the one for a positive difference. The trend can not be established when dealing with the first two points of the tool path, in these cases, by default the search direction associated to $(B_{j-1} - B_{j-2}) \geq 0$ is used. $|B_j| > B_{\text{max}}$ is used as the criterion to stop the search in a given direction. By selecting the first feasible angle that is

encountered, the smoothness of the solution prevails over minimizing $|\alpha|$ in this approach. The sub-algorithms *Generic2* rely on a very robust search strategy and can find feasible angles for a large range of shapes. And defining the best search strategy to use based on the solution's trend makes for fast algorithms.

The MATLAB functions `TPGeomConvex.m`, `TPGeomConcave.m` and `TPGeomGeneric.m` execute the algorithms *Convex*, *Concave* and *Generic*, respectively. Appendix 2 contains the code for these functions, as well as for `ToolPathGeomMaker.m`, which is the function called by the UFF software to create the tool path geometry. This function creates the inputs needed for `TPGeomConvex.m`, `TPGeomConcave.m` and `TPGeomGeneric.m`. It also executes them as needed.

3.3 Tool pivot point coordinates

After establishing the safe B_j along the tool path, `ToolPathGeomMaker.m` completes the tool path geometry by computing the coordinates (y_j, z_j) of the tool pivot point along the tool path. For a given part point (y_{0j}, z_{0j}) , and angle B_j , knowing the distance, L_{Tool} , between the tip of the tool and the pivot point,

$$y_j = y_{Cp} - (L_{Tool} - R_w) \sin(B_j), \quad (3.45)$$

$$z_j = z_{Cp} + (L_{Tool} - R_w) \cos(B_j), \quad (3.46)$$

where y_{Cp} and z_{Cp} are the coordinates of the center of the carrier wheel when subjected to the inward displacement δ into the part. These coordinates can be

obtained with $(y, z) = (0, R_W - \delta)$ in Eq. (3.30), in which $R_W - \delta$ must be substituted for R_W to account for the radius of the wheel after compression.

The feasibility of the pivot point coordinates computed with Eqs. (3.45) and (3.47) is established by verifying that they are in the ranges of linear motions achievable on the machine, defined as $[y_{\min}, y_{\max}]$ and $[z_{\min}, z_{\max}]$. If computed y_j or z_j are out of these ranges, the part cannot be polished on the machine and error code 4 is outputted by ToolPathGeomMaker.m. Since the machine is designed to accommodate tangent ogives of diameter 150 mm and aspect ratio of 1.5, the machine specifications should be appropriate for most conventional workpieces of diameter less than 150 mm.

3.4 Experimental validation

The algorithms described in the previous sections have been used to polish the concave surface of the hemispherical dome made of PCA provided by Ceranova Corporation [4] and shown in Figure 3.26. It has a diameter of 67.5 mm and an edge thickness of 3.3 mm. The preferred configuration, for which tool and part normals are aligned, is not possible all along the edge-to-edge tool path, because the part is a full hemisphere. The algorithms *Concave* made it geometrically possible to polish that surface. Because the part is well within the machine capabilities, the needed tool linear motions are within the feasible ranges. Graphical representations of the tool path geometry at various points along the half of the tool path corresponding to r larger than 0 are shown in Figure 3.27. The tool is represented by the contour of its

safety region and therefore, there is more clearance between the actual tool and the part than what might be observed in these plots. The outputted B_j values and the difference between B_j and $B_{j\text{norm}}$ are plotted versus y_{0j} in Figures 3.28 and 3.29, respectively. The smoothness of the achieved solution and therefore, of the tool motion can be observed. The tool and part normals could only be aligned for $|y_{0j}|$ less than 23.6 mm. The *Concave* algorithms established the best safe B angles for the tool path points out of that range.

3.5 References

[1] OptiPro Systems, 6368 Dean Parkway, Ontario, NY 14519, Phone: 585-265-0160, www.optipro.com.

[2] SolidWorks 2007, SolidWorks Corp., 300 Baker Avenue, Concord, MA 01742, Phone: 800-693-9000, www.solidworks.com.

[3] MATLAB R2007a (Version 7.4.0.287), The Mathworks Inc., 3 Apple Hill Drive, Natick, MA 01760-2098, Phone: 508-647-7000, www.mathworks.com.

[4] CeraNova Corp., 85 Hayes Memorial Drive, Marlborough, MA 01752, www.ceranova.com. Development of polycrystalline alumina by CeraNova is funded by NAVAIR through the US Government SBIR Program; SBIR Data Rights Apply.

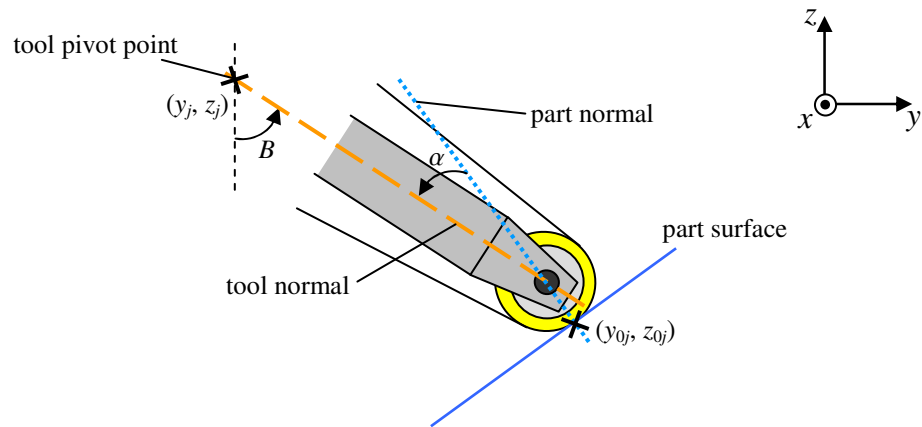


Figure 3.1 Definition of the parameters for the tool path geometry.

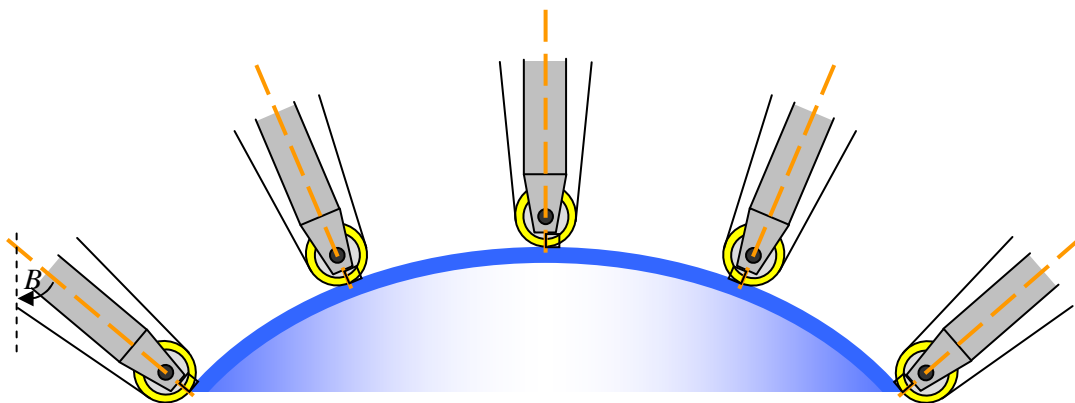


Figure 3.2 Feasible tool path with $\alpha = 0$ on a convex part.

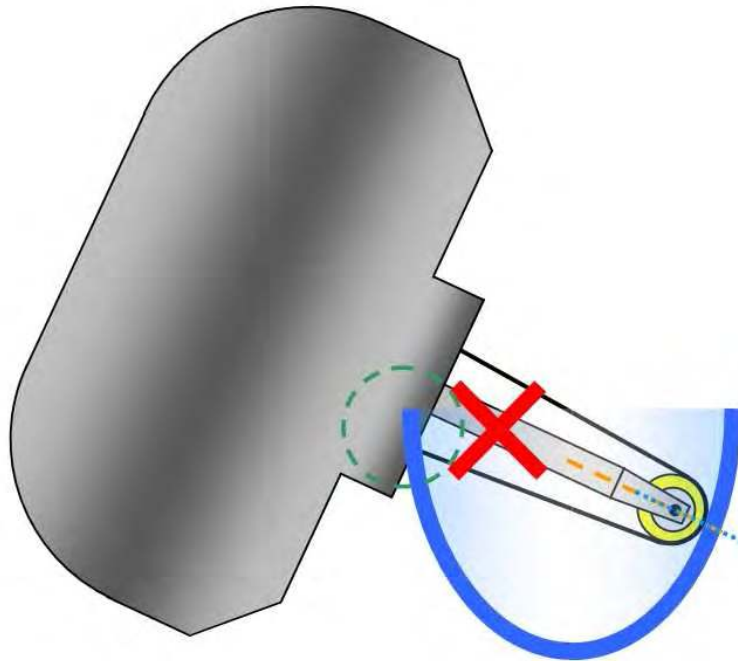


Figure 3.3 Unacceptable tool-part collision for a tool path with $\alpha = 0$ on a concave part.

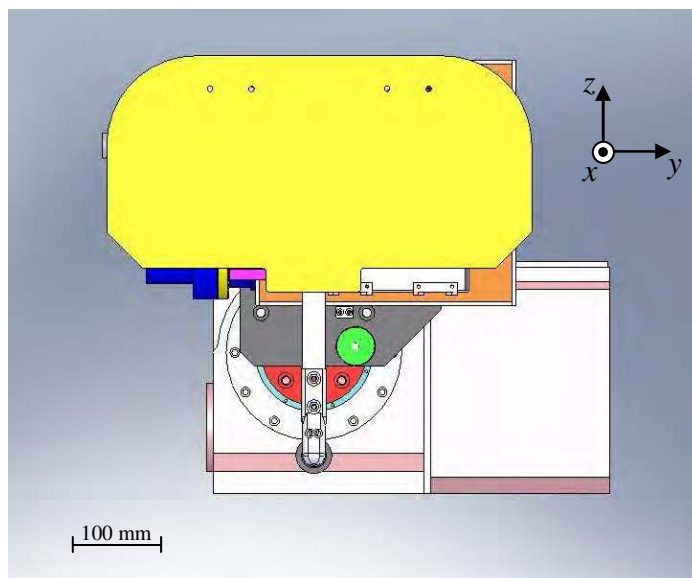


Figure 3.4 Front view of UFF Army configuration.

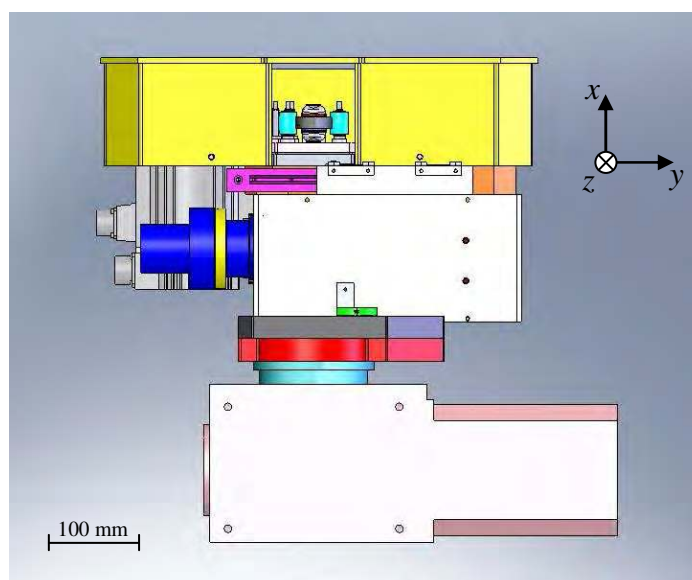


Figure 3.5 Bottom view of UFF Army configuration.

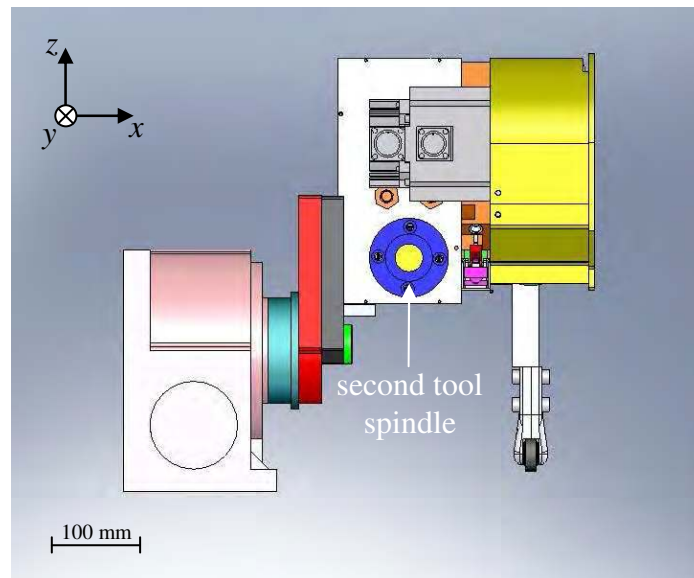


Figure 3.6 Left view of UFF Army configuration.

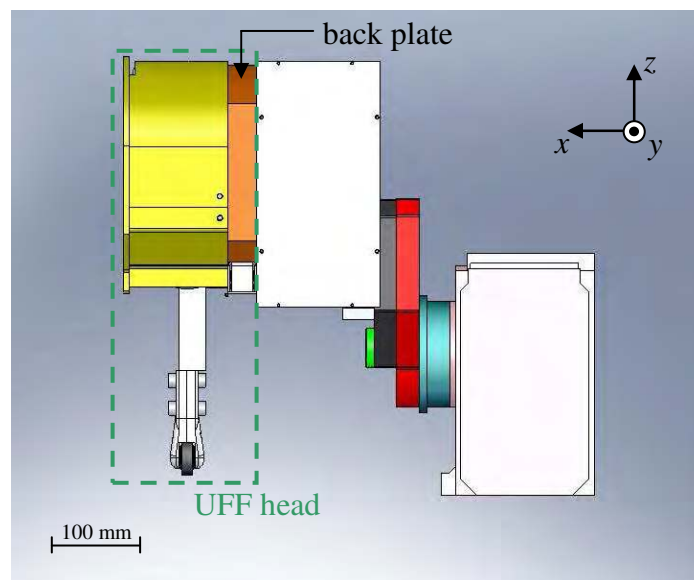


Figure 3.7 Right view of UFF Army configuration.

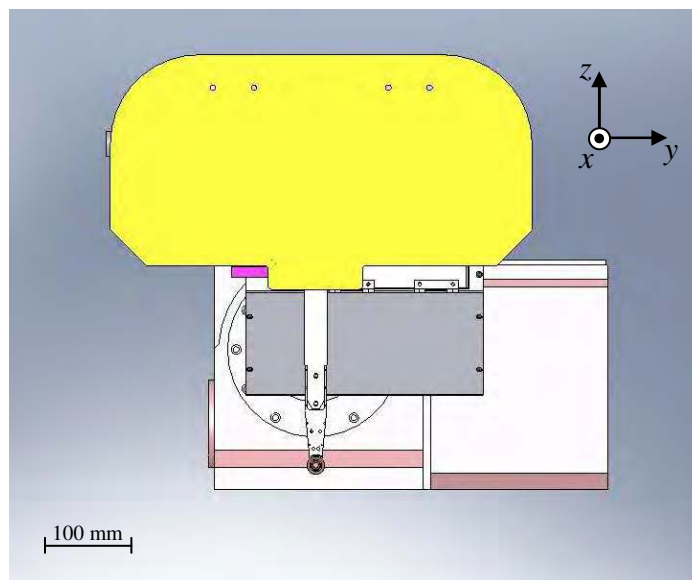


Figure 3.8 Front view of UFF Navy configuration.

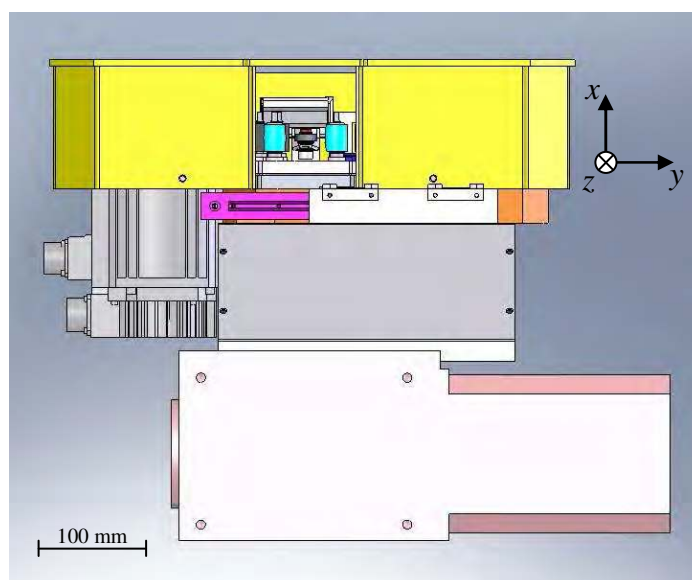


Figure 3.9 Bottom view of UFF Navy configuration.

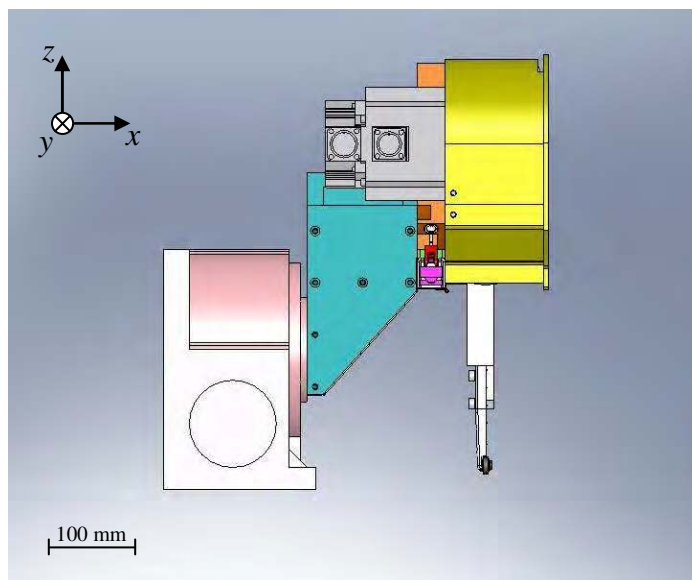


Figure 3.10 Left view of UFF Navy configuration.

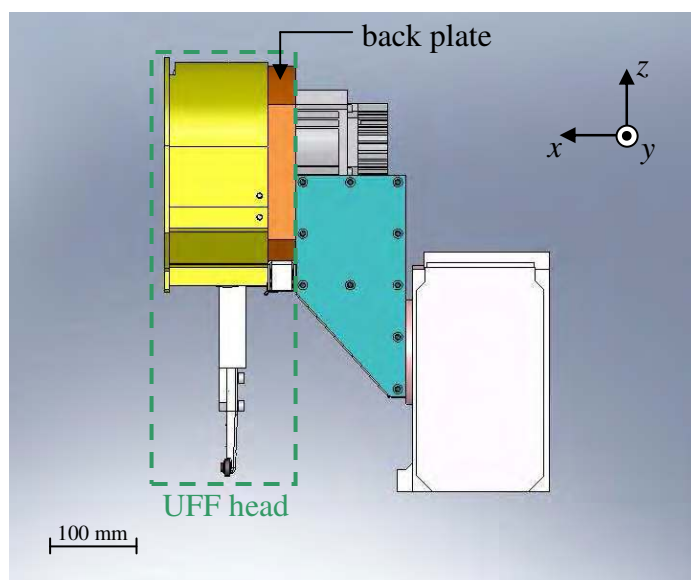


Figure 3.11 Right view of UFF Navy configuration.

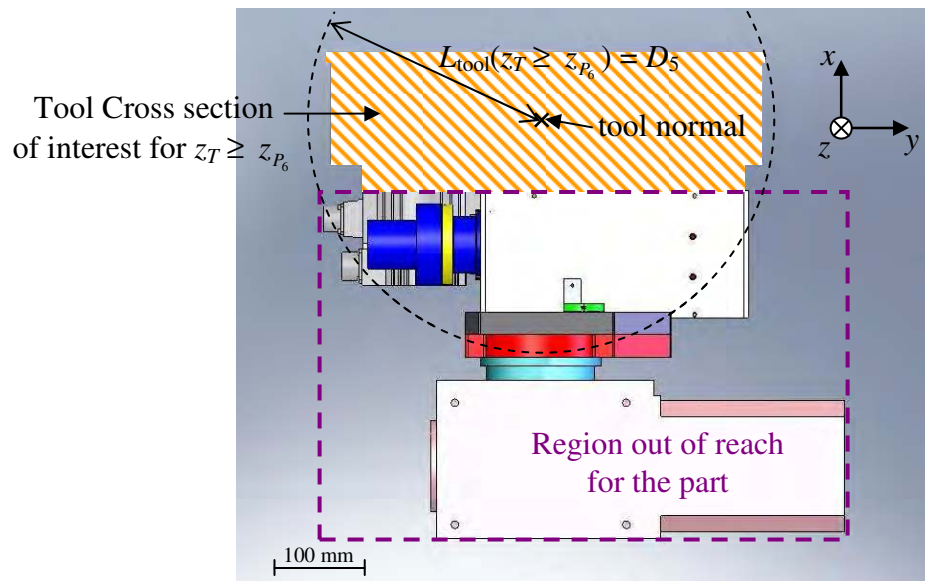


Figure 3.12 Illustration of tool interior region definition.

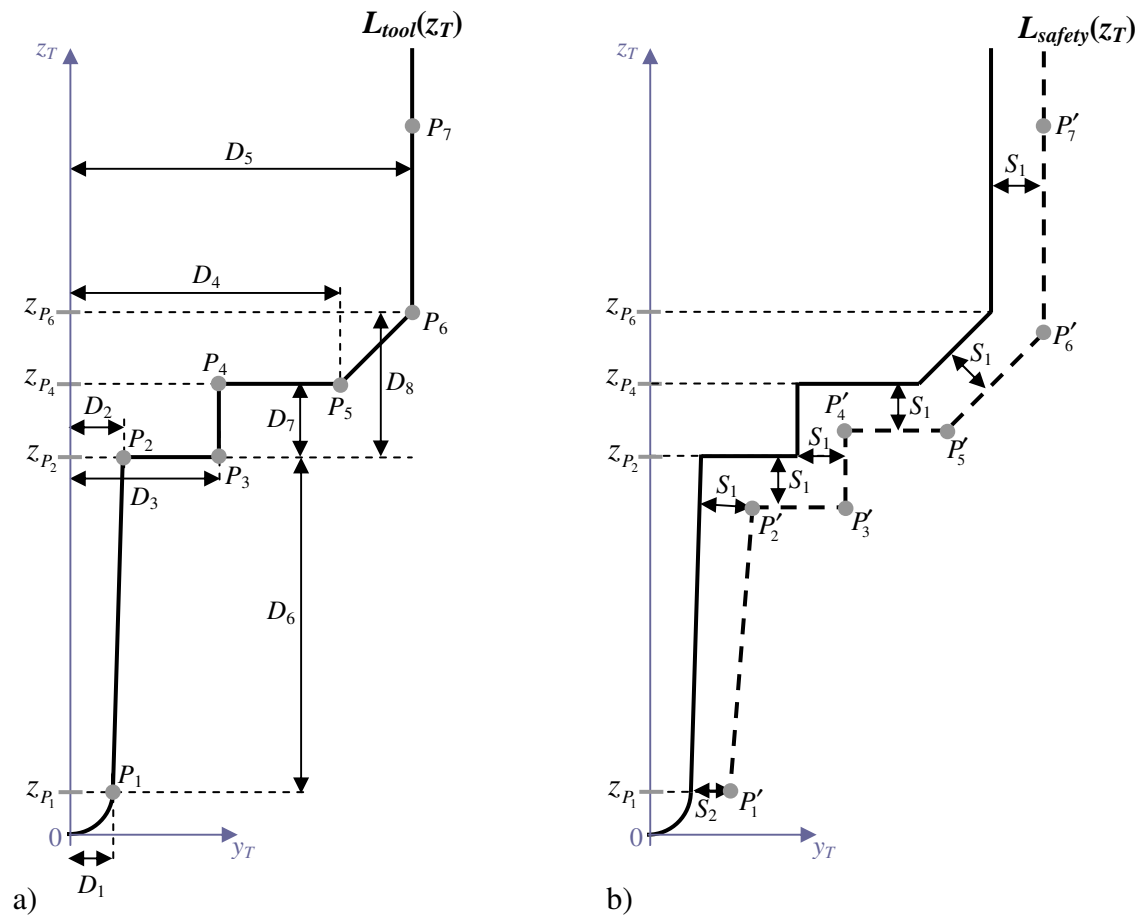


Figure 3.13 Geometry of the tool 2D model
 a) Tool interior region and points and dimensions used for its definition;
 b) Tool safety region and points defining the 2D model.

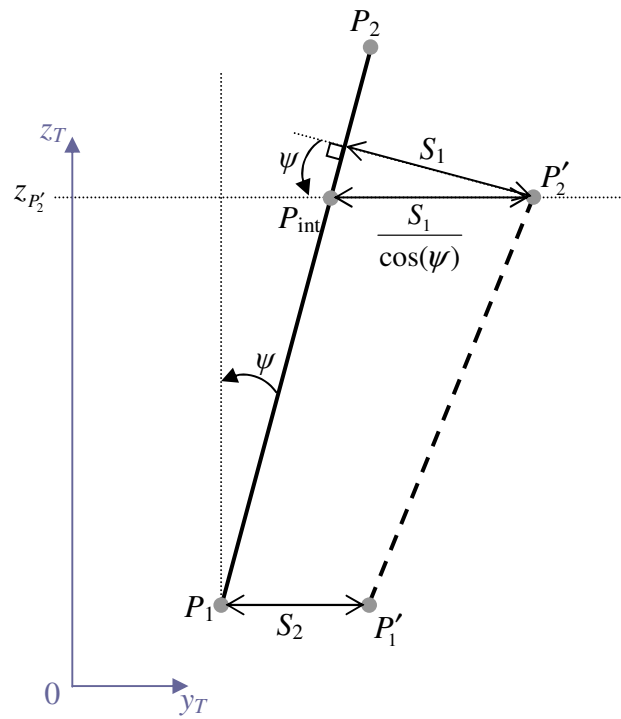


Figure 3.14 Geometry to define $y_{P'_2}$.

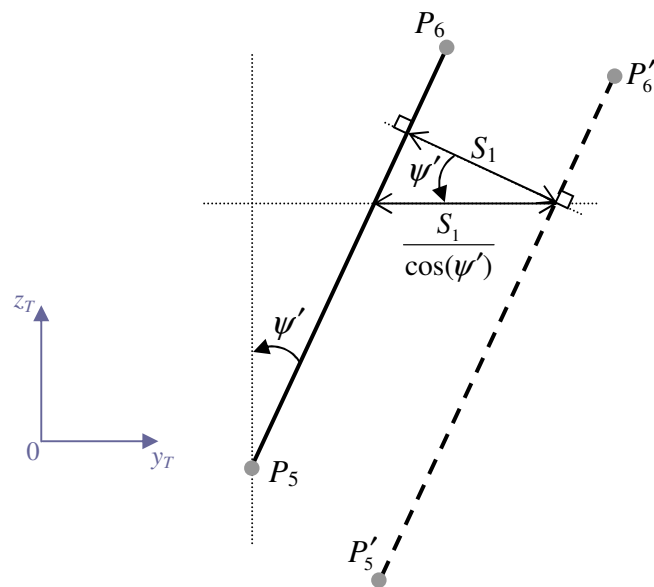


Figure 3.15 Geometry to define Δb .

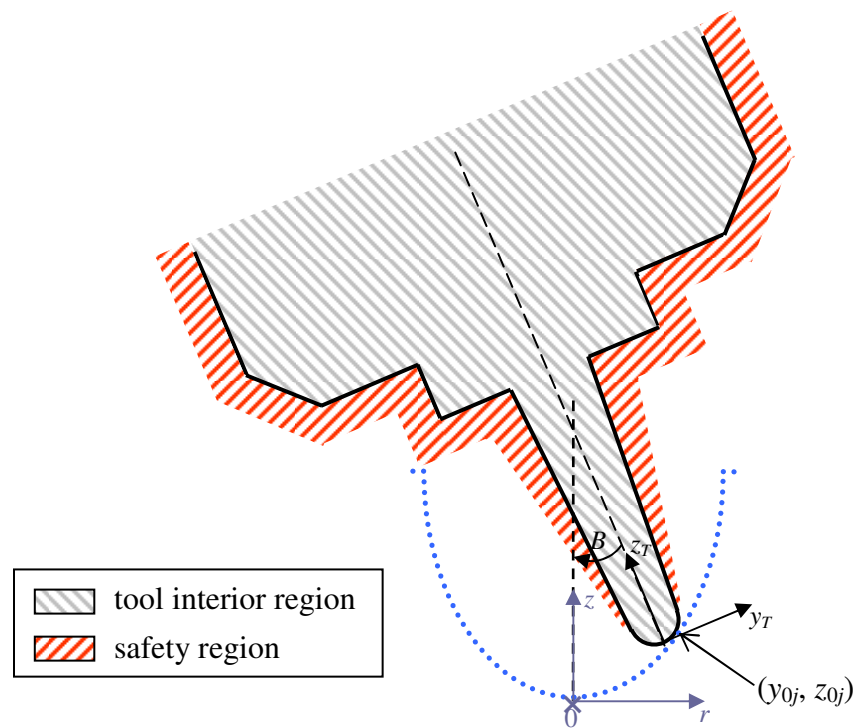


Figure 3.16 2D model used to define the tool path geometry.

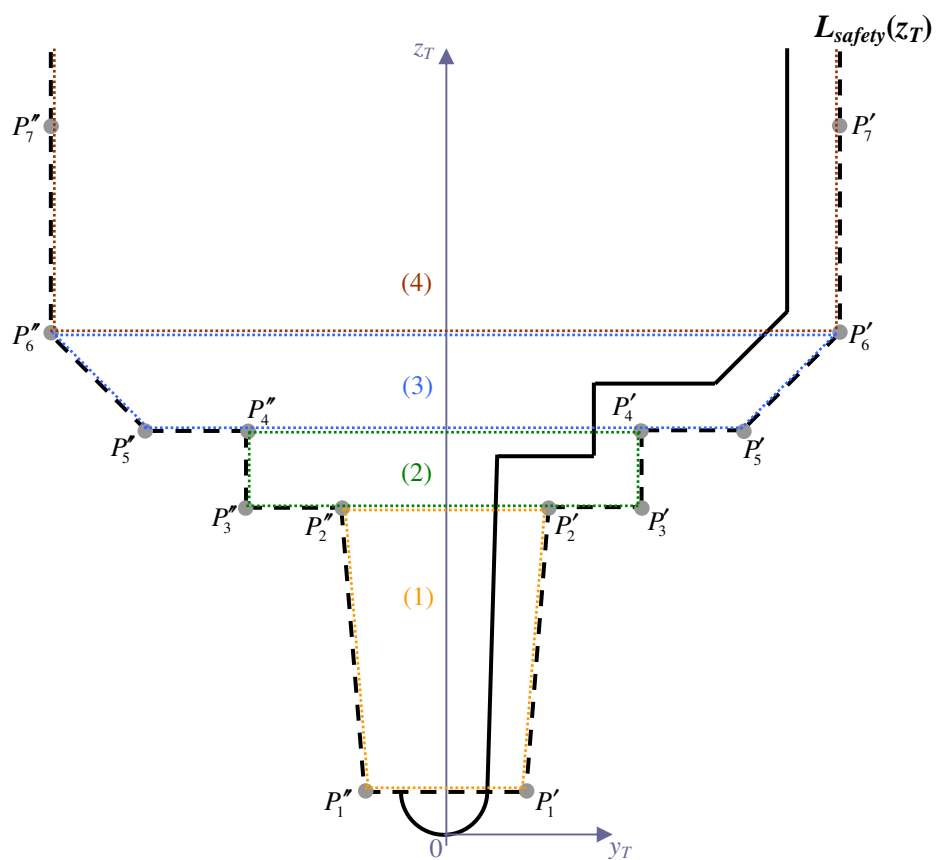


Figure 3.17 Points and regions defining the tool full 2D model.

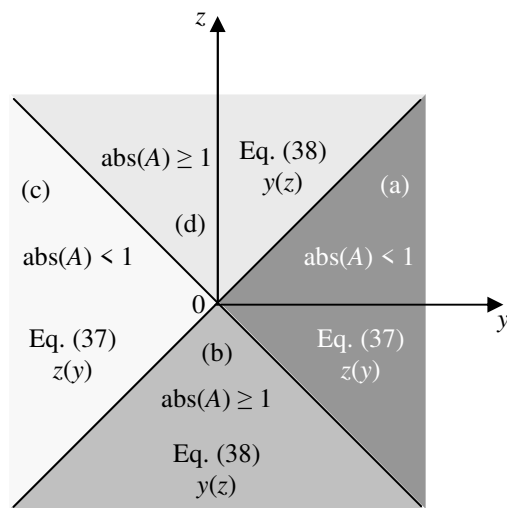


Figure 3.18 Regions and equations used to define the tool interior region.

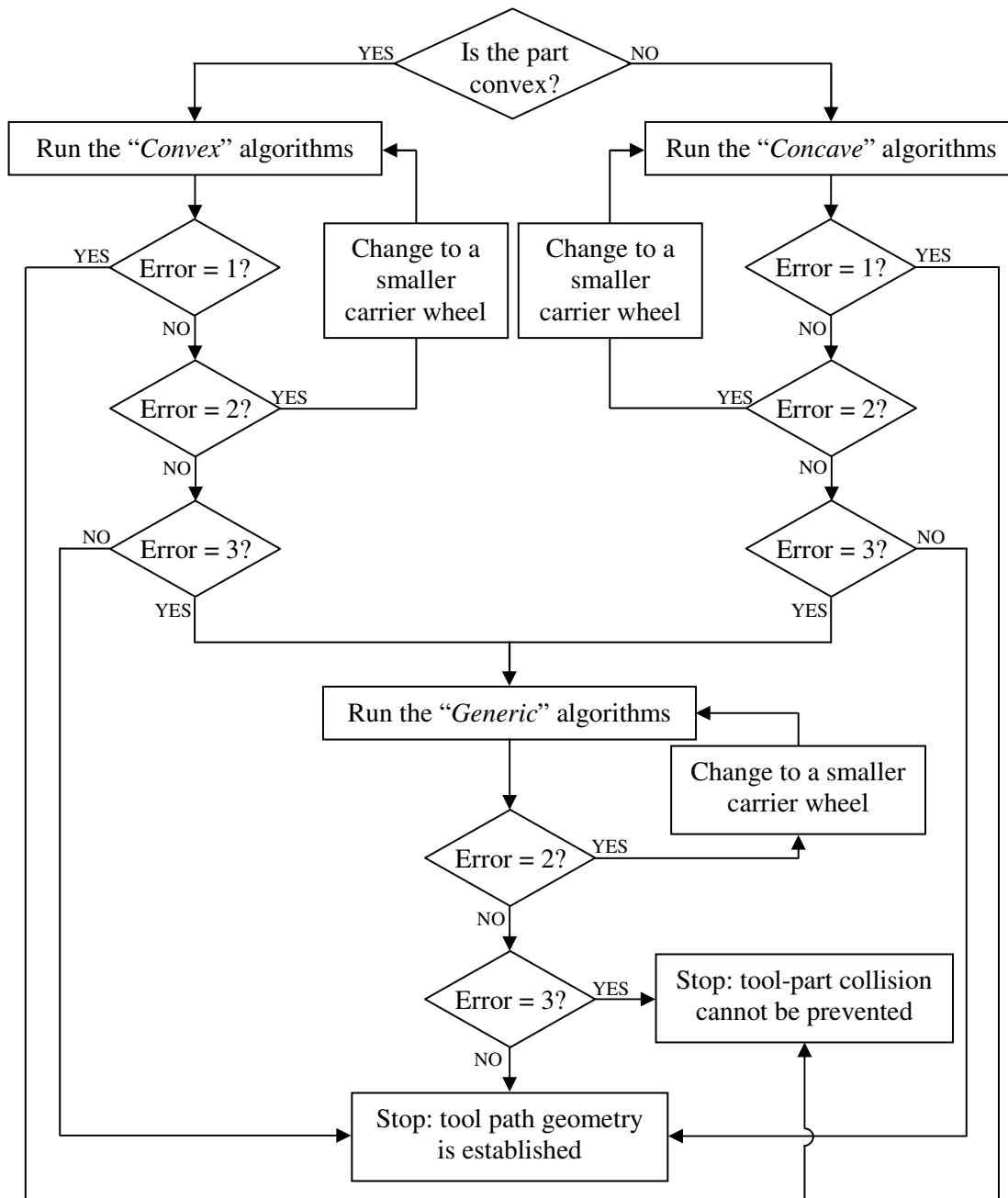


Figure 3.19 Overall flow chart for safe B angles search.

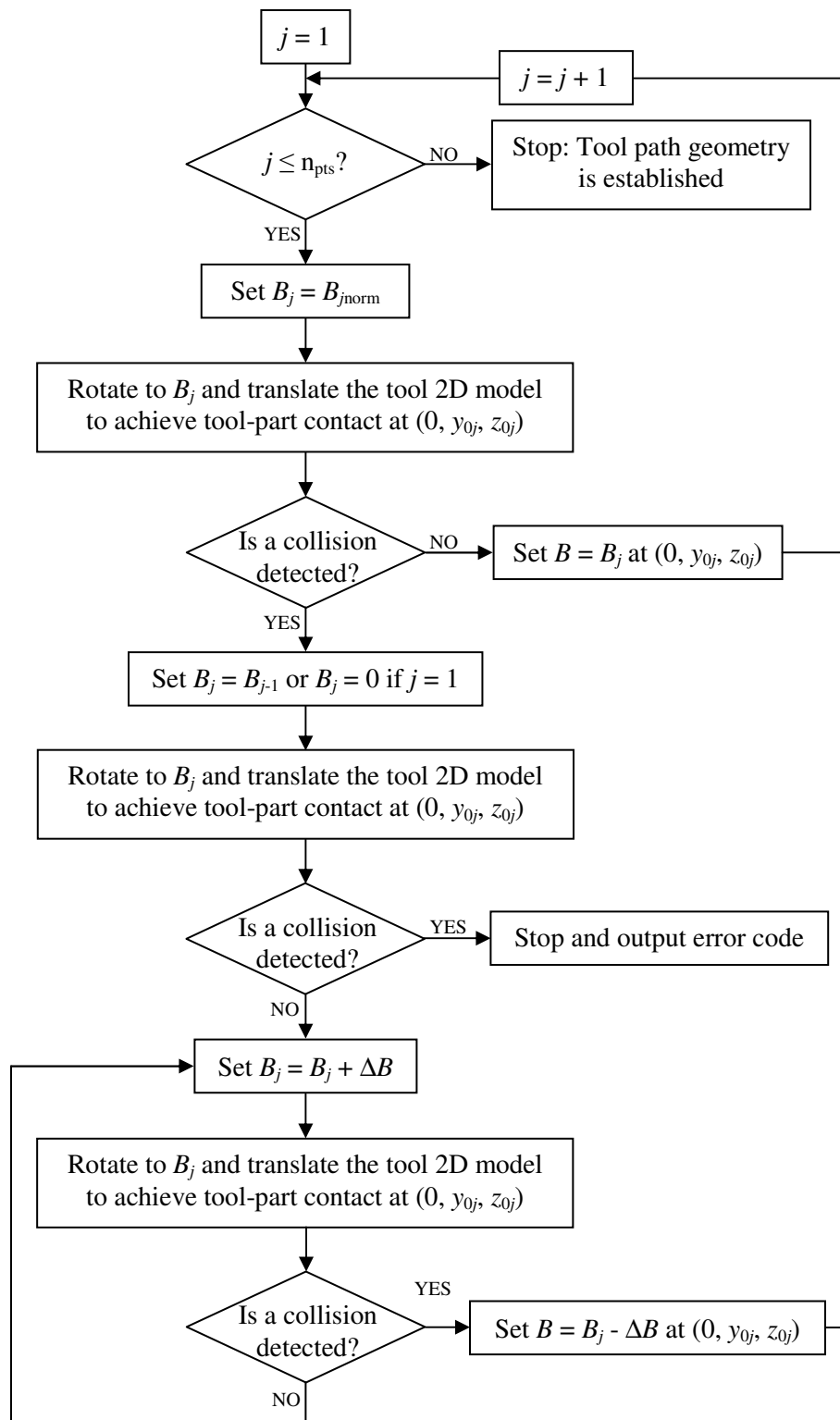


Figure 3.20 Flow chart of the *Concave* algorithms.

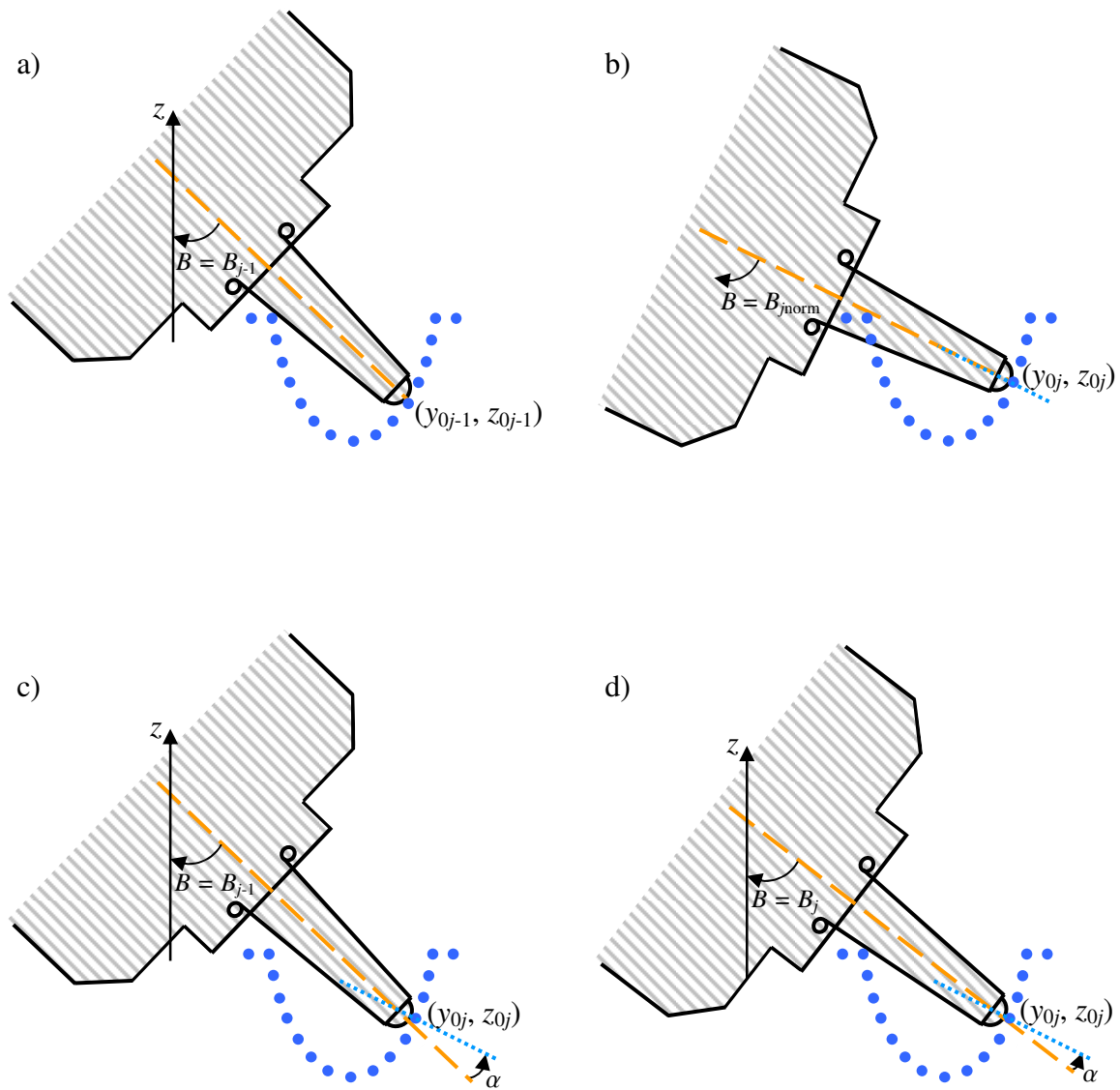


Figure 3.21 Strategy for adjusting B on concave parts

- a) solution B_{j-1} at y_{0j-1} ;
- b) tool and part normals aligned at y_{0j} ;
- c) using solution B_{j-1} at y_{0j} ;
- d) solution B_j at y_{0j} after increasing B .

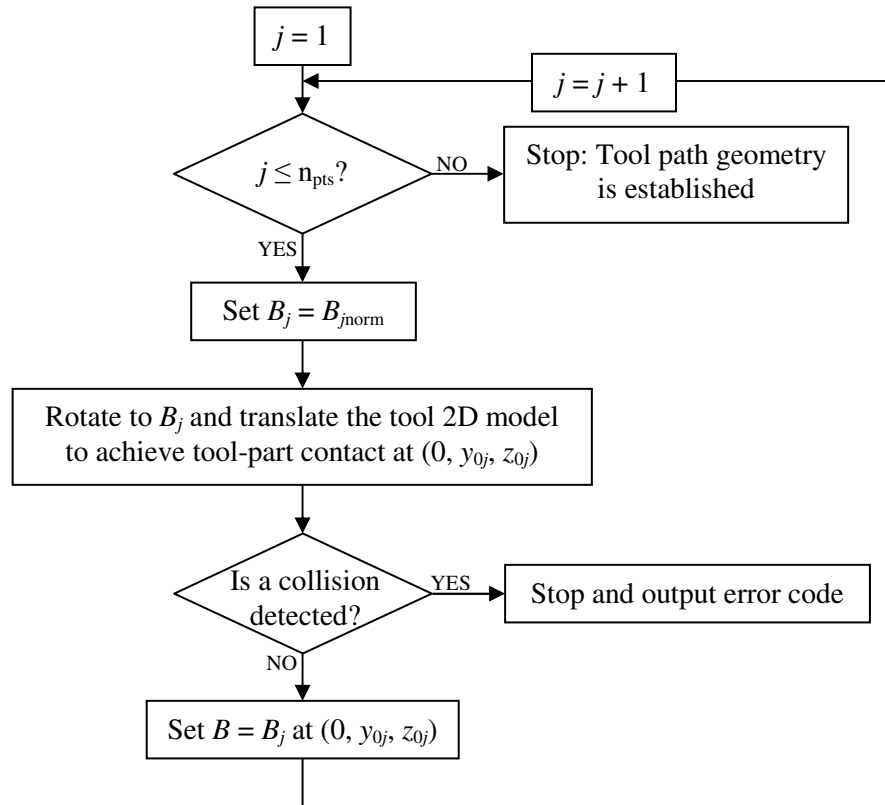
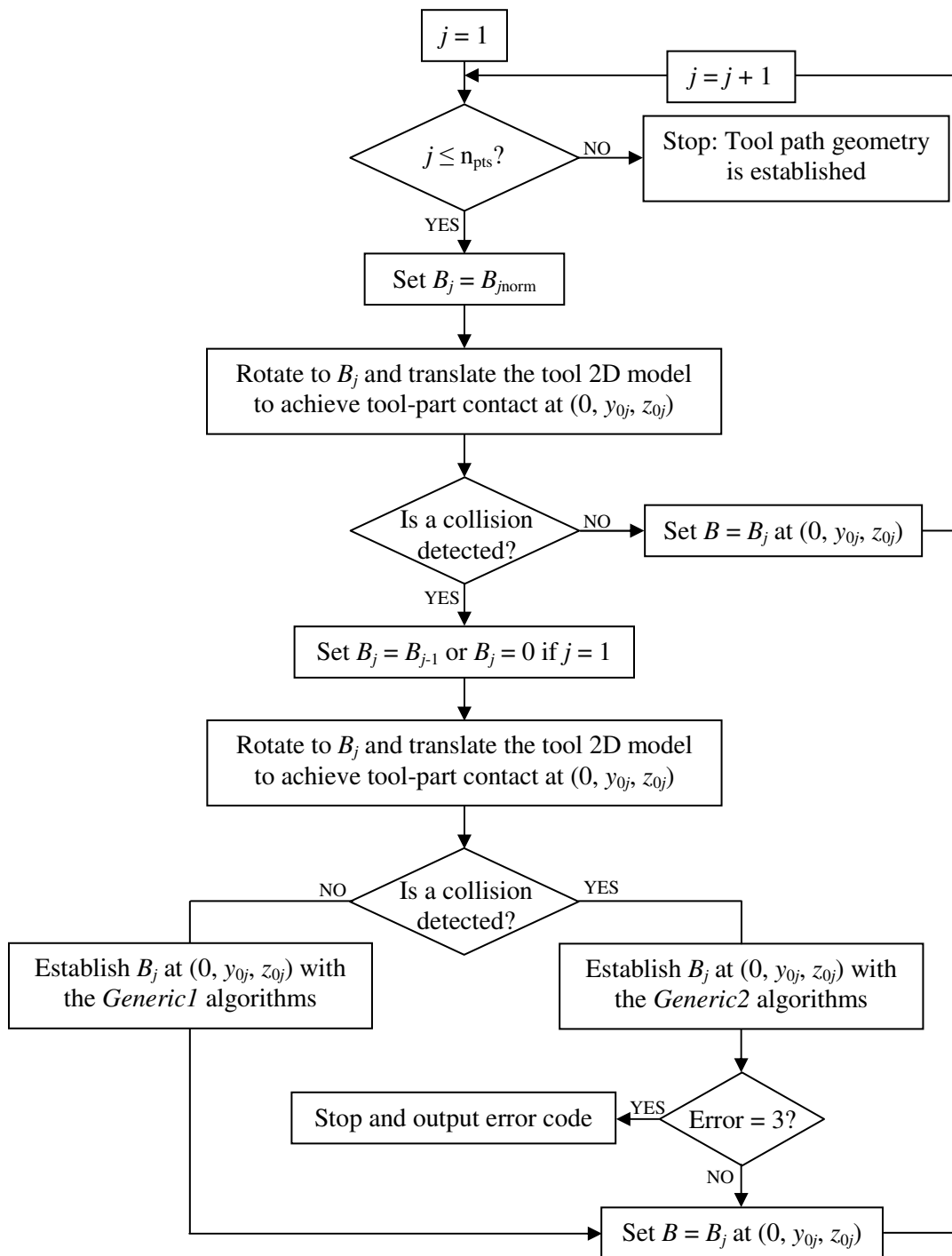


Figure 3.22 Flow chart of the *Convex* algorithms.

Figure 3.23 Flow chart of the *Generic* algorithms.

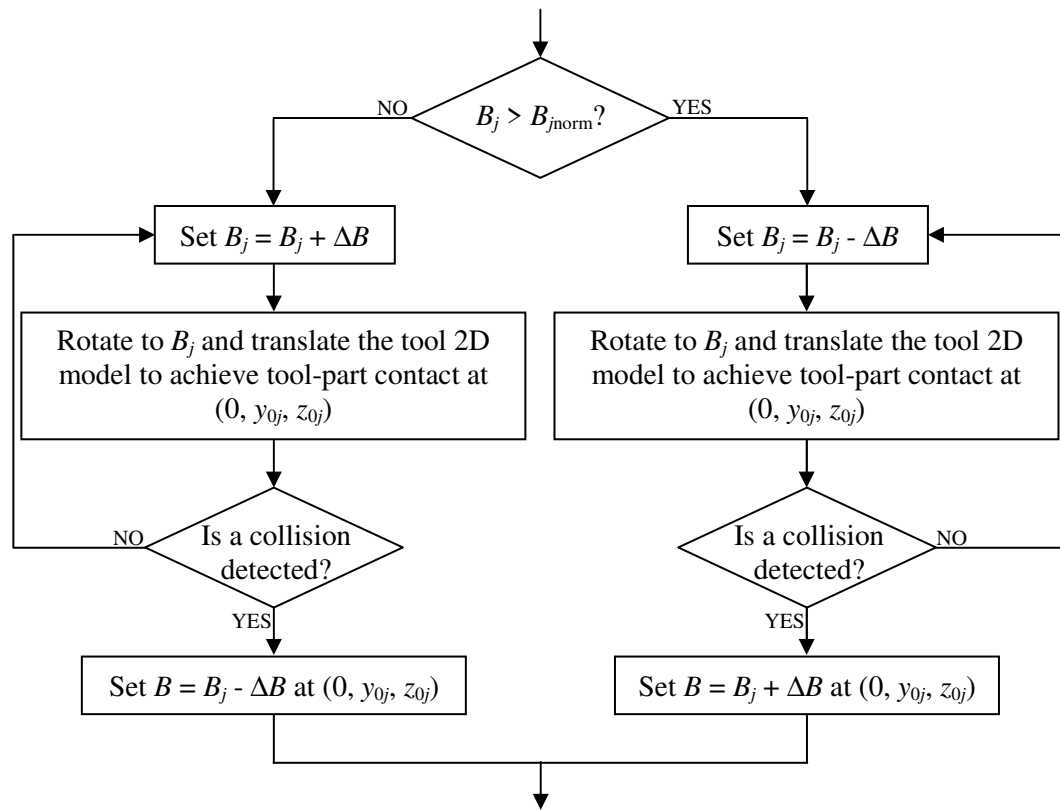


Figure 3.24 Flow chart of the *Generic1* algorithms.

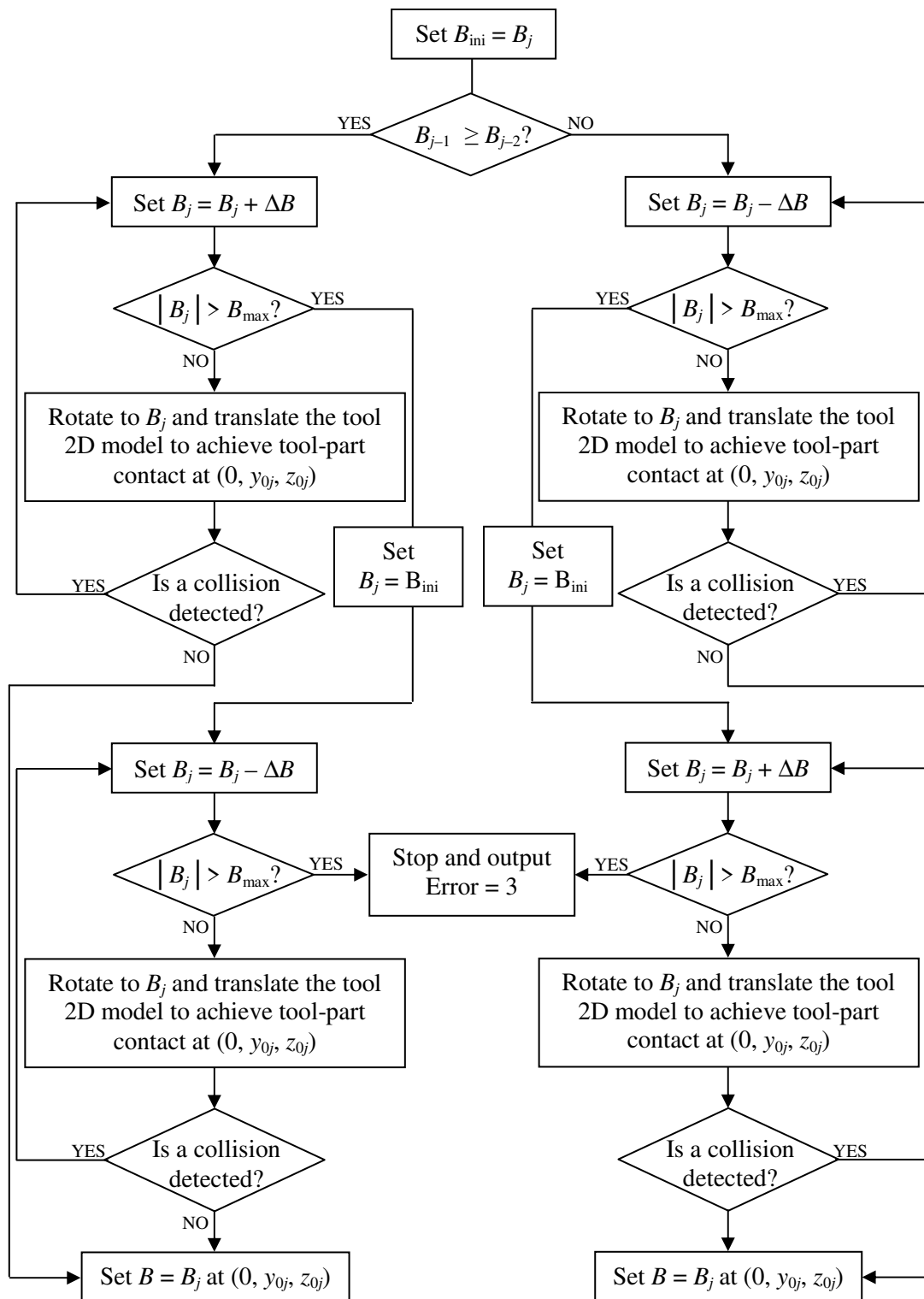


Figure 3.25 Flow chart of the *Generic2* algorithms.

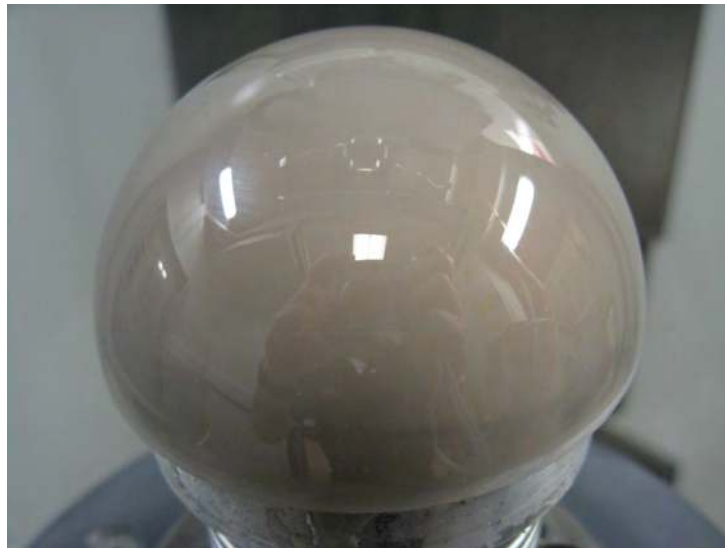


Figure 3.26 Hemispherical PCA dome [4].

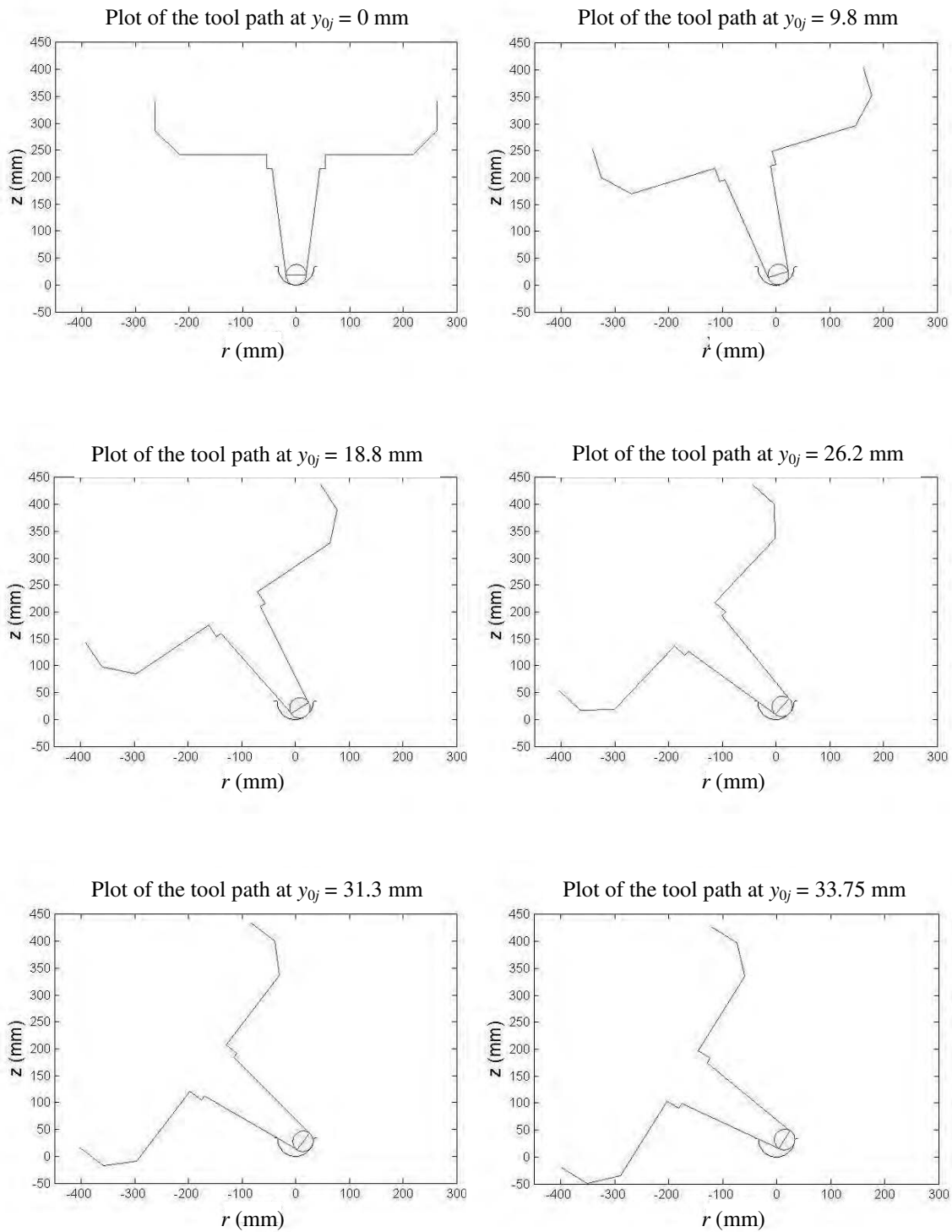


Figure 3.27 Plots of the tool path for the concave surface of a hemisphere of diameter 67.5 mm.

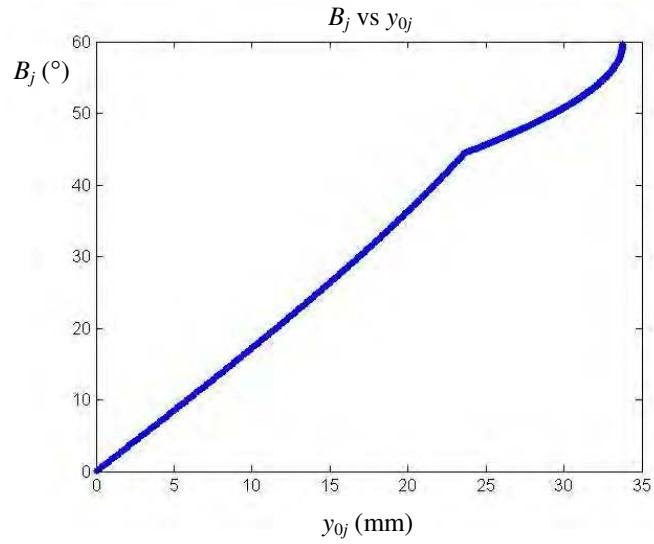


Figure 3.28 Plot of the B angles used to polish the concave surface of a hemisphere of diameter 67.5 mm.

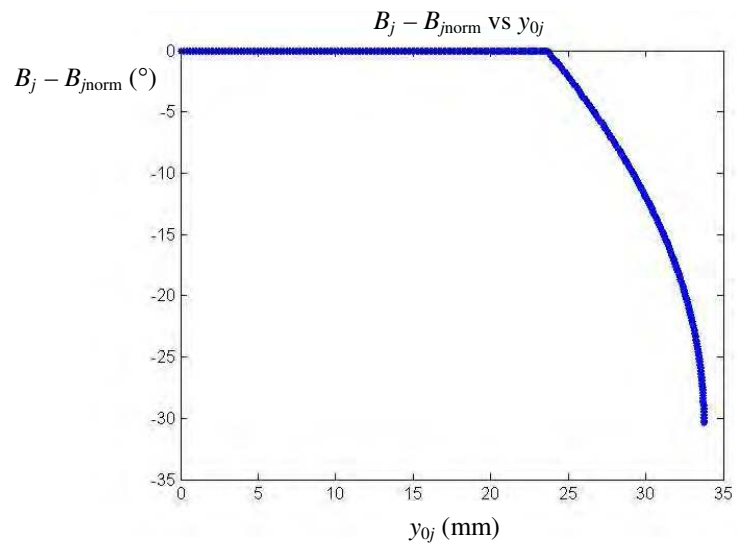


Figure 3.29 Plot of the difference between the B angles used to polish the concave surface of a hemisphere of diameter 67.5 mm and the angle of the local part normal.

Chapter 4 Removal function

Knowledge of the removal function is required to solve the form correction problem. In this chapter, the removal function is first defined. The effects of various process parameters, as well as the possibility of predicting the removal function for some of these parameters using Preston's equation and Hertz contact mechanics theory are examined. A method for achieving a desired removal profile without accurate knowledge of the removal function is also introduced.

4.1 Definition

The removal function, $c(x, y, y_0)$, is a topographic map, which represents the depth of material removed per unit of time within the tool-part contact patch centered at y_0 . The removal function is the footprint of the tool positioned at y_0 along the tool path. This footprint is generated by the abrading effect of the tool on the workpiece. Due to the nature of the removal process, this removal function is affected by several process parameters. Belt and part velocities, part and carrier wheel geometries, carrier wheel durometer, part material, abrasive and coolant all can influence the removal function.

The tool footprint can be examined by keeping the rotating tool and a stationary part in contact for a prescribed dwell time, t_d , to generate a removal spot. The topography of the induced spot divided by t_d is named the static removal function, $c_{ST}(x, y, y_0)$. As opposed to $c(x, y, y_0)$, which is considered dynamic as it occurs while the workpiece rotates, c_{ST} can be measured.

The computation of the removal matrix, introduced in Chapter 2 for the form correction problem, is based on the knowledge of the tool removal function. The goal of this work is to evaluate the possibility of predicting the dynamic removal function $c(x, y, y_0)$ along the tool path. This function is defined by the size of the contact patch resulting from the tool-part contact, and the removal distribution within the patch. During a typical polishing run the belt velocity remains constant, while the consistency of the carrier wheel, part material, abrasive and coolant is maintained. Therefore, the removal function should only be affected by geometry of the part and its velocity. With UFF, the use of Preston's equation is suggested to relate removal and applied pressure and contact mechanics theory to predict the pressure resulting from the tool-part contact.

4.2 Local material removal model

4.2.1 Preston's equation

Applied pressure and removal were related by Preston [1], who proposed in 1927 that the volumetric material removal rate for grinding or polishing is proportional to the rate at which work is done. The work, w , done during the dwell time t_d is defined as

$$w = \mu_F A p v_{rel} t_d, \quad (4.1)$$

where μ_F is the coefficient of friction, A the area of contact between the tool and the part, p is the interfacial pressure and v_{rel} the velocity of the abrasive relative to the

part. To be practical for grinding or polishing, Eq. (4.1) is typically rewritten in the following form

$$dh/dt_d = C_P v_{rel} p, \quad (4.2)$$

where h is the height of material removed and C_P the Preston coefficient. Eq. (4.2) is known as Preston's equation and implies a linear relation between material removal rate, dh/dt_d and the process parameters v_{rel} and p .

C_P represents the volume removed per unit energy input and therefore indicates the efficiency of polishing. It is a process parameter that accounts for the effects other than relative velocity and pressure. Thus, it includes the effects on material removal, either mechanical or chemical, of the abrasive, coolant, workpiece and tool. Work by DeGroot et al. [2] showed that the workpiece near surface layer mechanical properties, polishing particle properties and glass composition and chemical durability are part of C_P for Magnetorheological Finishing. Deriving Eq. (4.2) from Eq. (4.1) proves that C_P must include μ_F . In the case of UFF, C_P is expected to be a function of the abrasive, coolant, workpiece material, carrier wheel geometry and durometer and therefore, it is expected to be constant for a polishing run. For that reason, it is not necessary in this study to know the terms forming C_P , instead only its value is of interest.

4.2.2 Generalized form of Preston's equation

Preston's equation is widely accepted in the optical fabrication community. In particular, this equation has been used for removal prediction with various contact

deterministic polishers [3-10]. However, it does not perfectly model all processes. This is especially reported for wafer polishing or chemical mechanical planarization (CMP). For such processes, the following generalized form of Preston's equation is used [11, 12]

$$dh/dt_d = C_{GP} v_{rel}^{n_1} p^{n_2}, \quad (4.3)$$

where n_1 and n_2 are fitted parameters and C_{GP} is a generalized Preston coefficient playing the same role as C_P in Preston's equation. Table 4.1 summarizes three models established for different CMP processes. They exhibit n_1 and n_2 values less than or equal to 1.

Model	n_1	n_2	Reference
$dh/dt_d = C_{GP} v_{rel}^{n_1} p^{n_2}$	1/2	5/6	[13]
$dh/dt_d = C_{GP} v_{rel}^{n_1} p^{n_2}$	1/2	1/2	[14]
$dh/dt_d = C_{GP} v_{rel}^{n_1} p^{n_2}$	1	2/3	[15]

Table 4.1 Three removal models for CMP.

4.2.3 Model for UFF

To express the removal function of UFF, the pointwise relation of Eq. (4.3) can be extended to the whole contact patch to obtain

$$c(x, y, y_0) = C_{GP} v_{rel}(x, y, y_0)^{n_1} p(x, y, y_0)^{n_2}. \quad (4.4)$$

(x, y, z) is the coordinate system defined in Chapter 1. Once n_1 and n_2 are known, Eq. (4.4) expresses the removal function in terms of relative velocity between the

abrasive and the part and interfacial pressure distribution. As for CMP, n_1 and n_2 can be fitted so that Eq. (4.4) matches experimental data. However, the removal function and interfacial pressure distribution cannot be measured during the process. On the other hand, the static removal function can be measured by making a removal spot. Since, for a removal spot, $v_{rel} = v_{band}$ and p and C_{GP} can be assumed to be constant with respect to t_d , the generalized Preston's equation implies

$$h(x, y, y_0) = C_{GP} v_{band}^{n_1} p(x, y, y_0)^{n_2} t_d . \quad (4.5)$$

If that relation is now integrated with respect to x and y over the removal spot centered at y_0 ,

$$\iint_{spot} h(x, y, y_0) dx dy = C_{GP} t_d v_{band}^{n_1} \iint_{spot} p(x, y, y_0)^{n_2} dx dy , \quad (4.6)$$

The right hand side of Eq. (4.6) is equal to the volume, V , of the removal spot. The integral on the left hand side of Eq. (4.6) is equal to the normal force applied by the tool on the part, F , if $n_2 = 1$ as for Preston's equation. In the case $n_2 = 1$,

$$V = C_{GP} t_d v_{band}^{n_1} F . \quad (4.7)$$

Eq. (4.7) indicates that if $n_2 = 1$ and C_{GP} as well as two of the factors of the product $t_d v_{band}^{n_1} F$ are kept constant, the volume of the removal spot is proportional to the third factor of the product. In the case of Preston's equation, V is proportional to t_d , v_{band} and F . If n_2 is different from 1, F must be replaced in Eq. (4.7) by the integral of Eq. (4.6) that involves p .

The relationship between t_d , v_{band} , F and V was examined for UFF. For that purpose, series of removal spots were made so that only one parameter would be changed at a time. These experiments are part of a larger series of experiments described in further details in section 4.3.5.2.1. All the removal spots considered in this chapter, unless specified otherwise, were made in the preferred configuration, defined in Chapter 3, such that the tool and part normals are aligned or $\alpha = 0$. Different parts, carrier wheel and abrasive were used for each series. However, C_{GP} was kept constant by making all the removal spots for each series on the same part, with the same abrasive, carrier wheel and coolant. Furthermore, all the parts were made of BK7, which is a relatively inexpensive borosilicate glass having good mechanical properties. The removal spots were measured with the onboard STIL optical pen [16] allowing for evaluation of V . The principle of the pen and the model used are reported in Chapter 1. F was measured with the Tekscan system [17]. This system uses a thin and flexible tactile force sensor. An electrically conductive material is arranged in rows and columns to form a matrix-based sensor shown in Figure 4.1. The rows and columns are separated by a material that varies its electrical resistance with applied force, making each intersection a force sensor [18]. Measuring the change in resistance of the individual force sensors, the magnitude and location of the forces on the surface are determined. Knowing the area covered by an activated force sensor, the measurements can be displayed as pressure distributions. The geometry of the sensor is represented in Figure 4.2. The matrix is described by its width (MW) and height (MH). The spacing of the force sensors is given by the row

(RS) and column (CS) spacing. The sensor model number 5051 was used for this study. It is 0.1 mm thick and such that $CS = RS = 1.27$ mm, $MH = MW = 56$ mm resulting in a matrix of 1936 force sensors [19]. Therefore, the spatial resolution of this system is 1.27 mm. The primary purpose of the Tekscan system is measurement of pressure distributions, but because of its limited spatial resolution it provides few data within the UFF removal spots, which are typically about 5 mm wide. For this study, a sensor with a pressure range of 350 psi was selected and placed between the compressed static tool and part to measure F prior to making the removal spot.

An initial experiment consisting in making two removal spots at compressions of 0.05, 0.1, 0.15 and 0.2 mm with a 70 durometer wheel and a plano part was performed. A variation of less than 6 % between the volumes of the spots made under the same conditions showed the consistency and repeatability of the removal spots.

The linear relation between t_d and V is reported in Chapter 2 and is shown in Figure 2.4, with R^2 larger than 0.99. It was established by making removal spots with dwell times, t_d , of 2, 5, 10, 15 and 30 s.

The relationship between V and F was investigated with the removal spots made with compressions, δ , of 0.05, 0.1, 0.15 and 0.2 mm during the initial experiment. These spots were made with a 70 durometer wheel for which $\delta = 0.2$ mm is a typical value. The measured loads and volumes are plotted in Figure 4.3, showing a good linear relation since R^2 is larger than 0.99. This fit indicates that for UFF, $n_2 = 1$ in Eq. (4.5).

Removal spots have been made with band velocities, v_{band} , incremented by 0.25 m/s and ranging between 0.25 and 1.5 m/s. Typically for polishing $v_{band} = 1$ m/s. V is plotted versus v_{band} in Figure 4.4. A fairly good linear fit with R^2 larger than 0.95 is observed. However, a power fit performed with SigmaPlot [20] and shown in Figure 4.5 reveals that a linear function of $v_{band}^{0.788}$ is nearly a perfect fit to the data, since $R^2 = 0.998$. SigmaPlot also established that the standard error on n_1 is 0.02. Therefore, it can be concluded that n_1 is approximately equal to 4/5 for UFF.

The fitted experimental data suggest that for UFF, n_1 and n_2 must be set equal to 4/5 and 1, respectively. Therefore, the generalized Preston coefficient can be estimated from Eq. (4.7) as

$$C_{GP} = \frac{V}{t_d v_{band}^{4/5} F}. \quad (4.8)$$

Removal spots have been made and the associated load measured for carrier wheels of durometer 50 and 70 on flats. The 70 durometer wheel was also used to make removal spots on spherical parts. Three convex and two concave workpieces of radii of curvature, ROC , of -50, -100, -150 and 100, 150 mm, respectively, were used. The process parameters, measurements of F and V and the corresponding C_{GP} calculated according to Eq. (4.8) are reported in Table 4.2. In that table, the convex parts are denoted with a negative radius of curvature and the units of C_{GP} are $m^{2.2}/(s^{0.2} N)$. The initial repeatability experiment also revealed good repeatability of C_{GP} since

variations of less than 6 % were observed when evaluated for the same process conditions.

Durometer	50	70	70	70	70	70	70
δ (mm)	0.3	0.2	0.2	0.2	0.2	0.2	0.2
ROC (mm)	∞	∞	-150	-100	-50	150	100
t_d (s)	10	10	10	10	10	10	10
v_{band} (m/s)	1	1	1	1	1	1	1
F (N)	11.2	18.1	18.2	15.3	14.2	20.7	19.2
V (mm³)	0.10	0.18	0.14	0.11	0.14	0.25	0.33
C_{GP}	8.6E-13	9.7E-13	7.8E-13	7.2E-13	9.5E-13	1.2E-12	1.7E-12

Table 4.2 Removal spots parameters and corresponding values of C_{GP} .

It is interesting to note that since v_{band} is equal to 1 m/s, the values of C_{GP} reported in Table 4.2 are the same as the one that would be obtained for these same removal spots with Preston's model. C_P has the units of Pa⁻¹ and values reported in the literature are of the order of 10⁻¹³ Pa⁻¹ [21-24]. UFF exhibits values close to one order of magnitude larger. This indicates that UFF is a relatively aggressive process, which is actually an advantage for polishing workpieces made of tough materials such as PCA and ALON. Table 4.2 indicates that, in the same conditions, C_{GP} is larger for harder carrier wheels, meaning that with harder wheel the removal process is somewhat more efficient. From Table 4.2, it can also be concluded that C_{GP} is a function of the part radius of curvature. This result was also observed by Yang et al. [9]. C_{GP} appears to increase as the tool-part contact becomes more conformal, indicating an increased polishing efficiency.

Based on experimental observations, the removal function of UFF can be defined with the following expression

$$c(x, y, y_0) = C_{GP} v_{rel}(x, y, y_0)^{4/5} p(x, y, y_0), \quad (4.9)$$

where C_{GP} varies as a function of the part local radii of curvature. The dependence of C_{GP} on the part geometry could be established by fitting the variations of C_{GP} for additional experimental data. This approach is used by Yang et al. [9], who actually relate Preston coefficient to an equivalent radius that include both tool and part geometries. This equivalent radius will be defined in the following section on contact mechanics.

The removal function as defined by Eq. (4.9) involves $v_{rel}(x, y, y_0)$. This quantity is computed by examining the various motions occurring during polishing. The part and band are rotated while the tool traverses the part. The band and tool crossfeed velocities are of the order of 1 m/s and 1 mm/s, respectively. Therefore, the contribution of v_c in v_{rel} is negligible and effectively neglected. The part is typically rotated at constant rotational speeds on the order of 100 rpm resulting in non negligible part velocities. Therefore, v_{rel} is defined as the length of the difference between the vectors representing the part and band velocities,

$$v_{rel}(x, y, y_0) = |\underline{v}_{rel}(x, y, y_0)| = |\underline{v}_{band}(x, y, y_0) - \underline{v}_{part}(x, y, y_0)|, \quad (4.10)$$

with

$$|\underline{v}_{part}(x, y, y_0)| = \sqrt{x^2 + y^2} |\Omega_w(y_0)|. \quad (4.11)$$

Ω_W can vary as a function of y_0 , even though it has been kept constant in this work. In particular, by having Ω_W inversely proportional to y_0 , v_{rel} would be nearly constant. \underline{v}_{band} is assumed to be tangent to the workpiece within the contact patch and has no x component since the tool is moved across the part along y while the carrier wheel is rotated about the x axis. The carrier wheel rotation is in the negative x direction as the tool is moved in the positive y direction, therefore

$$\underline{v}_{band}(x, y, y_0) = \begin{bmatrix} 0 \\ -\cos(\gamma(x, y, y_0))v_{band} \\ -\sin(\gamma(x, y, y_0))v_{band} \end{bmatrix}, \quad (4.12)$$

where $\gamma(x, y, y_0)$ is the angle between the y axis and the tangent to the part at (x, y) .

$\gamma(x, y, y_0)$ is estimated with a forward difference as follows

$$\gamma(x, y, y_0) = \arctan\left(\frac{z_{part}(\sqrt{x^2 + (y + \Delta y)^2}) - z_{part}(\sqrt{x^2 + y^2})}{\Delta y}\right), \quad (4.13)$$

where Δy is a small increment in y and $z_{part}(r)$ is the profile of the workpiece. Figure 4.6 illustrates the definition of v_{rel} for a flat.

In addition to C_{GP} and v_{rel} , the interfacial pressure distribution, $p(x, y, y_0)$ is needed to evaluate $c(x, y, y_0)$ according to Eq. (4.9). Estimating that interfacial pressure distribution is a contact mechanics problem, which might be solved with contact mechanics theory such as Hertz theory presented in section 4.3. $p(x, y, y_0)$, by defining the extent of the contact patch, defines the extent of the removal function as a function of the part radii of curvature. It can also be noted that Eq. (4.5), with $n_1 = 4/5$ and $n_2 = 1$, can be rewritten as

$$p(x, y, y_0) = \frac{h_{spot}(x, y, y_0)}{C_{GP} v_{band}^{4/5} t_d}. \quad (4.14)$$

Therefore, the generalized Preston's equation implies that the topography of a removal spot, $h_{spot}(x, y, y_0)$, is an image of the pressure distribution that induced that removal spot. That pressure distribution can therefore be evaluated with Eq. (4.14).

Flats and spheres are particular in the sense that the part radii of curvature are constant at any point of their surfaces. With these geometries, by keeping δ constant with $\alpha = 0$, F is maintained constant while polishing, away from the edges. Under this condition, $p(x, y, y_0)$ is constant along the tool path. Eqs. (4.9) and (4.14) can then be combined to express the removal function at any y_0 in terms of the removal spot topography

$$c(x, y, y_0) = \left(\frac{v_{rel}}{v_{band}} \right)^{4/5} c_{ST}(x, y, y_0), \quad (4.15)$$

where the static removal function is defined as

$$c_{ST}(x, y, y_0) = \frac{h_{spot}(x, y, y_0)}{t_d} \quad (4.16)$$

and is not a function of y_0 on plano and spherical parts.

The effect of α , the angle between the tool and local part normals, is investigated in section 4.4.1 and the prediction of interfacial pressure distributions is considered in the following section.

4.3 Hertz contact mechanics theory

Hertz contact mechanics theory [25] deals with the contact of stationary elastic solids. This theory was developed by Heinrich Hertz in 1882 and is reported in contemporary English by Johnson [26] and Maugis [27].

4.3.1 Surfaces of the bodies in contact

Hertz theory considers two elastic solids in contact. For this purpose, the origin of a rectangular coordinate system (x_H, y_H, z_H) , in which the x_H - y_H plane is the common tangent plane to the bodies in contact, is taken as their first point of contact. Near this point, the surfaces in contact are assumed to be described by an equation of the following form,

$$z(x_H, y_H) = \frac{1}{2R_x} x_H^2 + \frac{1}{2R_y} y_H^2, \quad (4.17)$$

where z_H is parallel to the normal to the surface at the origin. R_x and R_y are the principal radii of curvatures in the x_H - z_H and y_H - z_H planes, respectively. These principal radii of curvature are the maximum and minimum values of the radius of curvature of all the surface profiles in planes perpendicular to the x_H - y_H plane and including the origin of (x_H, y_H, z_H) . The two principal radii of curvature of a surface are in principal directions perpendicular to one another. Eq. (4.17) is the equation of an elliptic paraboloid. Such a surface is represented in Figure 4.7.

In the general contact problem, the surfaces of the two bodies in contact are described with equations that are not necessarily expressed in the same Cartesian

coordinate system (x_H, y_H, z_H) . Instead two distinct coordinate systems are used. They have the same z_H axis and are rotated with respect to this axis so that the two bodies' principal radii of curvature lie in the planes defined by their respective x_H - z_H and y_H - z_H planes. However, for the tool-part contact problem of UFF, the same coordinate system can be used to describe the two contacting bodies in the form of Eq. (4.17).

In the case of UFF, the tool is brought into contact with axisymmetric workpieces. The surface of these parts, z_{part} , is described as a function of the radial distance, r , to its axis of symmetry. $z_{part}(r)$ can have the form of Eqs. (1.1) and (1.2) for aspheres or ogives, respectively. In the coordinate system (x, y, z) , introduced in Chapter 1, as the tool is moved along the y axis, the center of the removal function is defined as $(0, y_0, z_0 = z_{part}(y_0))$. Since $(0, y_0, z_0)$ is the center of the tool-part contact patch, it is the first point of contact as defined in Hertz theory to describe two contacting surfaces. Therefore, $(0, y_0, z_0)$ is set as the origin of the coordinates system used to describe locally the contacting part and tool surfaces.

The coordinate system (x_T, y_T, z_T) is attached to the tool. z_T is oriented along the normal to the part surface and positively into the tool. Since the tool is moved along y with the axis of the carrier wheel perpendicular to the y - z plane, as illustrated in Figure 4.8, that plane is a plane of symmetry of the tool. This plane is also a plane of symmetry for the part. These properties imply that one of the principal radii of curvature of both the tool and part surfaces at $(0, y_0, z_0)$ lie in the y - z plane [26]. Therefore, y_T is chosen so that the y_T - z_T and y - z planes are equal and $x_T = x$.

Furthermore, the part and tool second principal radii of curvature lie in the plane x_T - z_T , where x_T - y_T is the plane tangent to both surfaces prior to compression along the part normal. The principal radii of curvature of the tool and part in the planes x_T - z_T and y_T - z_T are denoted as R_{Tx} , R_{Px} and R_{Ty} , R_{Py} , respectively.

R_{Py} is defined as the local radius of curvature of $z_{part}(r)$ at y_0 . R_{Px} is the radius of curvature at $x = 0$ of the curve $f_P(x)$, which is the intersection of the part surface and the plane x_T - z_T , as shown in Figure 4.9. The computations of R_{Py} and R_{Px} are addressed in Appendix 1.3. The sign convention used with UFF is also described in that appendix. The principal radii of curvature are denoted as positive and negative if the part surface is concave and convex, respectively.

The carrier wheel is first manufactured as a section of a cylinder. Its final shape is achieved by grinding the cylinder's periphery. This operation is performed to achieve prescribed values for the wheel diameter and the radius of curvature on the wheel's periphery. The geometry of the carrier wheel is illustrated in Figure 4.10. The coordinate system (x_W, y_W, z_W) has for origin the center of the wheel and y_W - z_W is the plane of symmetry of the wheel orthogonal to its axis of rotation. The wheel geometry is defined by the radii of curvature, R_1 and R_2 . R_1 is half the wheel diameter measured in the y_W - z_W plane. R_2 is the radius of curvature generated on the wheel's periphery in the x_W - z_W plane. Various values of R_1 and R_2 can be achieved by grinding the wheel periphery. After applying the polishing band on the wheel, R_{Ty} and R_{Tx} , are of the order of but different from R_1 and R_2 , respectively. R_{Tx} and R_{Ty} , illustrated in Figure 4.11, can be evaluated by measuring the tool profiles in the x_T - z_T and y_T - z_T

planes, respectively, with a Mida laser probe [28] from Marposs [29]. The radii of curvature are the radii of the circle fitted to the measured tool profiles in the contact region. R_{Tx} and R_{Ty} are expected to vary as a function of α , the angle between tool and part normals defined in Chapter 3. Because, as α varies, the wrapping of the polishing band might change on the portions of the tool brought in contact with the part. The determination of R_{Tx} is also affected by anticlastic curvature [30]. This phenomenon consists in the formation on the polishing band of a curvature transverse to the band circumferential direction as the band is wrapped onto the carrier wheel. This effect is illustrated in Figure 4.12, which shows the profile of the tool measured in the plane x_T - z_T and a representation of the carrier wheel showing the separation between the two due to anticlastic curvature. One negative consequence of this curvature is that the band edges could contact the part and create removal artifacts.

The tool and part geometrical properties result in the radii of curvature of both the part and tool lying in the same planes. Therefore, the surfaces of the tool, Z_T , and the part, Z_P , near the point of first contact are described by the following equations,

$$Z_T(x_T, y_T) = \frac{1}{2R_{Tx}} x_T^2 + \frac{1}{2R_{Ty}} y_T^2 \quad (4.18)$$

$$Z_P(x_T, y_T) = \frac{1}{2R_{Px}} x_T^2 + \frac{1}{2R_{Py}} y_T^2, \quad (4.19)$$

corresponding to the tool-part contact being modeled as shown in Figure 4.13.

Hertz theory states that if the tool is compressed against the part with a displacement δ and a corresponding force F , the contact region will be an ellipse of

semi-major axis, a and semi-minor axis, b shown in Figure 4.14. In order to fully characterize the contact problem, a and b must be predicted as well as the pressure distribution within the patch. Hertz theory provides these results under the assumptions that the two surfaces in contact are continuous, smooth, frictionless and non-conforming (dissimilar profiles); that the strains must be small and that the two solids can be considered as elastic half-spaces [26].

4.3.2 Pressure distribution

The pressure distribution is given by the following equation [26]

$$p(x_T, y_T) = p_0 \sqrt{1 - \left(\frac{x_T}{L_x}\right)^2 - \left(\frac{y_T}{L_y}\right)^2}, \quad (4.20)$$

where

$$p_0 = \frac{3F}{2\pi L_x L_y}. \quad (4.21)$$

L_x and L_y are the half lengths of the patch in the x_T and y_T directions, respectively and are equal to a or b . Such a pressure distribution is represented in Figure 4.15, under the assumption that $L_x = a$ and $L_y = b$. The pressure varies smoothly from zero at the edge of the patch to its maximum p_0 at the center.

Combining the generalized Preston's equation derived for UFF and Hertz contact mechanics theory, Eqs. (4.9) and (4.20) imply that the removal function can

be described by an equation of the form

$$c(x_T, y_T) = C_{GP} v_{rel}(x_T, y_T)^{4/5} p_0 \sqrt{1 - \left(\frac{x_T}{L_x}\right)^2 - \left(\frac{y_T}{L_y}\right)^2}. \quad (4.22)$$

4.3.3 Size of the contact patch and load-displacement relation

The principal relative radii of curvature, R'_x and R'_y are defined as

$$\frac{1}{R'_x} = -\frac{1}{R_{Px}} + \frac{1}{R_{Tx}}, \quad (4.23)$$

and

$$\frac{1}{R'_y} = -\frac{1}{R_{Py}} + \frac{1}{R_{Ty}}. \quad (4.24)$$

The minus signs used in the definition of R'_x and R'_y are due to the sign convention associated with the part radii of curvature.

Assuming that $L_x = a$ and $L_y = b$, the ratios a/b and R'_x/R'_y are then related by

[26]

$$\frac{R'_x}{R'_y} = \frac{(a/b)^2 E(e) - K(e)}{K(e) - E(e)}, \quad (4.25)$$

where $E(e)$ and $K(e)$ are complete elliptic integrals of argument $e = (1 - b^2/a^2)^{1/2}$, with $b < a$. The relation between $(b/a)(R'_x/R'_y)^{1/2}$ and $(R'_x/R'_y)^{1/2}$ is plotted in Figure

4.16.

In addition, the product ab is given by [26]

$$ab = \left(\left(\frac{3FR_e}{4E^*} \right)^{1/3} F_1(e) \right)^2, \quad (4.26)$$

where F is the total load, F_1 is a function of e represented in Figure 4.16, R_e and E^* are the equivalent radius and plane strain elastic modulus, respectively and are defined by

$$R_e = (R'_x R'_y)^{1/2}, \quad (4.27)$$

$$\frac{1}{E^*} = \frac{1-\nu_p^2}{E_p} + \frac{1-\nu_T^2}{E_T}, \quad (4.28)$$

where E_p , E_T and ν_p , ν_T are the Young's moduli and Poisson's ratios of the part and tool. p_0 can be rewritten by combining Eqs. (4.21) and (4.26). The resulting expression includes $(F_1(e))^2$ which is named F_3 and plotted as a function of $(R'_x / R'_y)^{1/2}$ in Figure 4.16.

Load and displacement are related by the following expression

$$\delta = \left(\frac{9F^2}{16R_e E^{*2}} \right)^{1/3} F_2(e), \quad (4.29)$$

where $F_2(e)$ is plotted in Figure 4.16. Eq. (4.29) implies a linear relation between δ and $F^{2/3}$.

4.3.4 Some simplifications and procedure to predict interfacial pressures and contact patch dimensions in the case of UFF

Three specific cases are relevant to the contact problem of UFF with optics. First, a flat part has infinite principal radii of curvature, thus the principal relative radii of curvature are equal to the tool's principal radii of curvature. Second, a spherical part of radius R implies that wherever the contact occurs on the part, the part's principal radii of curvature are equal to $\pm R$. Third, if the part is assumed to be rigid ($E_p = \infty$), the equivalent plane strain elastic modulus is the plane strain elastic modulus of the tool. This is also true if the Young's modulus of the part is much larger than the one of the tool. This is typically the case, since the carrier wheel is made of rubberlike material. These assumptions and simplifications are summarized in Table. 1.

For the present contact problem, the principal radii of curvature of the part and tool can be used to evaluate a/b according to Eq. (4.25) or the associated plot of Figure 4.16. Since the tool is a composite body consisting of the carrier wheel (which is a composite body by itself) and the polishing band, but is assumed to be one elastic body for this approach, its Young's modulus and Poisson's ratio are not known. Equivalent values for this body are determined by measuring a load displacement curve which is curve fitted with Eq. (4.29) by adjusting the material properties of the tool. Knowledge of E^* , R_e and the measurement of F permits then the evaluation of ab

and p_0 via Eqs. (4.26) and (4.21). Values of ab and a/b imply a and b . a , b and p_0 provide the interfacial pressure distribution and dimensions of the contact patch.

Assumption	Simplification
Flat part	$R'_x = R_{Tx}$ and $R'_y = R_{Ty}$
Spherical part of radius R	$R_{px} = R_{py} = \pm R$
Rigid part OR $E_p \gg E_T$	$E^* = E_T / (1 - \nu_T^2)$

Table 4.3 Simplifications for the contact of the part and tool.

4.3.5 Experimental results

4.3.5.1 Preliminary results

A Redlake [31] *MotionPro* high speed camera was available for preliminary experiments. It was used at a rate of 400 frames per second to observe the consistency of the contact patch when the tool is rotating, as well as the effect of the tool rpm, Ω_T , on the size and shape of this patch. For these purposes, the camera was placed behind a transparent material against which the tool was compressed.

The consistency of the contact patch during the rotation of the tool is of particular interest because it is a key factor in making the UFF process deterministic. The high speed camera revealed the inconsistency of the first version of the UFF carrier wheel, which was similar to a wheel with a tubeless tire. A bladder inflated to a desired pressure with air acted as the tire. Frames taken with this camera and shown in Figure 4.17 showed that the size of the patch was varying by about 30% during one rotation of the tool. This inconsistency was linked to variations in the bladder

thickness that could not be reduced. On the other hand, the high speed camera frames shown in Figure 4.18 were obtained with a previous version of UFF using the same carrier wheel as the current version. These frames show that the size of the contact patch varies by less than 7% during one rotation of the wheel. Therefore, the consistency of the contact patch has been greatly improved as needed for deterministic processing.

The high speed camera was also used on an early version of the tool to investigate the influence of the tool rotational velocity Ω_T on the size and shape of the contact patch. The carrier wheel was rotated at $\Omega_T = 0, 50$ and 500 rpm, to record the frames shown in Figure 4.19. The tool is rotating from the right to the left. The edges of the abrasive band can be seen on the top and bottom of each picture. A mark was initially placed on the band in order to compare the contact patch with the tool at the same location. This mark is visible close to the edge of the band on the top of each picture. Due to the high rotational velocity, it is particularly elongated at 500 rpm. These frames show no noticeable change between the different patches. This result supports the use of Hertz theory that deals with contact between stationary bodies.

The similarity between removal spot topography and interfacial pressure distribution suggested by Eq. (4.14) was observed with a previous version of UFF using larger, softer carrier wheels. This configuration produced contact patches large enough to generate a large enough number of data points with the Tekscan system. The pressure distribution measured with the Tekscan system for the tool pressed with

$\delta = 1$ mm into a flat BK7 sample is shown in Figure 4.20. Figure 4.21, is the STIL measurement of a removal spot made with a cerium oxide bound abrasive band and the same tool subjected to the same δ and on a flat BK7 sample with $t_d = 60$ s and $v_{band} = 1$ m/s. After estimating C_{GP} to be equal to $7 \times 10^{-13} \text{ m}^{2.2}/(\text{s}^{0.2} \text{ N})$ using Eq. (4.8) and converting depths into pressures according to Eq. (4.14), R^2 was estimated to be 0.84 between these two sets of data. This correlation shows the validity of Eq. (4.14).

4.3.5.2 Applicability of Hertz contact mechanics theory to UFF

4.3.5.2.1 Removal spots making experiment

Experiments consisting in measuring load displacement curves and making removal spots with bound cerium oxide abrasive on BK7 planar and spherical parts have been carried out with various carrier wheels. The experiments performed on spherical parts are the ones used in section 4.2.3 to establish the effect of the part radius of curvature on C_{GP} .

The durometer and geometries of the three carrier wheels that were used are summarized in Table 4.4. One has a durometer of 50, while the two others are harder with a durometer of 70. R_{Tx} was not evaluated from a profile measured with the onboard laser probe, because the region to fit was unclear in part because of a low number of measured points. Instead R_{Tx} was evaluated using the removal spots dimensions and Eq. (4.25). For these experiments, the removal spots were nearly circular in shape and therefore L_x/L_y was nearly equal to 1. Eq. (4.25) can be simplified to give [26]

$$\frac{L_x}{L_y} = \left(\frac{R'_x}{R'_y} \right)^{2/3} . \quad (4.30)$$

Eq. (4.30) was used with the removal spots made on flats to evaluate R_{Tx} .

Eleven removal spots were made with $\alpha = 0$, $v_{band} = 1$ m/s and $t_d = 10$ s. The other process parameters, which were varied, are summarized in Table 4.5. The variations were intended to study the predictability of the removal function as the part radii of curvature and tool compression change. The removal spots are shown in Figure 4.22, their size, volume and maximum depth, h_{max} , are summarized in Table 4.6, which also indicates the figures corresponding to each removal spot.

Name	50	70_1	70_2
Durometer	50	70	70
R_{Tx} (mm)	25	23	22
R_{Ty} (mm)	19	22	21

Table 4.4 Carrier wheels durometer and tool geometry.

Spot #	1	2	3	4	5	6	7	8	9	10	11
Wheel	50	70_1	70_1	70_1	70_1	70_2	70_2	70_2	70_2	70_2	70_2
δ (mm)	0.3	0.2	0.15	0.1	0.05	0.2	0.2	0.2	0.2	0.2	0.2
ROC (mm)	∞	∞	∞	∞	∞	∞	-150	-100	-50	150	100

Table 4.5 Process parameters used to make the removal spots.

Spot #	1	2	3	4	5	6	7	8	9	10	11
F (N)	11.2	16.8	10.9	5.9	2.1	18.1	18.2	15.3	14.2	20.7	19.2
$2L_x$ (mm)	5.50	4.60	3.80	3.00	2.25	4.50	4.30	3.60	3.80	6.00	6.05
$2L_y$ (mm)	4.55	4.25	3.60	3.00	2.25	4.30	4.00	3.45	3.60	5.20	5.55
V (mm ³)	0.10	0.17	0.10	0.05	0.02	0.18	0.14	0.11	0.14	0.25	0.33
h_{\max} (μm)	8.8	17.6	14.8	11.4	9.5	19.5	18.0	19.0	21.3	20.3	23.5
Figure 4.22	1)	2)	2)	4)	5)	6)	7)	8)	9)	10)	11)

Table 4.6 Properties of the removal spots.

4.3.5.2.2 Load displacement relationship

Load displacement curves were measured by using the Tekscan system as a load cell while the tool was compressed at a constant feed rate of 6 mm/min against a BK7 part. The abrasive band was placed on the tool. Five measurements were performed at the same carrier wheel position, which was marked, before making the removal spots number 1, 2, 6, 7, 8, 9, 10 and 11 of Table 4.5. The measured data were curve fitted with a linear relation between F and $\delta^{3/2}$, of the form

$$F = \beta * \delta^{3/2}, \quad (4.31)$$

where β is the fitting parameter. The data were fitted over compressions no larger than 0.3 mm and 0.2 mm, for the carrier wheels of durometers 50 and 70, respectively. The fitted ranges include the compressions which are typically used with these wheels. A typical result obtained in the conditions used to make removal spot number 6 is shown in Figure 4.23. As for that example R^2 is greater than 0.99 in all cases, showing a very good fit, consistent with Eq. (4.29) of Hertz theory. The

average and standard deviations of the β coefficients used to fit the curves measured in the different cases are reported in Table 4.7.

According to Eq. (4.29)

$$\beta = \left(\frac{16R_e}{9} \right)^{1/2} \frac{E^*}{F_2(e)^{3/2}}. \quad (4.32)$$

Therefore, using Eq. (4.28), the plane strain modulus of the tool is given by

$$\frac{E_T}{1-\nu_T^2} = \frac{1}{\left(\frac{16R_e}{9} \right)^{1/2} \frac{1}{\beta F_2(e)^{3/2}} - \frac{1-\nu_P^2}{E_P}}. \quad (4.33)$$

BK7 has a Young's modulus, E_P , of 81 GPa and a Poisson's ratio, ν_P , of 0.208. Using these values the tool plane strain modulus was evaluated and reported in Table 4.7. The tool Young's modulus, assuming a Poisson's ratio of 0.5 typically associated with rubberlike materials, is also indicated in that table.

Low Young's moduli, consistent with rubberlike materials, are obtained. As expected, the plane strain elastic modulus is a strong function of the carrier wheel durometer. The plane strain modulus obtained with 50 and 70 durometer carrier wheels vary by a factor of almost 3. This variation illustrates the change in stiffness of the tool with these wheels. The plane strain modulus computed for the two 70 durometer wheels in the same conditions on flat shows a variation of less than 9 % revealing consistency between carrier wheels. The plane strain elastic modulus of the tool should not vary when measured with various part geometries. The results obtained with the spherical part and the plano part in the case of the wheel 70_2 reveal a decent consistency with a difference of 15 % between the largest and lowest

calculated values. These results indicate that the UFF load displacement curve could be modeled with Eq. (4.29).

Wheel	50	70_1	70_2	70_2	70_2	70_2	70_2	70_2
ROC (mm)	∞	∞	∞	-150	-100	-50	150	100
β (N/mm^{3/2})	68	188	202	203	171	159	231	215
σ (N/mm^{3/2})	2	11	5	3	1	1	2	2
$\frac{E_T}{1-\nu_T^2}$ (MPa)	11	30	32	35	30	31	34	30
E_T (MPa) with $\nu_T = 0.5$	8.2	22	24	26	23	23	26	23

Table 4.7 Coefficient used to fit the load displacement curves and resulting tool mechanical properties.

4.3.5.2.3 Pressure distribution

Eq. (4.14) relates the topography of the removal spot and the tool-part interfacial pressure distribution. Using the pressure distribution from Hertz theory, given by Eq. (4.20), the removal spot topography is expected to be of the form

$$h_{spot}(x_T, y_T) = h_0 \sqrt{1 - \left(\frac{x_T}{L_x}\right)^2 - \left(\frac{y_T}{L_y}\right)^2}, \quad (4.34)$$

where the maximum depth h_0 is given by

$$h_0 = C_{GP} \nu_{band}^{4/5} t_d p_0. \quad (4.35)$$

The correlation between the topography of the removal spots shown in Figure 4.22 and the topography subjected by Eq. (4.34) was evaluated by fitting that equation to

the experimental data. The fitting operation consists in adjusting h_0 , L_x and L_y to maximize R^2 . The values of these coefficients are reported in Table 4.8 for the eleven removal spots of Figure 4.22.

The low value of R^2 shows that the removal spot obtained with the 50 durometer carrier wheel can not be described with Eq. (4.34). This spot exhibits a large central region of nearly uniform removal with shallow peaks toward its edges, unlike the pattern predicted from Hertz theory, which is illustrated in Figure 4.15. On the other hand the harder 70 durometer wheels produce removal spots that can be fairly well described with Eq. (4.34) on both plano and spherical parts. R^2 is typically greater than 0.75, the main source of discrepancy being the region with the highest removal occurring slightly off-center. When for some reason, which is not well understood, that region appears to be at the center of the removal spot, as in the case of the spots number 4 and 5, R^2 is approximately equal to 0.9. Furthermore, the values of h_0 , L_x and L_y producing these results are found to be within 8 % of the actual removal spots characteristics reported in Table 4.6. The fitted and actual maximum depths are within 1 μm . The fitted and actual removal spot dimensions are typically within 0.2 mm. These results show that the removal spots made with harder wheels can be fairly well described with Eq. (4.34) and the Hertz equations. These removal spots can be qualified as Hertzian, as their pattern follows the pattern of the pressure distribution suggested by Hertz theory. However, removal spots made with softer wheels are not Hertzian and cannot be properly predicted with Hertz theory. This was expected as the assumption for Hertz theory that the strains must be small is most

likely violated with these softer wheels. These results indicate that the removal function generated by a hard carrier wheel could be modeled with Eq. (4.22).

Spot #	1	2	3	4	5	6	7	8	9	10	11
h_0 (μm)	7.2	18.2	15.2	11.8	9.8	20.5	18.9	19.6	22.3	19.7	23.0
$2L_x$ (mm)	6.64	4.51	3.84	3.02	2.19	4.35	4.09	3.61	3.70	5.21	5.57
$2L_y$ (mm)	7.08	4.28	3.60	2.80	2.09	4.36	4.06	3.38	3.50	5.37	5.66
R^2	0.14	0.80	0.84	0.90	0.88	0.71	0.75	0.74	0.86	0.71	0.79

Table 4.8. Results of fitting Eq. (4.34) to the different removal spots.

4.3.5.2.4 Removal function size and amplitude

The theoretical spot size can be calculated with Eqs. (4.25) and (4.26). h_0 can be estimated with Eqs. (4.35) and (4.21). The resulting theoretical values for the removal spots 2 through 11, for which δ and ROC are varied are reported in Table 4.9.

Spot #	2	3	4	5	6	7	8	9	10	11
Wheel	70_1	70_1	70_1	70_1	70_2	70_2	70_2	70_2	70_2	70_2
δ (mm)	0.2	0.15	0.1	0.05	0.2	0.2	0.2	0.2	0.2	0.2
ROC (mm)	∞	∞	∞	∞	∞	-150	-100	-50	150	100
h_0 (μm)	17.0	14.7	12.0	8.5	19.7	14.1	15.0	21.7	24.1	28.9
$2L_x$ (mm)	4.28	3.71	3.03	2.14	4.25	3.96	3.84	3.53	4.60	4.82
$2L_y$ (mm)	4.13	3.58	2.92	2.06	4.00	3.76	3.66	3.38	4.30	4.47

Table 4.9 Theoretical size and depth of the removal spots.

Hertz theory predicts fairly well the size of the removal spot for plano and convex spheres, as the theoretical dimensions are within 10 % of the measured values. The amplitude is similarly well predicted on flats and as a function of δ . However, the predicted amplitude of the removal spots on spherical parts differs from the actual value by more than 20 %. A 20 % error is also obtained for the size of the removal spots on concave parts. These discrepancies can be interpreted as a violation of the assumption of Hertz theory that the bodies in contact must be non-conforming. When the tool is pressed against a concave surface, a conformal contact problem arises, which requires a different approach that is not considered in this thesis.

In summary, Hertz theory and a generalized form of Preston's equation can predict with some accuracy the removal function in the case of hard carrier wheels and convex surfaces as a function of the part radii of curvature and tool compression. However, this method does not predict the removal function for softer wheels covered with an abrasive belt and convex surfaces.

4.4 Alternative to the prediction of the removal function

Even though Hertz contact mechanics theory can provide a good approximation of the removal function in some cases, it does not offer the needed accuracy for the form correction problem. The need for accurately predicting the removal function can be alleviated with a method that corrects the removal matrix, \underline{RM} , to achieve convergence between predicted and actual removal profiles. This method is particularly intended for removal function variations due to changes in

part radii of curvature. The method is typically not used for plano and spherical parts, because their radii of curvature are constant.

This method consists in first computing \underline{RM} with a removal function that does not vary as a function of the part radii of curvature. This removal function is defined using a removal spot according to Eqs. (4.15) and (4.16). That removal spot is typically made on a part made of the same material as the part to polish and of similar geometry. A tool path is computed with that initial \underline{RM} . The part is polished and the actual removal profile measured. \underline{RM} is then corrected by multiplying each of its lines by a scaling factor such that the predicted and actual removal profiles match. The scaling factor for a given line of \underline{RM} is the ratio of the actual and predicted depth of removal at the part point where the depth of removal is predicted by that line. The corrected \underline{RM} can then be used within the form algorithms to output tool paths capable of the desired form correction. This method does not produce a perfect \underline{RM} , because it does not correct each removal function. Instead, this correction method makes the removal matrix globally correct for some range of material removal and form correction while the process parameters are unchanged.

This method has been used to polish aspheres with drastic changes in radii of curvature. A form error of less than $0.5 \mu\text{m PV}$ was achieved on the asphere of diameter 40 mm, defined by Eq. (1.1) with the coefficients reported in Table 4.10. A plot of the part profile is shown in Figure 4.24. The radii of curvature variations are such that the surface is convex at the center and becomes concave near the edge of the

part. The form was effectively corrected by UFF as shown by the initial and final form error profiles in Figure 4.25. The initial PV form error was about 8 μm .

This correction method also compensates for the systematic machine errors that induce residual form errors. The origin of form errors and their effect is the subject of Chapter 5.

$1/C$ (mm)	K	A_4	A_6	A_8	A_{10}
-40	0	-3×10^{-6}	5×10^{-9}	-6×10^{-12}	7×10^{-14}

Table 4.10 Coefficients defining the asphere polished with UFF.

4.5 Other properties of UFF removal

4.5.1 Effect of α

The effect of the angle α between the part and tool normal is of particular interest for polishing deep concave surfaces. The effect of the angle was investigated by measuring load displacement curves with the tool compressed against a plano part for values of α ranging from 0° to 90° with increments of 15° . A 70 durometer carrier wheel was used for these experiments. The curves measured at these angles were also fitted with the linear relation between F and $\delta^{3/2}$ predicted by Eq. (4.31). For all the values of α , R^2 is larger than 0.99, the values of β and the corresponding standard deviations, σ , are reported in Table 4.11.

The relation of Eq. (4.31) is based on the assumption that the compliance of the tool is due to the soft carrier wheel, while the rest of the tool is considered rigid.

Since β is associated to the compliance of the carrier wheel, it should not vary with α . However, a 40 % variation is observed between the values of β at $\alpha = 0$ and 90° . This shows that the load displacement model should include the effect of other mechanical elements as α increases. In fact, the tool compliance is a combination of the carrier wheel and mechanical elements supporting the carrier wheel. An element of particular interest is the shaft seen in Figures 3.4 and 3.6. As α varies, this shaft is subjected to varying axial and bending loads. The extremes being pure axial load and bending at $\alpha = 0^\circ$ and 90° , respectively. The observed decrease of β with α indicates a reduction in tool stiffness as α increases. This behavior could be linked to the shaft because of its slender geometry.

The variations of the load displacement relationship with α could be explained and predicted with a load displacement model assuming that the tool compliance is equal to the in-line compliances of the mechanical elements supporting the carrier wheel and the carrier wheel, for which load and displacement satisfy Eq. (4.29). Because of the soft nature of the carrier wheel, in comparison with the other elements forming the tool, it is assumed that load displacement for UFF is properly modeled with Eq. (4.29) at low values of α . At larger values of α , an appropriate model would allow for the carrier wheel compliance and therefore, β to be constant. The compliance of the mechanical elements supporting the carrier wheel was modeled as a single spring. This model was found to be inappropriate, because it was unable to produce a constant value for β . Therefore, a more complex model should be considered to relate load and displacement as a function of α .

Even though there is no quantitative model for the load displacement relationship at large α , the values computed for β can be used to evaluate the effect of α on the removal function. Since a linear relation exists between the removal spot volume and F , the variations observed for β with α will also be observed for the removal spot volume and therefore, the volumetric removal rate of the removal function. Even though β varies by 40 % between $\alpha = 0^\circ$ and 90° , a variation of only 12 % is observed in the range $[0^\circ 75^\circ]$. Therefore, major variations only occur at very large values of α . The effect of α on the removal function will be moderate while it remains in the range $[0^\circ 75^\circ]$. Furthermore, the effect of α could be compensated for by using the knowledge of the load displacement curves to correct δ and consistently produce the load that would have been achieved in the $\alpha = 0^\circ$ configuration.

α ($^\circ$)	0	15	30	45	60	75	90
β ($\text{N}/\text{mm}^{3/2}$)	202	205	201	186	181	181	145
σ ($\text{N}/\text{mm}^{3/2}$)	5	1	1	2	1	3	1

Table 4.11 Values of β and standard deviation for different values of α .

4.5.2 Effect of the workpiece material

Removal spots were made on BK7, Fused Silica (FS), SF6 and LaF2 flats with a previous version of UFF using an 80 durometer carrier wheel. Lambropoulos

et al. [32] characterized a linear relation between material removal rate and a mechanical figure of merit, FOM , defined as follows

$$FOM = E^{7/6} / (K_c H_k^{23/12}), \quad (4.36)$$

where E is the Young's modulus, K_c the fracture toughness and H_k the Knoop hardness. The relevant mechanical properties found in [32, 33] and FOM for the four materials considered in this study are summarized in Table 4.12. The measured material removal rates are plotted versus FOM in Figure 4.26. In the case of UFF, a relatively good linear relation between material removal rate and FOM is also observed, since $R^2 = 0.84$. This relationship allows for rough material removal rate estimates prior to making a removal spot.

	E (GPa)	K_c (MPa)	H_k (GPa)	FOM
SF6	56	0.53	3.1	24
FS	73	0.75	6.5	5.5
BK7	81	0.82	5.2	8.7
LaF2	93	0.72	4.8	14

Table 4.12 Mechanical properties and FOM of SF6, FS, BK7 and LaF2.

4.6 References

- [1] F. W. Preston, "The theory and design of plate glass polishing machines," J. Soc. Glass Technol., 11, 214-256 (1927).
- [2] J. E. DeGroote, A. E. Marino, J. P. Wilson, A. L. Bishop and S. D. Jacobs, "Material removal rate model for Magnetorheological Finishing (MRF) of optical glasses with nanodiamond MR fluid," Optifab 2007: Technical Digest, Proc. SPIE TD040F (2007).

- [3] R. Aspden, R. McDonough and F. R. Nitchie Jr., "Computer assisted optical surfacing," *Applied Optics* 11, 2739-2747 (1972).
- [4] R. E. Wagner and R. R. Shannon, "Fabrication of aspherics using a mathematical model for material removal," *Applied Optics* 13, 1683-1689 (1974).
- [5] D. J. Bajuk, "Computer controlled generation of rotationally symmetric aspheric surfaces," *Optical Engineering* 15, 401-406 (1976).
- [6] A. P. Bogdanov, "Automation of the planning of technological processes for machining high-precision optical components," *Soviet Journal of Optical Technology* 51, 539-541 (1984).
- [7] A. S. Savel'ev and A. P. Bogdanov, "Automated polishing of large optical components with a small tool," *Soviet Journal of Optical Technology* 52, 294-297 (1985).
- [8] D. W. Small and S. J. Hoskins, "An automated aspheric polishing machine," *Optical Manufacturing, Testing, and Aspheric Optics, Proc. SPIE* 645, 66-74 (1986).
- [9] M. Y. Yang, H. C. Lee, "Local material removal mechanism considering curvature effect in the polishing process of the small aspherical lens die," *Journals of Materials Processing Technology*, 116, 298-304 (2001).
- [10] A. Y. Yi, M. Hezlep, T. Pol, "A computer controlled optical pin polishing machine," *Journal of Materials Processing Technology* 146, 156-162 (2004).
- [11] D. Castillo-Mejia and S. Beaudoin, "A locally relevant Prestonian model for wafer polishing," *Journal of the Electrochemical Society* 150, G96-G102 (2003).
- [12] P. Wrschka, J. Hernandez, Y. Hsu, T. S. Kuan, G. S. Oehrlein, H. J. Sun, D. A. Hansen, J. King and M. A. Fury, "Polishing parameter dependencies and surface oxidation of chemical mechanical polishing of Al thin films," *Journal of the Electrochemical Society* 146, 2689-2696 (1999).
- [13] W. T. Tseng and Y. L. Wang, "Re-examination of pressure and speed dependences of removal rate during chemical-mechanical polishing processes," *Journal of the Electrochemical Society* 144, L15-L17 (1997).
- [14] F. Zhang and A. Busnaina, "The role of particle adhesion and surface deformation in chemical mechanical polishing processes," *Electrochemical and Solid State Letters* 1, 184-187 (1998).

- [15] B. Zhao and F. G. Shi, "Chemical mechanical polishing: Threshold pressure and mechanism," *Electrochemical and Solid State Letters* 2, 145-147 (1999).
- [16] STIL SA, 595, Rue Pierre Berthier, Domaine de Saint Hilaire, 13855 Aix en Provence, France, Phone : +33 4-42-24-38-05, www.stilsa.com.
- [17] Tekscan Inc, 307 West First Street, South Boston, MA 02127-1309, Phone: 800-248-3669, www.tekscan.com.
- [18] <http://www.tekscan.com/technology.html>, retrieved on September 29, 2007.
- [19] <http://www.tekscan.com/industrial/catalog/5051-5076-5101.html>, retrieved on September 27, 2007.
- [20] SigmaPlot Version 10 (10.0.0.54), Systat Software Inc., 1735 Technology Drive, Ste 430, San Jose, CA 95110, Phone: 800-797-7401, www.systat.com.
- [21] M. J. Cumbo and S. D. Jacobs, "Determination of near-surface forces in optical polishing using atomic force microscopy," *Nanotechnology* 5, 70-79 (1994).
- [22] L. M. Cook, "Chemical processes in glass polishing," *Journal of Non-Crystalline Solids* 120, 152-171 (1990).
- [23] A. A. Tesar, B. A. Fuchs and P. P. Hed, "Examination of the polished surface character of fused-silica," *Applied Optics* 31, 7164-7172 (1992).
- [24] S. Tong, S. M. Gracewski and P. D. Funkenbusch, "Measurement of the Preston coefficient of resin and bronze bond tools for deterministic microgrinding of glass," *Precision Engineering* 30, 115-122 (2006).
- [25] H. Hertz, *Über die Berührung fester elastischer Körper* (On the Contact of Elastic Solids), *J. reine und angewandte Mathematik*, 92, pp 156-171, 1882. (For English translation see *Miscellaneous Paper by H. Hertz*, Macmillan, London, 1896.)
- [26] K. L. Johnson, *Contact Mechanics*, Cambridge University Press, New York, New York, 1987.
- [27] D. Maugis, *Contact, Adhesion and Rupture of Elastic Solids*, Springer, Berlin, 2000.
- [28] <http://www.us.marposs.com/library/LASERG.pdf>, retrieved on September 27, 2007.

[29] Marposs S.p.A., 40010 Bentivoglio (BO) Italy, Via Saliceto 13, Phone: +39 051-899111, www.marposs.com.

[30] R. C. Benson, "The interfacial mechanics of a tape wrapped around a flexible bumpy roll," *Tribology Transactions* 36, 375- 380 (1993).

[31] Redlake Inc., 3440 East Britannia Drive, Tucson, AZ 85706, Phone: 800-462-4307, www.redlake.com.

[32] J.C. Lambropoulos, S. Xu and T. Fang, "Loose abrasive lapping hardness of optical glasses and its interpretation," *Applied Optics*, 36, 1501-1516 (1997).

[33] T. Fang, "Near-surface mechanical properties of optical materials in deterministic microgrinding," Ph.D. thesis, 1997, University of Rochester.

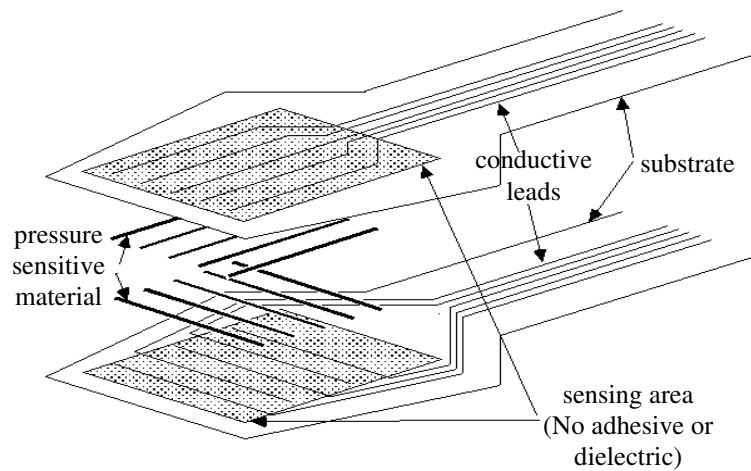


Figure 4.1 Structure of the Tekscan system. (Figure adapted from [18])

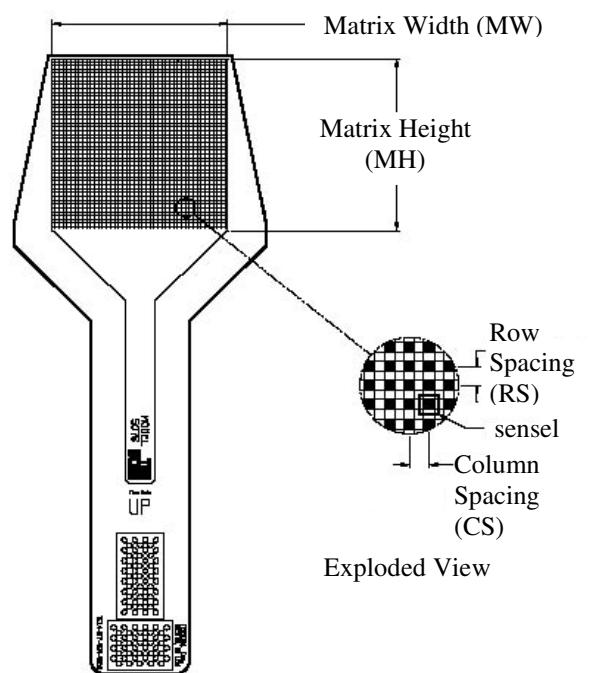


Figure 4.2 Geometry of the Tekscan system. (Figure adapted from [19])

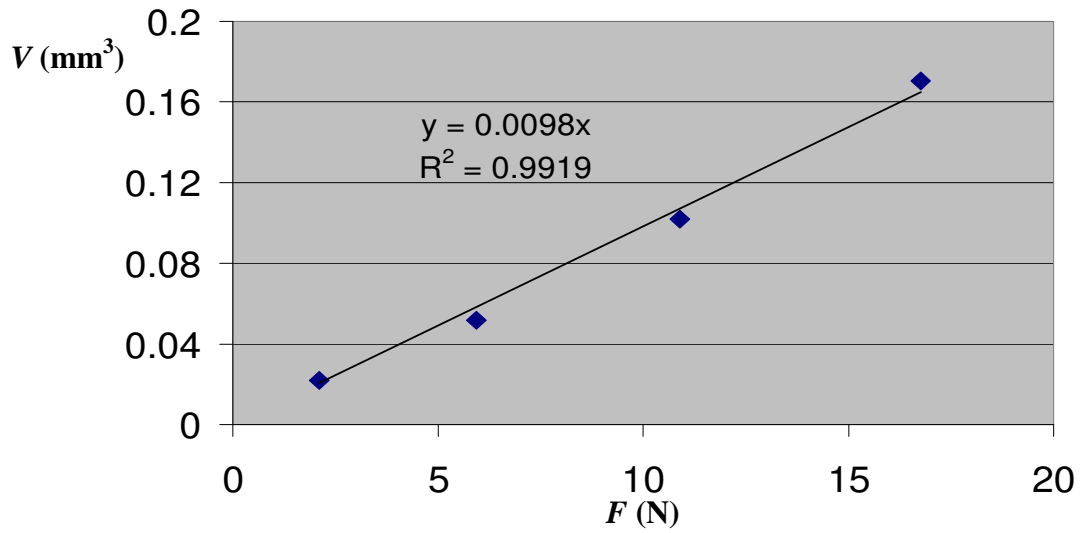


Figure 4.3 Removal spot volume versus applied load and linear fit.

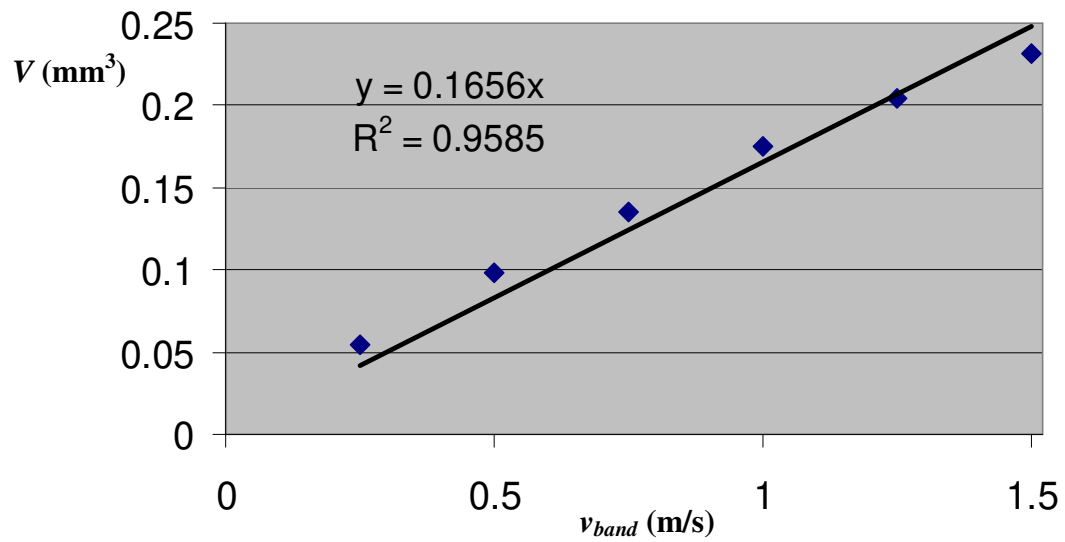


Figure 4.4 Removal spot volume versus band velocity and linear fit.

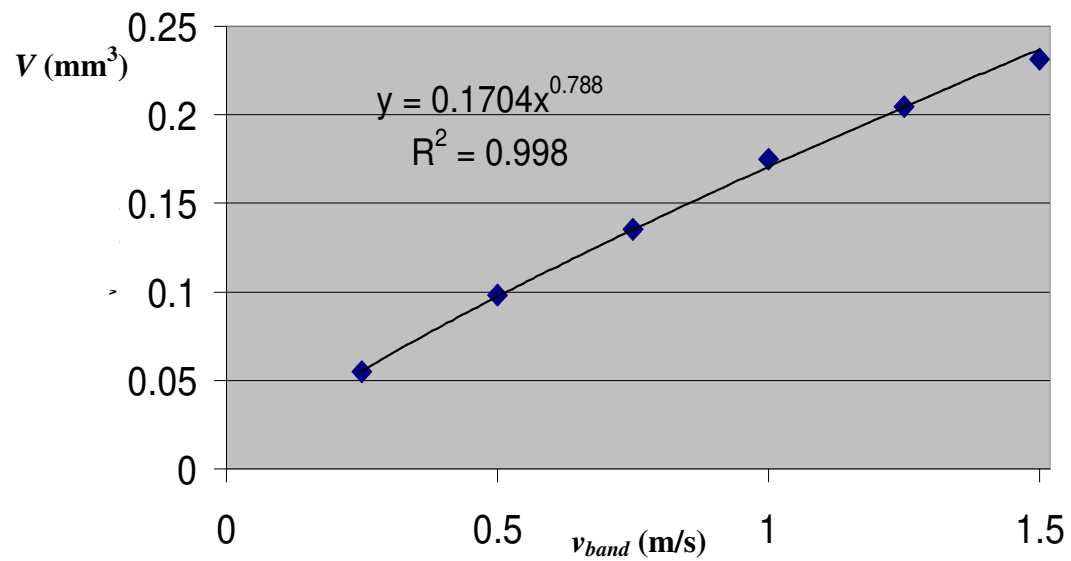


Figure 4.5 Removal spot volume versus band velocity and power fit.

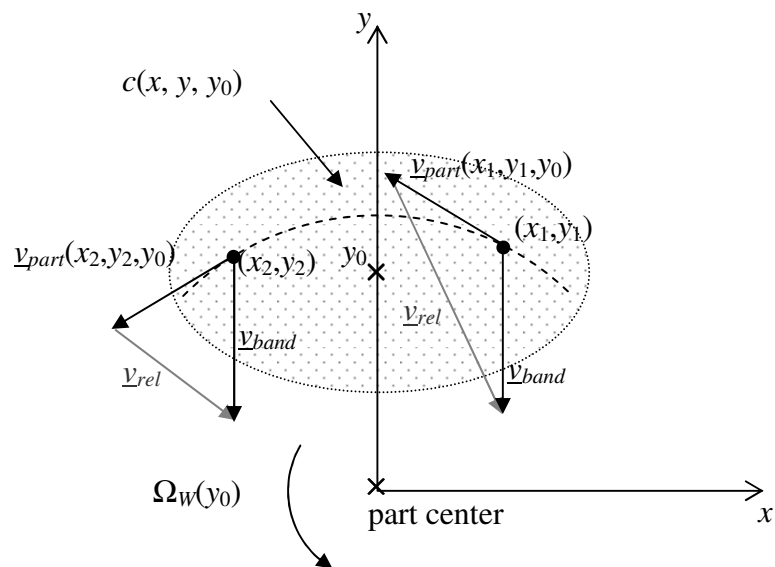


Figure 4.6 Illustration of v_{rel} as a function of (x, y, y_0) on a flat.



Figure 4.7 Definition of the surface used to model a contacting body in Hertz theory.

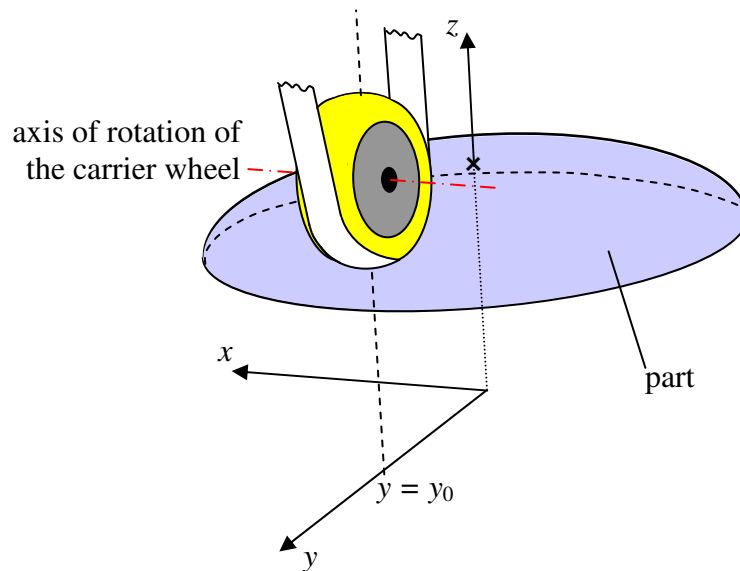


Figure 4.8 Geometry of the part and tool motion.

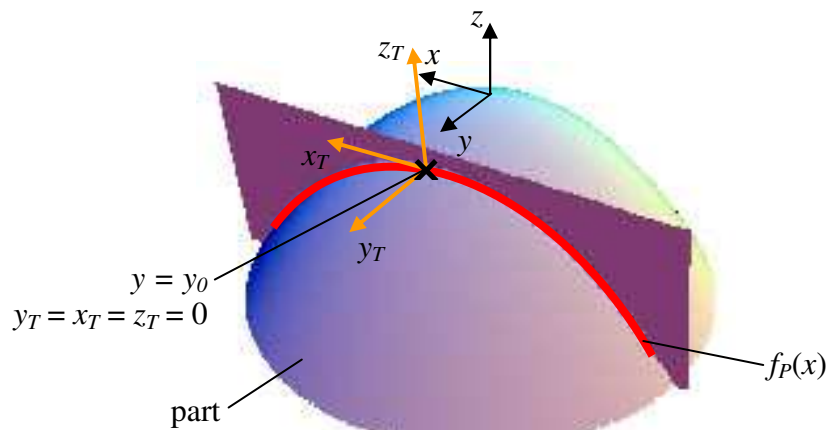


Figure 4.9 Geometry used for the definition of R_{P_x} .

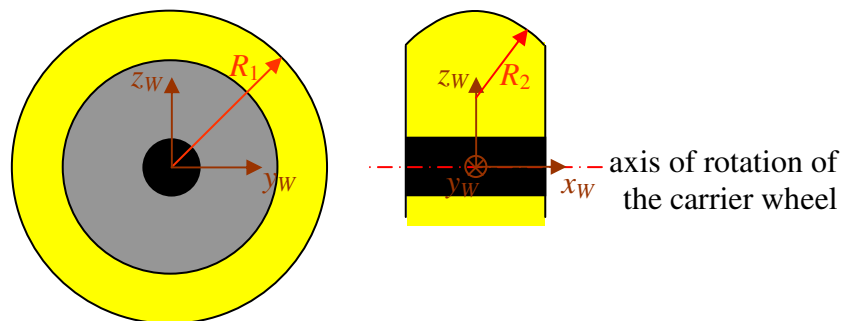


Figure 4.10 Carrier wheel geometry.

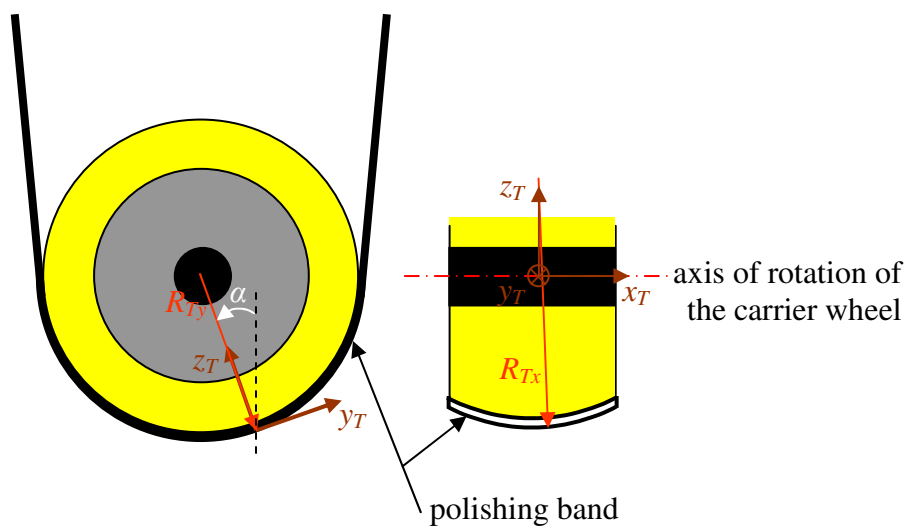


Figure 4.11 Principal radii of curvature of the tool.

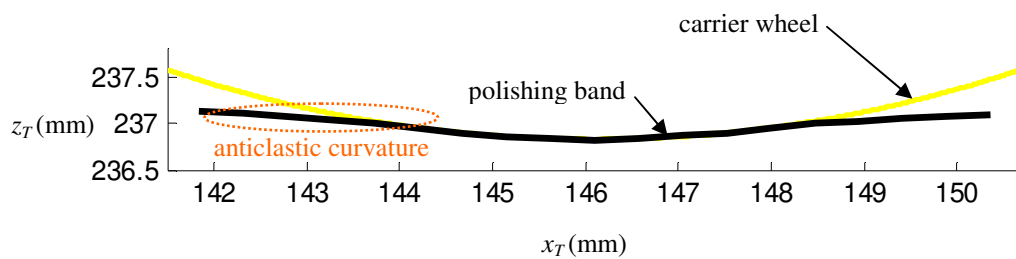


Figure 4.12 Tool profile in the plane x_T - z_T showing the anticlastic curvature of the polishing band.

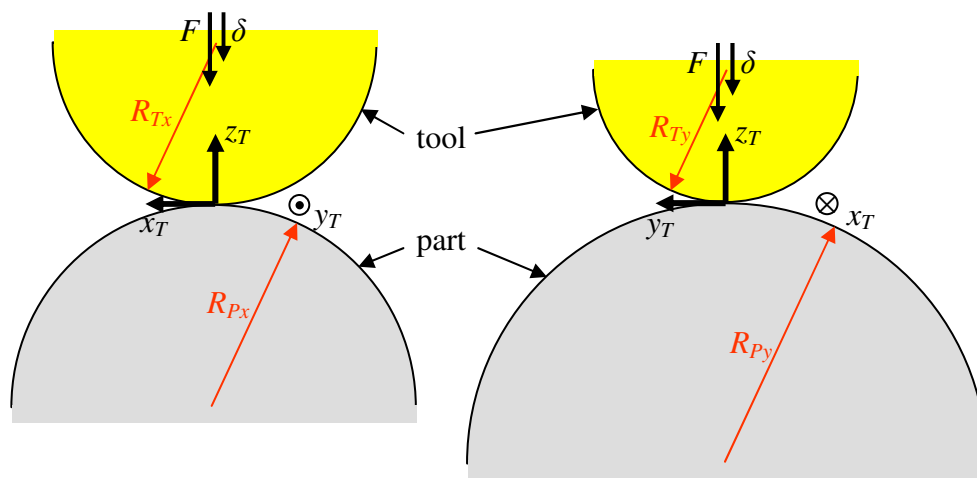


Figure 4.13 Contact of the part and the tool in the x_T - z_T and y_T - z_T planes.

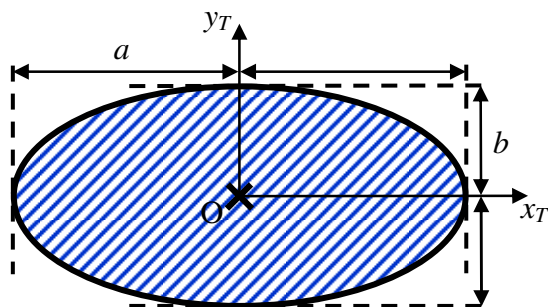


Figure 4.14 Geometry of the contact patch.

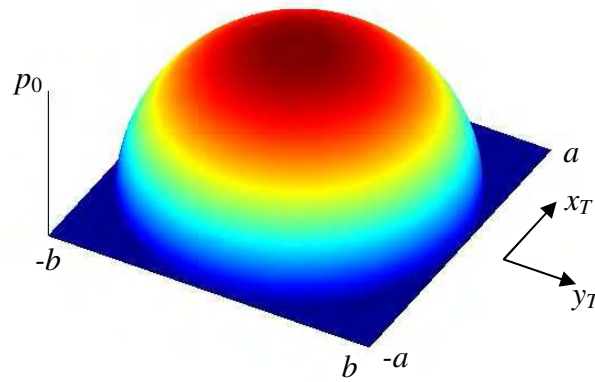


Figure 4.15 Hertz pressure distribution.

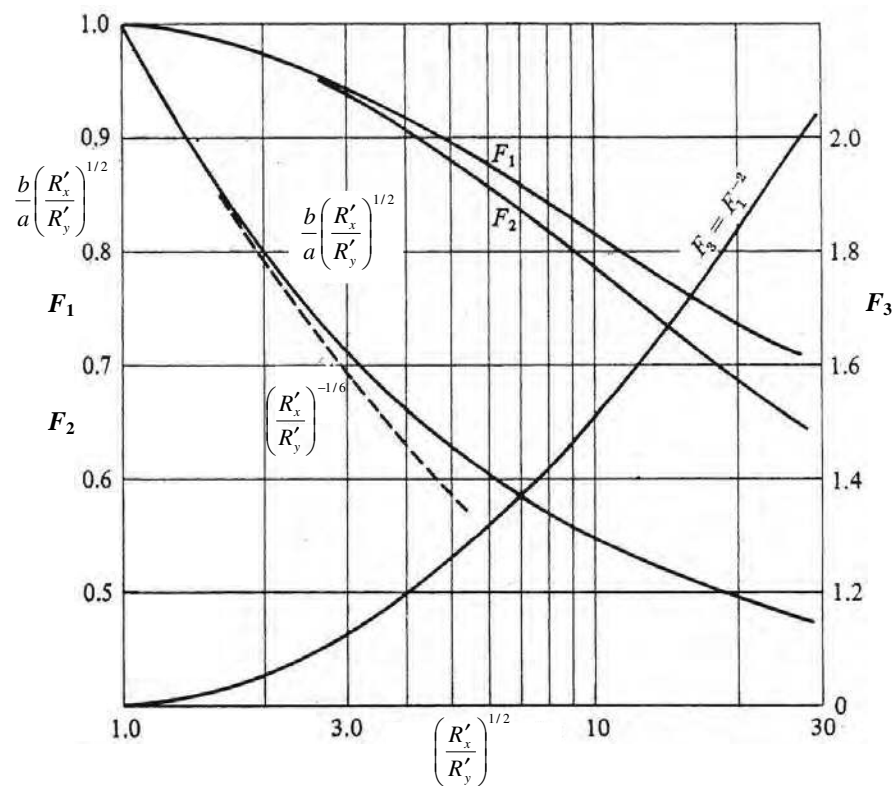


Figure 4.16 Functions of interest for Hertz theory. (Figure adapted from [26])

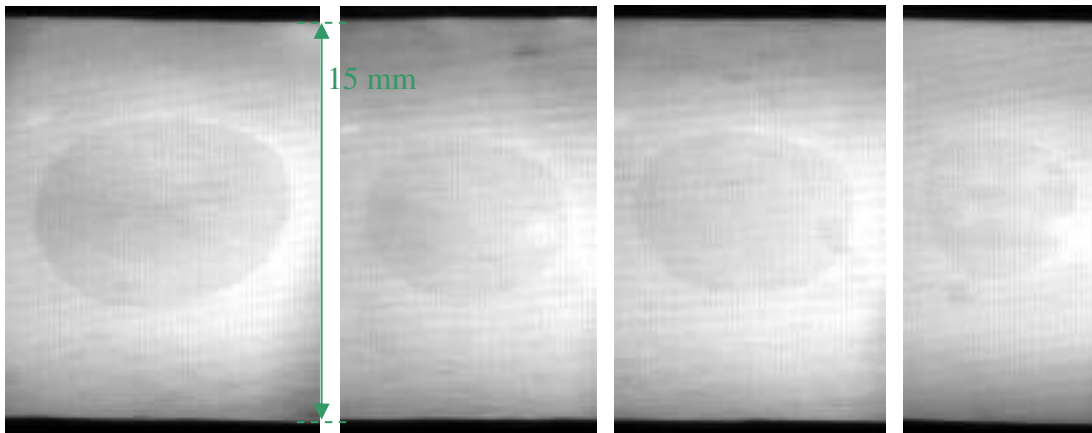


Figure 4.17 High speed camera frames revealing the inconsistency of the contact patch on the first version of UFF.

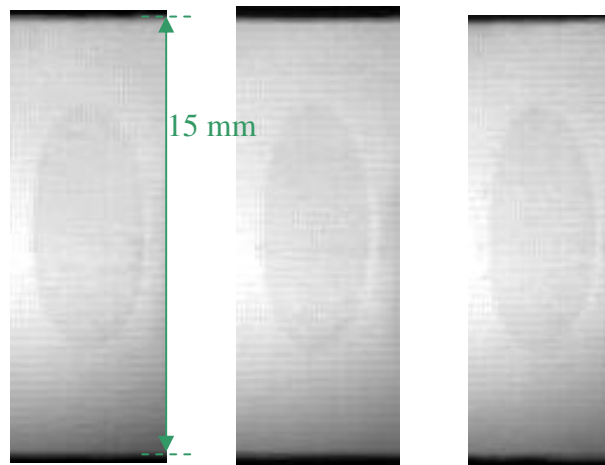


Figure 4.18 High speed camera frames showing the consistency of the contact patch.

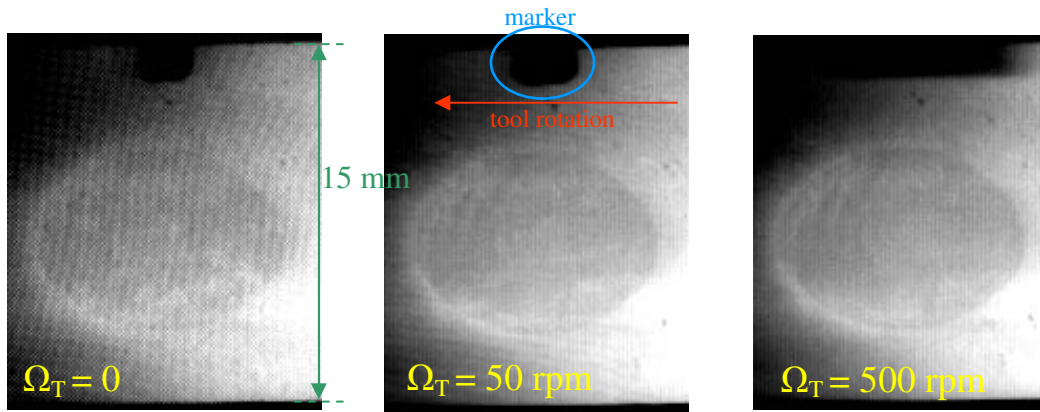


Figure 4.19 High speed camera frames for the tool at $\Omega_T = 0$, 50 and 500 rpm.

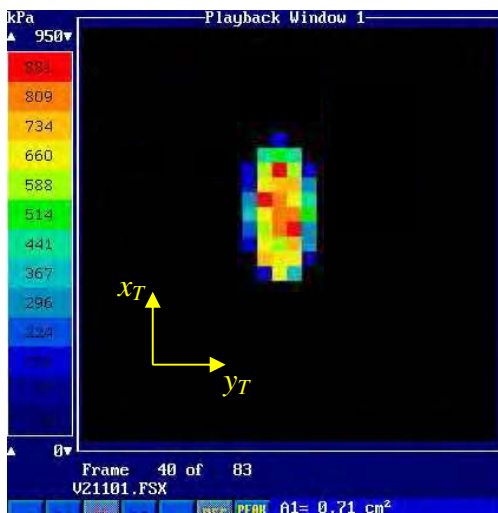


Figure 4.20 Tekscan measurement of the interfacial pressures encountered with the V2 tool.

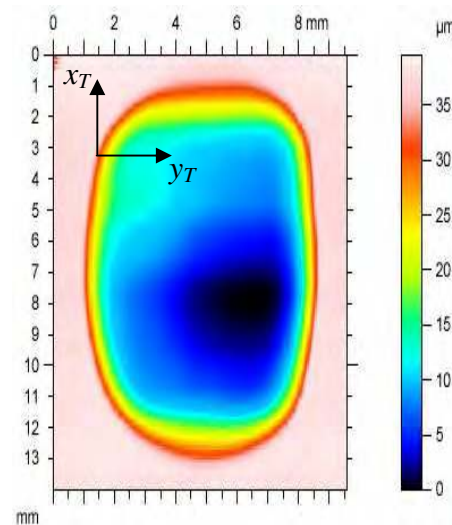


Figure 4.21 STIL measurement of a removal spot made with the V2 tool.

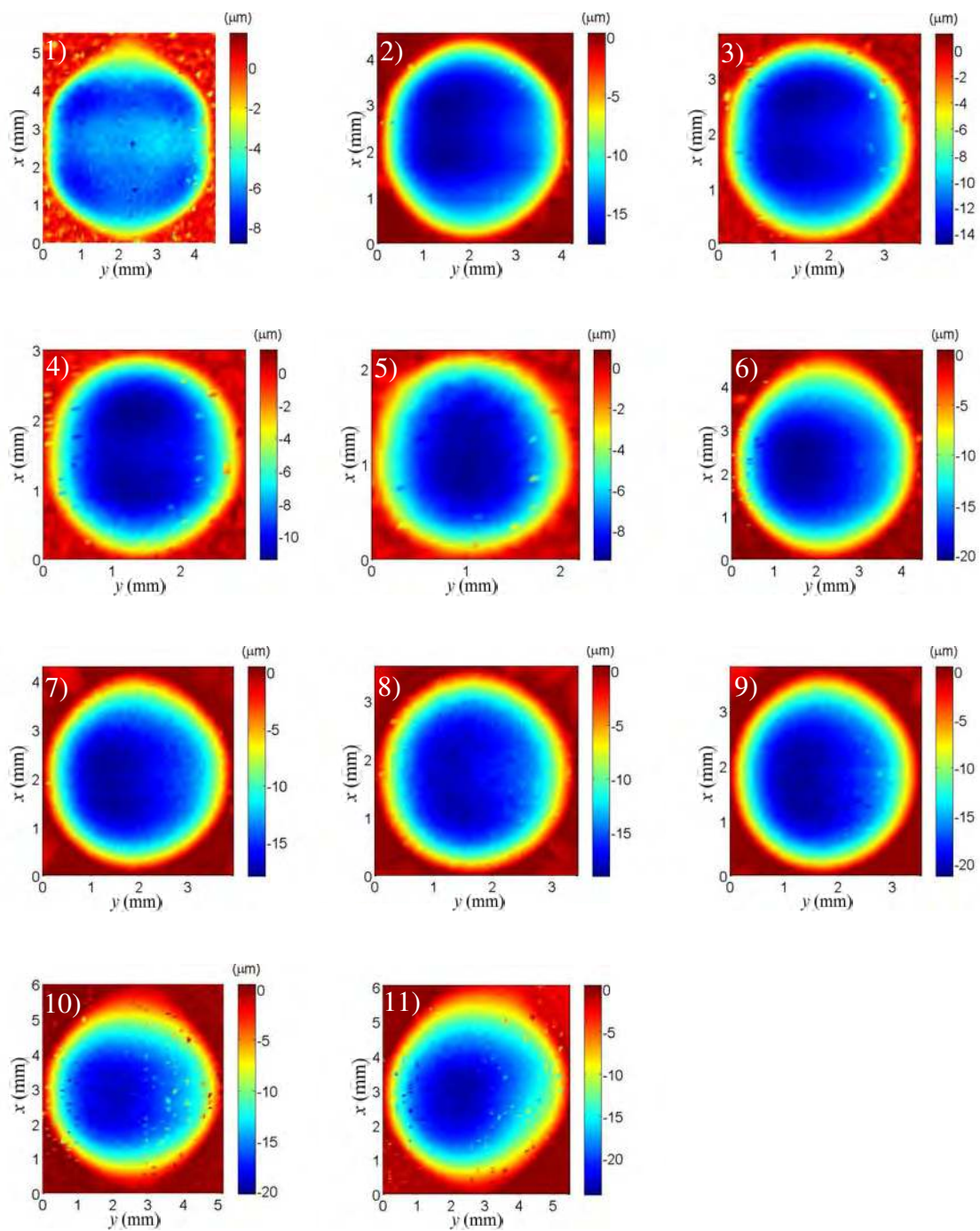


Figure 4.22 Removal spots made with the process parameters reported in Table 4.5.

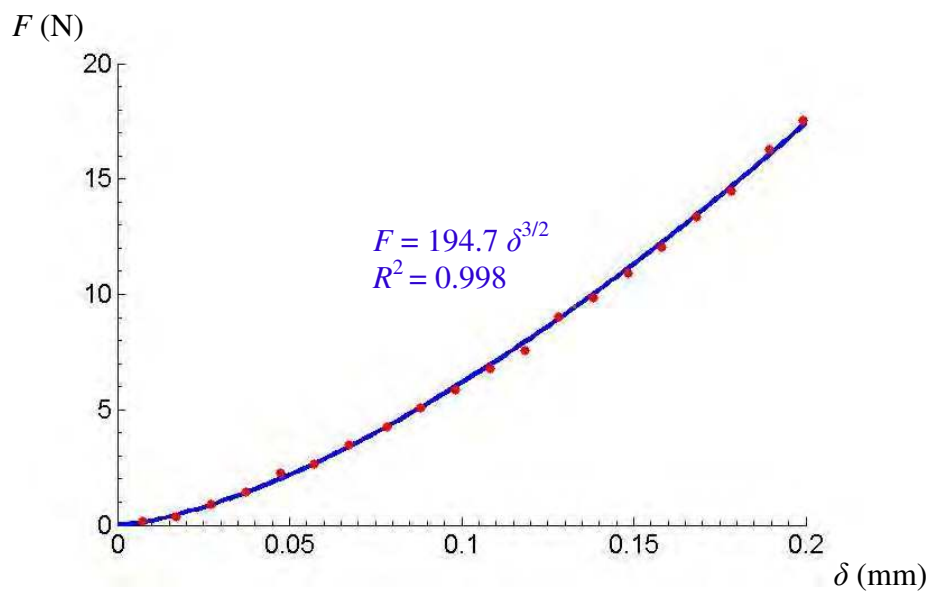


Figure 4.23 Load displacement curve in the conditions of the removal spot number 6. Data in red, theoretical curve in blue.

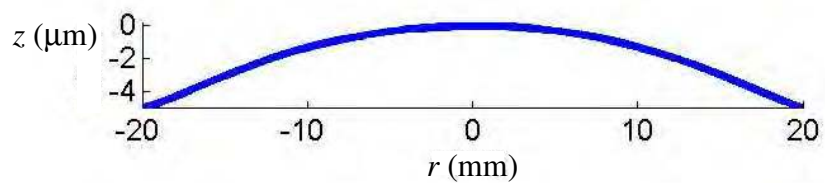


Figure 4.24 Desired form of an asphere polished with UFF.

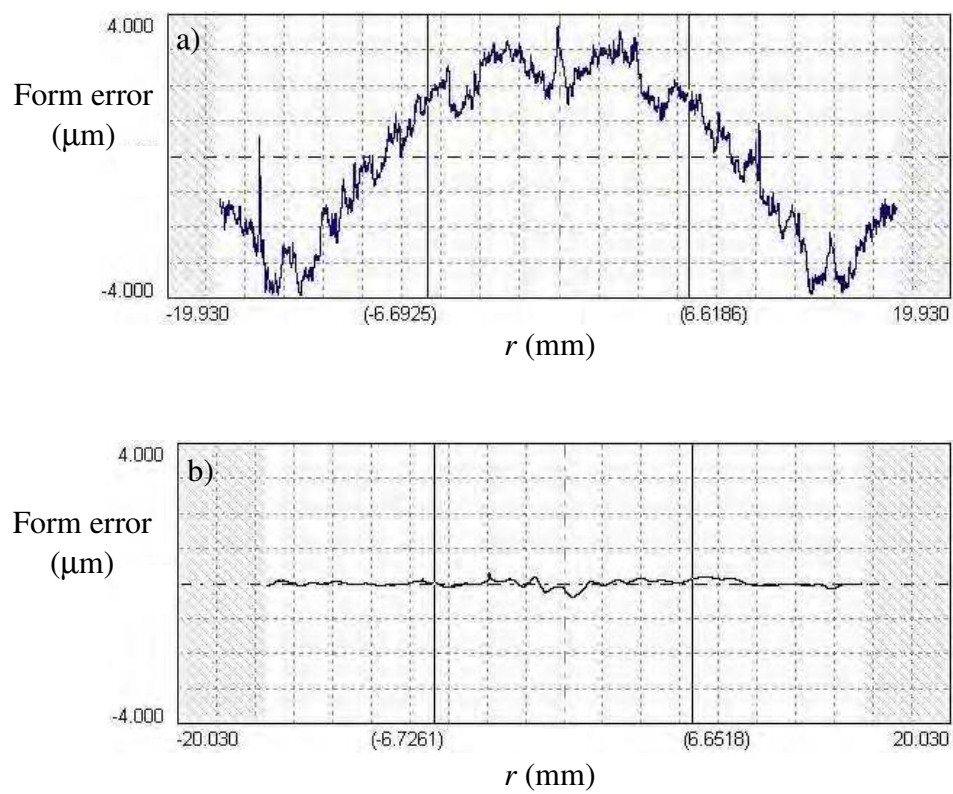


Figure 4.25 Form errors of the asphere polished with UFF
a) initial;
b) final.

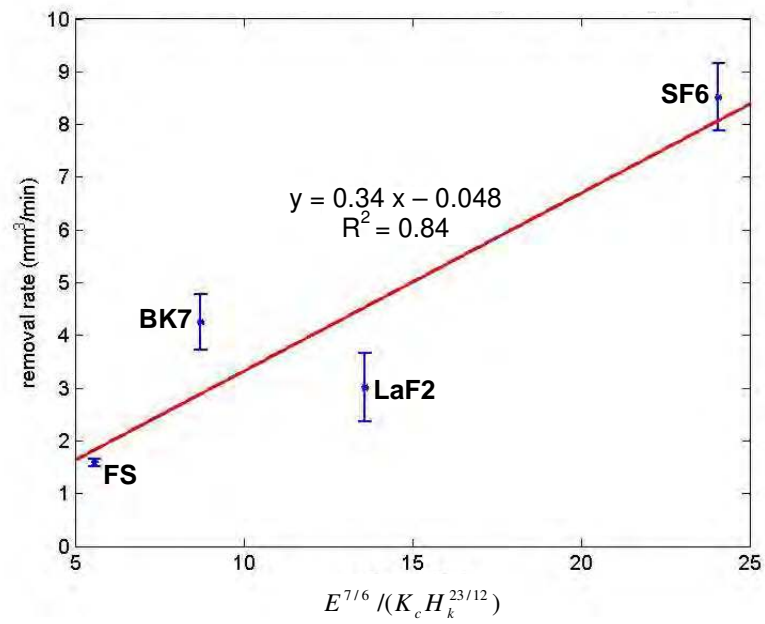


Figure 4.26 Removal rate versus mechanical figure of merit.

Chapter 5 Surface errors

Surface errors are the deviations of an optical surface from the target surface. The occurrence and amplitude of surface errors determine the quality of the grinding and polishing operations. Surface errors are typically categorized into three types, which are defined by specific spatial frequency ranges [1, 2]. They are figure error (low spatial frequency, $< 0.3 \text{ mm}^{-1}$), tool marks (mid spatial frequency, between 0.3 mm^{-1} and 10 mm^{-1}) and surface roughness and subsurface damage (high spatial frequency, $> 10 \text{ mm}^{-1}$). Table 5.1 reports these errors and possible sources. The actual surface is the sum of the desired shape and the contributions of these three types of errors.

<i>Surface error</i>	<i>Frequency range</i>	<i>Error sources</i>
Figure error	$< 0.3 \text{ mm}^{-1}$	<ul style="list-style-type: none"> ○ Erroneous inputted form ○ Errors in tool/part motion ○ Variations of material volumetric removal rate
Tool marks	$> 0.3 \text{ mm}^{-1}$ and $< 10 \text{ mm}^{-1}$	<ul style="list-style-type: none"> ○ Tool vibration
Surface finish	$> 10 \text{ mm}^{-1}$	<ul style="list-style-type: none"> ○ Abrasive size and penetration ○ Workpiece material mechanical properties

Table 5.1 Surface errors definition and possible sources. (Adapted from [2])

5.1 Surface roughness and subsurface damage (SSD)

Surface roughness affects the contrast of the image produced by an optic, because the light is scattered in all directions [3], and subsurface damage (SSD) may reduce the strength and optical damage threshold of the material [4]. The roughness

of the surface after polishing can be characterized by evaluating its peak-to-valley (PV) and root mean square average (RMS) with an interferometer such as the Zygo NewView 5000 [5]. These values are a good metric for the polishing process. SSD is traditionally evaluated with destructive techniques revealing the damage lying under the surface of the part. Nondestructive techniques have also been developed. Randi et al. [6] reviewed nondestructive and destructive techniques to evaluate SSD in brittle materials. Dimpling, taper polishing, etching, sectioning and MRF spotting are some of the destructive techniques. Nondestructive techniques include transverse electron microscopy, x-ray diffractometry and Raman spectroscopy. SSD depth can also be evaluated from a surface microroughness measurement. Lambropoulos et al. [7] established that SSD depth is less than 2 times the PV surface microroughness for a large variety of optical glasses ground with bound abrasive diamond tools. Randi et al. [6] considered optical single crystals and found a factor of 1.4 between maximum SSD depth and PV surface microroughness.

The surface finish errors are related to the material removal mechanisms [1]. Therefore, the amplitude of these errors are a function of all the factors influencing the removal process, which include the part material, polishing abrasive, coolant, part rpm, tool rpm and relevant tool characteristics, such as carrier wheel durometer and tool compression for UFF. An efficient polishing process must reduce surface roughness and limit induced subsurface damage. For a given material, the smoothest surface is typically achieved by determining empirically the best combination of

process parameters, which should also lead to minimized SSD. The numerous adjustable parameters of UFF offer a large range of combinations from which a satisfactory process solution can be found for most workpiece materials. For example, such solutions have been established by OptiPro Systems for BK7 and PCA. However, investigation and minimization of surface roughness and SSD induced by UltraForm Finishing is not within the scope of the present study.

5.2 Figure error

Figure or form error of an optical surface causes geometrical distortions of an image. This error is in the low spatial frequency range. It can be measured with interferometers such as the Zygo GPI phase shifting laser interferometer [8] and surface profilometers such as the Taylor Hobson Form Talysurf [9].

5.2.1 Sources of form errors

Form error is the difference between desired and actual part form. The goal with UFF is to minimize these errors by optimizing the tool path. The current approach typically results in low amplitude form errors. However, discrepancies exist between the predicted and observed form errors. The major sources of such errors are inaccurate specification of the desired removal profile, machine axes positioning or motion errors and unpredicted variations of the removal function. The cause and process effect of these problems are listed in Table 5.2.

Improper lateral or height calibrations of the metrology instrument could be the cause for erroneous amplitude or lateral position of the points representing the

actual part profile. This would lead to inaccurate desired removal profiles. For a profilometer, the lateral calibration is linked to the calibration of the CNC stage on which it is operated. However, for an interferometer, the lateral calibration must be performed for every modification of the measurement setup. In most cases, the height measurement can be accurately calibrated with a calibration master.

Tool misalignment or de-centering causes incorrect tool positioning that is characterized by constant x and y offsets Δx and Δy , respectively, between programmed and actual tool positions. z reference error is an improper adjustment of the z datum, which should be the surface of the part at its center. Following or tracking errors are the inaccuracy of the machine in positioning the tool at the desired location. This inaccuracy, which is intrinsic to CNC machines, is controlled by setting upper values for these following errors, typically on the order of $10\ \mu\text{m}$. Large following errors, expected or unexpected because of a machine problem, could cause a noticeable form error. A clock error corresponds to a discrepancy between the programmed and actual execution time for a machine command.

Assuming that the machine can accurately position and move the tool, the relative velocity between the abrasive and part and the pressure applied by the tool should be known. However, according to Eq. (4.9), the removal function could still vary unexpectedly, because of variations of the generalized Preston coefficient. This coefficient can be affected by band and abrasive wear as well as a change in chemistry, such as the flow of coolant and pH level.

<i>Source</i>	<i>Cause</i>	<i>Effect</i>
Inaccurate desired removal profile	Erroneous lateral or height calibrations of the metrology instrument	Inappropriate tool crossfeed velocities solution
Tool improper positioning and motion	Tool misalignment, z reference error, following and clock errors	Inaccurate removal prediction
Unexpected changes of the removal function	Band and abrasive wear, change in chemistry (coolant, pH, ...)	Inaccurate removal prediction

Table 5.2 Potential sources of form errors, their cause and effect.

5.2.2 Approach for the evaluation of the effect of the errors

An error such as tool de-centering can be qualitatively evaluated in grinding [1, 2]. However, such an approach is impossible with UFF for any of the errors reported in Table 5.2. This is due to the large extent of the removal functions and their overlaps as the tool traverses the part, as well as the variety of removal function topographies that occur. Instead in the case of UFF, the effect of a given error has to be evaluated for any given removal function. For that purposes, numerical simulations are used.

In order to evaluate the effect of a given error, the general scheme for the numerical simulations involves the three steps illustrated in Figure 5.1. During the first step, the tool path generator is executed with the given inputs. The outputs are the tool path commands that would be executed on the machine and the corresponding predicted final part profile. This is a reference profile representing the prediction without machine and process errors. The second step produces a second

profile that is the actual profile. It is predicted by taking into account the effect of the error that is under investigation. The actual effect of that error is evaluated at step 3 by taking the difference between the reference and actual profiles.

It is necessary to understand the effect of an error on the removal process in order to accurately take it into account at step 2. Establishing the effect of an error is difficult for parts other than plano, because for spheres and aspheres one error might induce several coupled effects. For example, tool misalignment as the tool is moved across a spherical or aspherical part will also induce a variable tool compression error, because of the varying height of the part. Therefore, to simulate a tool misalignment error on a spherical surface, the size of the actual removal function should also be dynamically adjusted along the tool path. On the other hand, for flats, a constant shift in the removal function position will be sufficient to model a tool misalignment error. It is preferable to diagnose the effect of a single error by running numerical simulations on flats to avoid the coupling of the different errors.

In the case of a flat, the different errors listed in Table 5.2 can be modeled according to the descriptions given in Table 5.3. Depending on the type of error, one of three different sets of operations or modes is used in step 2 as described in Figure 5.2.

Mode 1 is used when errors are present in the desired removal profile. Such errors can be due to erroneous lateral and height calibrations of the metrology instrument. They are modeled by changing the lateral and vertical scales of the inputted desired removal profile. The tool path generator is then run to compute the

actual tool crossfeed velocities that would achieve the modified removal profile. The predicted profile including the effect of the inaccurate desired removal profile is obtained by multiplying the removal matrix reference, \underline{RM}_{ref} , computed at step 1, and the vector \underline{v}_{act} having for elements the inverse of the tool crossfeed velocities calculated at step 2.

The tool path generator is also run with adjusted inputs for Mode 2. This mode is used for errors that result in changes of the removal matrix due to variations of the removal function. This occurs with tool misalignment, z reference error, following error, band and abrasive wear, change in chemistry. Tool misalignment and following error are modeled by shifts of the removal function equal to Δx or Δy in the x and y directions, respectively. For tool misalignment these shifts are constants. A constant or variable shift Δy is used for a following error. For example, the error in y could be proportional to the tool crossfeed velocity at each step of the tool path. In case of z reference error, band and abrasive wear or change in chemistry an actual removal function could be simulated from the one used at step 1 by scaling up or down the size and amplitude of the removal function. A case of uniform band wear can be simulated by applying a proportionality coefficient less than 1 to the initial removal function. For a z reference error, size and amplitude of the actual removal function are coupled and could be established by using the results from Chapter 4 relative to the prediction of the removal function as a function of the tool compression. In mode 2, once the error is taken into account to run the tool path

generator, the actual removal matrix, \underline{RM}_{act} that is computed, is multiplied by \underline{sC}_{ref} obtained at step 1.

<i>Error</i>	<i>Model</i>	<i>Step 2 mode #</i>
Desired removal profile	Change the lateral and vertical scales of the desired removal profile	1
Tool misalignment ($\Delta x, \Delta y$)	Shift the removal function in x and y by Δx and Δy , respectively	2
Following error (Δy)	Shift the removal function in y by Δy	2
z reference error	Use the actual removal function or modify the one from step 1 by scaling up or down its size and amplitude	2
Band and abrasive wear, change in chemistry	Use the actual removal function or modify the one from step 1 by scaling up or down its amplitude	2
Clock error	Adjust \underline{sC}_{ref} with constant or proportional time error	3

Table 5.3 Sources of form errors, model and simulation for flats.

Mode 3 is used for errors resulting in discrepancies between programmed and actual tool and part motions. A machine clock error could result in discrepancies between programmed and actual part rpm. Such an error could be modeled by adding a constant or proportional error to the programmed part rpm. A machine clock error can also induce tool motion errors, because even though tool crossfeed velocities are computed, the machine is actually operated in terms of time. Such an error is modeled by modifying \underline{sC}_{ref} outputted by the tool path generator at step 1. A simple constant or proportional error can be used at each step of the tool path. The resulting actual commands vector \underline{sC}_{act} is then multiplied by \underline{RM}_{ref} to generate the actual profile.

5.2.3 Numerical simulations

The effects of a variety of errors for two static removal functions were investigated with numerical simulations performed on a flat according to Figure 5.2. The two static removal functions are shown in Figure 5.3.a) and b). The first static removal function, shown in Figure 5.3.a) was virtually generated. It was created with an elliptical shape and a removal pattern in agreement with a Hertzian pressure distribution. The second static removal function, shown in Figure 5.3.b), was the actual removal generated on BK7 with a cerium oxide bound abrasive belt and a carrier wheel of durometer 50. That removal function was measured with the STIL profilometer. The effects of the removal function pattern on the predicted form can be highlighted with these two static removal functions. The simulated errors include shifts by Δx and Δy , variations in size and amplitude of the removal function and constant clock error. The removal function alterations for these simulated errors are illustrated in Figure 5.4. Shifts in x and y , size and amplitude scaling can be combined or used individually as shown in Figures 5.4,b), c), d) and e), respectively. The edge problem is not taken into account as the simulations only predict the part profiles away from the part edges. The part rotational speed was set equal to 300 rpm. To clearly visualize the effect of each error the desired removal was set uniform and equal to 10 μm . The desired, reference and “error” profile are consistently shown for the different considered errors.

Figures 5.5 and 5.6 show the effects of Δx and Δy taking values + and – 1 mm with the virtual elliptical static removal function. Such error simulations represent the

effect of tool misalignment or a constant following error in the case of Δy . Mode 2 was used for these simulations. The reference profile exhibits a PV of $0.15 \mu\text{m}$. Figures 5.5.b) and c) illustrate that $+\Delta x$ or $-\Delta x$ have drastically different effects, both degrade the form with PV of 0.25 and $0.5 \mu\text{m}$, respectively. In both cases, while different patterns are observed in the part center region, the form is preserved away from that region. A positive value of Δx results in less removal, because such a shift results in lower relative velocities between the abrasive and the workpiece. The opposite happens as a negative value of Δx is used. On the other hand positive or negative values of Δy have the same effect if the static removal function is symmetric with respect to y , because the tool crossfeed velocity solution is symmetric with respect to the part center. This case occurs with the virtual removal function as shown in Figures 5.6.b) and c). Whereas shifts in x induced “peaks” at the part center and excessive or insufficient removal away from the part center, shifts in y produce a “hole” at the part center and a nearly unchanged removal profile away from that region. The resulting PV is of about $0.4 \mu\text{m}$. The simulations show that these errors should have a noticeable effect at the part center. The center feature has a width approximately equal to the length of the removal function semi-major axis.

Figure 5.7 shows that shifts in x have similar effects with the measured and virtual removal functions. The main difference is the shape of the removal profile at the center. For the measured removal function, the observed effects are also function of the sign of Δy , as shown in Figure 5.8, because of the lack of y symmetry of this

static removal function. All the following numerical simulations were run with the real removal function.

The effect of a change in amplitude was simulated using mode 2 and scaling the removal function by multiplying its amplitude by 0.9. This case corresponds to a proportional decrease of the removal function suitable to model uniform band wear. The predicted profiles of Figure 5.9 show what seems to be a predicted profile that is shifted up. This profile is actually a scaling of the original one, because the depth of removal equation is linearly dependent on the amplitude of the removal function.

The effect of a change in size of the removal function was also simulated with mode 2 and is shown in Figure 5.10. Such simulations provide insights into the effect of z reference error. The removal function dimensions were scaled down in Figure 5.10.a) and scaled up in Figure 5.10.b) by factors of 0.9 and 1.1, respectively. However, by doing so, the volumetric removal rate of the removal function would change. In order to decouple the effects of the change in volumetric removal rate from the change in size, the amplitudes of the downsized and upsized removal functions were scaled to keep the volumetric removal constant. They were multiplied by 1.25 and 0.83, respectively. In both cases, the form is quite degraded in the center region and exhibits an exacerbated overall waviness when compared to the reference profile. The higher or lower volumetric removal rates that should occur with a z reference error would be expected to result in an additional scaling similar to what can be seen in Figure 5.9.

A constant clock error that would result in a constant increase of the command execution time is simulated in Figure 5.11. At every step, during which a radial distance of 0.1 mm is covered, an error time of 10 ms is added to the programmed time. Such an error was actually observed due to an error in the machine command format. For the simulation, the computed process time was originally 17 mins and the systematic errors only increased the process time by 2.6 s, which would be hardly noticeable. This small effect results in a profile that is shifted down by a variable offset decreasing with r . While the form is merely altered away from the part center region, that profile shift has noticeable consequences at the part center. The initially smooth profile exhibits a central hole and the overall PV is nearly doubled.

These numerical simulations show the variety of effects that can be induced by various sources of errors and removal functions. They are useful to evaluate the amplitude of the figure error that could be induced by a source of error. The center region of the part is particularly sensitive to most of the errors. The errors are amplified in that region because of the fast tool motions that are required. Because of the convolution nature of the process, the errors cannot be diagnosed and compensated for as with other CNC machine tools [10]. Instead numerical simulations can be used to define tolerances on the machines motion and positioning accuracies. However, they cannot be used as a diagnosis tool to identify the errors present a posteriori. Figure 5.12 is the result of a simulation run with the virtual removal function subjected to shifts Δx and Δy of 1 and 0.75 mm, respectively. The resulting profile conserves the main features of the reference profile and with a

0.2 μm translation. Assuming that this offset was detected, its origin could easily be mistaken for a change in amplitude of the removal function.

5.3 Midspatial frequency errors and diagnostic of induced spiral marks

Midspatial frequency errors or tool marks are caused by relative vibrations between the tool and workpiece. Such errors are responsible for a degradation of the achievable resolution of imaging systems [11]. These marks have been previously investigated in ring tool [1] and contour grinding [1, 2, 3]. The plano parts polished to investigate the occurrence of midspatials with UFF were initially ring tool ground. Tool marks generated by ring tool grinding appear as curves following contact lines between the tool and workpiece. The number of tool marks usually correlates with the k ratio, which is the ratio of the tool spindle to the work spindle speed [1]. Aspheres are typically contour ground. Tool marks generated by contour grinding can be categorized into annular rings, chatter marks and most noticeably spirals [1]. The amplitude of these marks can be reduced or increased by adjusting the grinding parameters and the intrinsic stiffnesses of the tool and machine. Since the relative vibration between the grinding tool and the workpiece cannot be eliminated, such marks will always occur during grinding. UFF was shown to efficiently remove tool marks induced by grinding [12]. This desired benefit could be greatly reduced if the UFF tool induced significant midspatials of its own. Therefore, it is important to understand the potential sources of UFF tool marks in order to reduce their amplitude as much as possible. Such marks have been measured and a diagnostic method has

been developed to find their origin. It relies on a simple model, a simulation tool and a method for the evaluation of the frequency inducing the observed marks.

5.3.1 Experimental procedure and characterization of the induced marks

Three ring tool ground BK7 flats were polished with UFF. Uniform removal of 5 μm was desired. Each part was polished at a different constant part rotational speed. Values used were 100, 300 and 500 rpm. The tool rotational speed was also kept constant such that the band was circulated at 1 m/s.

The parts polished at 100 and 500 rpm exhibited significant data dropout near the part center when measured with a Zygo GPI interferometer [8]. Only the part polished at 300 rpm could be fully measured with that interferometer. This measurement is shown in Figure 5.13.a). The form exhibits a peak to valley error of 0.26 μm and is dominated by concentric rings that could be reduced in subsequent form correction runs. However, careful examination of the part near its center reveals a series of about 15 curved marks. They are not clearly visible as their amplitude is significantly lower than that of the features dominating the topography of the part. The full extent of these marks and the underlying pattern is revealed with the use of the high pass average filter built-in the Zygo MetroProTM software [13]. A filter window size of 3 equivalent to a cutoff frequency of 2 mm^{-1} was set. The filtered data are shown in Figure 5.13.b). The marks take the form of 12 spirals emanating from the part center and curving counterclockwise. The degree of curvature of these spirals proves that these spirals were not introduced by the grinding process. Their amplitude

is rather low, on the order of 30 nm, but it is desired to reduce them further because of their negative impact on imaging systems.

Furthermore, the observed pattern is sensitive to the polishing parameters. The parts polished at 100 and 500 rpm could not be fully measured, but the spirals could be visually observed near the part center. They also appear highlighted on the part intensity map captured with the interferometer. This map is a picture of the part on which the interference fringes are visible. These maps were overlapped with the interferometric measurements, which provide lateral scales for the images. The composite images, shown in Figure 5.14, reveal the pattern in the part center region and away from it. A single spiral and five clockwise spirals are observed on the part polished with work rotational speed equal to 500 and 100 rpm, respectively.

5.3.2 Model for the generation of the marks and simulation tool

Spiral marks have been observed in contour grinding [1, 3, 14, 15] and diamond turning [16-17]. These artifacts are due to tool vibrations occurring at a constant frequency. Irregularly spaced spirals are explained by the simultaneous occurrence of multiple vibrations [17]. In contour grinding, the source is typically the constant rotational frequency of the grinding wheel [1, 3, 14, 15].

Because of the similarities in process geometries, the use of constant tool rpm and the similarity in pattern, it is also hypothesized that the pattern induced by UFF is formed of marks occurring at constant time intervals. With this model, the problem of finding the origin of these marks consists in establishing the mark frequency, f_{marks} ,

creating the observed pattern. For that purpose, a simulation tool has been developed. It consists of a code written with MATLAB [18]. It takes for input the actual tool path file that is executed on the CNC platform and the simulated frequency. The code computes and displays the marks' locations on the surface of the workpiece.

These computations are based on the structure of the tool path file and the manner in which the commands are executed. The tool path file is composed of lines of commands. The j^{th} line of the file includes

$$y_j \quad \Delta t_j \quad rpm_j \quad (5.1)$$

and defines step j , which consists of the y location, y_j to reach within the given time, Δt_j , with the part rotating at rpm_j . The control specifies constant tool crossfeed velocities, v_{c_j} , and part rotational speed over a step. Because the change in tool crossfeed velocity and part rotational speed for each step is small, it is assumed for the simulations that the time necessary to adjust these parameters from one step to the next is negligible. Therefore, the part rotational speed and tool crossfeed velocity are assumed to be piecewise constant functions of y . Furthermore, for flats,

$$v_c = \frac{dy_{tool}}{dt} \quad \text{and} \quad rpm = -\frac{60}{2\pi} \frac{d\theta_{part}}{dt}, \quad (5.2)$$

where θ_{part} is the angular position of the part in radians and the negative sign is due to the clockwise rotation of the part. y_{tool} and θ_{part} , the tool y and part angular positions, respectively, are piecewise linear functions of time as illustrated in Figures 5.15. At $t = t_0 = 0$, the part is at an angle equal to 0 and, because of the symmetry of the tool

path with respect to the part center, the tool is positioned at $y = -y_{\max}$, where y_{\max} is the extreme y position reached by the tool. y_{tool} and θ_{part} are defined as follows

$$t_j = \sum_{k=0}^j \Delta t_k$$

$$\Delta t_0 = t_0 = 0, \quad y_{tool}(t_0) = -y_{\max} \text{ and } \theta_{part}(t_0) = 0$$

$$\text{For} \quad t_j < t \leq t_{j+1}, \quad (5.3)$$

$$y_{tool}(t) = v_{cj}^* (t - t_j) + y_{tool}(t_j) \quad \text{and} \quad \theta_{part}(t) = -rpm_j \frac{2\pi}{60} (t - t_j) + \theta_{part}(t_j),$$

where j is a positive integer not exceeding the number of lines of the tool path file.

Taking the part as reference frame, the position of the tool in polar coordinates, is described by

$$(r_{tool}(t), \theta_{tool}(t)) = (|y_{tool}|, -\theta_{part}(t)), \quad (5.4)$$

where r_{tool} and θ_{tool} are the tool radial and angular coordinates.

These equations define the spiral followed by the tool on the part. Assuming that marks occur at a constant frequency f_{marks} , and that the first mark occurs at $t = 0$, the marks are expected to be left on the part surface at the times

$$t_i^* = 0, 1/f_{\text{marks}}, \dots, i/f_{\text{marks}}, \dots, i_{\max}/f_{\text{marks}} \text{ (in seconds, with } f_{\text{marks}} \text{ in Hz),} \quad (5.5)$$

where i is a positive integer and i_{\max} is such that $(i_{\max}+1)/f_{\text{marks}}$ is greater than the polishing time. Therefore, the locations of the marks in polar coordinates are given by

$$(r_{tool}(t_i^*), \theta_{tool}(t_i^*)), \quad i = 0, 1, \dots, i_{\max}. \quad (5.6)$$

These equations only compute the location of the predicted marks, which can be represented by points placed at the coordinates defined by Eq. (5.6). This model is

sufficient to simulate the number and the curvature of the observed spirals. However, this model will not provide insights into the mark formation mechanism and in particular the change in width of the spiral and the transition between marks being visible or not on the part surface. These aspects can be observed in Figure 5.13.b). To deepen the understanding of the observed patterns, options have been added to the simulation code. They offer the ability to represent the marks as scratches with length constant or corresponding to a constant scratching time. In the case of constant length scratches, the predicted point is replaced by a segment of the given length. This segment can be drawn either in the radial direction or perpendicular to it. For a constant scratching time, the point is replaced by the section of the spiral followed by the tool during that scratching time centered at the predicted point.

Under normal conditions, the tool traverses the part from edge to edge through the part center. During a typical polishing pass, 1 to 20 μm of material are removed. Therefore, during each half of the tool path, part edge to center and center to edge, 0.5 to 10 μm are removed and residual marks are induced, but their amplitude is on the order of 30 nm or 0.03 μm . Therefore, the marks induced during the first half of the tool path are removed during the second half of the tool path. Only the marks induced during the second half are then visible on the part surface at the end of the pass. Therefore, only the marks predicted during that period are plotted by the simulator.

5.3.3 Evaluation of candidate frequencies and simulations

Candidate frequencies potentially responsible for the observed spiral patterns were calculated and measured by evaluating potential and actual vibrations frequency present on the tool.

Candidate frequencies can be calculated from the potential periodic sources of error, including the carrier wheel ball bearing and the band splice. The frequencies associated with ball bearings are well known [19, 20]. Six frequencies including the wheel rotational frequency are determined by the number of balls N , their diameter Bd , the pitch diameter Pd , the contact angle γ , and the carrier wheel rotational speed rpm_w . Bd , Pd and γ are defined in Figure 5.16. Variable names and descriptions of the frequencies are summarized in Table 5.4. They are evaluated with the following expressions [19, 20]

$$f_0 = \frac{rpm_w}{60}, \quad (5.7)$$

$$f_1 = \frac{N}{2} \frac{rpm_w}{60} \left(1 - \frac{Bd}{Pd} \cos(\gamma) \right), \quad (5.8)$$

$$f_2 = \frac{N}{2} \frac{rpm_w}{60} \left(1 + \frac{Bd}{Pd} \cos(\gamma) \right), \quad (5.9)$$

$$f_3 = \frac{Pd}{2Bd} \frac{rpm_w}{60} \left(1 - \frac{Bd^2}{Pd^2} \cos^2(\gamma) \right), \quad (5.10)$$

$$f_4 = \frac{Pd}{Bd} \frac{rpm_w}{60} \left(1 - \frac{Bd^2}{Pd^2} \cos^2(\gamma) \right), \quad (5.11)$$

$$f_5 = \frac{1}{2} \frac{rpm_w}{60} \left(1 - \frac{Bd}{Pd} \cos(\gamma) \right). \quad (5.12)$$

The polishing belt is also a potential source of marks. The belt is originally a band of material that is transformed into a belt by splicing its ends together. For this operation, a small piece of cloth is glued to the two ends of the band. A region, slightly thicker than the rest of the band and about 2 cm long, is thus created. This region is expected to leave a signature or mark on the part when they come into contact. Therefore, the frequency of passage of the band splice on the part, f_6 , is a candidate for the observed patterns. The rotational frequency of the band is given by

$$f_6 = \frac{v_{band}}{L}, \quad (5.13)$$

where L and v_{band} are the length and velocity of the band, respectively.

The frequencies of the actual tool vibrations were measured with a PCB Piezotronics [21] accelerometer [22] placed on the tool shaft at about 10 cm from the carrier wheel with the tool subjected to the same conditions as during polishing. No significant peaks were revealed in the z direction, normal to the part. However, peaks in the x and y directions were measured, as shown in Figure 5.17. Because of the slender geometry of the shaft, it is more prone to transverse than longitudinal motions. A peak, f_{peak1} , is measured consistently in the x and y directions at 8.69 Hz. A second peak, f_{peak2} , of lower amplitude is also measured in the x direction at 15.69 Hz. The third peak measured at 17.38 Hz is the second harmonic of the signal whose fundamental frequency is f_{peak1} .

The candidate frequencies, both calculated and measured, are summarized in Table 5.5. The frequencies f_0 through f_6 were calculated with $L = 1,500$ mm, $v_{\text{band}} = 1$ m/s, $N = 7$, $Bd = 4$ mm, $Pd = 16$ mm, $\gamma = 0$ and $rpm_w = 500$. It can be seen that the frequencies cover a range from 0.67 to 36 Hz corresponding to the band splice and outer race defect frequencies, respectively. The range between these extrema is reflected in the third column of Table 5.5, which indicates the number of marks induced on the part for the second half of a 20 minutes pass. The total number of marks varies between 402 and more than 50 times this value. The measured vibration frequencies, f_{peak1} and f_{peak2} , are within 5 % of the carrier wheel's rotational frequency f_0 and ball defect frequency f_3 , respectively. Therefore, from these two sets of frequencies, approximately equal to 8 and 16 Hz, one set should likely be the frequency, f_{marks} , at which the marks are left on the workpiece.

It was expected that one of the candidate frequencies summarized in Table 5.5 would result in a close agreement between actual patterns and simulations. That frequency would then approximately indicate the value of f_{marks} responsible for the observed patterns. Simulations were run with the 9 candidate frequencies with the process conditions under which the 12 spirals of Figure 5.13.b) were created. However, as shown in Figure 5.18, they all fail to predict that pattern. Even the number of spirals does not match those of Figure 5.13.b) for any of the simulations. The simulated pattern is very sensitive to the value of f_{marks} , as illustrated by the simulations with f_0 and f_{peak1} , Figures 5.18.c) and d). The difference between the values of these frequencies is less than 5%, but the corresponding simulations differ

greatly. Because of this sensitivity, predictions and actual patterns may differ only because of a slight calibration error on the machine, such as the part rotational speed being off by a couple of rpm.

Simulations show that the calculated frequencies can not be used to match the observed pattern, but they are useful in giving a physical meaning to certain frequency domains. When a measured and a calculated frequency have similar values, a likely source of marks is found. However, as in the present case, it can occur for several calculated frequencies. Therefore, it is desirable to establish the precise value of f_{marks} needed to create an observed pattern using the simulation tool. Agreement between that needed frequency, calculated and measured frequencies would indicate the source of the observed marks.

<i>Frequency name</i>	<i>Description</i>
f_0	carrier wheel rotational frequency
f_1	defect on outer race
f_2	defect on inner race
f_3	ball defect
f_4	rolling element defect
f_5	fundamental train frequency

Table 5.4 Variable names and descriptions of the calculated candidate frequencies.

<i>Case</i>	<i>Frequency (Hz)</i>	<i>Number of marks*</i>
f_0	8.3	4,980
f_1	22	13,200
f_2	36	21,600
f_3	16	9,600
f_4	31	18,600
f_5	3.1	1,860
f_6	0.67	402
f_{peak1}	8.69	5,210
f_{peak2}	15.7	9,410

Table 5.5 Values of the calculated and measured frequencies and corresponding number of marks (*for half of a 20 mins run).

5.3.4 Establishing the values of f_{marks} generating a given pattern

Similar spiral marks are observed in contour grinding [1, 3, 14, 15] and diamond turning [16-17]. These patterns are commonly described as a function of the so-called k ratio [1, 2] or frequency ratio [16] defined as

$$k = f_{\text{marks}}/f_{\text{part}}, \quad (5.14)$$

where f_{part} is the rotational frequency of the part. Kim et al. [16] interpret the k ratio as

$$k = m + \mu, \quad (5.15)$$

where m is an integer equal to the number of spirals and μ a curvature term, such that

$$-0.5 \leq \mu < 0.5. \quad (5.16)$$

If μ is equal to 0, the curvature is zero and the lines are radially outward as seen in Figure 5.18.c). A change in the sign of μ implies a change in the curvature of the spirals from clockwise to counterclockwise or vice versa. Eqs. (5.14) and (5.15) lead to

$$f_{\text{marks}} = (m + \mu) * f_{\text{part}}. \quad (5.17)$$

For example, in order to observe 3 spirals, m must be set equal to 3 and some curvature can be introduced by setting μ equal to 0.01. For a part rotating at 300 rpm, $f_{\text{part}} = 5$ Hz and the corresponding f_{marks} is evaluated at 15.05 Hz with Eq. (5.17). The 3 spirals were confirmed with a simulation run at that frequency with $f_{\text{part}} = 5$ Hz and using the tool path file used to polish the part of Figure 5.13. The predicted pattern is shown in Figure 5.19.a).

A major limitation to this approach is that it only establishes the maximum frequency, $f_{\text{marks-max}}$, that will create a given pattern. Other frequencies that create the same pattern may also exist. They are the frequencies which adequately sample the marks left at the frequency $f_{\text{marks-max}}$ so that the pattern is preserved. For example in the case of the 3 spirals obtained with $f_{\text{marks-max}}$ equal to 15.05 Hz in Figure 5.19.a), the frequency $f_{\text{marks}} = f_{\text{marks-max}} / 2$, will induce only half of the marks but generate the same 3 spirals pattern as shown in Figure 5.19.b). The corresponding k ratio is 1.505 and can no longer be interpreted according to Eq. (5.15). Eqs. (5.15) through (5.17) are valid if f_{marks} is equal to $f_{\text{marks-max}}$. Therefore, it is preferable to rewrite Eq. (5.17) as

$$f_{\text{marks-max}} = (m + \mu) * f_{\text{part}}. \quad (5.18)$$

The use of Eq. (5.18) to evaluate the maximum frequency that can create a pattern with a desired number of spirals requires the knowledge of the value of μ that will produce the curvature of the observed pattern. If the tool traverses the part at a constant crossfeed velocity, the equations derived by Yoshihara et al. [15] can be

used to calculate exactly $f_{\text{marks-max}}$ without having to consider μ . However, for UFF the tool crossfeed velocity is varied to obtain the desired figure correction. Furthermore, if a constant tool crossfeed velocity is used for experimental purposes, the figure of the part will be degraded making its measurement difficult. For spirals generated while polishing with a tool path computed by the form correction algorithms, a trial error method is used to determine μ , according to the following steps:

- i) Calculate $f_{\text{marks-max}}$ creating the number of segments equal to the number of observed spirals, with μ equal to 0 in Eq. (5.18).
- ii) Run the tool marks simulator with $f_{\text{marks-max}}$ obtained for a small positive and a small negative value of μ such as 0.01 and -0.01 to find the sign that will produce the desired clockwise or counterclockwise curvature.
- iii) Use small increments to modify μ until the simulated spirals exhibit the desired degree of curvature, while satisfying Eq. (5.16).

The frequencies other than $f_{\text{marks-max}}$ that produce the same spiral pattern also need to be established. These frequencies are of the form

$$f_{\text{marks}}(q) = f_{\text{marks-max}}/q, \quad (5.19)$$

where q is a positive integer greater than 1. The sampling problem consists in finding all possible values of q , such that $f_{\text{marks}}(q)$ produces the same pattern as $f_{\text{marks-max}}$.

The first criterion for identifying a valid value of q is that q must be small enough so that a sufficient number of marks are generated to form the desired pattern.

A large q would mean few induced marks and because of the large gaps between them, their combination would not resemble the desired pattern. This situation would not correspond to an adequate sampling of the original pattern. The first criterion is subjective and requires simulations to visually determine the relevant frequencies.

In addition, q cannot take all the values between 2 and the maximum value defined by the first criterion. For instance, some values of q would inappropriately sample the initial pattern. A simple example using a pattern consisting of $m = 4$ segments with $\mu = 0$, shown in Figure 5.20, will be used to illustrate this restriction. The segments are numbered from 1 to 4. With the part rotating counterclockwise and assuming that the part is the frame of reference, the rotation of the part is equivalent to a clockwise rotation of the tool over the part. $f_{\text{marks-max}}$ is such that if m spirals are formed, a mark is left on each of these spirals at every rotation of the part. Therefore, in the present case, if $q = 1$, marks are left on each of the 4 segments in the order 1, 2, 3, 4 during one rotation of the part. If q is equal to 2, marks are only left on every other segment, this means that during the first part rotation, marks are left on segments 1 and 3. Continuing with the subsequent part rotations, marks will systematically be left only on these 2 segments. Therefore, 2 is not an appropriate value for q in this case since it does not generate all 4 segments. On the other hand, q equal to 3 would imply marks left consecutively on segments 1, 4, 3, 2, 1, 4, 3, 2, and so on. Therefore, 3 would be a suitable value for q . This example illustrates that m consecutive marks must be left on the m spirals without giving any importance to the order in which they occur. This is the second criterion for valid values of q .

The second criterion is addressed by examining the position of the marks for given q and m , in the case where segments are generated. For that purpose, the angular spacing, $\Delta\theta$, between two consecutive marks is considered. $\Delta\theta$ for marks left at the frequency $f_{\text{marks}}(q)$ is given by

$$\Delta\theta = \frac{q \times 2\pi}{m}. \quad (5.20)$$

To form an m segments pattern, it is necessary to create consistent series of m consecutive marks on each of the m segments. Therefore, assuming that the first mark is left on the part at $\theta = 0$, it is required that the $(m+1)^{\text{th}}$ mark be left at that same angle. This implies that the $(m+1)^{\text{th}}$ mark must be left at an angle $m \times \Delta\theta$ equal to 0 modulo 2π . Eq. (5.20) implies that q must satisfy

$$q \times 2\pi = 0 \pmod{2\pi} \quad (5.21)$$

and must therefore be an integer. Furthermore, the first m consecutive marks are left at the angles $\theta_{M1}, \theta_{M2}, \dots, \theta_{Mm}$, such that

$$\theta_{Mj} = (j-1) \frac{q \times 2\pi}{m} \quad (5.22)$$

where j is a positive integer denoting the j^{th} mark. In order to adequately sample the pattern created by $f_{\text{marks-max}}$, the first m marks must be left on the m segments. In particular, since the first mark is systematically assumed to be left at the segment located at $\theta = 0$, none of the following $m - 1$ marks can be left on that segment. This is the criterion defining the satisfactory values of q . It can be formulated as,

$$\theta_{Mj} \neq n \times 2\pi, \quad (5.23)$$

where n is a positive integer and $j = 2, 3, \dots, m$. Therefore, the adequate values of q are such that

$$q \neq \frac{n \times m}{j-1}. \quad (5.24)$$

Since q must be an integer, it can be concluded that the unsatisfactory values of q are the factors of m and their multiples.

Using the criteria described in the previous sections, the satisfactory values of q can be established. However, it can be noted that the appropriate frequencies correspond to k ratios either greater or less than 1. A k ratio is greater than 1 when f_{marks} is greater than f_{part} and in that case q is renamed Q , which is such that

$$1 \leq Q \leq m-1. \quad (5.25)$$

On the other hand, when q is greater than m , $f_{\text{marks}}(q)$ corresponds to a k ratio less than 1. Even though there are a large number of frequencies creating a given pattern, there are only a limited number of orders in which m consecutive marks can be left on the m segments to form the desired pattern. All of these possible orders are represented by the frequencies corresponding to k ratios greater than 1. Therefore, the frequencies corresponding to k ratios less than 1 can be obtained by intercalating complete parts rotations between the consecutive marks left on the segments at the frequencies corresponding to k ratios greater than 1. The frequencies corresponding to k ratios less than 1 are thus given by

$$f_{\text{marks}}(Q, n_{\text{rot}}) = \frac{1}{\frac{1}{f_{\text{marks}}(Q)} + \frac{n_{\text{rot}}}{f_{\text{part}}}}, \quad (5.26)$$

where n_{rot} is the number of complete part rotations intercalated between two consecutive marks. The denominator of Eq. (5.26) is the sum of the time between two consecutive marks for a frequency corresponding to a k ratio greater than 1 and the time necessary for the n_{rot} part rotations. Furthermore, f_{marks} must be of the form of Eq. (5.19) and by considering the case of m segments, which implies $\mu = 0$ and

$$f_{marks}(Q, n_{rot}) = \frac{1}{\frac{Q}{f_{marks-max}} + \frac{n_{rot} \times m}{f_{marks-max}}} = f_{marks-max} / (Q + n_{rot} \times m), \quad (5.27)$$

q can be expressed as

$$q = Q + n_{rot} \times m. \quad (5.28)$$

Therefore, Q is first established by determining the integers comprised between 2 and $m-1$, which are not factors of m or multiples of these factors. The frequencies corresponding to k ratios less and greater than 1 are then evaluated with Eqs. (5.19) and (5.28) for predetermined values of n_{rot} .

This method was applied to the calculation of the 8 largest frequencies consistently generating the 3 spiral pattern of Figure 5.19.a). The values of f_{marks} are summarized in Table 5.6. The two frequencies corresponding to k ratios greater than 1, were simulated in Figure 19. Eqs. (5.19) and (5.28) were used with $f_{marks-max} = 15.05$ Hz, $Q = 1$ and 2 and $n_{rot} = 1, 2$ and 3 to compute 6 frequencies corresponding to k ratios less than 1. Larger numbers of part rotations could be intercalated but it would result in very low frequencies. The marks' locations predicted with the frequencies reported in Table 5.6 are shown in Figure 5.21. All these simulations exhibit the same 3 spirals pattern at the part center. As f_{marks} and the

number of marks decrease, the sampled pattern can be interpreted as a different pattern. This is aliasing, which can occur in particular if the spirals are not identified near the part center like in Figure 5.21.e) where, for $f_{\text{marks}} = f_{\text{marks-max}}/8$, 38 potential spirals could be counted around the edge of the part.

Q	n_{rot}	$q(Q, j, m)$	f_{marks} (Hz)	k ratio	# of marks*
1	0	1	15.05	3.01	18,000
2	0	2	7.525	1.51	9,000
1	1	4	3.763	0.753	4,500
1	2	7	2.150	0.430	2,500
1	3	10	1.505	0.301	1,800
2	1	5	3.010	0.602	3,600
2	2	8	1.881	0.376	2,300
2	3	11	1.368	0.274	1,600

Table 5.6 Values of the frequencies creating the 3 spiral pattern of Figure 5.19 and corresponding number of marks (*for half of a 20 mins run).

5.3.5 Results for the experimentally observed spirals

The methods described in the previous section were applied to the case of the 12 spirals highlighted in Figure 5.13.b) and repeated in Figure 5.22.a) for convenience. For a part rotating at 300 rpm, the maximum frequency creating 12 segments is 60 Hz. Using trial error with the simulation tool it was determined that $\mu = -0.02$, so that $f_{\text{marks-max}}$ is equal to 59.9 Hz as illustrated in Figure 5.22. The 8 largest frequencies generating a consistent 12 spiral pattern are summarized in Table 5.7. Four frequencies correspond to k ratios greater than 1, for which q takes values 1, 5, 7 and 11. Four frequencies corresponding to k ratios less than 1 were computed

with $n_{rot} = 1$. Only the frequencies corresponding to k ratios greater than 1 were retained and plotted in Figure 5.23. It can be seen that $f_{marks-max}$ is greater than any of the calculated and measured frequencies. On the other hand $f_{marks-max}/5$, $f_{marks-max}/7$ and $f_{marks-max}/11$ are within the range of the calculated and measured frequencies. The second plot of Figure 5.23 shows that $f_{marks-max}/7$ falls within 3 % of the measured and calculated frequencies f_{peak1} and f_0 . While $f_{marks-max}/11$ and $f_{marks-max}/5$ are not close to any calculated or measured frequencies. This seems to indicate that a frequency of the order of $f_{marks-max}/7$, or 8.6 Hz, is responsible for the 12 observed spirals. Based on the calculated frequencies, this frequency corresponds to the carrier wheel rotational frequency.

This hypothesis is supported by the ability of that frequency to predict the patterns observed with two other part rotation speeds. These results are plotted in Figures 5.24 and 5.25 where the 5 and 1 spirals and their curvature are perfectly simulated at 100 and 500 rpm, respectively. Furthermore, a nearly invisible void was found on the carrier wheel that was produced by injection molding. This imperfection could create marks at the frequency $f_{marks} = f_0$. This error would be expected to produce consistent marks on the part. Using the options developed for the simulator, it was found that scratches on the part of constant length of 0.8 mm, oriented perpendicular to the radial direction, explain well the details of the spiral patterns in the three considered cases as shown in Figures 5.26, 5.27 and 5.28, for parts at respectively 300, 100 and 500 rpm. The change in width of the spirals near the part center and the ring-like pattern toward the edge of the part are well simulated. At 300

rpm, the relative disappearance of these spirals away from the part center is explained by the presence of significant gaps between the marks away from the part center region.

Q	n_{rot}	$q(Q, j, m)$	f_{marks} (Hz)	k ratio	# of marks*
1	0	1	59.9	11.98	72,000
5	0	5	11.98	2.40	14,000
7	0	7	8.557	1.71	10,000
11	0	11	5.446	1.09	6,500
1	1	13	4.608	0.922	5,500
5	1	17	3.524	0.705	4,200
7	1	19	3.153	0.631	3,800
11	1	23	2.604	0.521	3,100

Table 5.7 Values of the frequencies creating the 12 spiral pattern of Figure 5.13.b) and corresponding number of marks (*for half of a 20 mins run).

5.3.6 Summary of the diagnostic method for induced residual marks

A diagnostic method for the spiral marks induced by UFF and similar processes has been derived in the previous sections. That method, used in section 5.3.4, relies on a tool marks simulator, the measurement and calculation of candidate frequencies as well as the evaluation of all the frequencies generating the observed pattern. The source of the marks is identified by matching a frequency predicting the observed pattern and a measured and/or calculated frequency or by finding the frequency that consistently explains the patterns observed as process parameters, such as part rpm, are varied. The diagnostic method can be summarized with the following steps:

- i) Calculate and measure the candidate frequencies.
- ii) Identify the number of spirals m .
- iii) Calculate $f_{\text{marks-max}}$ for m segments, according to Eq. (5.18) with $\mu = 0$.
- iv) Use the trial-error method to find μ producing the right curvature and evaluate $f_{\text{marks-max}}$ for the m spirals, according to Eq. (5.18).
- v) Establish Q satisfying Eq. (5.25) and not Eq. (5.24).
- vi) Compute relevant frequencies with Eqs. (5.19) and (5.28).
- vii) Identify the actual frequency responsible for the observed pattern by matching one of the frequency established as predicting the observed pattern to a calculated frequency and/or by picking the frequency that consistently predicts the pattern while different values of part rpm are used.

5.4 References

- [1] Y. Li, "Surface errors in deterministic microgrinding of optical materials," Ph.D. thesis, 2000, University of Rochester.
- [2] S. Tong, "Chatter in contour deterministic microgrinding," Ph.D. thesis, 2004, University of Rochester.
- [3] J. Franse, "Aspects of Precision Grinding," Ph.D. thesis, 1991, Technische Universiteit Eindhoven.
- [4] D. W. Camp, M. R. Kozlowski, L. M. Sheehan, M. A. Nichols, M. Dovik, R. G. Raether and I. M. Thomas, "Subsurface damage and polishing compound affect the 355-nm laser damage threshold of fused silica surfaces," Laser-Induced Damage in Optical Materials, Proc. SPIE 3244, 356-364 (1998).
- [5] Zygo NewView™ 5000 white-light interferometer, Zygo Corporation, Laurel Brook Road, Middlefield, CT 06455-0448, Phone: 860-347-8506, www.zygo.com.

- [6] J. A. Randi, J. C. Lambropoulos, and S. D. Jacobs, "Subsurface damage in some single crystalline optical materials," *Applied optics* 44, 2241-2249 (2005).
- [7] J. C. Lambropoulos, Y. Li, P. D. Funkenbusch, and J. L. Ruckman, "Noncontact estimate of grinding-induced subsurface damage," *Optical Manufacturing and Testing III, Proc. SPIE* 3782, 41-50 (1999).
- [8] Zygo GPI phase-shifting laser interferometer, Zygo Corporation, Laurel Brook Road, Middlefield, CT 06455-0448, Phone: 860-347-8506, www.zygo.com.
- [9] TalySurf 2 PGI profilometer, Taylor Hobson Ltd, P.O. Box 36, 2 New Star Road, Leicester, LE4 9JQ, England, Phone: +44 116-276-3771, www.taylor-hobson.com.
- [10] H. C. Lee and G. J. Jeon, "Real time compensation of two-dimensional contour errors in CNC machine tools," *International Conference on Advanced Intelligent Mechatronics*, *Proc. IEEE/ASME*, 623-628 (1999).
- [11] J. E. Harvey and A. Kotha, "Scattering effects from residual optical fabrication errors," *International Conference on Optical Fabrication and Testing, Proc. SPIE* 2576, 155-174 (1995).
- [12] E. Fess, J. Schoen, M. Bechtold, D. Mohring, C. Bouvier, "UltraForm Finishing Processes for Optical Materials," *Optical Manufacturing and Testing VI, Proc. SPIE* 5869, 0F1-0F6 (2005).
- [13] Zygo MetroProTM software, Zygo Corporation, Laurel Brook Road, Middlefield, CT 06455-0448, Phone: 860-347-8506, www.zygo.com.
- [14] T. Kuriyagawa, N. Yoshihara, M. Saeki and K. Syoji, "Nano-topography characterization of axisymmetric aspherical ground surfaces," *Key Engineering Materials* 238-239, 125-130 (2003).
- [15] N. Yoshihara, T. Kuriyagawa, H. Ono and K. Syoji, "Nano-topography on axisymmetric aspherical ground surfaces," *International Journal of Manufacturing Technology and Management* 9, 51-63 (2006).
- [16] D. S. Kim, I. C. Chang and S. W. Kim, "Microscopic topographical analysis of tool vibration effects on diamond turned optical surfaces," *Precision Engineering* 26, 168-174 (2002).
- [17] W. B. Lee and C. F. Cheung, "A dynamic surface topography model for the prediction of nano-surface generation in ultra-precision machining," *International Journal of Mechanical Sciences* 43, 961-991 (2001).

[18] MATLAB R2007a (Version 7.4.0.287), The Mathworks Inc., 3 Apple Hill Drive, Natick, MA 01760-2098, Phone: 508-647-7000, www.mathworks.com.

[19] N. Tandon and A. Choudhury, "A review of vibration and acoustic measurement methods for the detection of defects in rolling element bearings," *Tribology International* 32, 469-480 (1999).

[20] Hewlett Packard, "Effective machinery measurements using dynamic signal analyzers," HP Application Note 243-1.

[21] PCB Piezoelectronics Inc., 3425 Walden Avenue, Depew, NY 14043-2495, Phone: 800-828-8840, www.pcb.com.

[22] Triaxial accelerometer model 356A12
http://www.pcb.com/contentstore/docs/PCB_Corporate/Vibration/products/Manuals/356A12.pdf. retrieved on October 10, 2007.

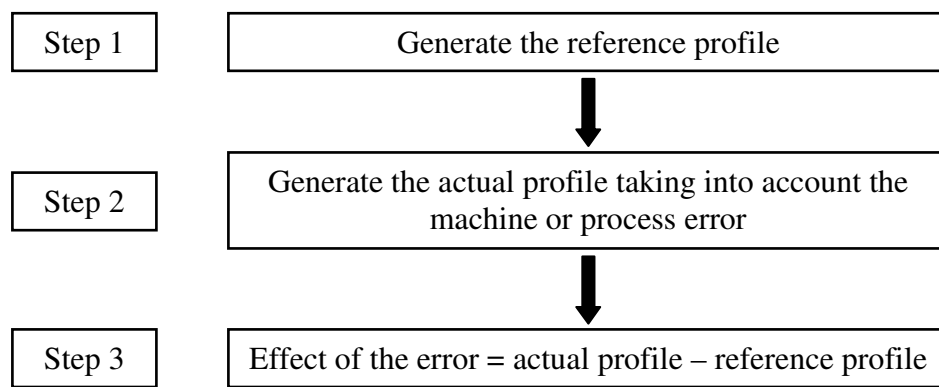


Figure 5.1 Principle of the numerical simulations.

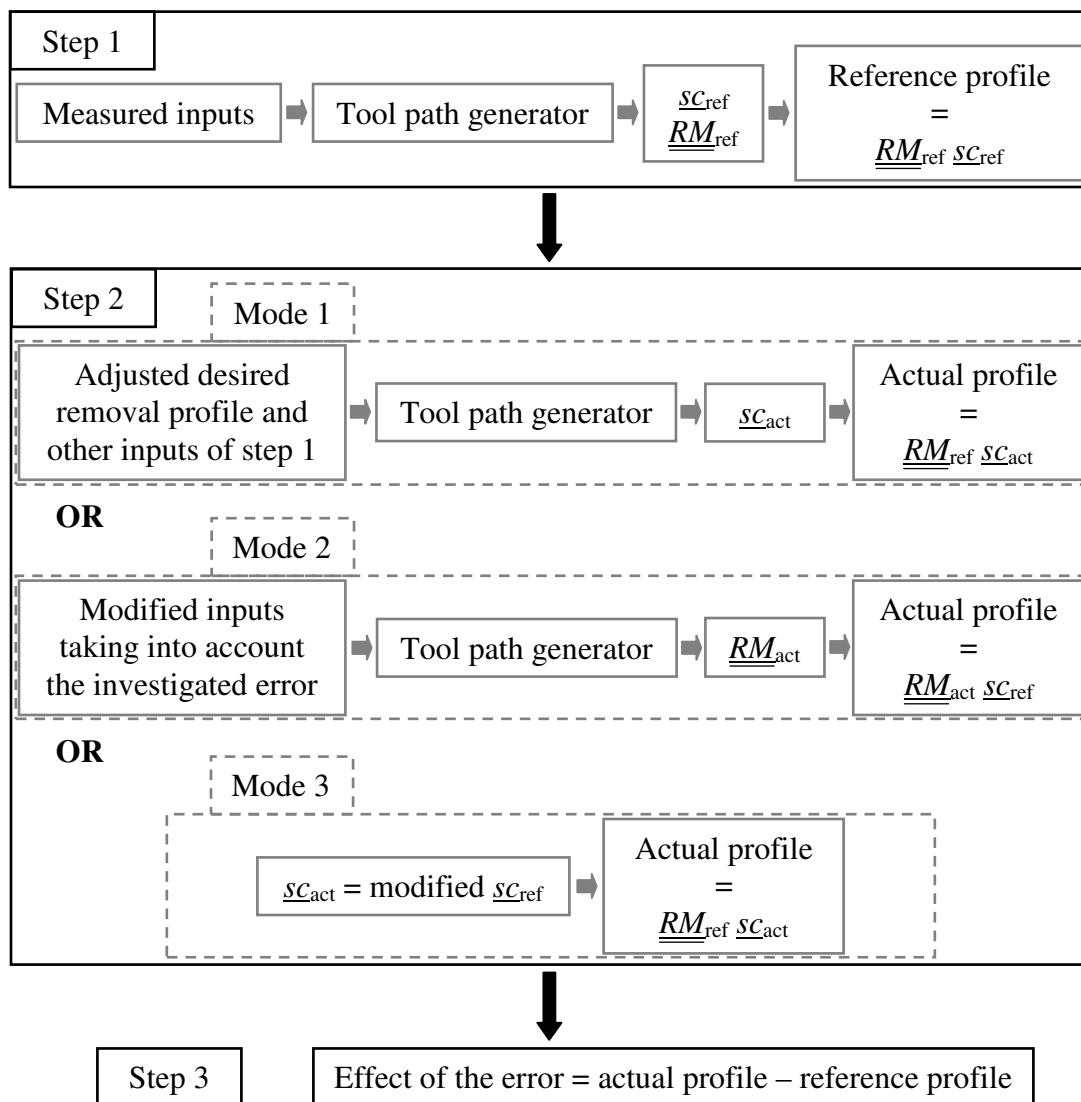


Figure 5.2 Detailed procedure for the numerical simulations.

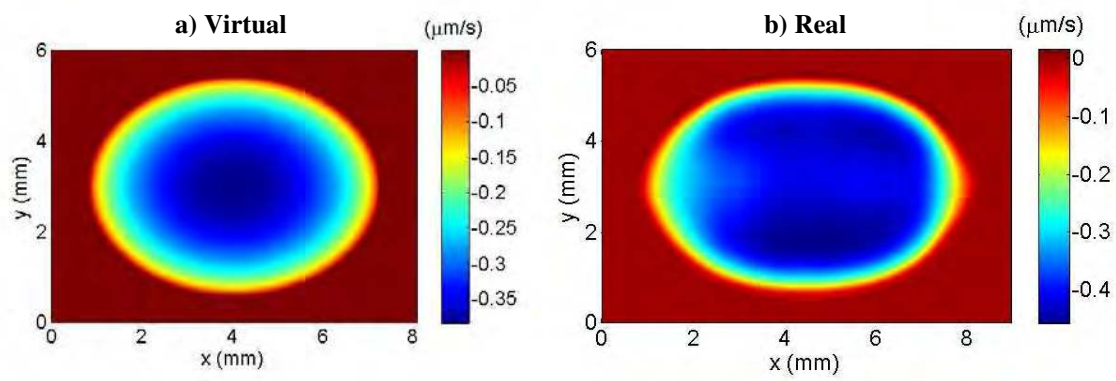


Figure 5.3 Static removal functions used for numerical simulations.

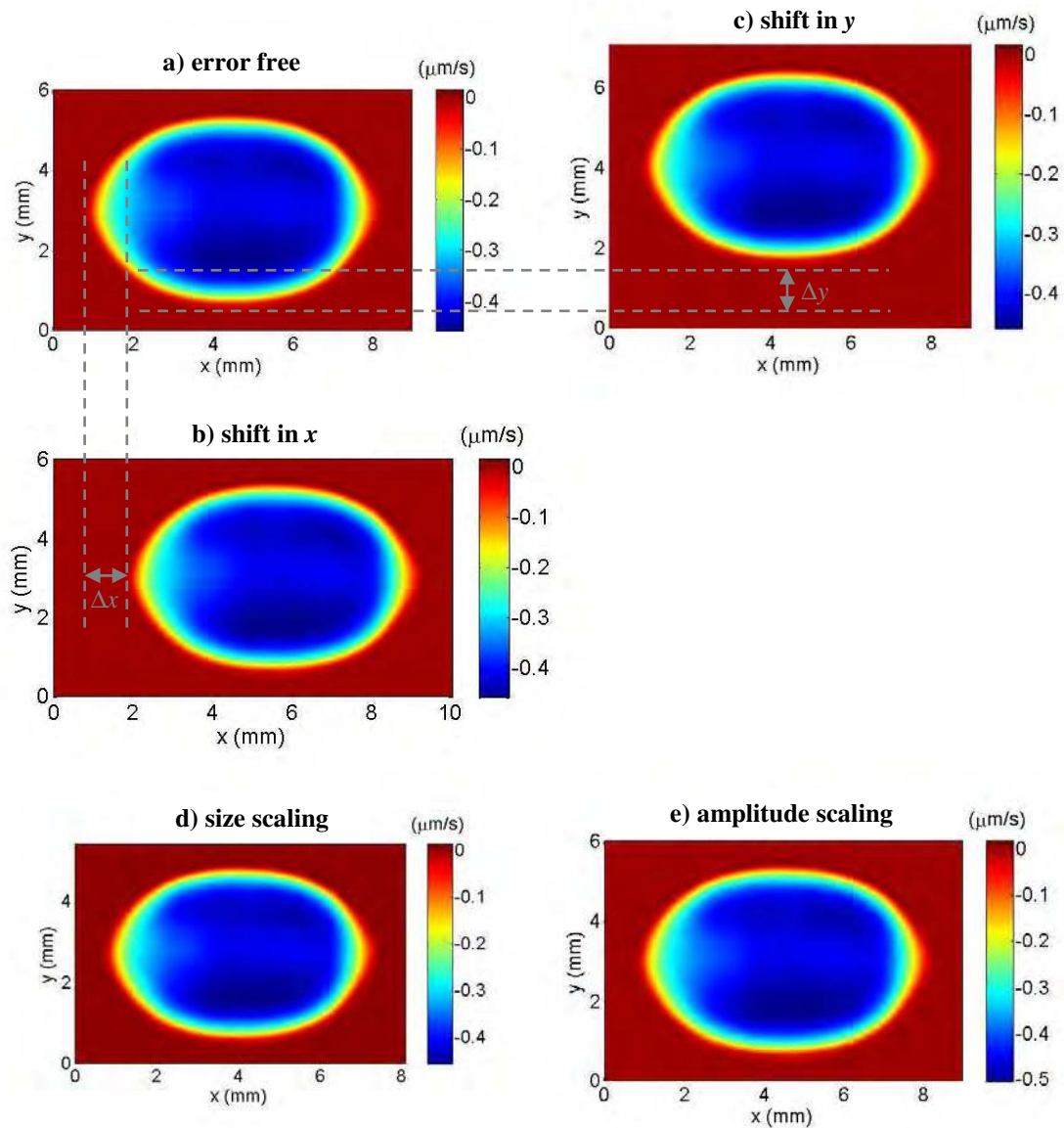


Figure 5.4 Error free removal function and induced alterations
 a) error free removal function;
 b) shift in x by $\Delta x = 1$ mm;
 c) shift in y by $\Delta y = 1$ mm;
 d) size scaling, new size is 0.9 times the original size;
 e) amplitude scaling, new amplitude is 1.1 times the original amplitude.

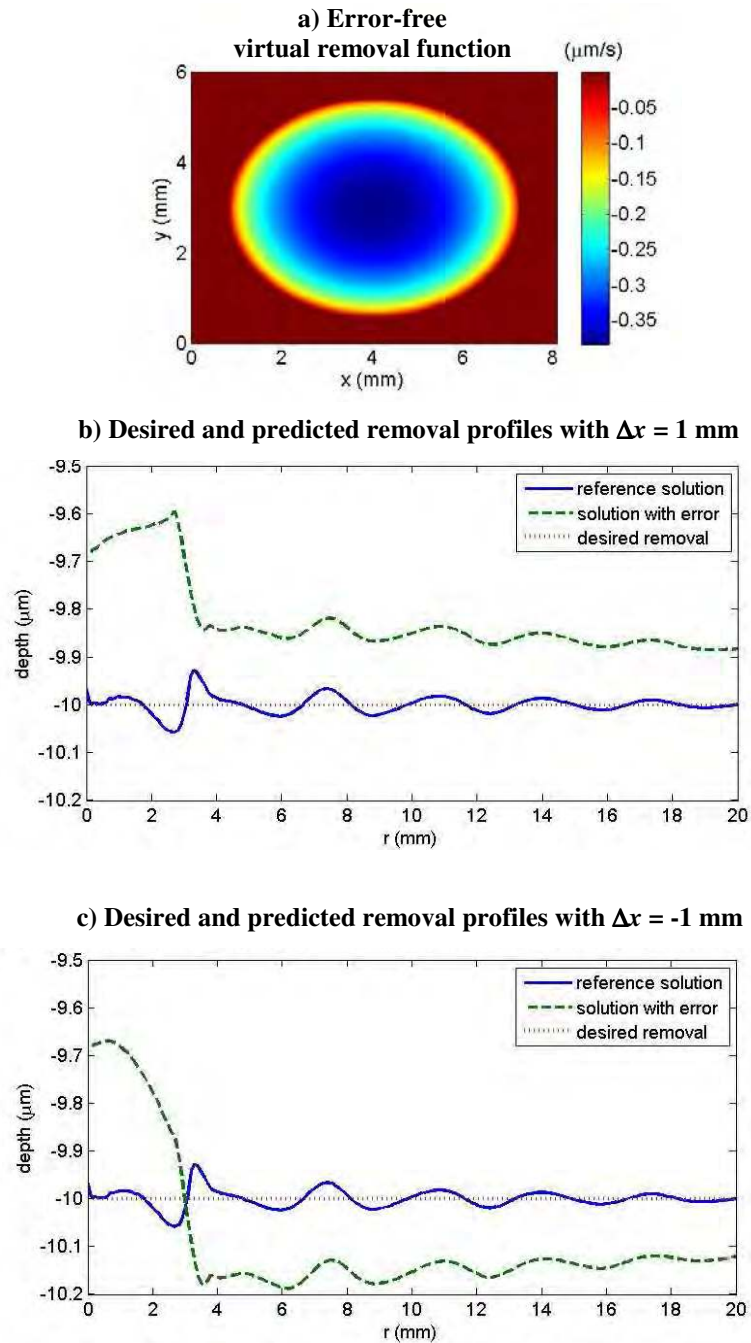


Figure 5.5 Effect of shifts in x of the elliptical Hertzian removal function
 a) error-free elliptical Hertzian removal function;
 b) desired, reference and actual profiles for $\Delta x = 1$ mm;
 c) desired, reference and actual profiles for $\Delta x = -1$ mm.

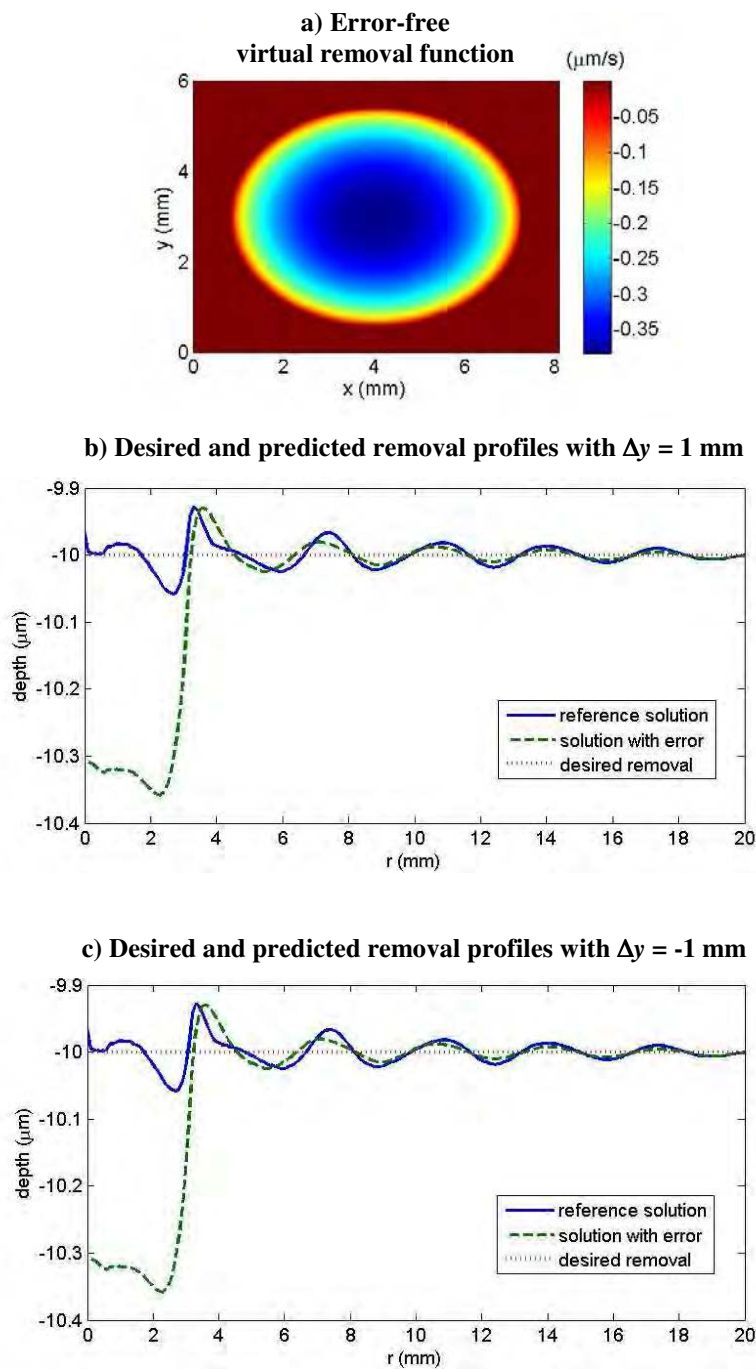


Figure 5.6 Effect of shifts in y of the elliptical Hertzian removal function
 a) error-free elliptical Hertzian removal function;
 b) desired, reference and actual profiles for $\Delta y = 1$ mm;
 c) desired, reference and actual profiles for $\Delta y = -1$ mm.

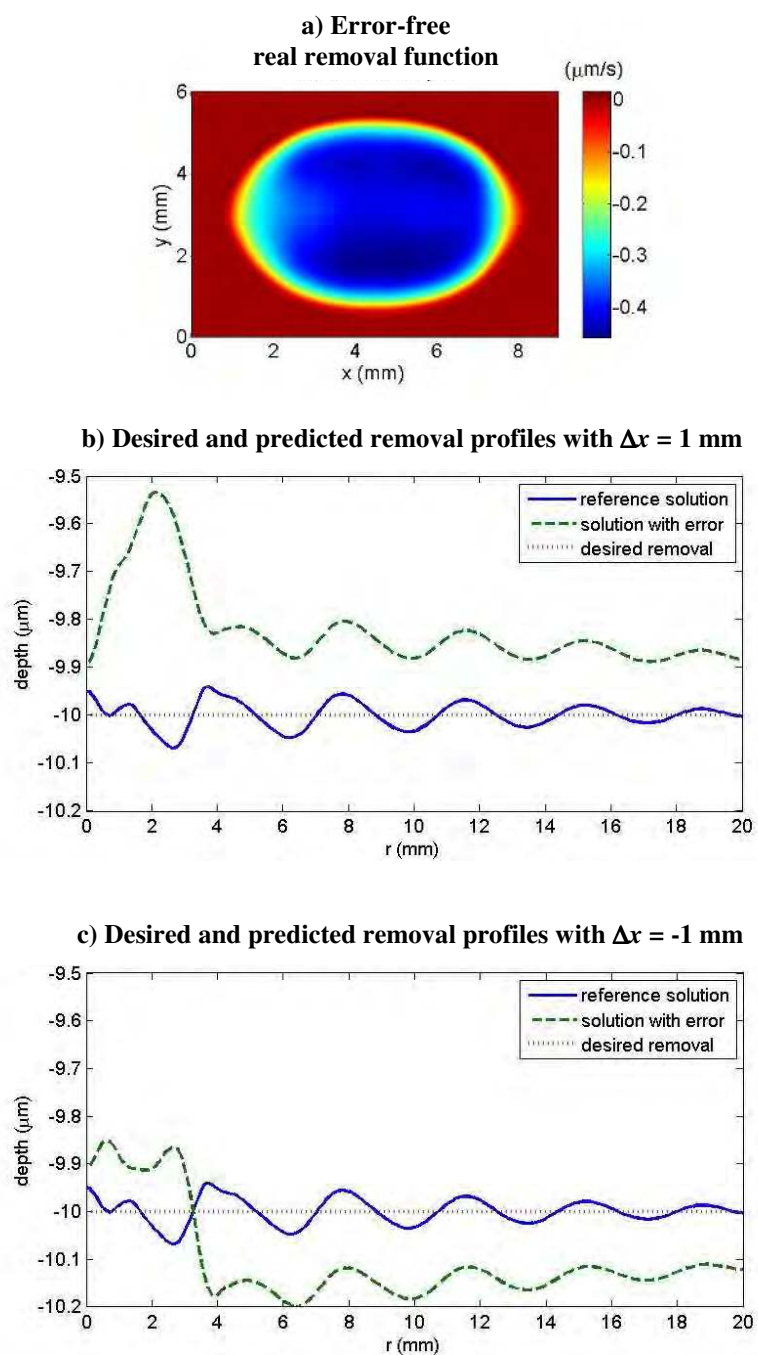


Figure 5.7 Effect of shifts in x of the real removal function
 a) error-free removal function;
 b) desired, reference and actual profiles for $\Delta x = 1$ mm;
 c) desired, reference and actual profiles for $\Delta x = -1$ mm.

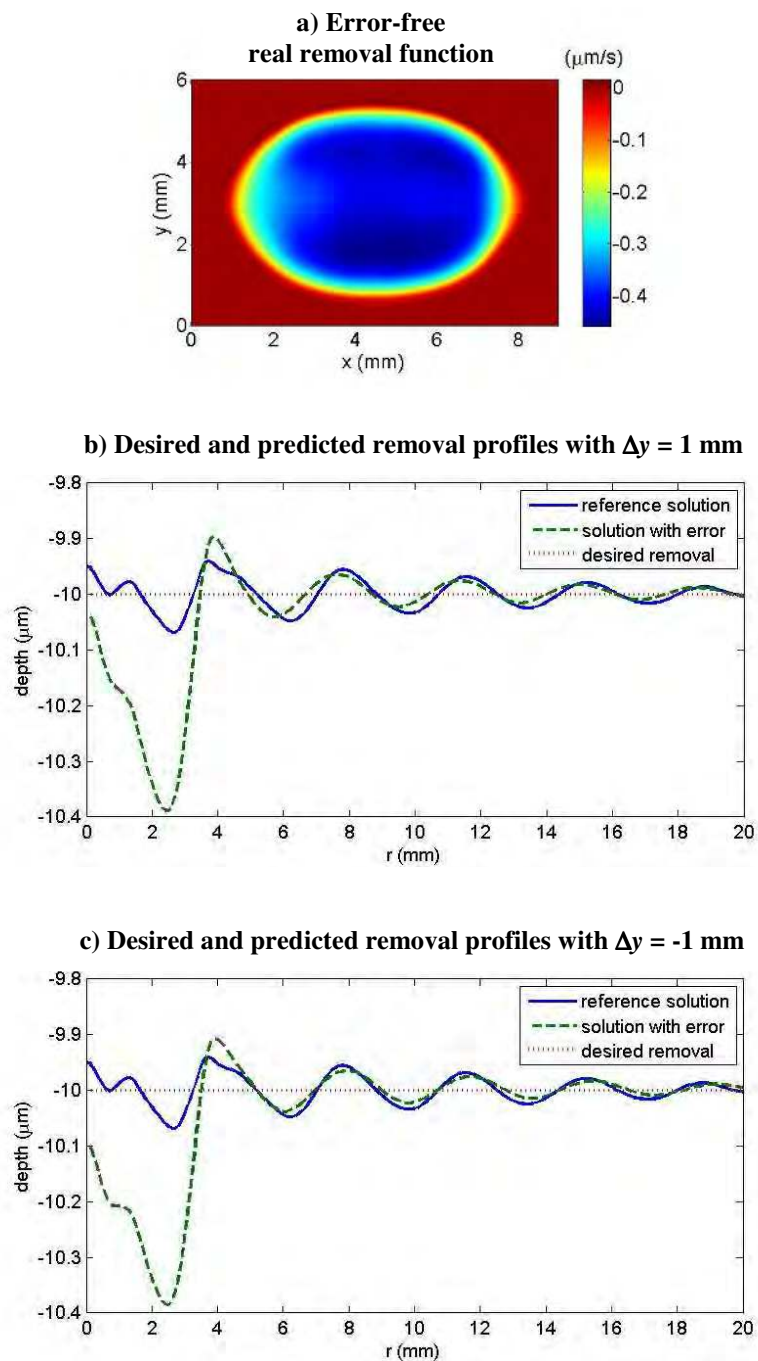


Figure 5.8 Effect of shifts in y of the real removal function
 a) error-free removal function;
 b) desired, reference and actual profiles for $\Delta y = 1$ mm;
 c) desired, reference and actual profiles for $\Delta y = -1$ mm.

Desired and predicted removal profiles with amplitude of the initial removal function multiplied by 0.9

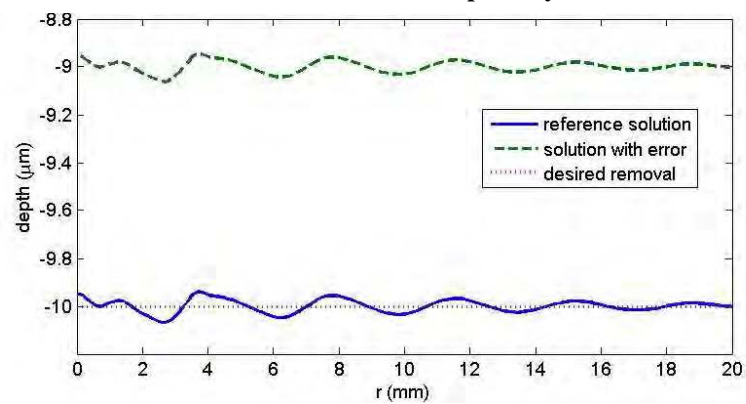
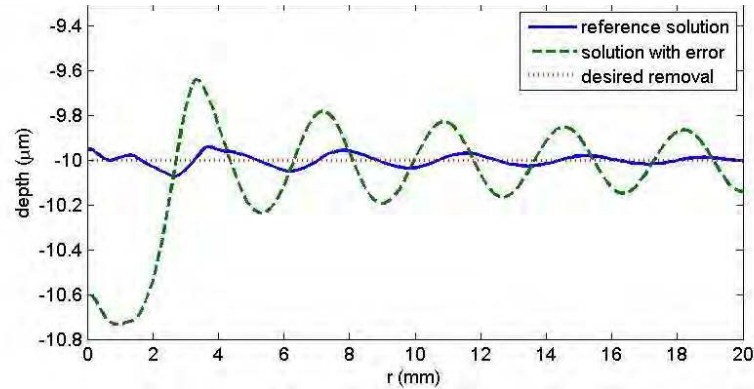


Figure 5.9 Effect of a change in amplitude of the removal function.

a) Desired and predicted removal profiles with size and amplitude of the initial removal function multiplied by 0.9 and 1.25, respectively



b) Desired and predicted removal profiles with size and amplitude of the initial removal function multiplied by 1.1 and 0.83, respectively

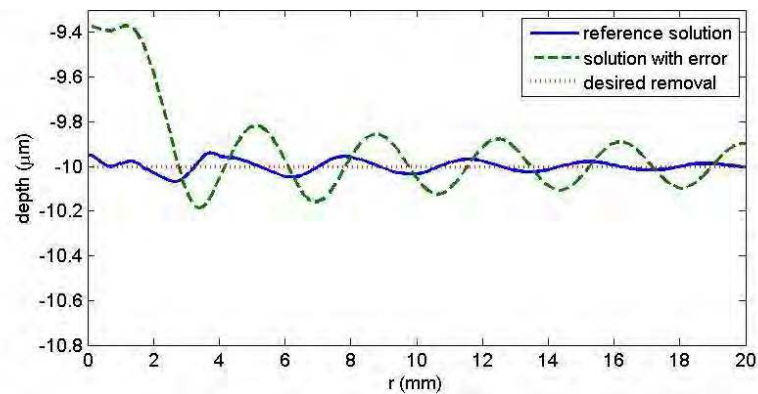


Figure 5.10 Effect of a change in size of the removal function while the volumetric removal rate is kept constant

- a) desired, reference and actual profiles with size and amplitude multiplied by 0.9 and 1.25, respectively;
- b) desired, reference and actual profiles with size and amplitude multiplied by 1.1 and 0.83, respectively.

Desired and predicted removal profiles with systematic clock error of 10 ms

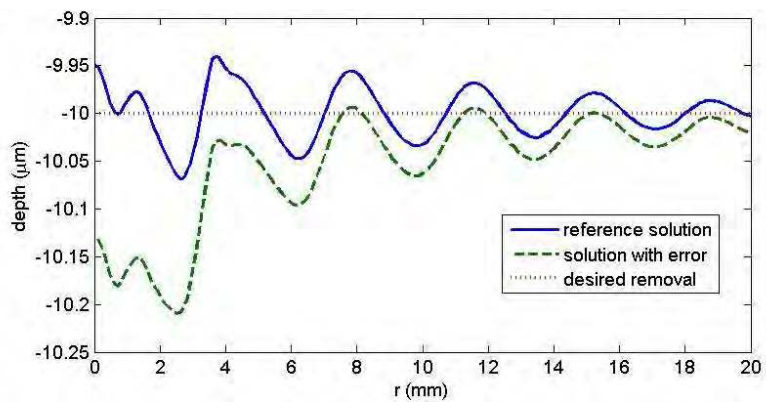


Fig. 5.11 Effect of a systematic clock error.

Desired and predicted removal profiles with $\Delta x = 1$ mm and $\Delta y = 0.75$ mm

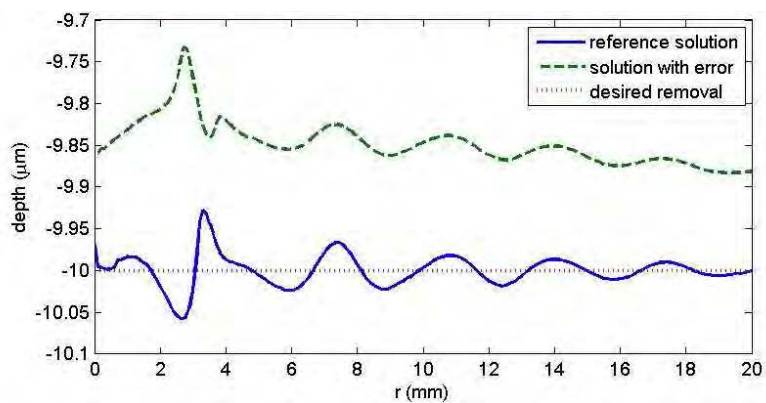


Figure 5.12 Effect of two simultaneous errors, $\Delta x = 1$ mm and $\Delta y = 0.75$ mm.

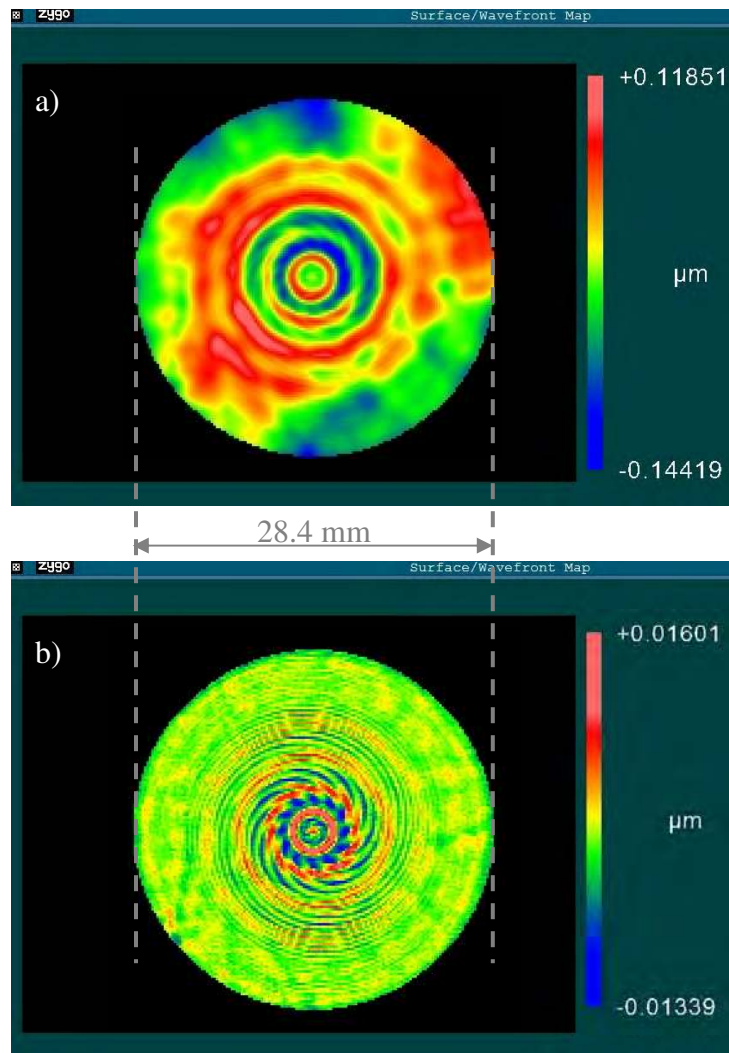


Figure 5.13 Raw and filtered measurement of part polished at 300 rpm
a) interferometric measurement.
b) after high pass average filtering.

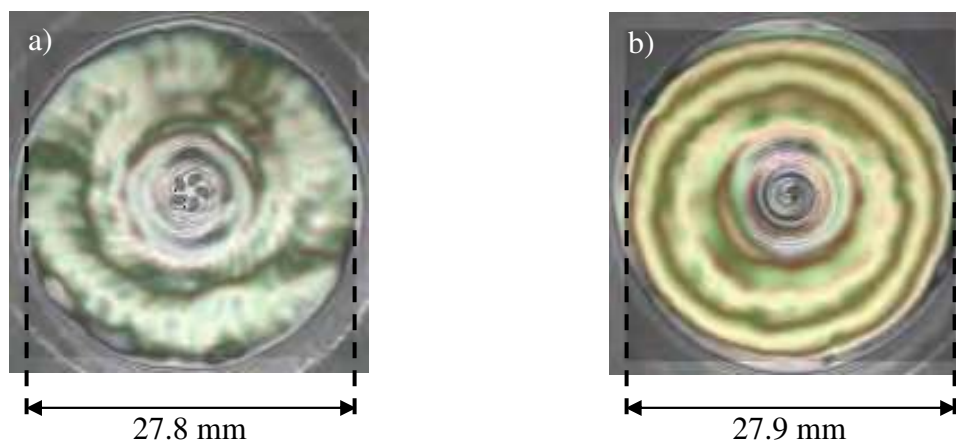


Figure 5.14 Composite images showing the induced marks at
 a) 100 part rpm;
 b) 500 part rpm.

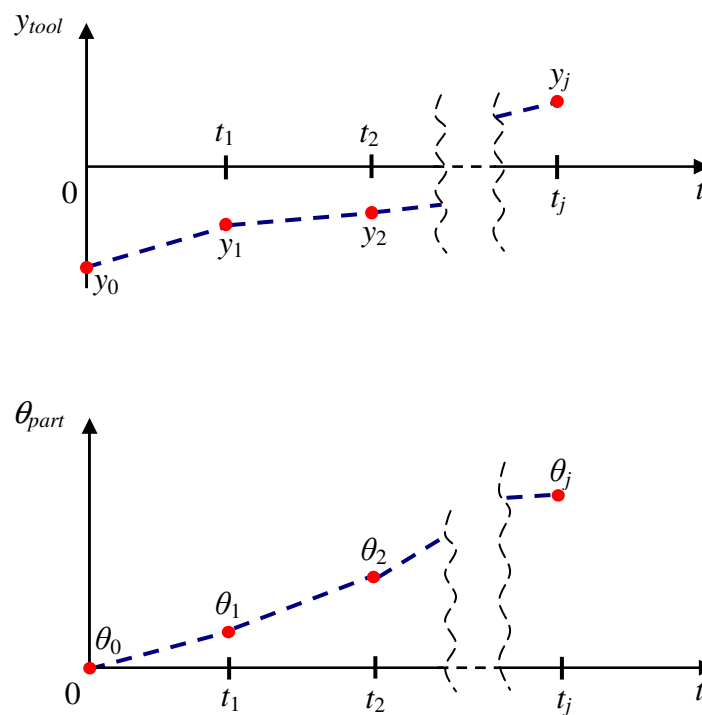


Figure 5.15 Piecewise linear functions for $r_{\text{tool}}(t)$ and $\theta_{\text{part}}(t)$.

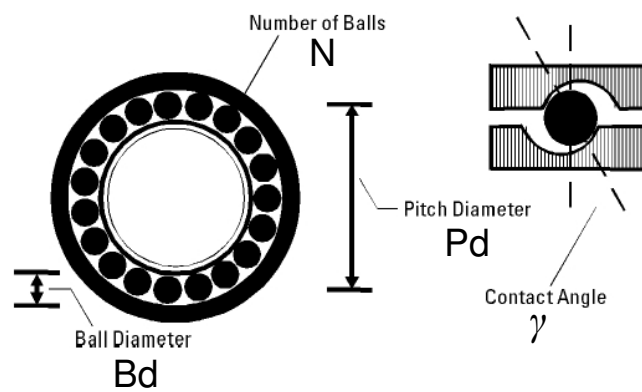


Figure 5.16 Geometry of a ball bearing. (Figure taken from [19])

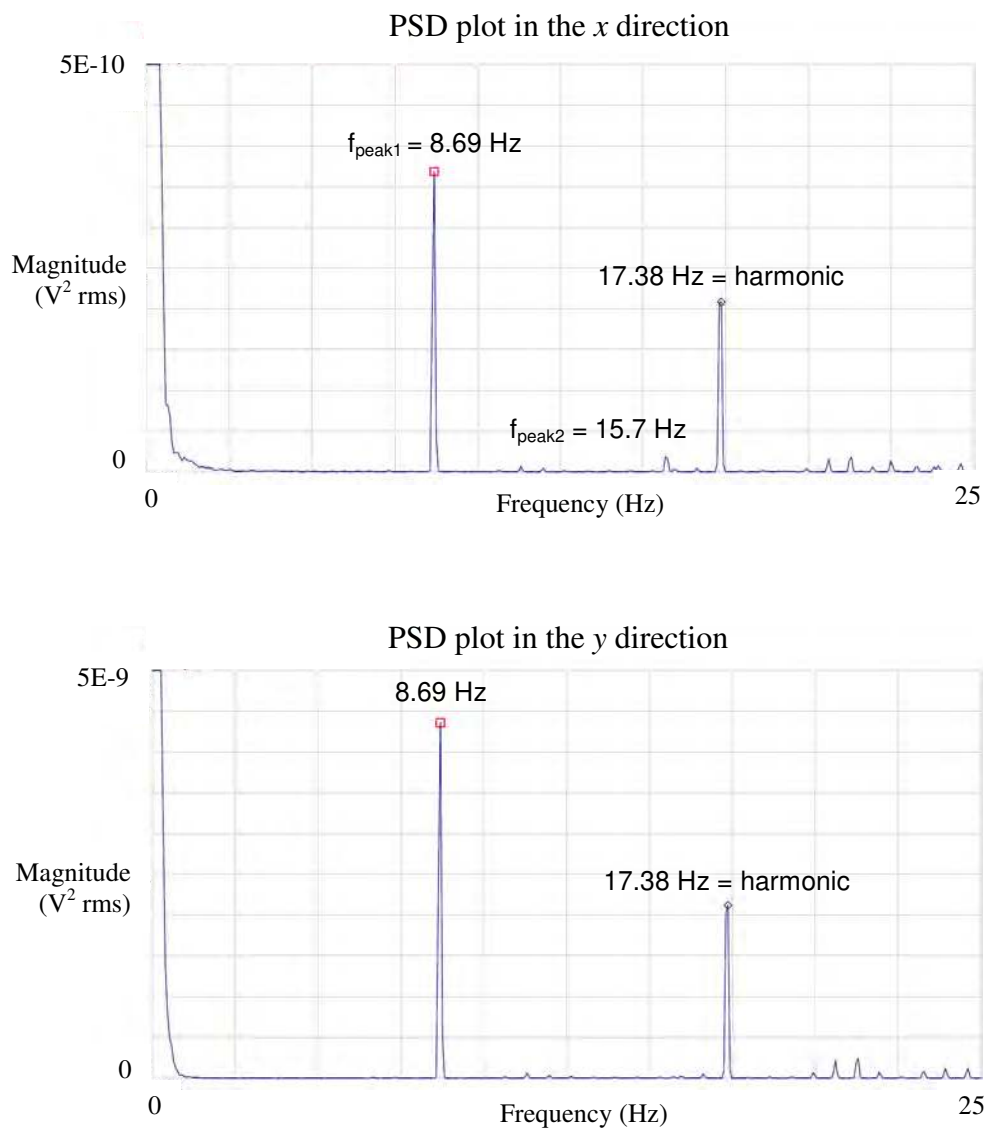


Figure 5.17 Power spectral density (PSD) plots for actual vibrations measurements in the x and y directions.

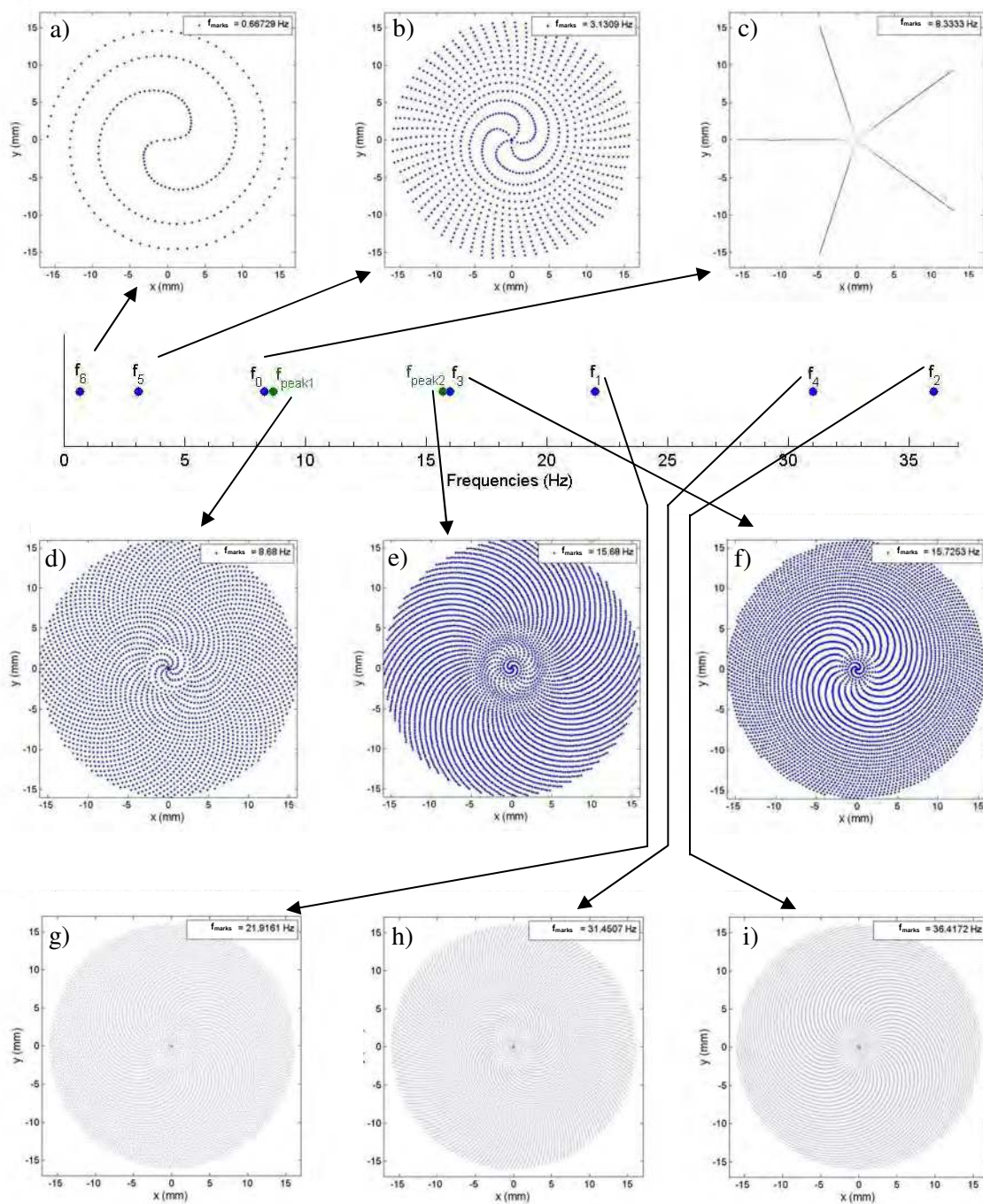


Figure 5.18 Simulations with the 9 candidate frequencies of table 5.5.

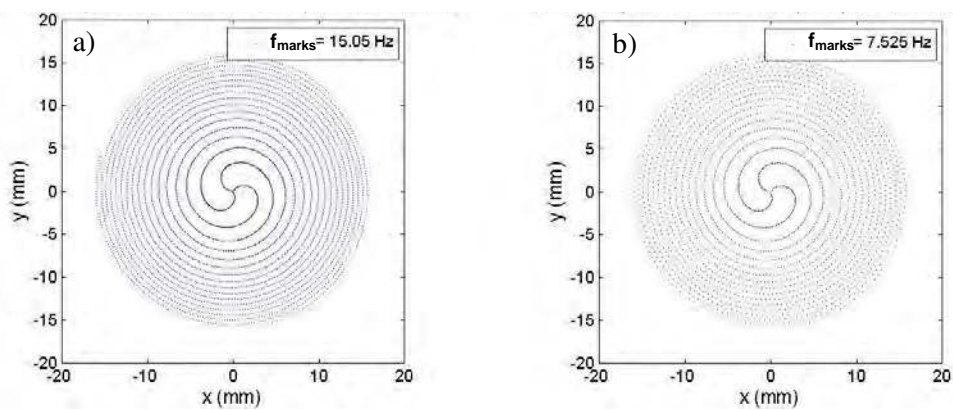


Figure 5.19 3 spirals patterns achieved with the tool path file used to polish the part shown in Figure 5.13, $f_{\text{part}} = 5 \text{ Hz}$ and
 a) $f_{\text{marks}} = 15.05 \text{ Hz}$;
 b) $f_{\text{marks}} = 0.5 * 15.05 = 7.525 \text{ Hz}$.

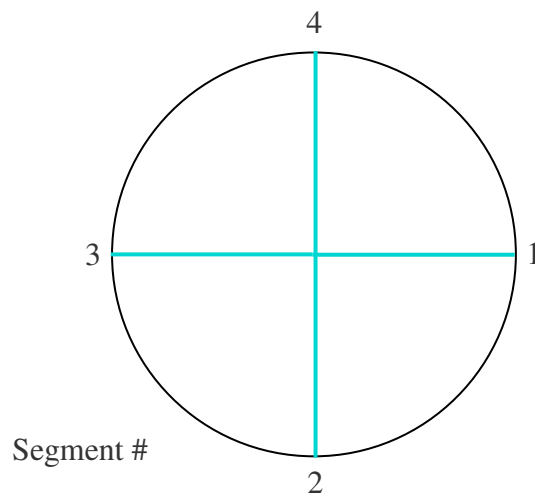


Figure 5.20 Schematic of a part with a pattern consisting of 4 segments.

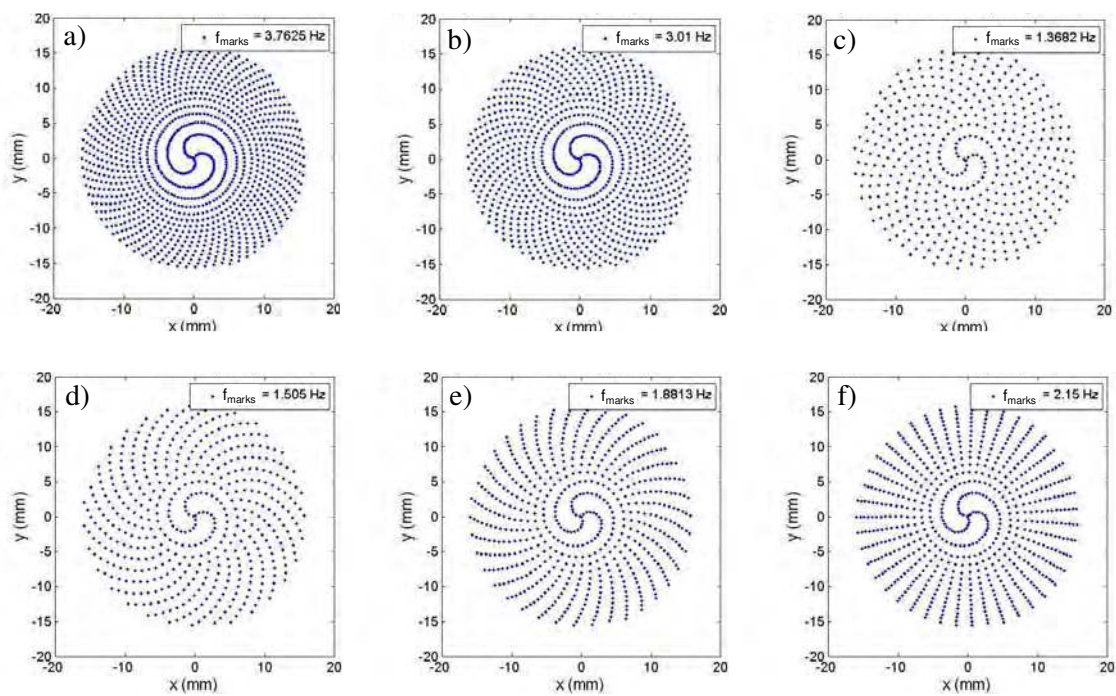


Figure 5.21 3 spirals patterns achieved with the 6 lower frequencies of Table 5.6.

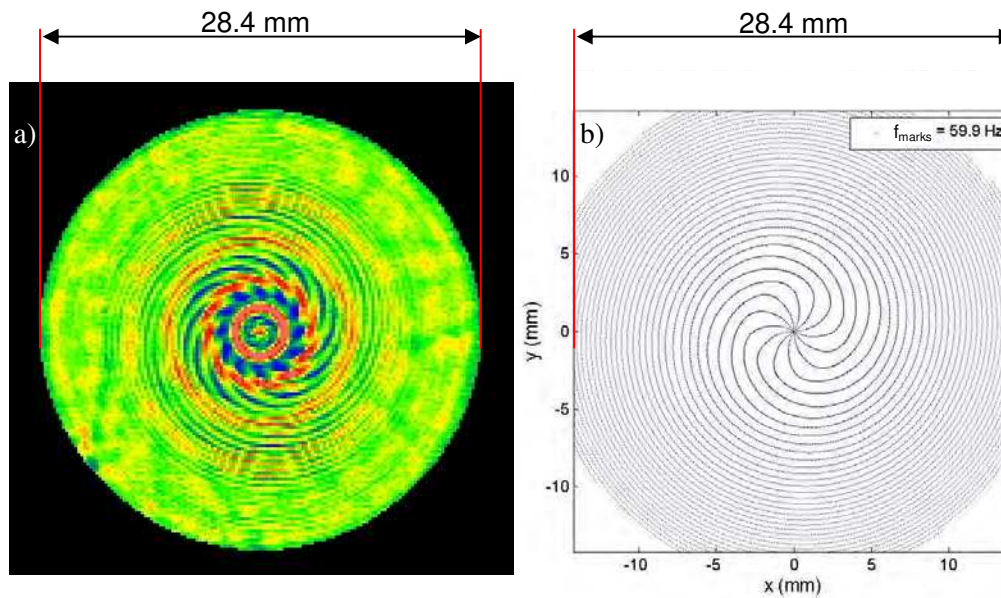


Figure 5.22 Observed and simulated patterns with $f_{\text{marks}} = 59.9$ Hz and part at 300 rpm.

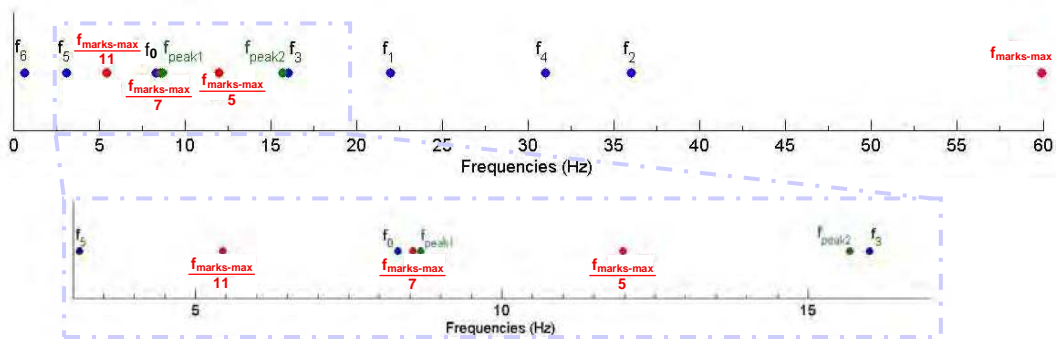


Figure 5.23 Plots of the candidate frequencies: calculated, measured and predicting the observed pattern.

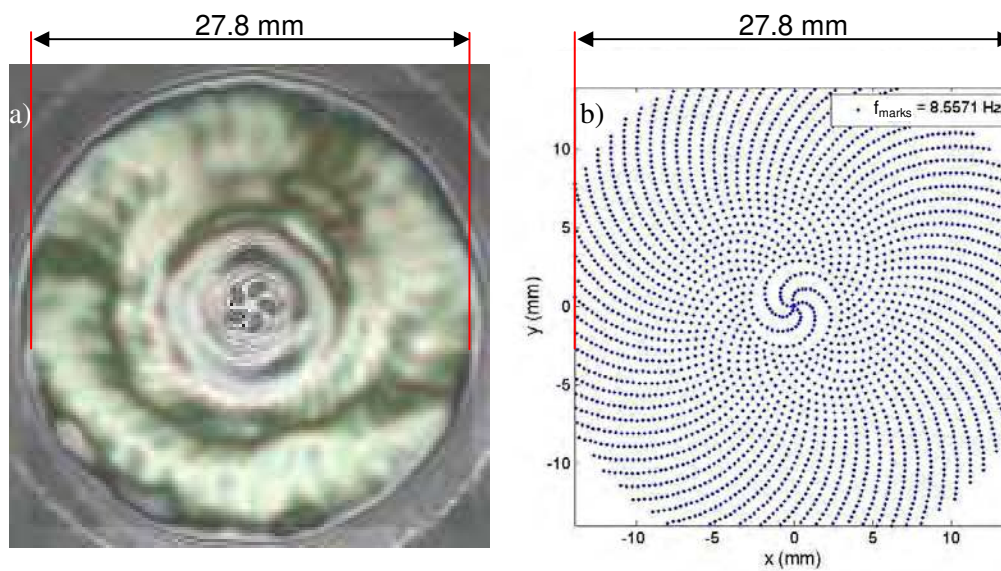


Figure 5.24 Observed and simulated patterns with $f_{\text{marks}} = 59.9/7 \text{ Hz}$ and part at 100 rpm.

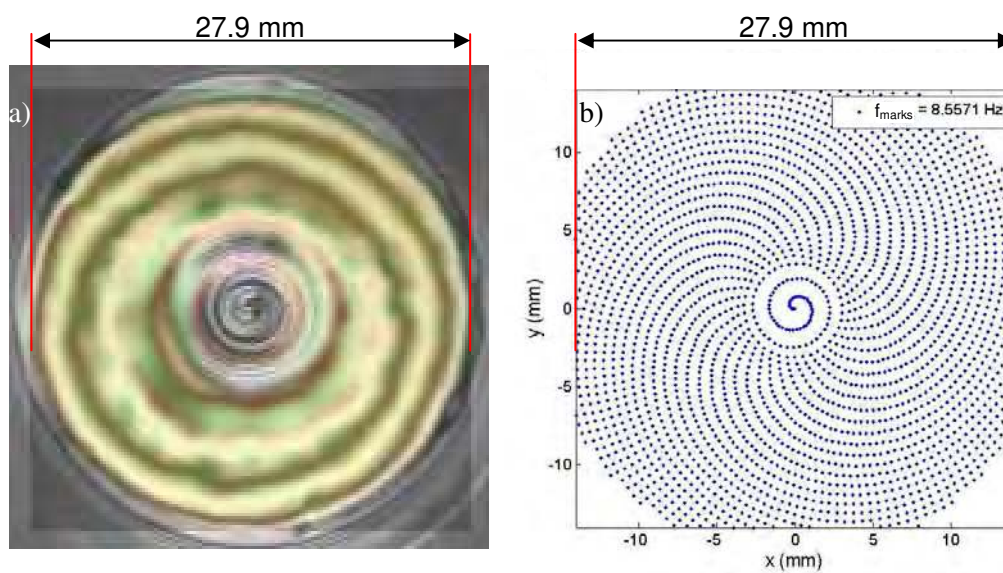


Figure 5.25 Observed and simulated patterns with $f_{\text{marks}} = 59.9/7 \text{ Hz}$ and part at 500 rpm.

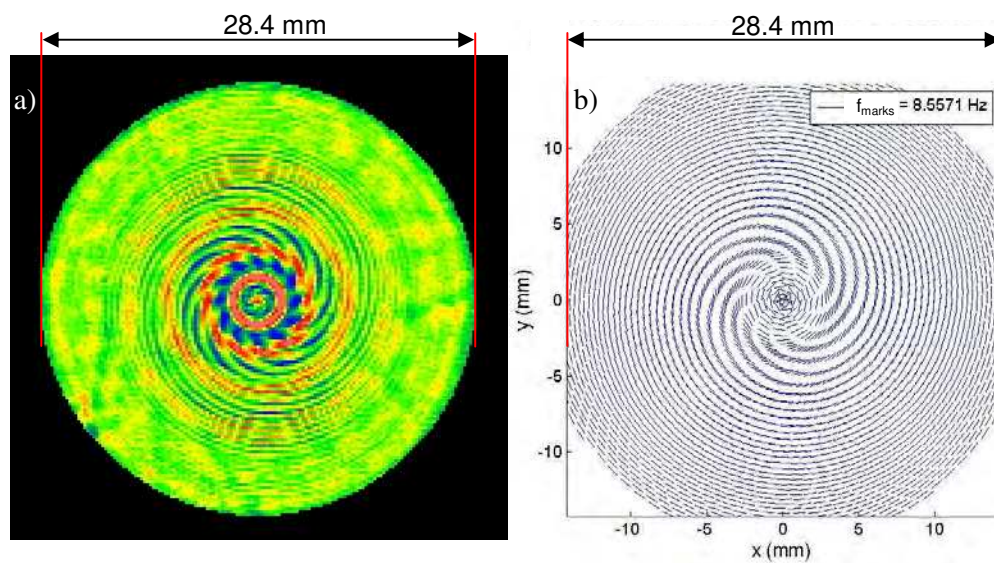


Figure 5.26 Observed and simulated patterns with $f_{\text{marks}} = 59.9/7$ Hz, part at 300 rpm and scratches of constant length equal to 0.8 mm.

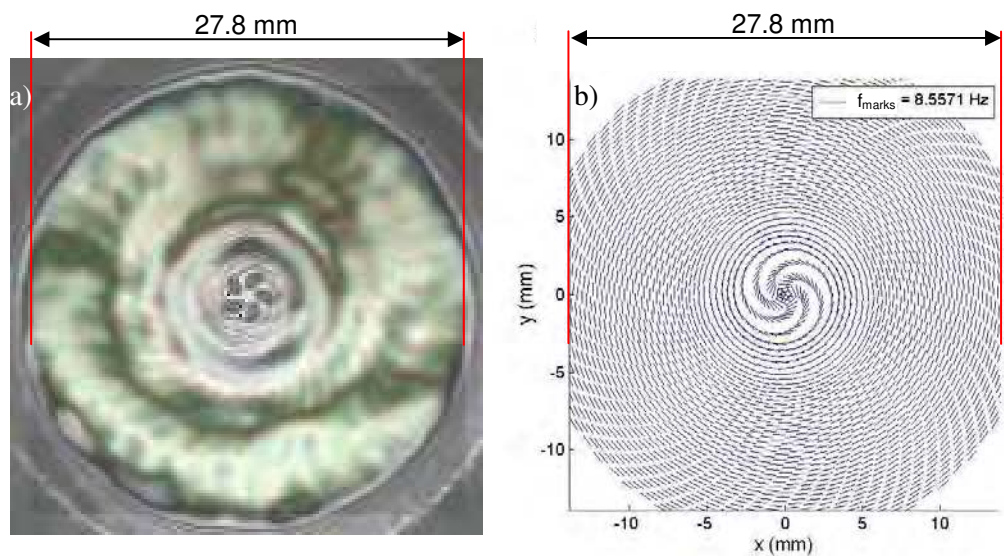


Figure 5.27 Observed and simulated patterns with $f_{\text{marks}} = 59.9/7$ Hz, part at 100 rpm and scratches of constant length equal to 0.8 mm.

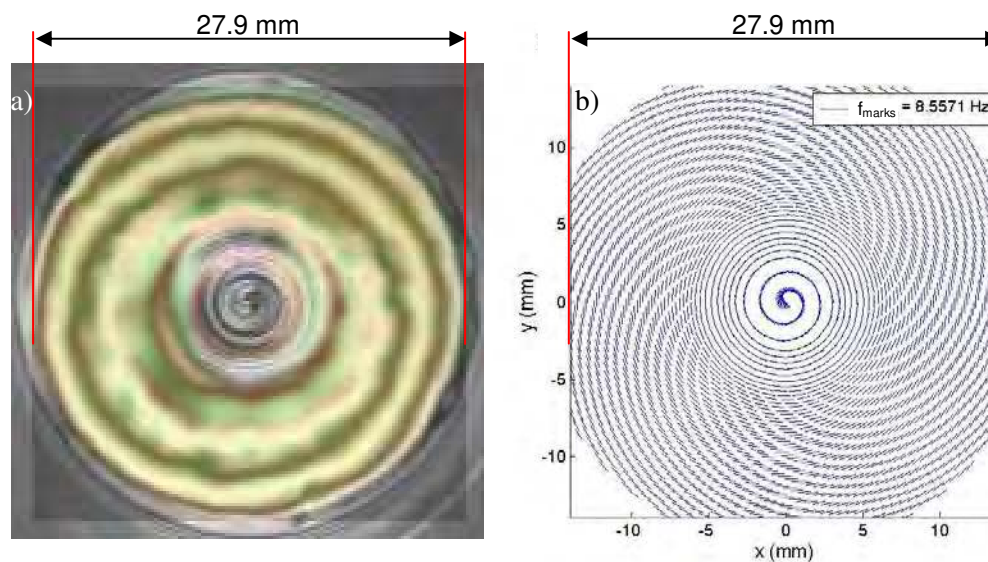


Figure 5.28 Observed and simulated patterns with $f_{\text{marks}} = 59.9/7 \text{ Hz}$, part at 500 rpm and scratches of constant length equal to 0.8 mm.

Chapter 6 Summary and suggestions for future work

6.1 Summary

This thesis provides a basis for deterministic polishing with UFF so that this process can be operated according to the flow chart of Figure 1.7 for aspheres and ogives polishing. For that purpose, the form correction problem for rotationally symmetric errors of axisymmetric workpieces has been addressed as well as the problem of establishing a collision free tool path. Some of the properties of the UFF removal function have been characterized. Its predictability as a function of the process parameters with classical contact mechanics theory and Preston's equation has been investigated. Potential sources of errors that may create discrepancies between actual and predicted removal profiles and their effect have been examined. The origin of induced tool marks taking the form of spirals has been identified. The methods developed in this thesis could be applied to other deterministic polishers.

The form correction problem was formulated by deriving an equation for the depth of removal for a given removal function and tool crossfeed velocity. Because of the relatively large size of the UFF removal function, the removal profile is given by the convolution of an equivalent one-dimensional removal function and the tool crossfeed velocity. The form correction problem, which consists in adjusting the tool crossfeed velocity to achieve a desired removal profile, was treated by discretizing the tool path and rewriting the equation for the depth of removal in matrix form. The discrete depth of removal profile is then the product of a removal matrix and a vector

having for elements the inverse of the tool crossfeed velocity along the tool path. Closed form expressions have been derived for the computation of the removal matrix in the case of plano and spherical parts. An approximate formulation has been introduced for aspheres and ogives. To take into account the variations of the removal function, the removal matrix is computed in a fashion such that a different removal function can be used at every point of the discretized tool path. A method establishing the tool crossfeed velocities such that they are feasible, i.e. such that the tool's velocity and acceleration constraints are satisfied, and produce a removal profile with minimum deviation from the desired removal profile has been developed. Because of the convolution nature of the problem, the problem is ill-conditioned and can lead to non-satisfactory solutions. Therefore, the problem is formulated as a constrained optimization problem and Tikhonov regularization was used to overcome this issue by including the smoothness of the crossfeed velocity solution in the objective function to minimize.

Algorithms establishing a collision free tool path have been developed. They define the safe positions that the tool can occupy to polish the part by finding the tool B angle that prevents tool part collisions. These algorithms are based on a two-dimensional model that detects tool-part collision and search strategies for safe values of B . The two-dimensional model consists of a discretized profile of the part and a region of the plane representing the tool interior region that could interfere with the part. Fast and robust search strategies have been derived for B by defining pertinent

starting points and favoring the most likely successful search direction based on the specificity of deep, ogive-like, concave surfaces.

The effect of process parameters on the removal function as well as the predictability of this function as these parameters vary has been investigated. The applicability of Preston's equation to relate the removal function to the contact interfacial pressure distribution, relative velocity between the part and abrasive was examined. This equation predicts a linear relation between removal and dwell time, relative velocity and pressure. In the case of UFF, the linear relation was observed with dwell time and pressure. However, removal appears to vary linearly with the relative velocity to the power $4/5$. This power law dependence between removal and relative velocity was taken into account in a generalized form of Preston's equation. This equation predicts the removal function as a function of the interfacial pressure distribution. Hertz contact mechanics theory was considered to establish the size of the contact patch and this interfacial pressure distribution. It was shown that with UFF, the generalized Preston coefficient is a function of the part radii of curvature. Removal spots were made with wheels of various durometers on parts with different geometries to evaluate the generalized Preston coefficient and the predictability of the removal function. The generalized Preston coefficients obtained with the different carrier wheels and part geometries were of the order of values reported for other polishing processes. A good predictability of the removal function on convex surfaces with hard carrier wheel was also observed. A similar predictability of the removal

function on plano parts as a function of tool compression was also shown. However, Hertz theory was inaccurate for soft carrier wheels and concave surfaces.

The difficulty of predicting the removal function was overcome by correcting the removal matrix obtained with an approximate removal function so that actual and predicted removal profiles agree. This method uses scaling factors by which each line of the removal matrix is multiplied. This method was used to perform successful form corrections on aspheres with significant part radii of curvature variations.

The preferred configuration for tool positioning is to have tool and part local normals aligned. However to prevent tool-part collisions, the angle α between those normals has to vary. α was shown to affect the tool stiffness, resulting in load and therefore, removal function variations. Moderate, 12%, and large, 40%, stiffness variations were observed for α in the ranges $[0^\circ 75^\circ]$ and $[75^\circ 90^\circ]$, respectively.

Finally, removal spots made on various materials indicated a fair linear relation between material volumetric removal rate and a mechanical figure of merit including the material's Young modulus, fracture toughness and Knoop hardness. This is in agreement with observations made for other processes and allows for rough material removal rate estimates prior to making removal spots.

Sources of errors that may affect the predicted removal profile were examined. For that purpose, the potential errors were identified to be inaccurate desired removal profile, tool improper positioning and motion and unexpected changes in removal function. These errors were modeled to perform simulations

revealing the induced discrepancies between predicted and actual removal profiles. The effects were showed to depend strongly on the removal function, requiring specific simulations for every removal function of interest. However, numerical simulations showed that the center region of the part is particularly sensitive to these errors. The difficulty to diagnose such errors can potentially be overcome with the correction method also used to account for variations of the removal function.

Tool marks induced by UFF and taking the form of spirals have been observed. Their number and curvature were shown to be a function of part rotational speed. These marks were explained by a mark generation model assuming that the tool leaves marks on the part at a constant frequency. It was found that multiple frequencies can create the same pattern. A method establishing all the frequencies that can create a given pattern was developed. The physical cause for these marks was established by calculating candidate frequencies taking into account potential sources of marks on the tool and by measuring the tool vibrations. It was concluded that the observed spirals were generated by marks left at a frequency matching the rotational frequency of the carrier wheel. The cause of these marks was found to be a small void present on the carrier wheel's periphery.

6.2 Suggestions for future work

The work presented in this thesis provides a baseline for deterministic polishing with UFF. This work can be extended in the major areas covered by the present work, namely algorithms for form correction and tool path geometry, as well

as removal function studies to improve the UFF process and expand its capabilities. In particular, correction of non-rotationally symmetric errors and polishing of freeform surfaces or parts with diameters exceeding the machine's current capabilities could be considered. The algorithms needed for the various form correction problems are also of interest to other figuring processes.

6.2.1 Form correction

The current solution for form correction has been used to achieve form errors of less than $0.5 \mu\text{m PV}$. Non-rotationally symmetric errors, such as astigmatism, become predominant in this range of form errors. These errors can not be reduced with the current form correction algorithms, since they only address rotationally symmetric errors. To significantly improve form errors, on the order of $0.1 \mu\text{m PV}$ and below, it will be necessary to correct for these non-rotationally symmetric errors.

The correction of these errors requires variations of the tool dwell time not only as a function of the tool radial position but also as a function of its angular or azimuthal position on the part. For that purpose, the part rotational speed must be varied during each revolution to dwell appropriately over high and low spots.

This problem can be addressed in a fashion similar to the one used for the axisymmetric approach reported in this thesis. For that purpose, the form correction problem must be formulated in matrix form such that the two-dimensional removal map resulting from given tool crossfeed velocities and part rotational speeds can be computed. For this approach the tool path must be discretized radially and

azimuthally. The removal map will then be the sum of the removal functions at these discrete points multiplied by the respective tool dwell times. This complete two-dimensional model will accurately model removal and its formulation is relatively simple. However, it will require large matrices which will be time consuming to compute.

On the other hand, as suggested by Walker et al. [1] in the case of the Zeeko Precessions process, an approximate and possibly satisfactory solution could be derived based on the form correction algorithms for rotationally symmetric errors. In the case of parts with non-rotationally symmetric errors, by inputting a part profile formed of azimuthal averages of the part full map measurement, the present form correction algorithms output the tool dwell time that will correct this averaged azimuthal error at a given radial position. This result is the total dwell time for this radial position. At this radial position, the part circumference can be divided into arcs to which a corresponding fraction of the total dwell time can be associated. The dwell time in each separate region could then be adjusted to compensate for the difference between averaged and actual form error while maintaining a constant dwell time for that radial position. This approach would be relatively simple to implement. However, this is only expected to be accurate for non-rotationally symmetric errors slowly varying in the radial and azimuthal directions, so that the error is relatively uniform over the extent of the removal function. The solution must also be established such that constraints on the part rotational velocity and acceleration are satisfied.

It must be noted that according to Eqs. (4.9), (4.10) and (4.11), the removal functions which are required to determine the part rotational speed for form correction are function of that speed through the relative velocity, v_{rel} , between the abrasive and the part. Therefore, to simplify the problem it will be desirable to make v_{rel} relatively insensitive to the part rotational speed. This can be achieved by using relatively large band velocities or low part rotational speeds.

The next challenge is deterministic polishing of non-axisymmetric or freeform surfaces. Polishing of such shapes will typically require a spiral or raster tool path across a static part. With these shapes, the form correction problem can only be treated with a complete two-dimensional model for removal such as the one described previously.

Polishing the edge of a part is a problem for figuring processes involving contact between the tool and part and it has not yet been addressed for UFF. As a result of the tool overhanging the edge of the workpiece, the edge is typically turned down. Greater removal at the part edge is likely due to an increase of the interfacial pressures as the contact area decreases. Work could be done to predict the removal function as the tool overhangs the part edge. However, this is a very difficult contact problem. A solution, preventing this issue, could consist in adding a ring, or border piece [2] to extend the part, as Jones [2], Walker et al. [3] and Brown [4] suggested. This is convenient from an algorithm point of view as the removal function will not

dramatically change, but it is not very practical as each part needs its own customized disposable ring. Instead, it is suggested to continuously lift the tool as it reaches the edge of the part to adjust the size of the contact patch so that $|y_0| + L_y$ is equal to half the part diameter as illustrated in Figure 6.1. The goal is to prevent the tool from overhanging the part edge. For UFF, this strategy has also the advantage of preventing band damages induced by the part's edge. However, the reduction in size and amplitude of the removal function as the tool is lifted up might produce low removal rates that would significantly increase the process time. This potential problem could possibly be overcome by increasing the band velocity. The feasibility of this approach depends on the predictability of removal function as a function of the displacement of the tool into the part, δ , and if a crossfeed velocity solution producing the desired depths of removal can be established. In Chapter 4, it was shown that the removal function can be fairly well predicted as a function of δ on plano parts.

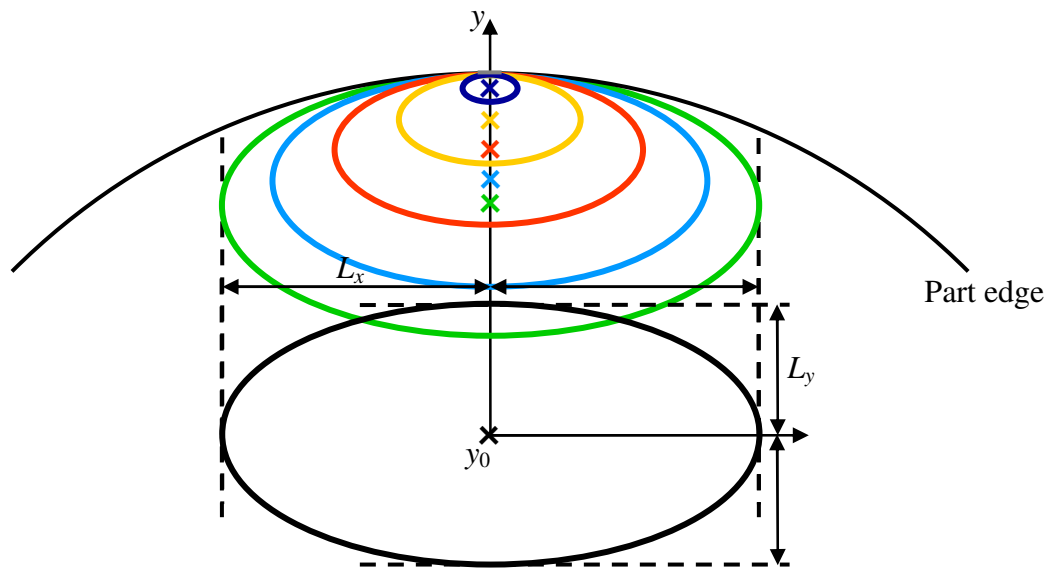


Figure 6.1 Edge strategy.

The present algorithms for form correction minimize the PV error of the predicted form. It might also be desirable to reduce the residual slope errors of the predicted surface. Periodic slope errors can take the form of midspatial frequency error and therefore, might cause light scattering [5, 6]. To reduce slope errors, it is suggested to modify the formulation of the form correction problem to include the minimization of the profile slope errors within the objective function or within the constraints.

6.2.2 Tool path geometry

Faster search strategies for B angles producing safe tool-part contact could be investigated. The algorithms for tool path geometry could also be modified to expand the machine capabilities beyond the initial maximum part diameter specification of 150 mm. The current model for tool-part collision only takes into account the tool and machine elements that might interfere with parts of diameter less than 150 mm. By including machine elements that would interfere with oversized parts in the tool-part collision model, tool part collisions could be prevented for these parts as well and therefore, make it geometrically possible to polish such shapes. In the case of oversized parts, the limits on y and z tool translations should also be taken into account while searching for a safe B angle.

Specific algorithms will be needed to deal with freeform surfaces. A full three-dimensional model will be needed to model tool part collisions and the desired tool-part contact configurations will have to be defined as a function of the part local normal orientation.

6.2.3 Removal function

The correction method introduced in Chapter 4 alleviates the need for a precisely predictable removal function in the case of rotationally symmetric errors. However, the process could be improved if the removal function was well predicted as a function, in particular, of the part local radii of curvature. This information is necessary to formulate the complete two-dimensional model for non-rotationally

symmetric errors and non-axisymmetric parts. In this thesis, the removal function has been expressed with Eq. (4.9) as a function of the contact interfacial pressure distribution and a generalized Preston coefficient which have to be predicted as a function of process parameters.

As for Yang et al. [7], the generalized Preston coefficient could be expressed empirically as a function of the part local radii of curvature. In the present work, it has been shown that the measured pressure distribution is in good agreement with the pattern of the removal spot, as suggested by Eq. (4.14). Furthermore, the size of the contact patch and pressure distribution can be fairly well predicted using Hertz contact mechanics theory with hard carrier wheels on convex surfaces. With such wheels and part geometries, the discrepancies between actual and predicted removal function are essentially due to slight differences between actual and predicted removal pattern, such as the region of maximum removal being slightly off center in reality. This issue could potentially be addressed by evaluating numerically the actual pressure distribution from the measurement of a removal spot according to Eq. (4.14). That actual pressure distribution could be used to define the pattern of the pressure distribution as the removal function size and amplitude vary. This can be achieved by stretching the “pressure reference” Eq. (4.14) to match the size of the predicted contact patch and applying a scaling factor to the pressure distribution. This factor would be chosen so that the integral of the new pressure distribution over the predicted contact patch is equal to the force measured or predicted by Hertz theory. Corrections to Hertz theory might also be needed to achieve a better accuracy.

The use of that approach for softer carrier wheels which exhibit non-Hertzian pressure distributions could be investigated under the assumption that Hertz theory can predict fairly accurately the size of the removal function and the actual load in these conditions. If Hertz theory is not satisfactory for soft bodies, possible corrections to the theory could be investigated. The use of empirical approximations based on experimental result, as in Yang et al. [7], or finite element analysis could also be considered to predict the size of the contact patch and the interfacial pressure distribution.

Hertz contact mechanics theory was also shown to inaccurately predict size and amplitude of the removal function on concave surfaces. This is because in that case a conformal contact problem arises. Since Hertz theory is only appropriate for non-conformal contact [8], another approach is needed for concave surfaces. For spherical and cylindrical contacting bodies, Steuermann [9, 8] has expressed the pressure distribution as an infinite series of known functions. However, for more general cases, such as UFF, a closed form solution to the conforming contact problem cannot be achieved. In that case it is necessary to use numerical methods such as the ones reported by Johnson [8] and Liu et al. [10]. The feasibility and accuracy of such methods for UFF could be investigated. The results could be compared to finite element analysis of the conformal contact problem.

The tool-part contact problem is complicated, because the tool is a composite body including rubberlike materials on which a band is wrapped. This is part of the reason why it is difficult to derive a closed form solution to this problem. Instead

methods that rely on a pressure distribution estimated from a removal spot have been suggested. A better understanding of the contact problem could be gained by building a finite element model for the contact of the tool with the ABAQUS finite element analysis software [11]. If this model is able to predict the actual interfacial pressure distributions with some accuracy, it could be used to characterize the effect of the part geometry, carrier wheel geometry and durometer, band thickness and rigidity on the interfacial pressure. This could lead to prediction of interfacial pressure distributions as a function of these parameters. A better understanding of the role of the band in the contact problem could also be possible as well as a better insight into the compliance at the contact that might help in explaining and predicting the removal of cutter marks.

6.3 References

- [1] D. D. Walker, D. Brooks, R. Freeman, A. King, G. McCavana, R. Morton, D. Riley and J. Simms, "The first aspheric form and texture results from a production machine embodying the Precessions process," *Optical Manufacturing and Testing IV*, Proc. SPIE 4451, 267-276 (2001). Zeeko Ltd, 4 Vulcan Way, Vulcan Court, Hermitage Industrial Estate, Coalville, Leicestershire, LE67 3FW, England, Phone: +44 530-815-832, www.zeeko.co.uk.
- [2] R. A. Jones, "Optimization of computer controlled polishing," *Applied Optics* 16, 218-224 (1977).
- [3] D. D. Walker, A. T. H. Beaucamp, D. Brooks, R. Freeman, A. King, G. McCavana, R. Morton, D. Riley, J. Simms, "Novel CNC polishing process for control of form and texture on aspheric surfaces," *Proc. SPIE* 4767, 99-105 (2002).
- [4] N. J. Brown, "Computationally directed axisymmetric aspheric figuring," *Optical Engineering* 17, 602-620 (1978).

- [5] A. Kotha and J. E. Harvey, "Scattering effects of machined optical surfaces," *Optical Scattering in the Optics, Semiconductor, and Computer Disk Industries*, Proc. SPIE 2541, 54-65 (1995).
- [6] E. L. Church and J. M. Zavada, "Residual surface roughness of diamond-turned optics," *Applied Optics* 14, 1788-1795 (1975).
- [7] M. Y. Yang, H. C. Lee, "Local material removal mechanism considering curvature effect in the polishing process of the small aspherical lens die," *Journals of Materials Processing Technology*, 116, 298-304 (2001).
- [8] K. L. Johnson, *Contact Mechanics*, Cambridge University Press, New York, New York, 1987.
- [9] E. Steuermann, "On Hertz theory of local deformation of compressed bodies," *Comptes Rendus (Doklady) de l'Académie des Sciences de l'URSS*, 25, 359-361 (1939).
- [10] C. S. Liu, K. Zhang and L. Yang, "Normal force-displacement relationship of spherical joints with clearances," *Journal of Computational and Nonlinear Dynamics* 1, 160-167 (2006).
- [11] SIMULIA, Rising Sun Mills, 166 Valley Street, Providence, RI 02909-2499, Phone: 401-276-4400, www.simulia.com.

Appendix 1 Initial operations

1.1 Description

Initial operations are run before the main algorithms used for generating the tool path geometry and form correction. The initial operations consist of two utilities used successively. They discretize the part and tool path and evaluate the part principal radii of curvature along the tool path. For that purpose, the MATLAB function `InitialOperations.m`, copied at the end of this section, calls successively the functions `ProfileDiscretizer.m` and `PartPrincipalRoCEstimator.m`. The operations performed in these MATLAB functions are described in details in sections 1.2 and 1.3.

`ProfileDiscretizer.m` discretizes the part profile. It is used to create the part model for tool-part collisions presented in Chapter 3 and the points along the part profile needed to compute the solution to the form correction problem as described in Chapter 2. For the computation of the removal matrix, the removal function is assumed to be constant over the prescribed arc length, L_{arc} . Therefore, the mid-points of these arcs are needed to compute the removal matrix. The extremities of these arcs are also needed to formulate the tool path commands as defined in Chapter 3. Therefore, it is desirable to have the part profile discretized at an arc length equal to half the desired value, because it will provide the points for removal computation and tool path geometry definition with one execution of the function. As mentioned in section 2, using half the desired arc length will also improve the accuracy of the

computed points. Therefore, ProfileDiscretizer.m performs the discretization at half the desired arc length. The coordinates of the discretized points are stored in the matrix TPDiscreteProfile. The matrix PDiscreteProfile contains the points used to model the part to predict tool-part collisions. They are obtained by sampling TPDiscreteProfile to keep the points separated by the desired arc length. Additional points representing the edge are added for concave surfaces. If the part has no physical center, that region can be ignored, or replaced by a series of points forming a horizontal line that could model part fixtures that could collide with the tool. TPDiscreteProfile will also be sampled as needed to select the relevant points for the form correction and tool path geometry algorithms described in Chapters 2 and 3, respectively.

PartPrincipalRoCEstimator.m evaluates the part principal radii of curvature at the points where the removal function has to be known for removal computation. These radii of curvature are needed to take into account the variations of the removal function as described in Chapter 4.

Code of the MATLAB function InitialOperations.m

```
function [TPDiscreteProfile,PDiscreteProfile,PartRadiiOfCurv] =
InitialOperations(Larc)
% InitialOperations: Function performing the preliminary operations
needed
% for the tool path server
% Reference: Appendix 1 on "Initial operations"
```

```

% Inputs: Scalar equal to the desired arc length between the
discretized
% points.
% Outputs: Matrices containing the discretized part and tool path.
Matrix
% containing the part principal radii of curvature along the tool
path.

global Pgeom TPgeom

% Run the profile discretizer.
% Define the matrix containing the discretized tool path. 1st
column: y.
% 2nd column: z.
if sign(TPgeom(1))~=sign(TPgeom(2))
    TPDiscreteProfile=ProfileDiscretizer(0,TPgeom(2),Larc);
else
    TPDiscreteProfile=ProfileDiscretizer(TPgeom(1),TPgeom(2),Larc);
end

% Define the matrix containing the discretized part profile.
PDiscreteProfile=ProfileDiscretizer(Pgeom(1),Pgeom(2),Larc);
% Sample to achieve desired arc length.
PDiscreteProfile=PDiscreteProfile(1:2:size(PDiscreteProfile,1),:);
% Add flat at center if needed.
if Pgeom(4)==1
    Pcenter=(0:Larc:PDiscreteProfile(1,1)-Larc)';

PDiscreteProfile=[Pcenter,ones(size(Pcenter,1),1)*zPart(Pgeom(1));PDiscreteProfile];
end
% Add the part edge for concave surfaces.
if Pgeom(3)==1
    Pedge=(Pgeom(2):Larc:Pgeom(2)+Pgeom(5))';
    if Pedge(size(Pedge,1)~=Pgeom(2)+Pgeom(5))
        Pedge=[Pedge;Pgeom(2)+Pgeom(5)];
    end

PDiscreteProfile=[PDiscreteProfile;Pedge,ones(size(Pedge,1),1)*zPart(Pgeom(2))];
end

% Run the estimator for the part principal radii of curvature.
% Define the matrix containing the part principal radii of curvature
along
% the tool path. 1st column: y. 2nd column: Rpx. 3rd column: Rpy.
[PartRadiiOfCurv]=PartPrincipalROCEstimator(TPDiscreteProfile);

```

1.2 Profile discretizer

A matrix approach is used to solve the form correction problem. This approach is based on a discretization of the tool path. A discrete representation of the part profile is also needed for the tool path geometry algorithms. For both cases, a profile discretizer is needed. The point spacing is defined as the arc length, L_{arc} , along the part profile between two consecutive discretized points. For the problems addressed in this work, a constant point spacing is desired.

Because the parts are axisymmetric, only half of the part profile is discretized, starting from the part center or its inner edge, if the part has no physical center. Uniform arc length between discretized part points can be simply achieved for flats and spheres. For flats, points equidistantly spaced along y are satisfactory. For spheres, the spherical coordinates shown in Figure 2.2 are used, and points of the part profile separated by a constant angular increment $\Delta\phi$ can be selected. On the other hand, for aspheres, which can take a large variety of shapes, there is no convenient way to simply and quickly achieve such a discretization. Therefore, a robust method for the uniform discretization of all kind of parts profile is needed.

Algorithms for general shapes are derived by approximating the arc length from one point along the part profile by the length along the tangent to the curve at that point. This approximation, illustrated in Figure A.1, is valid, because the desired arc length is low, typically 0.1 mm, and because most part profiles and their

derivative with respect to y are continuous functions of y . In the case of a larger arc length, the accuracy can be improved. For that purpose, the profile is discretized with an arc length equal to the desired one divided by an integer n , chosen so that the arc length becomes small enough for the approximation to hold. By selecting every n points of the resulting discretized profile, a discretization with the desired arc length can be achieved. The case $n = 2$ is illustrated in Figure A.2. Similarly, in the present algorithms, one intermediate point and therefore, half of the desired arc length is actually used. The algorithms take for inputs the y values, y_{\min} and y_{\max} , between which the part profile must be discretized and L_{arc} . They output the discretized profile in the form of a matrix. The first and second columns of this matrix contain the y and z values, respectively, of the points forming the discretized profile.

The algorithms contained in `ProfileDiscretizer.m`, copied at the end of this section, perform the following operations. For a point of abscissa y_1 , the abscissa y_2 of the point situated on the part profile, such that $y_2 > y_1$ and the arc length between these two points is L_{arc} , is approximately given by

$$y_2 = y_1 + \frac{L_{arc}}{\sqrt{1 + slope^2}}, \quad (\text{A.1})$$

where $slope$ is the slope of the tangent to the part profile at y_1 , such that

$$slope = \frac{z_{part}(y_1) - z_{part}(y_1 - \Delta y)}{\Delta y}, \quad (\text{A.2})$$

where Δy is a small increment in y . Eq. (A.2) uses a backward difference to approximate $slope$. A forward approximation is not used, because it might result in

attempts at evaluating z_{Part} at points passed the range over which it is defined. This could in particular occur near the edge of hemispheres or tangent ogives. Starting with $y_1 = y_{min}$, y_2 is computed with Eqs (A.1) and (A.2). y_1 is set equal to y_2 and the process is iterated while y_2 is lower than y_{max} . Once y_2 becomes larger than y_{max} , the code is stopped and the last, out of range, point is removed.

The accuracy of the profile discretizer can be verified with hemispheres. The arc length between two points situated on these profiles is equal to half the part diameter times the difference of the ϕ coordinates of these points. For a programmed arc length of 0.1 mm, the profile discretizer establishes points separated by an arc length within 1% of the desired value for points up to 0.2 mm from the part edge in the case of parts of diameters ranging from 40 to 150 mm.

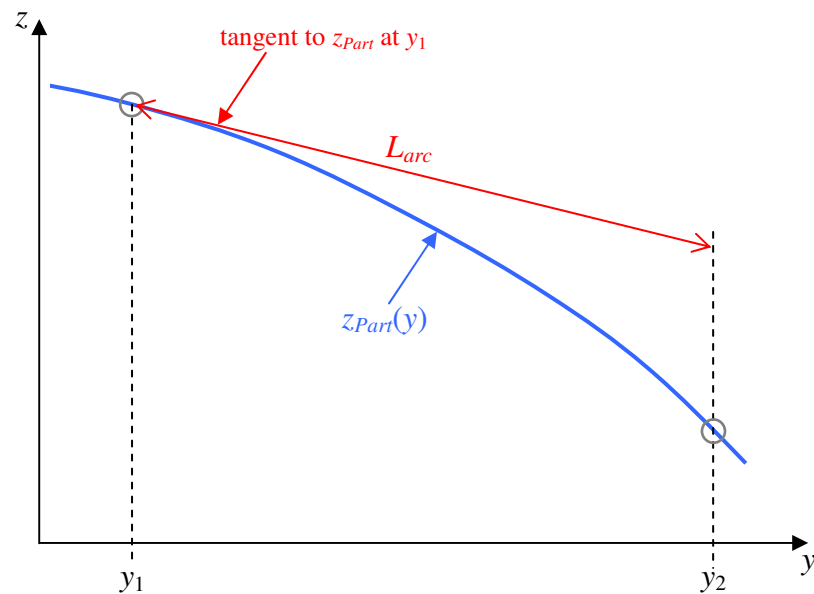


Figure A.1 Illustration of approximation to establish points spaced by the desired arc length.

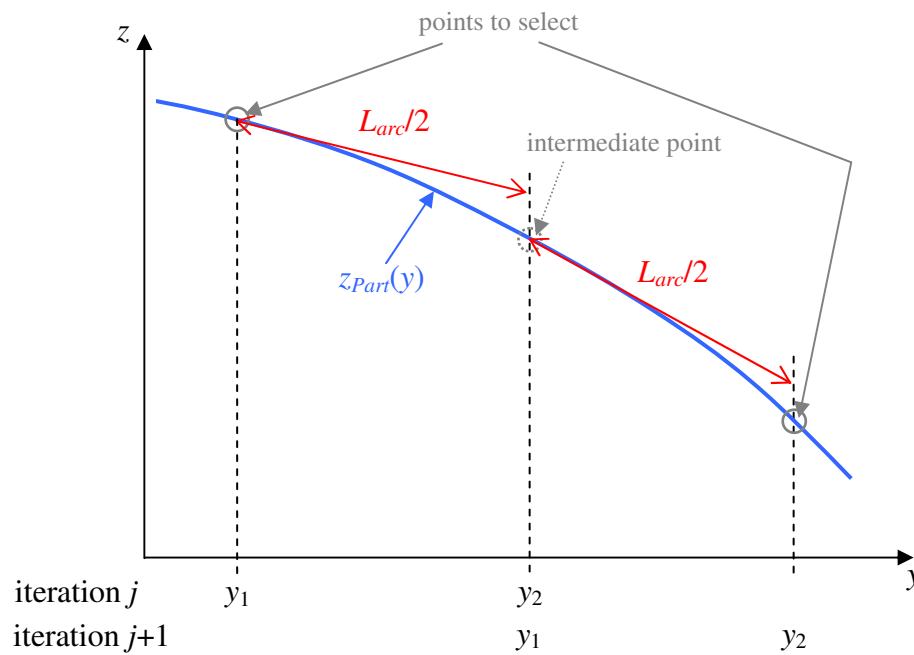


Figure A.2 Illustration of the use of intermediate points to improve the arc length spacing between the selected points.

Code of the MATLAB function ProfileDiscretizer.m

```

function DiscreteProfile = ProfileDiscretizer(ymin,ymax,Larc)
% ProfileDiscretizer: Function discretizing the part profile such
that the
% arc length between two consecutive points is constant.
% Reference: Appendix 1 on "Initial operations"
% Inputs: Scalars equal to the desired extremities of the
discretized
% profile and arc length between the discretized points.
% Outputs: Matrix containing the discretized profile.

Larc=Larc/2; % arc length spacing in mm used for the computations
deltay=10^(-9); % small increment in y used for evaluation of the
slope

y1=ymin;
% Define the matrix DiscreteProfile containing the discretized
profile: 1st
% column: y values, 2nd column: z values
DiscreteProfile=[y1,zPart(y1)];
k=1;
while y1<=ymax
    k=k+1;
    % estimate the slope of the tangent to the part profile at
    % (y1,zPart(y1))
    a=(zPart(y1)-zPart(y1-deltay))/deltay;
    % Compute y2
    y2=y1+Larc/(1+a^2)^0.5;
    % Store the point
    DiscreteProfile(k,1)=y2;
    DiscreteProfile(k,2)=zPart(y2);
    % Set y1=y2 for the next iteration
    y1=y2;
end
% Remove the last line for which y1>rmax
DiscreteProfile(size(DiscreteProfile,1),:)=[];

```

1.3 Part principal radii of curvature

The part principal radii of curvature are needed to predict the variations of the removal function on aspheres and ogives. These radii of curvature are evaluated by the MATLAB function `PartPrincipalROCEstimator` reported at the end of this section. These algorithms take for inputs `TPDiscreteProfile`, the matrix containing the discretized tool path established as described in section 1.2. Because the parts are axisymmetric, only the half of the part profile corresponding to $y \geq 0$ needs to be discretized. For the same reason, the part principal radii of curvature only need to be computed for that same half of the part profile.

The starting point for the computations of these radii of curvature is the following equation defining the radius of curvature of $f(x)$ at x_0

$$R_f = \frac{\left(1 + \left(\frac{\partial f(x)}{\partial x}\right)^2\right)^{3/2}}{\left|\frac{\partial^2 f(x)}{\partial x^2}\right|} \Bigg|_{x=x_0} . \quad (\text{A.3})$$

Based on this mathematical definition, the radius of curvature of $f(x)$ is always a positive value. Therefore, the convex or concave nature of $f(x)$ cannot be determined based on the value of its radius of curvature. But in the optics world, sign conventions, which vary depending on the context, are used to distinguish convex and concave surfaces. For the problem of predicting the removal function it is also desired to know if the surface is locally concave or convex through its radius of curvature. To

determine if the part is locally convex or concave, the part principal radii of curvature are evaluated with a modified version of Eq. (A.3) in this work. The modification consists in having the denominator of Eq. (A.3) equal to the second derivative of $f(x)$ evaluated at x_0 instead of its absolute value.

The part principal radii of curvature R_{P_x} and R_{P_y} are defined in Chapter 4 and given by

$$R_{P_y} = \frac{\left(1 + \left(\frac{\partial z_{Part}(y)}{\partial y}\right)^2\right)^{3/2}}{\frac{\partial^2 z_{Part}(y)}{\partial y^2}} \Bigg|_{y=y_0} \quad (\text{A.4})$$

and

$$R_{P_x} = \frac{\left(1 + \left(\frac{\partial f_P(x)}{\partial x}\right)^2\right)^{3/2}}{\frac{\partial^2 f_P(x)}{\partial x^2}} \Bigg|_{x=0}, \quad (\text{A.5})$$

where $f_P(x)$ is the intersection of the part surface and the plane x_T - z_T , as shown in Figure 4.9. The coordinate system (x_T, y_T, z_T) is defined in Chapter 4. $f_P(x)$ is such that $f_P(0) = 0$ and basically gives the value of the coordinate z_T of the points of the part surface intersecting with x_T - z_T . Because z and z_T are oriented positively out of the surface to polish, concave and convex surfaces would imply positive and negative denominators, respectively, in Eqns (A.4) and (A.5). Therefore, positive and negative values of R_{P_x} and R_{P_y} indicate concave and convex surfaces, respectively.

Approximations are used to evaluate the first and second derivatives of $f_P(x)$ and $z_{Part}(y)$ at the points of interest. To insure that z_{Part} is evaluated at points within the range on which it is defined, forward

$$\left. \frac{\partial z_{Part}(y)}{\partial y} \right|_{y=y_0} \approx \frac{z_{Part}(y_0 + 2\Delta y) - z_{Part}(y_0)}{2\Delta y}, \quad (\text{A.6})$$

$$\left. \frac{\partial^2 z_{Part}(y)}{\partial y^2} \right|_{y=y_0} \approx \frac{z_{Part}(y_0 + 2\Delta y) - 2z_{Part}(y_0 + \Delta y) + z_{Part}(y_0)}{\Delta y^2} \quad (\text{A.7})$$

and backward

$$\left. \frac{\partial z_{Part}(y)}{\partial y} \right|_{y=y_0} \approx \frac{z_{Part}(y_0) - z_{Part}(y_0 - 2\Delta y)}{2\Delta y}, \quad (\text{A.8})$$

$$\left. \frac{\partial^2 z_{Part}(y)}{\partial y^2} \right|_{y=y_0} \approx \frac{z_{Part}(y_0) - 2z_{Part}(y_0 - \Delta y) + z_{Part}(y_0 - 2\Delta y)}{\Delta y^2} \quad (\text{A.9})$$

differences are used to estimate the first and second derivatives of $z_{Part}(y)$ for the first and second half, respectively, of the points forming `TPDiscreteProfile`.

The algorithms of `PartPrincipalROCEstimator` store the y coordinates of the points of `TPDiscreteProfile` which are of interest into the vector `yPts`. The values contained in that vector are used to compute `deriv1` and `deriv2`, the first and second derivatives, respectively, of z_{Part} with respect to y_0 according to Eqns (A.6) through (A.9). These values are then used to compute R_{Py} according to Eq. (A.4).

The first and second derivatives of f_P are established by only using the following forward approximation

$$\left. \frac{\partial f_p(x)}{\partial x} \right|_{x=0} \approx \frac{f_p(2\Delta x) - f_p(0)}{2\Delta x}, \quad (\text{A.10})$$

$$\left. \frac{\partial^2 f_p(x)}{\partial x^2} \right|_{x=0} \approx \frac{\frac{f_p(2\Delta x) - f_p(\Delta x)}{\Delta x} - \frac{f_p(\Delta x) - f_p(0)}{\Delta x}}{\Delta x}. \quad (\text{A.11})$$

These two approximations are illustrated in Figure A.3. The points F , G and H of coordinates $(0, 0, 0)$, $(\Delta x, 0, f_p(\Delta x))$ and $(2\Delta x, 0, f_p(2\Delta x))$, respectively, in the coordinate system (x_T, y_T, z_T) are used to derive Eqs (A.10) and (A.11). In order to establish $f_p(\Delta x)$ and $f_p(2\Delta x)$ for a given y_0 , the coordinates of F , G and H are first established in the coordinate system (x, y, z) . In that coordinate system, F has the coordinates $(0, y_0, z_{part}(y_0))$. G and H are defined as the intersections of the part surface and the plane x_T - z_T at $x = \Delta x$ and $2\Delta x$, respectively. In (x, y, z) , the plane x_T - z_T , named Pn , is described by

$$z = z_{pn}(y, y_0) = SLOPE \times (y - y_0) + z_{part}(y_0), \quad (\text{A.12})$$

where $SLOPE$ is the slope of the normal to z_{part} at y_0 . That slope is the opposite of the inverse of the slope of the tangent to z_{part} at y_0 . Therefore,

$$SLOPE = \frac{-1}{\left. \frac{\partial z_{part}(y)}{\partial y} \right|_{y=y_0}}. \quad (\text{A.13})$$

The points G and H have the coordinates $(\Delta x, y_G, z_{part}(\sqrt{\Delta x^2 + y_G^2}))$ and $(2\Delta x, y_H, z_{part}(\sqrt{(2\Delta x)^2 + y_H^2}))$, respectively, in (x, y, z) . Because G and H belong to Pn and the part surface, y_G and y_H are such that

$$z_{Pn}(y_G, y_0) = z_{Part}(\sqrt{\Delta x^2 + y_G^2}), \quad (\text{A.14})$$

$$z_{Pn}(y_H, y_0) = z_{Part}(\sqrt{(2\Delta x)^2 + y_H^2}). \quad (\text{A.15})$$

Therefore, y_G and y_H are obtained by finding the roots, near y_0 of the functions

$$f_1(y) = z_{Pn}(y, y_0) - z_{Part}(\sqrt{\Delta x^2 + y^2}) \quad (\text{A.16})$$

and

$$f_2(y) = z_{Pn}(y, y_0) - z_{Part}(\sqrt{(2\Delta x)^2 + y^2}), \quad (\text{A.17})$$

respectively. The built-in MATLAB function `fzero.m` is used to find the desired roots of f_1 and f_2 .

The z_T coordinates, which are the needed values of f_{Pn} , of the points G and H are finally obtained by performing a coordinate transformation from (x, y, z) to (x_T, y_T, z_T) . These coordinate systems are illustrated in Figure A.4. Therefore, since z_T is oriented positively out of the part and $f_n(0) = 0$,

$$f_p(x) = \frac{z_{Part}(\sqrt{x^2 + y_0^2}) - z_{Part}(y_0)}{\cos(\alpha)}, \quad (\text{A.18})$$

where α , the angle between the normal to the part surface at y_0 and the z axis, is defined by

$$\alpha = \arctan\left(\left.\frac{\partial z_{Part}(y)}{\partial y}\right|_{y=y_0}\right). \quad (\text{A.19})$$

Using the method and the equations presented in this section, `PartPrincipalRoCEstimator.m` estimates the part principal radii of curvature along the tool path. The output is a matrix having three columns. The first column contains the

y values of the tool path points at which the values of R_{Px} and R_{Py} , contained in columns two and three, respectively, have been evaluated.

The accuracy of PartPrincipalRoCEstimator.m has been verified with spheres of diameters ranging from 10 to 150 mm. In all cases, within 0.1 mm of the part edge, the algorithms predicted radii of curvature within 1% of the actual value, that is equal to half the part diameter.

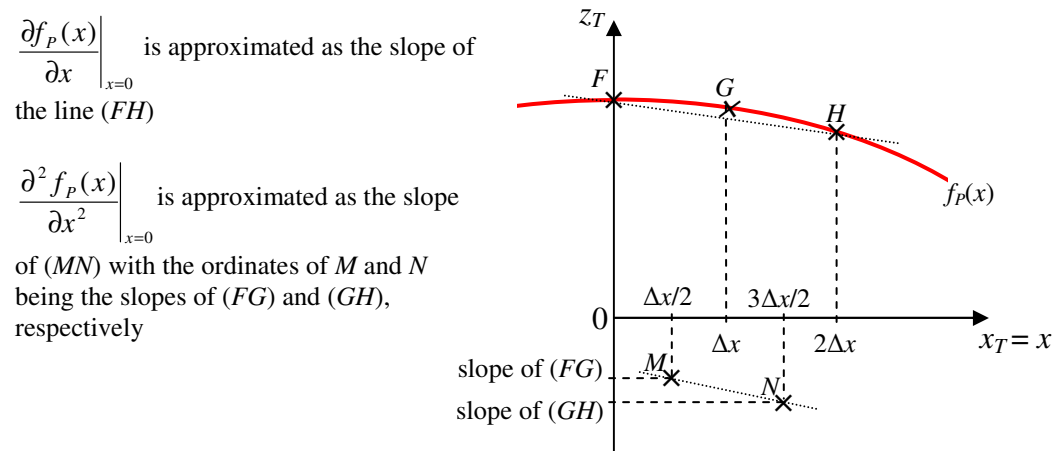


Figure A.3 Numerical approximation of R_{Px} .

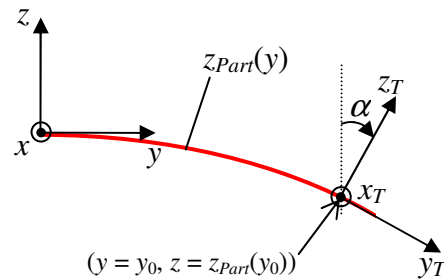


Figure A.4 Coordinate systems (x, y, z) and (x_T, y_T, z_T) .

Code of the MATLAB function PartPrincipalROCEstimator.m

```
function [PROC] = PartPrincipalROCEstimator(TPDiscreteProfile)
% PartPrincipalROCEstimator: Function discretizing the part profile
such
% that the arc length between two consecutive points is constant.
% Reference: Appendix 1 on "Initial operations"
% Inputs: Scalars equal to the desired extremities of the
discretized
% profile and arc length between the discretized points.
% Outputs: Matrix containing the discretized profile.

% Declare as global the variables needed to evaluate f1 and f2.
global deltax SLOPEii y0

% Store the y coordinates of the points of TPDiscreteProfile used
for
% computations.
if TPDiscreteProfile(1,2)==0
    yPts=TPDiscreteProfile(1:2:size(TPDiscreteProfile,1),1);
else
    yPts=TPDiscreteProfile(2:2:size(TPDiscreteProfile,1),1);
end

% 1) Computation of Rpy
deltay=10^(-3); % small increment in y
```

```

% Separate the first and second half of yPts.
yPtsHalf1=yPts(1:round(size(yPts,1)/2));
yPtsHalf2=yPts(round(size(yPts,1)/2)+1:size(yPts,1));
% Evaluate the 1st and 2nd derivative of zPart at yPts using forward
and
% backward approximations for yPtsHalf1 and yPtsHalf2.
deriv1=[(zPart(yPtsHalf1+2*deltay)-
zPart(yPtsHalf1))/(2*deltay);(zPart(yPtsHalf2)-zPart(yPtsHalf2-
2*deltay))/(2*deltay)];
deriv2=[(zPart(yPtsHalf1+2*deltay)-
2*zPart(yPtsHalf1+deltay)+zPart(yPtsHalf1))/deltay^2;(zPart(yPtsHalf
2)-2*zPart(yPtsHalf2-deltay)+zPart(yPtsHalf2-2*deltay))/deltay^2];
% Evaluate Rpy based on the definition of the radius of curvature of
a
% function.
Rpy=(1+deriv1.^2).^ (3/2) ./deriv2;

% 2) Computation of Rpx
deltax=10^(-2); % Small increment in x
SLOPE=-1./deriv1; % Vector of the slopes of the normals to zPart at
yPts
% Preallocate the matrix containing yG and yH
yBandCs=zeros(size(yPts,1),2);
% Fill yGandyHs with the roots of f1 and f2 near y0.
for ii=1:size(yPts,1)
    SLOPEii=SLOPE(ii);y0=yPts(ii);
    yGandHs(ii,:)=abs([fzero(@f1,y0),fzero(@f2,y0)]);
end
% Evaluate the 1st and 2nd derivative of zPart at yPts using forward
% approximations.
deriv1_2=1./cos(atan(deriv1)).*(zPart(sqrt((2*deltax)^2+yGandHs(:,2)
.^2))-zPart(yPts))./(2*deltax);
deriv2_2=1./cos(atan(deriv1)).*(zPart(sqrt((2*deltax)^2+yGandHs(:,2)
.^2))-
2*zPart(sqrt(deltax^2+yGandHs(:,1).^2))+zPart(yPts))./deltax^2;
% evaluate Rpy based on the definition of the radius of curvature of
a
% function
Rpx=(1+deriv1_2.^2).^ (3/2) ./deriv2_2;

% Define the matrix containing the calculated radii of curvature.
1st
% column: y. 2nd column: Rpx. 3rd column: Rpy.
PROC=[yPts,Rpx,Rpy];

% Functions called by PartPrincipalROCEstimator

function z=f1(y)
% f1 is such that its root near y0 is yG
global SLOPEii y0 deltax
z=SLOPEii*(y-y0)+zPart(y0)-zPart(sqrt(deltax^2+y^2));

```

```
function z=f2(y)
% f2 is such that its root near y0 is yH
global SLOPEii y0 deltax
z=SLOPEii*(y-y0)+zPart(y0)-zPart(sqrt((2*deltax)^2+y^2));
```

Appendix 2 MATLAB code for tool path geometry

Code of the MATLAB function ToolPathGeomMaker.m

```

function [ToolPathGeom,PlotMatrix] =
ToolPathGeomMaker (TPDiscreteProfile,PDiscreteProfile)
% ToolPathGeomMaker: Function creating the tool path geometry.
% Reference: Chapter 3 on "Tool path geometry determination"
% Inputs: Matrices containing the tool and part discretized profiles
% Outputs: Matrices containing the tool path geometry and data to
plot the
% tool path

global Tgeom Pgeom TPgeom Larc AP5pP6p0

% *****
% *** Inputs assignment ***
% *****
% tool dimensions
LTool=Tgeom(1);
D1 = Tgeom(2);
D2 = Tgeom(3);
D3 = Tgeom(4);
D4 = Tgeom(5);
D5 = Tgeom(6);
D6 = Tgeom(7);
D7 = Tgeom(8);
D8 = Tgeom(9);
Rw=D1;
% safety region dimensions
S1=Tgeom(10);
S2=Tgeom(11);
% tool path parameters
Delta=TPgeom(4);
BlimPlus=TPgeom(5);
BlimMinus=TPgeom(6);
yMin=TPgeom(7);
yMax=TPgeom(8);
zMin=TPgeom(9);
zMax=TPgeom(10);
% offset (in mm) used for P7p
offs=50;
% *****
% *****
% *****

% *****
% *** Part matrix ***
% *****
% Define the matrix containing the coordinates of the points forming
the
% part 2D model. 1st column: y, 2nd column: z.

```

```

Part2DModel=[-
flipud(PDiscreteProfile(:,1)),flipud(PDiscreteProfile(:,2));PDiscret
eProfile];
% Remove point that might be repeated at part center
if Part2DModel(size(PDiscreteProfile,1),1)==0
    Part2DModel(size(PDiscreteProfile,1),:)=[];
end
% *****
% *****
% *****

% *****
% *** Inputs definition ***
% *****
% Define the matrix containing the coordinates of the points forming
the
% tool 2D model. 1st column: y, 2nd column: z. The lines 1 to 14
represent
% contain the coordinates of P7pp,P6pp,...,P1pp,P1p,P2p,...,P7p
aPSI=atan((D2-D1)/D6); % Angle for computation of P2p
aPSIp=atan((D5-D4)/(D8-D7)); % Angle for computation of P5p and P6p
ToolHalf2DModel=[ [D1+S2,D1]; [D2+S1*( (D1-D2)/D6+1/cos(aPSI) ),D1+D6-
S1]; [D3+S1,D1+D6-S1]; [D3+S1,D1+D6+D7-S1]; [D4+S1*( (D4-D5)/(D8-
D7)+1/cos(aPSIp) ),D1+D6+D7-S1]; [D5+S1,D1+D6+D8+S1*(1-
1/cos(aPSIp) )*( (D8-D7)/(D5-D4) ) ]; [D5+S1,D1+D6+D8+S1+offs]];
Tool2DModel=[-
flipud(ToolHalf2DModel(:,1)),flipud(ToolHalf2DModel(:,2));ToolHalf2D
Model];
AP5pP6p0=(D8-D7)/(D5-D4); % Slope at B=0 of (P5'P6')

% Define the matrix containing the polar coordinates of the points
forming
% the tool 2D model. 1st column: r, 2nd column: Theta.
Tool2DModelPC = [ ((Tool2DModel(:,1)).^2+(Tool2DModel(:,2)-
Rw).^2).^0.5,atan((Tool2DModel(:,2)-Rw)./Tool2DModel(:,1))];
idx=find(Tool2DModel(:,1)<=0); % find the points with y<=0
Tool2DModelPC(idx,2) = Tool2DModelPC(idx,2)+pi();

% Define the matrix containing the coordinates of the part points for
which
% the tool path geometry is computed. 1st column: y, 2nd column: z.
if TPDiscreteProfile(1,2)==0

TPPts=[[0,0];TPDiscreteProfile(2:2:size(TPDiscreteProfile,1),:)];
else
    TPPts=TPDiscreteProfile(1:2:size(TPDiscreteProfile,1),:);
end

% Define the maximum B angle, so that the toolpath is symmetric with
% respect to z.
Bmax=min(abs(BlimPlus),abs(BlimMinus))*pi()/180;

```

```

% Define the maximum permissible y translations, so that the
toolpath is
% symmetric with respect to z.
yTrMax=min(abs(yMin),abs(yMax));

% Define the vector containing Bjnorm
Deltay = 10^(-9); % small increment in y
Bnorm=atan((TPPts(:,2)-zPart(TPPts(:,1)-Deltay))/Deltay); %start at
Deltarow/2 so that B calculated at (0.5,1.5,2.5,...) otherwise use
zero to get (0,1,2,3,...)
if TPPts(1,1)==0
    Bnorm(1)=0;
end

% Define matrix containing the y and z offsets used to translate the
rotated tool along the tool path
% 1st column: y offset, 2nd column: z offset
TrMat=[-Rw*sin(Bnorm)+TPPts(:,1),-Rw*(1-cos(Bnorm))+TPPts(:,2)];
% *****
% *****
% *****

% *****
% *** B angle determination ***
% *****

if TPgeom(11)==0 % algorithms chosen according to part geometry
    if Pgeom(3)==1 % concave algorithms
        DeltaB=0.1*pi()/180; % increment (in rad) used for the
search of B

[PlotMatrix,BsolMatrix]=TPGeomConcave(Part2DModel,Tool2DModelPC,Bmax
,Bnorm,TrMat,Rw,TPPts,DeltaB);
    elseif Pgeom(3)==-1 % convex algorithms

[PlotMatrix,BsolMatrix]=TPGeomConvex(Part2DModel,Tool2DModelPC,Bmax,
Bnorm,TrMat,Rw,TPPts);
    end
elseif TPgeom(11)==1 % generic algorithms
    DeltaB=0.1*pi()/180; % increment (in rad) used for the
search of B

[PlotMatrix,BsolMatrix]=TPGeomGeneric(Part2DModel,Tool2DModelPC,Bmax
,Bnorm,TrMat,Rw,TPPts,DeltaB);
end
% *****
% *****
% *****

% *****
% *** Pivot point coordinates calculation ***
% *****
% Define the matrix containing the tool path geometry. 1st and 2nd
column:

```



```

% y and z coordinates, respectively, of the pivot point. 3rd column:
B.
% 4th and 5th column are preallocated for tool crossfeed velocity
and time
% for each tool path step
% But if an error code is encountered, the outputted matrix is a
scalar
% equal to the error code.
if size(BsolMatrix,1)==1
    ToolPathGeom=BsolMatrix;
else
    y0=TPPts(:,1); % y coordinates of the part points of interest
    z0=TPPts(:,2); % z coordinates of the part points of interest
    Bsol=BsolMatrix(:,2); % B angle to apply
    ToolPathGeom=[y0+(Rw-Delta)*sin(-Bnorm)+(LTool-Rw)*sin(-
Bsol), z0+(Rw-Delta)*cos(-Bnorm)+(LTool-Rw)*cos(-Bsol), -
180/pi*Bsol, zeros(size(TPPts,1),1), Larc*ones(size(TPPts,1),1)];
    % Test feasibility of the positions established for the pivot
point
    if
min(abs(ToolPathGeom(:,1))<=yTrMax)*min(ToolPathGeom(:,2)<=zMax)*min
(ToolPathGeom(:,2)>=zMin)==0
        % if these positions cannot be reached error code 4 is
outputted
        ToolPathGeom=4;
    end
end
end
% *****
% *****
% *****

```

Code of the MATLAB function TPGeomConvex.m

```

function
[PlotMatrix,BsolMatrix]=TPGeomConvex(Part2DModelIN,Tool2DModelPCIN,B
max,Bnorm,TrMatIN,RwIN,TPPts)
% TPGeomConvex: Function verifying than on a convex part, the
preferred
% tool path configuration (tool and part normals aligned) can be
achieved
% along the tool path
% Reference: Chapter 3 on "Tool path geometry determination"
% Inputs: Matrices containing the tool and part discretized
profiles,
% maximum permissible B angle. Vector containing Bnorm. Matrix
containing
% the y and z offsets used to translate the rotated tool along the
tool
% path. Carrier wheel radius. Matrix contining the coordinates of
the part

```

```

% points for which the tool path geometry is computed.
% Outputs: Matrix containing data to plot the tool path. Matrix
containing
% the B angle and corresponding y0j to use for a collision-free tool
path.

global Rw TrMat Part2DModel Tool2DModelPC

% Inputs assignment
TrMat=TrMatIN;
Tool2DModelPC=Tool2DModelPCIN;
Part2DModel=Part2DModelIN;
Rw=RwIN;

% Preset the variable indicating the error code.
ErrorCode=0;
% Preallocate the matrices containing the outputted B angles and
data for
% plotting.
Bsol=zeros(size(Bnorm));
PlotToolMatrix=zeros(28,size(TPPTS,1));
% Loop defining B along the tool path.
jj=0;
while jj+1<=size(TPPTS,1) && ErrorCode==0
    jj=jj+1;
    % Set B equal to desired angle = angle of local part normal if
not
    % larger than Bmax, otherwise set equal to Bmax.
    if abs(Bnorm(jj))>Bmax
        if Bnorm(jj)>0
            Bsol(jj)=Bmax;
        else
            Bsol(jj)=-Bmax;
        end
    else
        Bsol(jj)=Bnorm(jj);
    end
    % Rotate and translate the tool to contact the jjth part points
for
    % which the tool path geometry is computed and store the
coordinates of
    % the points forming the tool model.
    PlotToolMatrix(:,jj)=ToolRotation(Bsol(jj),jj);
    % Check for tool-part collision.

test=TestPtInterior(Bsol(jj),jj);%test(jj)=TestPtInterior(Bsol(jj),j
j);

% Define ErrorCode, based on occurrence of tool-part collision.
if test>=1
    if TPPTS(jj,1)==0 % check if part center
        if test==2
            ErrorCode=2;

```

```

        else
            ErrorCode=1;
        end
    else
        if test==2
            ErrorCode=2;
        else
            ErrorCode=3;
        end
    end
end
end

% Define BsolMatrix.
if ErrorCode~=0 % If error found, pass error code in BsolMatrix.
    BsolMatrix=ErrorCode;
else % Store the solution in BsolMatrix. 1st column: y0j, 2nd
column: Bsol.
    BsolMatrix=[TPPts(:,1),Bsol];
end
% Define the matrix containing the data for plotting the tool path.
1st
% and 2nd lines: transpose of TPPts. 3rd line: B angle solutions in
degrees
% as used to program UFF. 4th line: difference between Bnorm and
Bsol. 5th
% and 6th lines: transpose of TrMat. 7th line: PlotToolMatrix.
PlotMatrix=[TPPts';-180/pi()*Bsol';-180/pi()*(Bnorm-
Bsol)';TrMat';PlotToolMatrix];

```

Code of the MATLAB function TPGeomConcave.m

```

function
[PlotMatrix,BsolMatrix]=TPGeomConcave(Part2DModelIN,Tool2DModelPCIN,
Bmax,Bnorm,TrMatIN,RwIN,TPPts,DeltaB)
% TPGeomConcave: Function establishing the B angles preventing tool-
part
% collisions along the tool path. The search strategy is optimized
for deep
% concave surfaces.
% Reference: Chapter 3 on "Tool path geometry determination"
% Inputs: Matrices containing the tool and part discretized
profiles,
% maximum permissible B angle. Vector containing Bjnorm. Matrix
containing
% the y and z offsets used to translate the rotated tool along the
tool
% path. Carrier wheel radius. Matrix containing the coordinates of
the part
% points for which the tool path geometry is computed.

```

```

% Outputs: Matrix containing data to plot the tool path. Matrix
containing
% the B angle and corresponding y0j to use for a collision-free tool
path.

global Rw TrMat Part2DModel Tool2DModelPC

% Inputs assignment
TrMat=TrMatIN;
Tool2DModelPC=Tool2DModelPCIN;
Part2DModel=Part2DModelIN;
Rw=RwIN;

% Preset the variable indicating the error code.
ErrorCode=0;
% Preallocate the matrices containing the outputted B angles and
data for
% plotting.
Bsol=zeros(size(Bnorm));
PlotToolMatrix=zeros(28,size(TPPTS,1));
% Loop defining B along the tool path.
jj=0;
while jj+1<=size(TPPTS,1) && ErrorCode==0
    jj=jj+1;
    % Set B equal to desired angle = angle of local part normal.
    B=Bnorm(jj);
    % Rotate and translate the tool to contact the jjth part points
for
    % which the tool path geometry is computed and store the
coordinates of
    % the points forming the tool model.
    PlotToolMatrix(:,jj)=ToolRotation(B,jj); %rotated/translated
tool
    % check for tool-part collision.
    test=TestPtInterior(B,jj);

    % "fast" algorithms finding a safe B angle
    if test~=0 || abs(B)>Bmax % if collision, set Bj = Bj-1.
        % If j=1, set = 0.
        if jj==1
            B=0;
        else
            B=Bsol(jj-1);
        end
        % If previous solution was Bmax, the current one is set
equal to
        % Bmax if no collision is predicted.
        if B==Bmax
            % Rotate and translate the tool to contact the jjth part
points
            % for which the tool path geometry is computed and store
the
            % coordinates of the points forming the tool model.

```

```

PlotToolMatrix(:,jj)=ToolRotation(B,jj);
% Check for tool-part collision.
test=TestPtInterior(B,jj);
if test==0
    Bsol(jj)=Bmax;
end
else
% Rotate and translate the tool to contact the jjth part
points
% for which the tool path geometry is computed and store
the
% coordinates of the points forming the tool model.
PlotToolMatrix(:,jj)=ToolRotation(B,jj);
% Check for tool-part collision.
test=TestPtInterior(B,jj);
if test==0
    % If no collision with previous solution, DeltaB is
added
    % to B until collision occurs.
    while test==0
        B=B+DeltaB;
        % Rotate and translate the tool to contact the
jjth
        % part points for which the tool path geometry
is
        % computed and store the coordinates of the
points
        % forming the tool model.
        PlotToolMatrix(:,jj)=ToolRotation(B,jj);
        % Check for tool-part collision.
        test=TestPtInterior(B,jj);
    end
    % Once collision is detected, Bsol is set equal to
B-DeltaB
    % to compensate for last operation leading to
collision.
    Bsol(jj)=B-DeltaB;
    % Reset value of test.
    test=0;
end
end
else % if no collision, set equal to the preferred angle
    Bsol(jj)=Bnorm(jj);
end

% If statement detecting the first solution larger than Bmax.
That
% solution is replaced by Bmax if no collision occurs. This "if"
% section is only used once, the section starting with "if
B=Bmax"
% will act to replace the following solutions.
if test==0 && abs(Bsol(jj))>=Bmax
    Bsol(jj)=Bmax;

```

```

    % Rotate and translate the tool to contact the jjth part
points
    % for which the tool path geometry is computed and store the
    % coordinates of the points forming the tool model.
    PlotToolMatrix(:,jj)=ToolRotation(Bmax,jj);
    % Check for tool-part collision.
    test=TestPtInterior(Bmax,jj);
end

% Define ErrorCode, based on occurrence of tool-part collision.
if test>=1
    if TPPTs(jj,1)==0 % check if part center
        if test==2
            ErrorCode=2;
        else
            ErrorCode=1;
        end
    else
        if test==2
            ErrorCode=2;
        else
            ErrorCode=3;
        end
    end
end
end

% Define BsolMatrix.
if ErrorCode~=0 % If error found, pass error code in BsolMatrix.
    BsolMatrix=ErrorCode;
else % Store the solution in BsolMatrix. 1st column: y0j, 2nd
column: Bsol.
    BsolMatrix=[TPPTs(:,1),Bsol];
end

% Define the matrix containing the data for plotting the tool path.
1st
% and 2nd lines: transpose of TPPTs. 3rd line: B angle solutions in
degrees
% as used to program UFF. 4th line: difference between Bnorm and
Bsol. 5th
% and 6th lines: transpose of TrMat. 7th line: PlotToolMatrix.
PlotMatrix=[TPPTs';-180/pi()*Bsol';-180/pi()*(Bnorm-
Bsol)';TrMat';PlotToolMatrix];

```

Code of the MATLAB function TPGeomGeneric.m

```

function
[PlotMatrix,BsolMatrix]=TPGeomGeneric(Part2DModelIN,Tool2DModelPCIN,
Bmax,Bnorm,TrMatIN,RwIN,TPPts,DeltaB)
% TPGeomGeneric: Function establishing the B angles preventing tool-
part
% collisions along the tool path for all types of geometries.
% Reference: Chapter 3 on "Tool path geometry determination"
% Inputs: Matrices containing the tool and part discretized
profiles,
% maximum permissible B angle. Vector containing Bjnorm. Matrix
containing
% the y and z offsets used to translate the rotated tool along the
tool
% path. Carrier wheel radius. Matrix containing the coordinates of
the part
% points for which the tool path geometry is computed.
% Outputs: Matrix containing data to plot the tool path. Matrix
containing
% the B angle and corresponding y0j to use for a collision-free tool
path.

global Rw TrMat Part2DModel Tool2DModelPC

% Inputs assignment
TrMat=TrMatIN;
Tool2DModelPC=Tool2DModelPCIN;
Part2DModel=Part2DModelIN;
Rw=RwIN;

% Preset the variable indicating the error code.
ErrorCode=0;
% Preallocate the matrices containing the outputted B angles and
data for
% plotting.
Bsol=zeros(size(Bnorm));
PlotToolMatrix=zeros(28,size(TPPts,1));
% Loop defining B along the tool path.
jj=0;
while jj+1<=size(TPPts,1) && ErrorCode==0 %stop before covering edge
thickness
    jj=jj+1;
    % Set B equal to desired angle = angle of local part normal if
not
    % larger than Bmax or lower than -Bmax, otherwise set equal to
Bmax or
    % -Bmax, respectively.
    if abs(Bnorm(jj))>Bmax
        if Bnorm(jj)>0
            B=Bmax;
        else

```

```

        B=-Bmax;
    end
else
    B=Bnorm(jj);
end
Bsol(jj)=B;
% Rotate and translate the tool to contact the jjth part points
for
% which the tool path geometry is computed and store the
coordinates of
% the points forming the tool model.
PlotToolMatrix(:,jj)=ToolRotation(B,jj);
% Check for tool-part collision.
test=TestPtInterior(B,jj);

% Algorithms finding a safe B angle
if test>=1 % if a collision is detected, set Bj=Bj-1.
    if jj-1==0
        B=0;
    else
        B=Bsol(jj-1);
    end
% Rotate and translate the tool to contact the jjth part
points
% for which the tool path geometry is computed and store the
% coordinates of the points forming the tool model.
PlotToolMatrix(:,jj)=ToolRotation(B,jj);
% Check for tool-part collision.
test=TestPtInterior(B,jj);
% If no collision is detected, try to set B "closer" to
Bnorm.
if test==0
    if B>Bnorm(jj) %if B>Bnorm, decrease B until collision
        while test==0 && B>=Bnorm(jj)
            B=B-DeltaB;
            % Rotate and translate the tool to contact the
jjth
            % part points for which the tool path geometry
is
            % computed and store the coordinates of the
points
            % forming the tool model.
            PlotToolMatrix(:,jj)=ToolRotation(B,jj);
            % Check for tool-part collision.
            test=TestPtInterior(B,jj);
        end
        % Once collision is detected, undo the last
operation.
        Bsol(jj)=B+DeltaB;
        % Reset value of test.
        test=0;
    else % if B<Bnorm, increase B until collision
        while test==0 && B<=Bnorm(jj)

```



```

        B=B+DeltaB;
        % Rotate and translate the tool to contact the
jjth
        % part points for which the tool path geometry
is
        % computed and store the coordinates of the
points
        % forming the tool model.
        PlotToolMatrix(:,jj)=ToolRotation(B,jj);
        % Check for tool-part collision.
        test=TestPtInterior(B,jj);
    end
    % Once collision is detected, undo the last
operation.
        Bsol(jj)=B-DeltaB;
        % Reset value of test.
        test=0;
    end
    % Rotate and translate the tool to contact the jjth part
points
    % for which the tool path geometry is computed and store
the
    % coordinates of the points forming the tool model.
    PlotToolMatrix(:,jj)=ToolRotation(Bsol(jj),jj);
else % If a collision is detected,
B0=B; % Store initial value of B,
% Search is first performed in direction following
solution
    % trend.
    if jj==1 || jj==2 || Bsol(jj-1)>=Bsol(jj-2)
        while test~=0 && abs(B+DeltaB)<=Bmax
            B=B+DeltaB;
            PlotToolMatrix(:,jj)=ToolRotation(B,jj);
            test=TestPtInterior(B,jj);
        end
    else
        while test~=0 && abs(B-DeltaB)<=Bmax
            B=B-DeltaB;
            PlotToolMatrix(:,jj)=ToolRotation(B,jj);
            test=TestPtInterior(B,jj);
        end
    end
    % If no solution is found, the other search direction is
used.
    if test~=0 || abs(B)>Bmax
        % Set B equal to the initial search value.
        B=B0;
        if jj==1 || jj==2 || Bsol(jj-1)>=Bsol(jj-2)
            while test~=0 && abs(B-DeltaB)<=Bmax
                B=B-DeltaB;
                PlotToolMatrix(:,jj)=ToolRotation(B,jj);
                test=TestPtInterior(B,jj);
            end
        else

```

```

        while test~=0 && abs(B+DeltaB)<=Bmax
            B=B+DeltaB;
            PlotToolMatrix(:,jj)=ToolRotation(B,jj);
            test=TestPtInterior(B,jj);
        end
    end
end
if test==0
    if abs(B)<=Bmax
        Bsol(jj)=B;
    else
        test=3; % Set test to get ErrorCode=3.
    end
end
end
end

% Define ErrorCode, based on occurrence of tool-part collision.
if test>=1
    if TPPTs(jj,1)==0 % check if part center
        if test==2
            ErrorCode=2;
        else
            ErrorCode=1;
        end
    else
        if test==2
            ErrorCode=2;
        else
            ErrorCode=3;
        end
    end
end
end

end

% Define BsolMatrix.
if ErrorCode~=0 % If error found, pass error code in BsolMatrix.
    BsolMatrix=ErrorCode;
else % Store the solution in BsolMatrix. 1st column: y0j, 2nd
column: Bsol.
    BsolMatrix=[TPPTs(:,1),Bsol];
end
% Define the matrix containing the data for plotting the tool path.
1st
% and 2nd lines: transpose of TPPTs. 3rd line: B angle solutions in
degrees
% as used to program UFF. 4th line: difference between Bnorm and
Bsol. 5th
% and 6th lines: transpose of TrMat. 7th line: PlotToolMatrix.
PlotMatrix=[TPPTs';-180/pi()*Bsol';-180/pi()* (Bnorm-
Bsol)';TrMat';PlotToolMatrix];

```

Code of the MATLAB function ToolRotation.m

```

function PlotTool2DMoRT=ToolRotation(B,jj)
% ToolRotation: Function computing the coordinates of the points
forming
% the rotated and translated tool 2D model and the coefficients A,
% B, C and D used to define the lines passing through these points.
% Reference: Chapter 3 on "Tool path geometry determination"
% Inputs: Value of B and index of the point of the part at which the
tool
% path geometry is computed.
% Outputs: Vector containing the coordinates of the points forming
the
% rotated and translated tool 2D model for tool path plot. The
coefficients
% A, B, C, D of all the lines of interest are stored in vectors
defined as
% global.

global Rw TrMat Tool2DModelPC
global Avect Bvect Cvect Dvect

% Define the matrix containing the coordinates of the points forming
the
% part 2D model after rotation and translation to achieve contact at
the
% jjth point of the tool path. 1st column: y, 2nd column: z.
Tool2DMoRT=[Tool2DModelPC(:,1).*cos(Tool2DModelPC(:,2)+B)+TrMat(jj,1)
),Tool2DModelPC(:,1).*sin(Tool2DModelPC(:,2)+B)+Rw+TrMat(jj,2)];
PlotTool2DMoRT=[Tool2DMoRT(:,1);Tool2DMoRT(:,2)];%stored in 1 line
for plot

% Define the vectors containing the coefficients A, B, C, D for the
lines
%
% (P6'P6"); (P5'P5"); (P3'P3"); (P1'P1"); (P6'P7'); (P6"P7"); (P5'P6'); (P5"
P6");
% (P3'P4'); (P3"P4"); (P1'P2'); (P1"P2") ]
Vect1=[Tool2DMoRT(13,:);Tool2DMoRT(12,:);Tool2DMoRT(10,:);Tool2DMoRT
(8,:);Tool2DMoRT(14,:);Tool2DMoRT(1,:);Tool2DMoRT(13,:);Tool2DMoRT(2
,:);Tool2DMoRT(11,:);Tool2DMoRT(4,:);Tool2DMoRT(9,:);Tool2DMoRT(6,:)
];
Vect2=[Tool2DMoRT(2,:);Tool2DMoRT(3,:);Tool2DMoRT(5,:);Tool2DMoRT(7,
:);Tool2DMoRT(13,:);Tool2DMoRT(2,:);Tool2DMoRT(12,:);Tool2DMoRT(3,:)
;Tool2DMoRT(10,:);Tool2DMoRT(5,:);Tool2DMoRT(8,:);Tool2DMoRT(7,:)]

Avect=(Vect2(:,2)-Vect1(:,2))./(Vect2(:,1)-Vect1(:,1));
Bvect=(Vect2(:,2).*Vect1(:,1)-Vect1(:,2).*Vect2(:,1))./(Vect1(:,1)-
Vect2(:,1));
Cvect=1./Avect;
Dvect=(Vect2(:,1).*Vect1(:,2)-Vect1(:,1).*Vect2(:,2))./(Vect1(:,2)-
Vect2(:,2));

```

Code of the MATLAB function TestPtInterior.m

```

function test=TestPtInterior(B,jj)
% ToolPtInterior: Function determining if any point of the part
model
% becomes interior to the tool interior and safety region.
% Reference: Chapter 3 on "Tool path geometry determination"
% Inputs: Value of B and index of the point of the part at which the
tool
% path geometry is computed.
% Outputs: Scalar, test, indicating if no collision (test=0), a
collision
% in the carrier wheel region (test=2) or another type of collision
% (test=1) is predicted.

global Rw TrMat Part2DModel AP5pP6p0
global Avect Bvect Cvect Dvect

% Preset the variable indicating the occurrence of tool-part
collisions
test=0;

% Region 0: circle modeling the carrier wheel
test01=Part2DModel(:,2)<Rw+TrMat(jj,2)+(Rw^2-(Part2DModel(:,1)-
TrMat(jj,1)).^2).^0.5;
test02=Part2DModel(:,2)>Rw+TrMat(jj,2)-(Rw^2-(Part2DModel(:,1)-
TrMat(jj,1)).^2).^0.5;
% if test01 and test02 are positive, a part point is within the
carrier
% wheel
if max(test01+test02)==2
    test=2;
end

% if no collision in the carrier wheel region, the other regions are
% considered by establishing the relative position of the points
modeling
% the part with respect to the lines delimiting the different
regions.
if test==0
    % Region (1)
    % (P1"P2")
    if abs(Avect(12))>=1

test1=Part2DModel(:,1)>=Cvect(12)*Part2DModel(:,2)+Dvect(12);
    else
        if B>0

test1=Part2DModel(:,2)>=Avect(12)*Part2DModel(:,1)+Bvect(12);
        else

test1=Part2DModel(:,2)<=Avect(12)*Part2DModel(:,1)+Bvect(12);

```

```

        end
    end
    % (P1'P2')
    if abs(Avect(11))>=1
test2=Part2DModel(:,1)<=Cvect(11)*Part2DModel(:,2)+Dvect(11);
        else
            if B>0
test2=Part2DModel(:,2)<=Avect(11)*Part2DModel(:,1)+Bvect(11);
                else
test2=Part2DModel(:,2)>=Avect(11)*Part2DModel(:,1)+Bvect(11);
                    end
                end
            % (P1'P1")
            if abs(Cvect(4))>=1
                test3=Part2DModel(:,2)>=Avect(4)*Part2DModel(:,1)+Bvect(4);
            else
                if B>0
test3=Part2DModel(:,1)<=Cvect(4)*Part2DModel(:,2)+Dvect(4);
                    else
test3=Part2DModel(:,1)>=Cvect(4)*Part2DModel(:,2)+Dvect(4);
                        end
                    end
                % (P2'P2")
                if abs(Cvect(3))>=1
                    test4=Part2DModel(:,2)<=Avect(3)*Part2DModel(:,1)+Bvect(3);
                else
                    if B>0
test4=Part2DModel(:,1)>=Cvect(3)*Part2DModel(:,2)+Dvect(3);
                        else
test4=Part2DModel(:,1)<=Cvect(3)*Part2DModel(:,2)+Dvect(3);
                            end
                        end
                    % if test1, test2, test3 and test4 are positive, the point is
                    within
                    % region (1)
                    if max(test1+test2+test3+test4)==4
                        test=1;
                    end

                    % Region (2)
                    % (P3"P4")
                    if abs(Avect(10))>=1
test5=Part2DModel(:,1)>=Cvect(10)*Part2DModel(:,2)+Dvect(10);
                        else
                            if B>0

```

```

test5=Part2DModel(:,2)>=Avect(10)*Part2DModel(:,1)+Bvect(10);
    else

test5=Part2DModel(:,2)<=Avect(10)*Part2DModel(:,1)+Bvect(10);
    end
end
% (P3'P4')
if abs(Avect(9))>=1
    test6=Part2DModel(:,1)<=Cvect(9)*Part2DModel(:,2)+Dvect(9);
else
    if B>0

test6=Part2DModel(:,2)<=Avect(9)*Part2DModel(:,1)+Bvect(9);
    else

test6=Part2DModel(:,2)>=Avect(9)*Part2DModel(:,1)+Bvect(9);
    end
end
% (P3'P3")
if abs(Cvect(3))>=1
    test7=Part2DModel(:,2)>=Avect(3)*Part2DModel(:,1)+Bvect(3);
else
    if B>0

test7=Part2DModel(:,1)<=Cvect(3)*Part2DModel(:,2)+Dvect(3);
    else

test7=Part2DModel(:,1)>=Cvect(3)*Part2DModel(:,2)+Dvect(3);
    end
end
% (P4'P4")
if abs(Cvect(2))>=1
    test8=Part2DModel(:,2)<=Avect(2)*Part2DModel(:,1)+Bvect(2);
else
    if B>0

test8=Part2DModel(:,1)>=Cvect(2)*Part2DModel(:,2)+Dvect(2);
    else

test8=Part2DModel(:,1)<=Cvect(2)*Part2DModel(:,2)+Dvect(2);
    end
end
if max(test5+test6+test7+test8)==4
    test=1;
end

% Region (3)
% (P5"P6") - take into account the slope at B=0
if abs(AP5pP6p0)==1
    if B>=0

test9=Part2DModel(:,2)>=Avect(8)*Part2DModel(:,1)+Bvect(8);

```



```

        if single(abs(Cvect(7)))>=1
test10=Part2DModel(:,2)>=Avect(7)*Part2DModel(:,1)+Bvect(7);
        else
            if B>0
test10=Part2DModel(:,1)<=Cvect(7)*Part2DModel(:,2)+Dvect(7);
            else
test10=Part2DModel(:,1)>=Cvect(7)*Part2DModel(:,2)+Dvect(7);
            end
        end
    end
    end
    % (P5'P5")
    if abs(Cvect(2))>=1
        test11=Part2DModel(:,2)>=Avect(2)*Part2DModel(:,1)+Bvect(2);
    else
        if B>0
test11=Part2DModel(:,1)<=Cvect(2)*Part2DModel(:,2)+Dvect(2);
        else
test11=Part2DModel(:,1)>=Cvect(2)*Part2DModel(:,2)+Dvect(2);
        end
    end
    end
    % (P6'P6")
    if abs(Cvect(1))>=1
        test12=Part2DModel(:,2)<=Avect(1)*Part2DModel(:,1)+Bvect(1);
    else
        if B>0
test12=Part2DModel(:,1)>=Cvect(1)*Part2DModel(:,2)+Dvect(1);
        else
test12=Part2DModel(:,1)<=Cvect(1)*Part2DModel(:,2)+Dvect(1);
        end
    end
    end
    if max(test9+test10+test11+test12)==4
        test=1;
    end
    end
    % Region (4)
    % (P6"P7")
    if abs(Avect(6))>=1
        test13=Part2DModel(:,1)>=Cvect(6)*Part2DModel(:,2)+Dvect(6);
    else
        if B>0
test13=Part2DModel(:,2)>=Avect(6)*Part2DModel(:,1)+Bvect(6);
        else
test13=Part2DModel(:,2)<=Avect(6)*Part2DModel(:,1)+Bvect(6);
        end
    end
    end

```



```

end
% (P6'P7')
if abs(Avect(5))>=1
    test14=Part2DModel(:,1)<=Cvect(5)*Part2DModel(:,2)+Dvect(5);
else
    if B>0

test14=Part2DModel(:,2)<=Avect(5)*Part2DModel(:,1)+Bvect(5);
        else

test14=Part2DModel(:,2)>=Avect(5)*Part2DModel(:,1)+Bvect(5);
        end
    end
    % (P6'P6")
    if abs(Cvect(1))>=1
        test15=Part2DModel(:,2)>=Avect(1)*Part2DModel(:,1)+Bvect(1);
    else
        if B>0

test15=Part2DModel(:,1)<=Cvect(1)*Part2DModel(:,2)+Dvect(1);
            else

test15=Part2DModel(:,1)>=Cvect(1)*Part2DModel(:,2)+Dvect(1);
            end
        end
        if max(test13+test14+test15)==3
            test=1;
        end
    end
end

```